

Diss. ETH No. 20429

# **Interaction Mechanisms Between Rim Seal Purge Flow and Profiled End Walls in a Low-Pressure Turbine**

A dissertation submitted to

**ETH ZURICH**

for the degree of

**Doctor of Sciences**

presented by

**PHILIPP JENNY**

Master of Science - Mechanical Engineering ETH  
Master of Science - Aeronautical Engineering ISAE

born August 05, 1982

citizen of Glarus, Switzerland

accepted on the recommendation of  
Prof. Dr. Reza S. Abhari, examiner  
Prof. Dr. Michael G. Dunn, co-examiner  
PD Dr. Martin G. Rose, co-examiner

Zurich 2012



# Acknowledgements

The work leading to the results of this thesis is the outcome of a joint industrial and academic research program between the Laboratory of Energy Conversion at the ETH Zurich and MTU Aero Engines in Munich. The program was part of the “Luftforschungsprogramm LuFo4“ supported by the German Federal Ministry of Economics and Technology.

First I would like to thank Professor Dr. Reza S. Abhari for his guidance and for the challenging and goal-oriented inputs during the last four years. He has given me the opportunity to run a complex and multidisciplinary project in a very dynamic working environment, a great experience for which I am thankful.

Special thanks go to Professor Dr. Michael G. Dunn for accepting the role as co-examiner. I feel honoured to have him as a co-examiner for this thesis.

I owe a dept of gratitude to PD Dr. Martin G. Rose for his patience and for all the countless hours of discussion and explanation related to turbine aero- and thermodynamics, on the phone, by e-mail or during meetings. He is a very motivating teacher and a never-ending source of ideas.

I would like to thank the industrial partner MTU Aero Engines for the intellectual and financial support. Special thanks go to Dr. Jochen Gier for his helpful technical comments and reviews and to Dr. Irene Raab for the management of the project on the industry side.

I gratefully acknowledge Dr. Peter Schüpbach who was my predecessors on this project and from whom I have learnt many very useful things which turned out to be reliable and efficient guidelines during my work.

I would like to thank Dr. Christian Lenherr for his support with the instrumentation and for sharing with me the nearly endless measurement days during my first measurement campaign.

Many special thanks go to the colleagues at the laboratory for their support and encouragement. It was a pleasure to be part of such a dynamic and friendly team. I would like to specially acknowledge the cooperative support and help of Dr. Michel Mansour when I was using his probe. Many thanks go to my test rig neighbour Armin Zemp for his continuous and very competent help with issues related to Ansys, for the interesting discussions and for the many great hours we spent together, in the office, in the machine hall or outside of ETH. I would also like to thank Altug Basol for the enlightening CFD discussions. Special thanks go to Marlene Hegner for the very competent and efficient management of all administrative issues and for all the smiles.

Ein herzliches Dankeschön geht auch an das Werkstatt Team, namentlich Hans Suter, Thomas Künzle, Rolf Rütimann und Claudio Troller. Dank Ihrer präzisen Arbeit und den vielen hilfreichen Ideen waren Sie massgeblich am Gelingen dieser Arbeit beteiligt. Ich möchte mich auch Bei Cornel Reshef möchte ich mich für seine Unterstützung und Geduld im Zusammenhang mit der Datenerfassung danken.

I would like to thank the famous and entertaining coffee and lunch group consisting of Rachel Schwitter, Armin Zemp und Dr. Peter Schüpbach for all the encouraging and memorable moments, particularly during challenging times in the first part of this work.

Finally I want to thank my family for their support and patience and for providing a safe place in stormy times.

Zurich, April 2012  
Philipp Jenny

# Abstract

The principle scope of this research work is the understanding of the influence of non-axisymmetric rotor end wall profiling on the unsteady interaction between the rim seal purge flow and the rotor secondary flows. Rotor end wall profiling is used to mitigate the negative effects on the turbine performance caused by the rim seal purge flow injected between the first nozzle guide vane and the rotor. Experimental investigations in low-pressure turbine representative conditions are carried out. In the open literature the amount of available experimental taken in rotating machines is very limited and the unsteady interaction between injected purge flow and the rotor secondary flows has not been experimentally investigated in great detail.

For this work, the unshrouded rotor of the standard 1.5-stage turbine configuration of the experimental research facility at the LEC was replaced by a shrouded rotor with the same blade count, but with thinner airfoils more representative of a low-pressure rotor. Two sets of non-axisymmetric end walls for the hub and the shroud were designed and experimentally compared to an axisymmetric rotor. The purge flow was included in the end wall design process. For each of the three rotor geometries measurements were made at three purge flow injection rates providing a consistent 3x3 result matrix for the study. The main measurement probe technology used in the context of this experimental investigation are the two-sensor fast response aerodynamic probe (FRAP) and the fast entropy probe (FENT). In addition, the results of time-accurate RANS simulations are compared to the measurements and the computations are also used to detail the flow field inside the rotor blade row where no probe data can be acquired.

Both designs of the non-axisymmetric end walls showed the beneficial effects in improved measured total-to-total turbine stage efficiency by  $0.75\% \pm 0.32\%$  and  $1.05\% \pm 0.32\%$  respectively. Furthermore the inclusion of the purge flow in the end wall design process was also successful giving a 30% reduction in sensitivity to purge flow. Or in other words the second end wall design was found to provide an efficiency compensation equivalent to 0.8% of additional purge flow. The efficiency benefits are primarily caused by

an improved flow field in the rotor hub region. For instance the measured average radial migration, circulation and unsteadiness of the rotor hub passage vortex were significantly reduced in the presence of profiled end walls. Furthermore, for all tested rotor geometries the purge flow was found to strongly interact with the rotor hub passage vortex and to reduce the beneficial effects of the end wall profiling. Additional purge flow was found to increase the radial migration, unsteadiness and circulation of the rotor hub passage vortex, however with different sensitivities depending on the rotor geometry. Hence the effects on the rotor hub secondary flows caused by the purge flow and the end wall profiling are intrinsically similar. A proposed approach to quantify the additional loss generated in the rotor flow field by the purge flow complements the presented analysis.

For the operating point under investigation two of the three tested rotors have pressure side separations that were detected by the time-accurate predictions. The first non-axisymmetric end wall design positively influences the unsteady size and shape of the pressure side bubble and also causes the bubble fluid to be shed and convected out of the rotor blade row at reduced mixing loss. Additional purge flow increases the volume of the pressure side bubble and the amount of fluid that is shed, but does not appear to be the principal reason for the separation.

For the first time the rim seal purge flow was present in the CFD calculations during the end wall design process and the optimiser had the possibility to modify the shape of the entire hub and tip end wall platform. As a consequence the rotor hub end wall profiling goes up to the leading edge of the rotor hub platform, giving it a wavy shape. Therefore not only the flow field between the leading and trailing edges is affected, but also the rim seal cavity exit flow field is significantly influenced by the end wall design. Beside other changes to the flow field, the results revealed a reduction of the maximum radial velocities and more homogenous mass flow distribution at the rim seal exit.

The unsteady spatial movement of the rotor hub loss core caused by the blade row interaction and the resulting consequences for the downstream nozzle guide vane were analysed based on the time-resolved measurements at the rotor exit. The centre of the rotor hub loss core was found to oscillate in the circumferential and radial direction by approximately 10% span and 40% rotor pitch respectively in the presence of the potential field of the second nozzle guide vane. The amount of injected rim seal purge flow was found to affect the overall radial height and the dynamics of the orbit of the rotor hub loss core, but not its maximum amplitudes.

# Kurzfassung

Die vorliegende Forschungsarbeit untersucht den Einfluss von nicht-rotationssymmetrischen Laufradseitenwänden auf die instationäre Wechselwirkung zwischen der Rotorscheibenkühlluft und den Sekundärströmungen des Laufrades. Die untersuchte Kühlluft wurde zwischen dem Leit- und dem Laufrad eingedüst. Die Seitenwandkonturierung wird verwendet, um die negativen Auswirkungen auf die Leistung der Turbine, welche durch die Rotorscheibenkühlluft verursacht werden, abzuschwächen. Diese Arbeit präsentiert Resultate aus Messungen welche in realitätsnahen Bedingungen für Niederdruckturbinen durchgeführt wurden. Die Anzahl der Publikationen zu diesem Themenbereich, welche auf experimentellen Daten von rotierenden Maschinen basieren, sind in der öffentlich zugänglichen Literatur sehr begrenzt. Die instationäre Interaktion zwischen Rotorscheibenkühlluft und den Sekundärströmungen des Laufrades wurde experimentell nicht im Detail analysiert.

Für diese Arbeit wurde das deckbandlose Standardlaufrad der bestehenden 1,5-stufigen Turbinenkonfiguration des Prüfstandes am LEC durch ein Laufrad mit Deckband ersetzt. Die neue Laufradgeometrie weist die gleiche Anzahl Schaufeln auf, diese sind jedoch dünner und entsprechen deshalb eher einer Niederdruckturbinengeometrie. Zwei Auslegungen der nichtrotationssymmetrischen Seitenwände an der Nabe und am Deckband wurden experimentell mit einem Laufrad mit zylindrischen Seitenwänden verglichen. Die Rotorscheibenkühlluft wurde in die Auslegung der Seitenwände mit einbezogen. Für jede der drei Laufradgeometrien wurden Messungen an drei verschiedenen Kühlluft Eindüsungsraten gemacht. Das ergibt eine konsistente 3x3 Datenmatrix welche der Untersuchung zu Grunde liegt. Das Strömungsfeld wurde am Eintritt und Austritt der Schaufelreihen anhand von pneumatischen und hochauflösenden schnellen Sonden vermessen. Zum einen sind das die pneumatischen Vier- und Fünflochsonden und zum anderen die schnelle aerodynamische 2-Sensor-Sonde (FRAP) und die schnelle Entropie Sonde (FENT). Darüber hinaus werden die experimentellen Ergebnisse durch entsprechende zeitaufgelöste numerische Simulationen ergänzt. Die Berechnungen werden auch verwendet, um das Strömungsfeld

innerhalb der Schaufelreihen, wo keine Sondenmessungen gemacht werden können, zu detaillieren.

Beide Auslegungen der nichtrotationssymmetrischen Seitenwände an der Nabe und am Deckband hatten eine signifikante Erhöhung des Turbinenwirkungsgrades zur Folge. Die erste Auslegung erhöhte den gemessenen Wirkungsgrad um  $0.75\% \pm 0.32\%$ , die zweite Auslegung um  $1.05\% \pm 0.32\%$  im Vergleich zum Laufrad mit rotationssymmetrischen Seitenwänden. Zudem hat sich die Miteinbeziehung der Rotorscheibenkühlluft in den Designprozess der Seitenwände positiv ausgewirkt. Der Abfall des Turbinenwirkungsgrades pro eingedüstem Kühlluftmassenstromprozent konnte um 30% reduziert werden. Oder mit anderen Worten kann die zweite Auslegung der nichtrotationssymmetrischen Seitenwände die Wirkungsgradeinbussen, welche durch 0.8% Kühlluft-Massenstrom verursacht werden, kompensieren. Die Hauptgründe für die Wirkungsgradsteigerung sind eine beträchtliche Verbesserung der Aerodynamik in der Region der Nabe. Zum Beispiel konnten die radiale Migration, die Zirkulation und das Turbulenzniveau des Passagenwirbels an der Nabe durch die Seitenwandkonturierung stark reduziert werden. Bei allen untersuchten Rotorgeometrien wurde eine starke Interaktion zwischen der an der Tellerranddichtung eingedüsten Kühlluft und dem Passagenwirbel festgestellt. Zusätzliche Kühlluft mindert jedoch die positiven Effekte der Seitenwandkonturierung; die radiale Migration, die Zirkulation und das Turbulenzniveau steigen proportional mit der Eindüsungsrate bei allen untersuchten Rotorgeometrien. Mit Hilfe der Seitenwandkonturierung werden die entsprechenden Sensitivitäten pro eingedüstem Massenstromprozent jedoch erfolgreich reduziert. Die Analyse des Einflusses der Kühlluft auf den Passagenwirbel wird durch einen Ansatz zur Quantifizierung des durch die Kühlluft verursachten zusätzlichen Verlustes im Passagenwirbel ergänzt.

Gemäss den zeitaufgelösten numerischen Simulationen haben zwei der drei getesteten Laufradgeometrien Ablösungen an der Druckseite am gewählten Betriebspunkt der Turbine. Die erste Auslegung der nichtaxialsymmetrischen Seitenwände reduziert die maximale Grösse und das Volumen der Ablöseblase signifikant. Des Weiteren verringern die nichtrotationssymmetrischen Seitenwände die Mischungsverluste wenn die Ablöseblase entleert wird, und die darin enthaltene Luft diese verlässt. Zusätzlich wurde eine starke Interaktion zwischen der Grösse und dem Volumen der Ablöseblase und der Eindüsungsrate der Kühlluft festgestellt. Zusätzliche Kühlluft vergrössert das Volumen der Ablöseblase auf der Druckseite und die Menge der Luft welche die Blase verlässt, scheint aber nicht der Haupt-

grund für die Ablösung selbst zu sein.

Zum ersten Mal wurde die Rotorscheibenkühlluft in die CFD Berechnungen zur Auslegung der Seitenwandkonturierung mit einbezogen, und der Optimierer hatte die Möglichkeit die Form der gesamten Nabe und der gesamten Deckbankinnenseite zu modifizieren. Als Folge geht die Seitenwandkonturierung an der Nabe bis zu deren Vorderkante bei der Tellerranddichtung, so dass diese eine gewellte Form aufweist. Deshalb beeinflussen die nichtrotationssymmetrischen Seitenwände an der Nabe nicht nur die Strömung im Laufrad zwischen der Vorder- und Hinterkante, sondern auch das Strömungsfeld am Austritt der Tellerranddichtung wird durch die Seitenwandkonturierung an der Nabe beeinflusst. Neben anderen Einflüssen auf das Strömungsfeld ergaben die Resultate eine Reduktion der maximalen Radialgeschwindigkeit und eine homogenere Massenstromverteilung am Austritt der Tellerranddichtung. Dies hatte eine Verringerung der Mischungsverluste zur Folge.

Die instationäre räumliche Bewegung des Passagenwirbels des Laufrades, welche durch die Interaktion zwischen den Schaufelreihen verursacht wird, und die daraus resultierenden Konsequenzen für die stromabwärts liegende Leitrad-schaufelreihe werden anhand von zeitaufgelösten Messungen am Laufradaustritt analysiert. Unter dem Einfluss des Potentialfeldes des stromabwärts liegenden Leitrades beschreibt die Mitte des Passagenwirbels einen Orbit mit einer maximalen Ausdehnung von 10% Schaufelhöhe in radialer Richtung und 40% Schaufelpassage in Umfangsrichtung. Die Menge der eingedüsten Rotorscheibenkühlluft beeinflusst die durchschnittliche radiale Höhe und die Dynamik des Orbits des Passagenwirbels, jedoch nicht dessen maximalen Amplituden.



# Contents

<b>1. Introduction</b>	<b>1</b>
1.1. Motivation . . . . .	1
1.2. Literature Review . . . . .	4
1.2.1. Losses in Axial Flow Turbines . . . . .	4
1.2.2. Unsteady Flow Interaction . . . . .	5
1.2.3. Secondary Flows . . . . .	7
1.2.4. Secondary Flow Control . . . . .	12
1.2.5. Non-Axisymmetric End Wall Contouring . . . . .	13
1.2.6. Rim Seal Purge Flow . . . . .	14
1.2.7. Pressure Side Separation . . . . .	16
1.3. Research Objectives . . . . .	18
1.4. Thesis Outline . . . . .	18
<b>2. Experimental Methods</b>	<b>21</b>
2.1. Experimental Facility . . . . .	21
2.1.1. Operating Point . . . . .	22
2.1.2. Measurement Planes and Grid . . . . .	23
2.1.3. Purge Flow Injection System . . . . .	24
2.1.4. Data Acquisition Systems . . . . .	25
2.2. Turbine Geometries . . . . .	28
2.2.1. Rotor Designs . . . . .	29
2.2.2. Blade Root Stress . . . . .	32
2.3. Probe Technology . . . . .	34
2.3.1. Probe Types . . . . .	34
2.3.2. Traversing System . . . . .	38
2.3.3. Calibration . . . . .	38
2.4. Data Reduction . . . . .	41
2.4.1. Pneumatic Probes . . . . .	41
2.4.2. FRAP and FENT . . . . .	43
2.4.3. Mass- and Area-averaging . . . . .	44
2.4.4. Pressure and Temperature Normalisation . . . . .	45

2.4.5.	Turbine Efficiency . . . . .	46
2.4.6.	Non-deterministic Unsteadiness . . . . .	46
2.4.7.	Streamwise Vorticity and Circulation . . . . .	46
2.4.8.	Dissipation . . . . .	47
2.4.9.	Entropy . . . . .	49
2.5.	Measurement Uncertainty . . . . .	49
2.5.1.	Probes . . . . .	49
2.5.2.	Turbine Efficiency . . . . .	50
2.6.	Time-Resolved Computational Model . . . . .	51
2.6.1.	Grid and Boundary Conditions . . . . .	51
2.6.2.	Solver . . . . .	52
2.6.3.	Validation . . . . .	53
2.6.4.	Particle Tracker . . . . .	54
<b>3.</b>	<b>Unsteady Purge Flow Migration and Interaction Mechanisms</b>	<b>57</b>
3.1.	Purge Flow Effects at the NGV1 Exit . . . . .	57
3.2.	Influence of Purge Flow on Rim Seal Exit Cavity Flow . . . . .	63
3.3.	Purge Flow Effects at the Rotor Exit . . . . .	73
3.4.	Purge Flow Losses . . . . .	87
3.4.1.	Measured Loss in the Rotor Hub Passage Vortex . . . . .	87
3.4.2.	Purge Flow Losses: Lagrangian Perspective . . . . .	90
3.4.3.	Flow Structures Involved in the Hub Loss Core . . . . .	93
3.5.	Summary . . . . .	95
<b>4.</b>	<b>Unsteady Effects of Profiled Rotor End Walls</b>	<b>99</b>
4.1.	Upstream Effects at the NGV1 Exit . . . . .	100
4.2.	Influence on Rim Seal Exit Cavity Flow . . . . .	102
4.3.	Effects of Profiled Hub End Wall at the Rotor Exit . . . . .	107
4.4.	Effects of Shroud End Wall Profiling at the Rotor Exit . . . . .	120
4.5.	End Wall Effects at the NGV2 Exit . . . . .	126
4.6.	Summary . . . . .	133
<b>5.</b>	<b>Unsteady Pressure Side Bubble Behaviour</b>	<b>135</b>
5.1.	Effect of End Wall Profiling on Pressure Side Bubble . . . . .	136
5.1.1.	Unsteady Size and Shape of Bubble . . . . .	136
5.1.2.	Bubble Shedding Mechanism . . . . .	139
5.2.	Purge Flow Interaction with Pressure Side Separation . . . . .	145
5.3.	Influence of Bubble on Rotor Exit Flow Field . . . . .	148
5.4.	Summary . . . . .	151

---

<b>6. Combined Effects of Profiled End Walls and Purge Flow</b>	<b>155</b>
6.1. Combined Interaction Mechanisms at the NGV1 Exit . . . . .	156
6.2. Combined Interaction Mechanisms at the Rotor Exit . . . . .	158
6.2.1. Sensitivity of Efficiency to Purge Flow . . . . .	158
6.2.2. Turbine Reaction . . . . .	162
6.2.3. Impact on Rotor Hub Loss Core . . . . .	163
6.3. Summary . . . . .	177
<b>7. Unsteady Rotor Hub Passage Vortex Behaviour</b>	<b>179</b>
7.1. Spatial Movement . . . . .	179
7.2. Influence on NGV2 . . . . .	185
7.3. Summary . . . . .	187
<b>8. Summary and Conclusions</b>	<b>189</b>
8.1. Concluding Remarks . . . . .	189
8.2. Summary . . . . .	191
8.3. Suggestions for Future Work . . . . .	195
<b>Bibliography</b>	<b>197</b>
<b>A. Nomenclature</b>	<b>211</b>
<b>B. List of Publications</b>	<b>215</b>
<b>C. Curriculum Vitae</b>	<b>217</b>



# 1. Introduction

## 1.1. Motivation

Global energy consumption has increased remarkably over the past half century mainly due to the increasing population and economic development, particularly in developing and fast-growing countries such as China and India. The demand of electrical energy is rapidly increasing due to the technological achievements that become accessible for a rapidly growing number of people worldwide. Figure 1.1 [1] shows the overall world wide consumption of electricity and the percentage produced based on a thermal cycle. The trend in the last three decades shows a constant growth rate and reflects the evolution of the population and the related economic growth, the electricity consumption has tripled since 1980. Approximately 80% of the world energy consumption has been produced by turbines integrated in a thermal cycle, such as Brayton or Rankine cycle, which transform heat into mechanical work that can be used for the electricity production. The Airports Council International (AIC) reports that commercial and non-commercial aircraft movements are expected to nearly double by 2029 [43]. Over the next two decades aircraft movements are expected to increase by 2.8% a year reaching 129 million by 2029, also increasing the demand for more and bigger aircrafts powered by turbomachines.

On the other hand the price for fossil fuels required to satisfy the raising power consumption and transport activity is constantly rising, The extraction techniques for fossil fuels are becoming more expensive and the danger of them running out is reflected in the price. In the last years the oil price was subject of volatility also related to political issues. In 2011 the barrel of oil has again exceeded the price of 100\$ [70].

The combination of the growing demand for electrical energy, the increasing prices for fossil fuels and the discussions about global warming in the context of the usage of fossil fuels intensifies the need for highly efficient axial flow turbines which are responsible for most of the electricity generation and aircraft propulsion. The economical success of axial gas turbines in these fields of application is based on their very high power density.

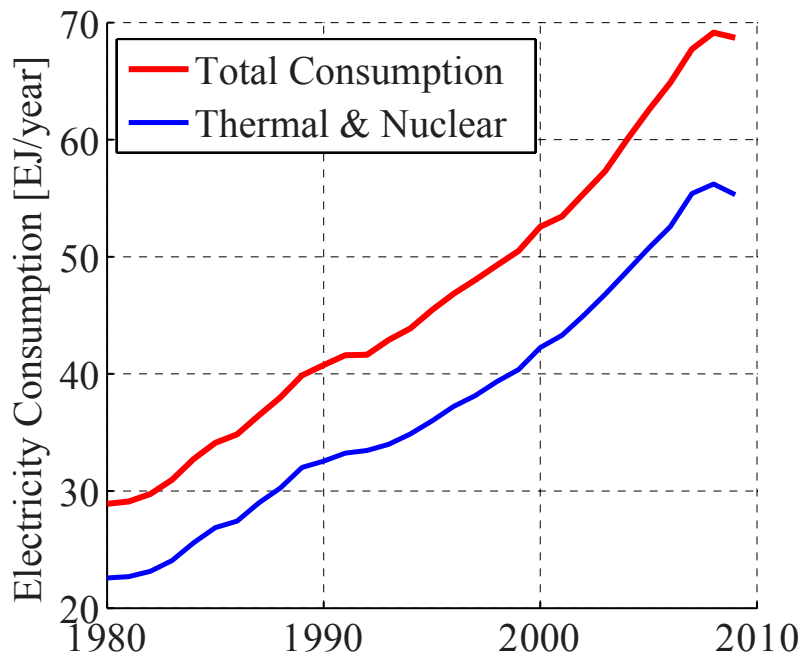


Figure 1.1.: Global electricity consumption during the last 30 years.

In axial flow turbines the fluid flows inside an annular duct in a direction along the central axis. Rows of airfoils in the duct change the swirl and angular momentum of the flow. Some of these aerofoils are fixed inside the annulus and are known as stators or nozzle guide vanes, and some are free to rotate around the central axis, the rotors. Pairs of stators and rotors are known as stages. In a turbine the stator is the first element of a stage and it accelerates the flow in the circumferential direction in order to make it spin rapidly around the annulus. Then the rotor's job is to reduce and redirect the angular momentum of the spinning fluid that hits the rotor blade. In doing so the rotor is extracting work from the fluid. In the relative frame the two roles are exchanged, the rotor accelerates and turns the flow while the stator reduces the angular momentum. The static pressure and temperature of the working fluid drops over both, the rotor and stator.

Today turbine efficiencies can exceed 90% and the thermal efficiencies of the cycles where they provide mechanical energy are on the order of 35% to 40%. The manufacturers of the latest generations of combined cycle power plants have announced efficiencies above 60%. Although turbine efficiencies are already relatively high, there is still potential for improvement. There are two possibilities to improve the overall efficiency of gas turbines. On the one hand the efficiency of the thermal cycle can be increased by either increasing the temperature of the first turbine stage or by increasing

the overall compression ratio of the compressor. On the other hand the propulsive efficiency of airplane engines can be increased at even higher bypass ratios. Furthermore, in aircraft engines not only the efficiency alone is of importance but also the weight of the engine. A turbine efficiency improvement that increases the aircraft engine weight can have a negative effect due to the additional fuel burn caused by the additional mass during flight. Hence, a reduction of the number of components in a aircraft engine is beneficial. Reducing the number of components also cuts the manufacturing and maintenance costs. If the number of stages and blades per row are reduced, the stage loading and lift coefficients are continuously pushed up. As a consequence the secondary losses rise and become the dominant loss source leading to a deterioration of the efficiency. They can reach up to half of the total loss. Therefore, methods to reduce secondary losses are of great value to optimise aerodynamic efficiency of axial flow turbines.

Furthermore, today's turbine inlet temperatures are up to 300K above the melting temperature of the turbine components and therefore need to be protected by the secondary cooling air. For instance, bypassed compressor air is injected through the rim seals between the rotating and stationary parts in order to prevent ingestion of hot gases that can cause overheating of the disks as well as thermal fatigue of the components. This bypassed cooling air has a negative effect on the engine efficiency and its use therefore needs to be minimised. Further, it has been shown in the open literature that purge flow significantly interacts with the secondary flow structures in the subsequent blade rows. The understanding and optimisation of these interaction mechanisms can improve the turbine performance.

A very attractive solution to improve the interaction of purge flow with the secondary flows in the hub regions is non-axisymmetric end wall profiling. Emerging CFD capabilities have made it possible to design more complex three-dimensional non-axisymmetric end walls and to link the end wall design with the purge flow requirements and secondary flow loss production. This is the research field where the proposed work is located.

Schuepbach [91] performed the first combined experimental investigation of purge flow effects and non-axisymmetric end wall profiling using the same experimental test facility in combination with high accuracy time-resolved instrumentation. A very significant efficiency improvement due to successful nozzle guide vane end wall profiling and a strong sensitivity of efficiency to the amount of injected purge flow was reported. This thesis continues the work performed by Schuepbach [91] and focuses on the related why-questions. Different rotor end wall designs taking into account the

purge flow are investigated in a low-pressure turbine environment and the sensitivity of the turbine efficiency to purge flow is reduced. The influence of profiled rotor end walls on the interaction mechanisms between the rim seal purge flow, the rotor secondary flows and a pressure side separation bubble is studied.

## 1.2. Literature Review

In this section the research fields related to this work are briefly reviewed and a number of references are given for the interested reader.

### 1.2.1. Losses in Axial Flow Turbines

There are a vast number of mechanisms present in turbomachinery which cause loss generation and which have been investigated in the open literature, Sharma and Butler [96], Moore et al. [65], Bindon [12] and Harrison [34] among others. The different loss sources are seldom independent. Denton [25] gives an overview and identifies three main loss sources in turbomachines:

- Profile loss
- End wall loss or secondary loss
- Leakage loss

In turbomachinery the listed loss sources approximately contribute in equal parts to the overall loss. Traupel [102] analyses different loss sources in axial flow turbines and presents a number of correlations to quantify these loss sources. Denton [25] defines loss as any flow feature that reduces the efficiency of a turbomachine and introduces entropy as the only reliable measure of loss in turbomachinery. In thermodynamics the lost work can be expressed as a reduction of availability  $\chi$ .

$$\chi = h_t - Ts \tag{1.1}$$

The available work is the difference of the specific stagnation enthalpy  $h_t$  of the fluid and the product of an environmental temperature  $T$  and specific entropy  $s$ . In an isentropic and reversible process the available work of a fluid corresponds to its stagnation enthalpy. The entropy is independent of

the frame of reference and is evaluated based on two thermodynamic properties such as temperature and pressure. Equation 2.34 gives the entropy rise compared to a reference for a perfect gas. Denton [25] identified three processes which create entropy:

- Viscous friction and mixing
- Heat transfer
- Non-equilibrium processes

The secondary flows presented in subsection 1.2.3 are not intrinsically a source of loss. However, due to the high velocity gradients associated with the secondary flows, the secondary kinetic energy is converted to loss by mixing, viscous dissipation and unsteady chopping by adjacent blade rows. As with the secondary flows, the unsteadiness itself is not considered as a source of loss per se; it does not directly generate entropy. In a highly unsteady flow field additional shear forces are generated and in consequence the loss may be expected to increase through viscous dissipation and mixing.

### 1.2.2. Unsteady Flow Interaction

The unsteadiness caused by the blade row interaction in an axial turbine can be divided into two groups, deterministic and non-deterministic. The deterministic unsteady flow structures occur at blade passing frequency or at its harmonics and are therefore associated with the blade movement. The non-deterministic unsteadiness is the remaining part of the overall unsteadiness and is typically high in regions of elevated turbulence, eddy shedding or boundary layer transition. The flow features related to a turbine blade row are alternatively facing an open channel or the leading edge of the subsequent row, due to the relative motion of the rotating and stationary blade rows. According to Sharma et al. [97] the flow downstream of a turbine rotor can be divided into two different events. Maximum interaction occurs when the vane flow structures interact with the rotor leading edge. As a consequence these flow structures become part of the rotor wake and secondary flow structures. At maximum interaction the turbulence level in the rotor free stream is low. Hence minimum interaction occurs when the vane flow structures enter the rotor passage without interaction with the rotor blades. The turbulence level of the free stream is therefore much more elevated. Schlienger [90] characterised the unsteady flow interaction

with the help of a relative throat, which corresponds to the downstream area the flow sees, and is a function of the relative blade row position.

**Potential Flow Interaction** The static pressure field around a stationary or rotating blade is known as its potential field. The potential field is seen by the neighbouring upstream and downstream blade rows and acts in contrast to the convective mechanisms. As a result of the potential interaction of vanes and blades a fluctuating pressure field is generated. Dean [23] stated that the temporal variation of the static pressure is a work process. As a consequence the total pressure field is modulated by the upstream potential field effect, often called bow waves. Parker and Watson [72] analysed the potential effect and found that it exponentially attenuates with increasing distance from the blade. Kachel and Denton [45] give a description of the unsteady interaction mechanisms. Matsunuma et al. [57] reported an intensive interaction between nozzle guide vane and the rotor flow due to the rotating potential field of the rotor.

**Wake-Blade Interaction** The velocity deficit that forms behind the trailing edge of an airfoil where the suction and pressure side boundary layers merge is called the wake. These wakes behind the vane or rotor blades are cut into lumps of low momentum fluid by the relative motion of the subsequent blade row. This wake-blade interaction was first investigated by Meyer [60]. The concept Meyer introduced is the so called 'negative jet', which is essentially a perturbation of the uniform flow. The negative jet causes an accumulation of wake fluid on the blade suction side and as a consequence a removal on the pressure side. According to Hodson and Dawes [39] this negative jet effect can be described in the following way. Before the wake enters the blade passage, it undergoes 'bowing', due to the higher velocities at the centre of the passage. On the one hand the higher convection velocities cause the wake fluid to be sheared on the blade suction side. On the other hand the wake experiences stretching on the pressure side. As a consequence most of the wake fluid leaves the blade row at the suction side with a tail across the passage and reaching the pressure side. Hodson and Dawes [39] also reported an unsteady recirculation when the wake impinges onto the suction side of the subsequent blade row. This recirculation causes pressure and lift variations on the blade surface. The convection of the wake fluid causes the formation of temporal pressure gradients. As observed by Dean [23], temporal gradients of static pressure represent a work mechanism. In return these work mechanisms cause fluc-

tuations of the stagnation temperature which are much more significant compared to the defects of stagnation temperature present in the wakes at the blade row inlet. Rose and Harvey [85] reported that the work of the free stream and the work of the wake are not identical. They introduced the concept of "Differential Work" and stated that in a turbine less work is extracted from the wake than from the free stream fluid. As a consequence the mixing losses related to the wakes are reduced. Their model shows that more the deficit of the total temperature and pressure in the wake is pronounced, more the potential work extraction from the wake is reduced compared to the free stream. Rose [84] estimated the wake mixing loss for an HP turbine at around 1% of the stage efficiency. The temperature of the wake was found to have a strong effect on the entropy rise as it mixes out.

**Vortex Interaction** One of the first to investigate vortex interaction is Binder et al. [11] who found that the vane passage vortices are cut into pieces by the downstream rotor blades. They assumed that the vortex is breaking down during this process, and in doing so the kinetic energy is converted into turbulence. In contrast Chaluvadi [17] and Behr [6] have shown that the upstream vortices are not chopped, but bent around the blade leading edge. Accordingly the upstream vane vortex is forming a suction side and a pressure side limb due to the blade row interaction. Using smoke visualisation techniques Chaluvadi [17] identified the suction side leg of the upstream vane passage vortex above the forming passage vortex of the downstream blade row. Chaluvadi et al. [18] also reported a 21% increase of stagnation pressure loss in the stator secondary flows due to the interaction with the upstream rotor vortex. They also found that the pressure side limb of the upstream passage vortex is merging with the forming blade passage vortex. On the other hand Behr et al. [9] identified the suction side leg of the upstream vane passage vortex to be below, and not above, the newly developed blade passage vortex. Kasper et al. [46] undertook a three dimensional visualisation of the vortex instability at rotor inlet. They reported the vortex as breaking down in a spiral mode due to the blade row interaction.

### 1.2.3. Secondary Flows

Secondary losses are one of the three main loss sources in axial turbines, as described in section 1.2.1. Secondary losses occur when the secondary

flows are mixing out. The secondary flow structures are occupying a large portion of the passage, especially in low aspect ratio turbines. A lot of work dedicated to the description of the secondary flows has been published in the last decades. The classical secondary theory was originally proposed by Squire and Winter [100] in 1951, and for the first time described by Hawthorne [37], [38] for a planar cascade. According to this inviscid theory, the normal vorticity introduced by the inlet boundary layer is transformed into a normal and a streamwise vortex component when deflected through a cascade, Figure 1.2. The passage vortex presents the distribution of secondary circulation, which occurs due to the distortion of the vorticity contained in the inlet boundary layer. Cumpsty [20] later described the secondary flows as the flow at right angles to the intended primary flow direction.

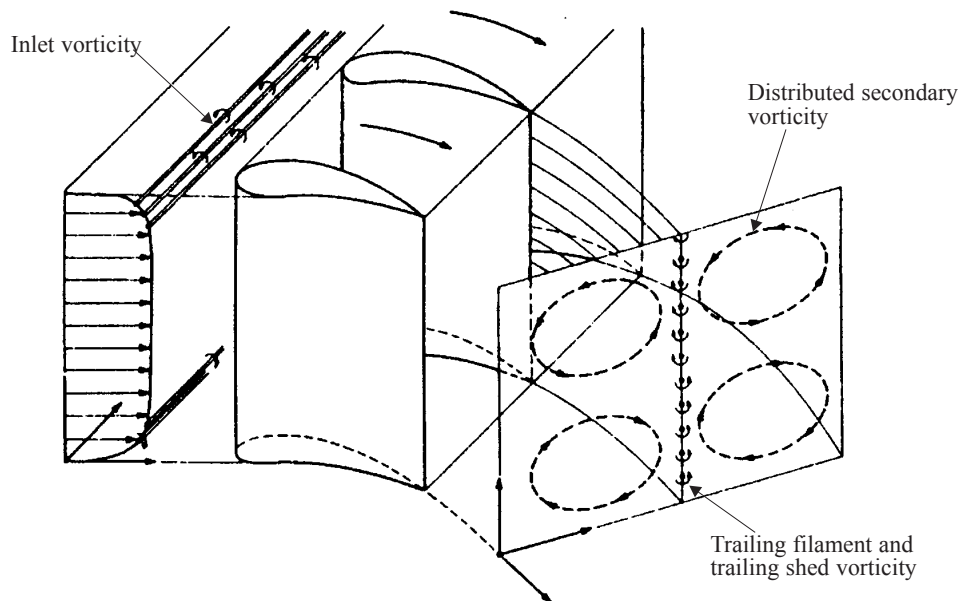


Figure 1.2.: Classical secondary flow model by Hawthorne [37].

A very detailed review of the secondary flows investigations and findings is given by Sieverding [98], and more recently by Langston [49]. These two review papers present a number of experimental investigations in linear and annular cascades revealing that secondary flows are highly three-dimensional and that viscous effects play an important role. The model proposed by Langston is shown in Figure 1.3. Sharma and Butler [96], using detailed measurement data of viscous flow development through cascades, reinterpreted the secondary flow theories and concluded that the effects of the inlet boundary layer as predicted by the classical secondary flow theory are incorrect for turbomachinery configurations. They reported

that the formation of the leading edge horseshoe vortex additionally transforms normal vorticity into streamwise vorticity and that this process is independent of the flow turning. A number of typical secondary flow features investigated by various researchers in linear or annular cascades are reviewed next.

**Passage Vortex** The passage vortex is the most dominant and largest secondary flow structure at the exit of a shrouded turbine blade row. According to the radial momentum equation the centrifugal forces and the cross-passage pressure gradient are at equilibrium in the free stream. However in the boundary layer, the slower moving fluid has to follow a tighter radius of curvature in order to balance the cross-passage pressure gradient. This leads to a tangential flow across the passage from the pressure side to the suction side and along the end walls. Then in order to preserve the continuity a vortical flow structure is formed, the so-called passage vortex. This secondary flow structure has been investigated in the context of loss generation by many researchers. Moore et al. [64] and Moustapha et al. [67] were among the first. The pressure side limb of the horseshoe vortex also migrates to the suction side of the adjacent blade under the effect of the cross-passage pressure gradient. In doing so it entrains low-momentum fluid and subsequently forms the passage vortex. As reported by Sharma and Butler [96] this entrainment of low-momentum fluid strongly influences the formation of the passage vortex and is a key mechanism in the generation of secondary flows and end wall losses.

**Horseshoe Vortex** The unsteady interaction between the inlet boundary layer on the end walls and the blade leading edge causes the formation of a three-dimensional separation in the form of a saddle point upstream of the blade leading edge. Langston et al. [50] provide visualisations of this interaction. The so-called horseshoe vortex forms between the blade leading edge and the separation saddle point and consists of a pressure and suction side limb. The unsteady separation process transforms the normal vorticity of the inlet boundary layer into streamwise vorticity. The two limbs of the horseshoe vortex are of opposite rotation. Under the effect of the cross passage pressure gradient the pressure side limb of the horseshoe vortex is convected across the passage. The location where the pressure side limb impinges onto the neighbouring blade suction side is normally defined as the starting point of the passage vortex. The suction side leg of the horseshoe vortex is accelerated along the blade suction side. At

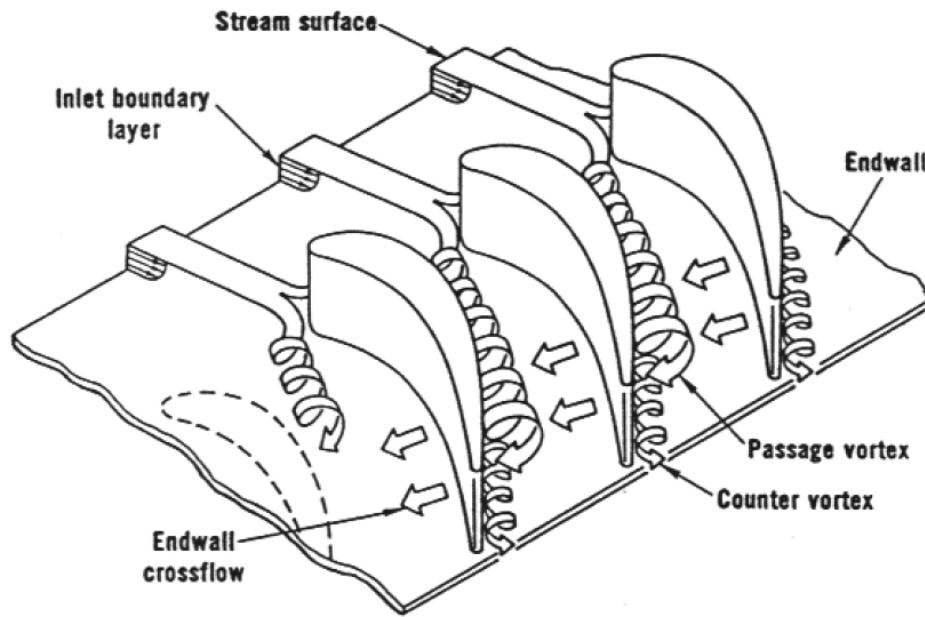


Figure 1.3.: Secondary flow model by Langston [50].

the location where the pressure side limb of the horseshoe vortex meets the suction side, the suction side limb is forced to lift off the blade end wall. According to Sieverding and Van den Bosche [99] the spatial position of the suction side limb of the horseshoe vortex depends strongly on the rotational speed of the passage vortex. The vorticity of the passage vortex itself depends on the turning that is imposed by the blades. Gregory-Smith et al. [32] observed that the suction side limb of the horseshoe vortex mixes out within the passage. The convection process of the horseshoe vortex is illustrated in Figure 1.4.

**Corner Vortex** The corner vortex is a vortical structure rotating in the opposite direction of the passage vortex and located in the end wall suction side corner, as described by Sieverding [98]. The corner vortex is formed when a strong cross-flow on the end wall caused by the high turning hits the suction side and has an opposite sense of rotation compared to the larger passage vortex. Therefore the corner vortex is rotating about the axis of the passage vortex. The position of the counter vortex relative to the passage vortex may be different depending on the turning and the blade geometry. This feature is relatively small and that is the reason why it is rarely observed in experimental investigations. Yamamoto [104, 105] presented experimental results for two cascades with different turning. In the case with  $110^\circ$  turning representative of a typical rotor blade row the effect of the corner vortex is seen as the result of reduced underturning

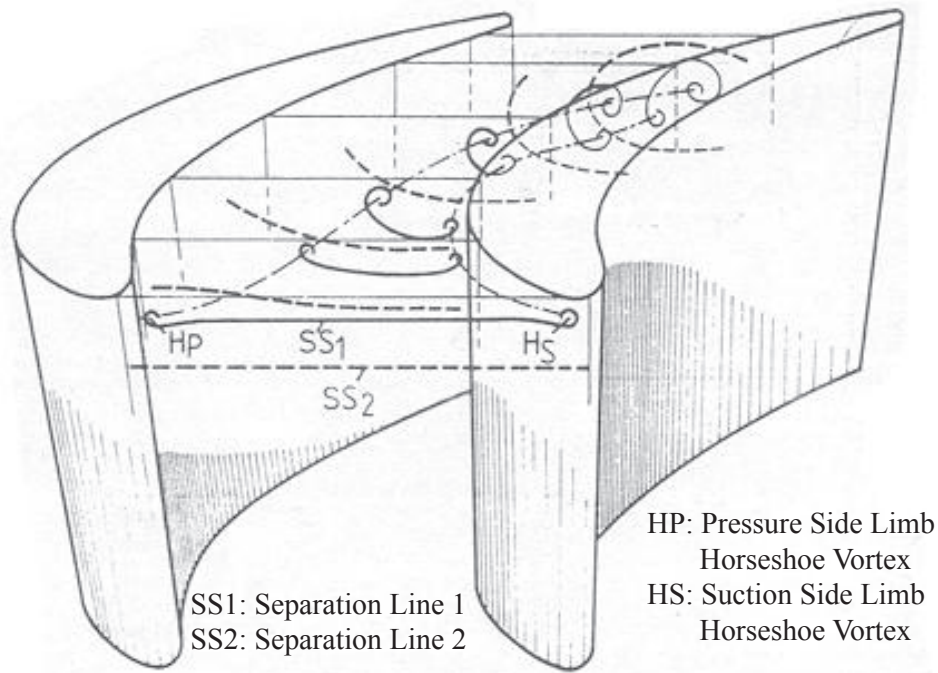


Figure 1.4.: Secondary flow model by Sieverding and Van den Bosche [99].

close to the end wall. The case with lower turning ( $68^\circ$ ) representative of a stator cascade the results did not show this effect. Yawamoto concluded that a corner vortex only develops beyond a certain level of blade turning.

Gregory-Smith et al. [32] studies the influence of the incoming boundary layer thickness on the development of the secondary flows. They concluded that an increased boundary layer thickness increases the intensity and strength of the secondary flow structures but does not affect their relative position. Based on investigations performed with different inlet boundary layer thicknesses Sharma and Butler [96] reported that the boundary layer loss convects through the passage without causing additional loss. In his review on secondary flows in axial turbines Langston [49] concluded, based on the available results in linear and annular cascades, that accurate routine predictions of secondary losses have not yet been achieved. According to Langston the principal reasons for this lack of understanding are inadequate turbulence models and a still limited knowledge of end wall loss production mechanisms.

The secondary flow development in a linear cascade does not include all the unsteady effects present in rotating machines. The principal differences with regard to the secondary flow development between rotating machines and linear cascades are the annular shape of the blade rows and the strong

skewing of the inlet boundary layer caused by the relative movement of stationary and rotating rows. The annular shape of the blade rows introduces radial pressure gradients. Walsh [103] found increased loss when investigating the effect of inlet skew in turbines. Moustapha [67] compared an annular with an linear cascade and found higher and more concentrated losses for the annular cascade. Furthermore, real machines often need cooling flow in order to assure the integrity of the hardware. The injected coolant flow strongly interacts with the secondary flows.

#### 1.2.4. Secondary Flow Control

The attempts to control secondary flows can be divided into active and passive methods. The active control methods are of very limited success and usually have no net benefit. Examples of active methods are boundary layer blowing investigated by Sturm et al. [101] and Biesinger [10]. Biesinger injected air tangentially through an upstream slot so as to oppose the secondary flow production. However, no net loss reduction was achieved. However, some blowing configuration lead to a reduction in mixed out losses. Behr et al. [8] successfully investigated an active control of the rotor blade tip leakage flow by means of cooling injection from the casing in a high work turbine.

The passive secondary flow control techniques are more often studied by researchers. The most frequently used are blade leaning, axisymmetric and non-axisymmetric end wall profiling.

The effects of blade leaning were investigated with great detail by Harrison [34]. He concluded that there is no net loss reduction within the row in which blade leaning is applied. The reduced loss at the end wall achieved through blade leaning is compensated by higher blade losses at mid-height. The only potential benefit related to blade leaning is a more homogenous flow field which is going into the subsequent blade row and which can be expected to reduce the loss generation.

The design concept of axisymmetric end wall contouring was introduced by the russian engineer Dejc [24] as a contraction of the annulus from the leading edge to the trailing edge. Morris and Hoare [66] verified the concept and reported a loss reduction of up to 20% in the context of a linear cascade test. The most successful axisymmetric end wall design included a strong contraction in the early passage, often known as the “Russian kink“. The acceleration of the flow field due to this early contraction causes thinner boundary layers and hence reduces the end wall losses. Different end wall

contours were studied in a linear cascade by Atkins [2]. He showed that the losses created near the end wall can be influenced by modifying its shape and the resulting local pressure field. In the presence of successful axisymmetric end wall profiling Dossena et al. [26] reported a 35% reduction of the overall loss and a 54% reduction of the secondary loss. However, it is suspected that the reported benefits are partially caused by the reduced blade loading.

Sauer et al. [88] propose blade leading edge modifications as defined in [88] with the objective of reducing the loss. The leading edge modification consisted of a bulb over the lowest 5% of the blade span. The rationale was to increase the strength of the suction leg of the horseshoe vortex in order to prevent the impingement of the pressure side limb of the horseshoe vortex on the suction side of the adjacent blade. They reported a reduction of the end wall losses by approximately 50% at an inlet Mach number of 0.2 due to the modified leading edge.

### 1.2.5. Non-Axisymmetric End Wall Contouring

The generic geometry of non-axisymmetric end wall profiling was proposed in the early patent of Gilbert Riollot [82] originally in Paris in 1965. The basic idea of the non-axisymmetric end wall profiling is to use streamwise curvature to locally control the static pressure. Concave curvature leads to an increase in local static pressure as the cross section of the passage increases and the velocity is reduced. Convex end wall curvature has a contrary effect.

Such end walls designed 30 years later in the axial flow gas turbine context and with the benefit of three-dimensional CFD were first proposed by Rose [83]. The profiled end walls were designed to homogenise the end wall static pressure field at the rim seal with the aim of reducing the required turbine disk coolant mass flow. The technique was theoretically demonstrated using three dimensional viscous CFD and the results showed a reduction of the static pressure non-uniformities by 70%.

Later, non-axisymmetric end wall profiling was used by Harvey et al. [36] to reduce the late cross passage pressure gradient in order to reduce the formation of the secondary flows. They parametrised the end walls with the use of circumferential fourier curves and splines in streamwise direction. Considering the secondary kinetic energy as a target function for the optimisation, a sensitivity matrix for the Fourier coefficients was constructed and the optimal shape derived. Hartland et al. [35] and Ingram et al. [42]

showed in the Durham linear cascade that significant secondary loss reductions of 24% can be achieved using non-axisymmetric end walls in order to reduce the cross passage gradient. Brennan et al. [16] and Rose et al. [86] redesigned the end walls of an HP turbine model rig and reported an increase in stage efficiency of 0.4% from computations and  $0.6\% \pm 0.25\%$  from measurements. Duden et al. [27] investigated the combined effects of blade thickening and end wall contouring. Praisner et al. [79] have confirmed that end wall contouring is an effective method for reducing end wall losses in a high-lift airfoil cascade using a CFD based end wall optimiser. Schuepbach et al. [92] performed measurements with the model axial turbine test rig used for the experimental work of this thesis and reported an efficiency improvement of  $1.0\% \pm 0.4\%$  due to the non-axisymmetric end walls designed by Germain et al. [29]. The improvement was mainly found in the nozzle guide vane and was due to a significant reduction of the secondary flow losses as well as a substantial reduction in mid-span losses.

### 1.2.6. Rim Seal Purge Flow

The secondary cooling mass flow considered for this work is the purge flow injected at the rim seal between the nozzle guide vane and rotor. The purge flow prevents the ingestion of hot gases into the disk cavities in order to prevent the disk's overheating and to avoid thermal fatigue. Therefore bypassed compressor air is injected through the rim seals between the rotating and stationary parts. The obvious design intent is to minimise the amount of purge mass flow and to reduce the aerodynamic losses, which can be attributed to the purge flow, in order to maximise the turbine efficiency. The ingestion of hot gases is driven by disk pumping and the external non-axisymmetric static pressure field. This has been experimentally investigated in a previous study carried out at the Laboratory for Energy Conversion, Schuepbach et al. [93, 94]. Other researchers such as Kobayashi et al. [47] found that the pressure difference criterion underestimated the minimum cooling flow rate. Chew et al. [19] and Dadkhah et al. [22] analysed the minimum required coolant flow required for different rim seal shapes and compared this to the differential pressure criterion. Roy et al. [87] showed that the effect of the unsteady pressure field is much more pronounced inside the cavity than the time-averaged circumferential external pressure field. Mirzamoghadam et al. [62, 61] showed that low levels of ingestion were observed even when sealing flows were above the minimum injection rate. They compared their work to Roy et al. [87] and found

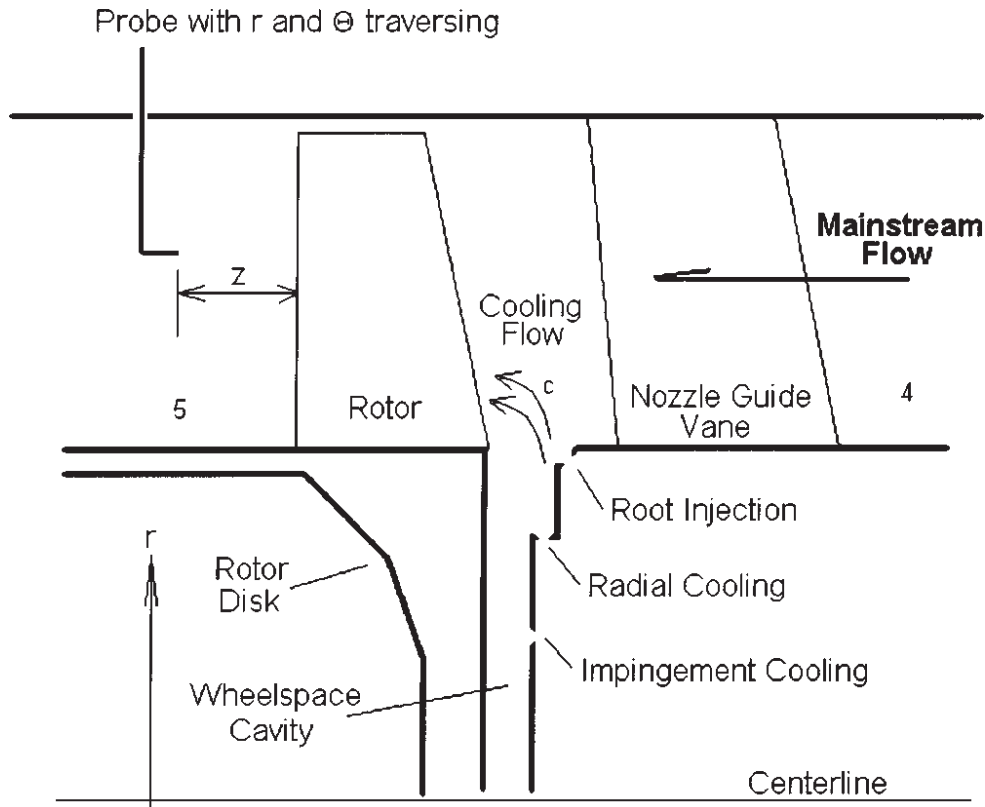


Figure 1.5.: Illustration of the different cooling injection strategies investigated by McLean et al. [58].

reasonable agreement. Okita et al. [68] proposed a novel design change intended to reduce the amount of purge flow required for a downstream purge cavity in a one-and-half stage turbine rig. Based on experimental and numerical results, they found an improved cooling effectiveness due to the redesigned cavity, which incorporated a divider plate on the stationary side.

The strong effect of injected cooling air on the development of the secondary flow structures has been reported in the open literature. McLean et al. [59] experimentally tested "radial, impingement and root injection" cooling configurations as defined in reference [59]. Figure 1.5 illustrates these three different cooling strategies. They found the three-dimensional secondary flow structure and stage performance to be significantly affected by the cooling mass flow and reported average total-to-total efficiency benefits up to 1.5 %. Girgis et al. [30] compared radial injection to compound injection and observed that the latter resulted in an efficiency improvement. Ong et al. [69] found that the introduction of a swirl component to the coolant jet reduces the efficiency penalty caused by the coolant due to a reduction in viscous dissipation and secondary flow strength. Furthermore,

they found that most of the coolant is entrained by the downstream blade hub secondary flow. Paniagua et al. [71] reported that there is an intensification of the rotor hub vortex and an enhancement of the radial migration due to injection in a transonic high pressure turbine. In recent studies the importance of the unsteady interaction of the free stream and the cavity were highlighted. Boudet et al. [13] investigated the unsteady interaction of the main flow and the rim seal cavity and found frequencies that are unrelated to the blade passing frequency. They attributed this to a non-linear coupling of the blade passing frequency with an instability formed inside the cavity. They concluded that only full annulus and unsteady modelling would capture the experimentally observed flow phenomena. Reid et al. [81] quantified the efficiency penalty caused by the rim seal flow as being about 0.56% per percent of injection mass flow. The effect of the blade leading edge platform was investigated in a numerical study by Marini and Girgis [56]. They presented a design offering a 0.07% stage efficiency benefit and a reduced sensitivity to an increasing cavity mass flow. Schuepbach et al. [93] have shown a 0.6% efficiency drop for 0.9% purge flow with axisymmetric end walls. Additionally, intensification of the secondary flows at the exit of the rotor as well as a higher radial migration of the secondary flows with purge flow were observed.

### 1.2.7. Pressure Side Separation

Due to the strong competition in the aircraft industry the manufactures of modern engines constantly strive to reduce aircraft engine weight and production cost. According to Curtis et al. [21] the low-pressure turbine of a Rolls-Royce turbofan accounts for approximately one third of the total engine weight, due to its large diameter and the relatively high number of stages required to drive high bypass ratio fans. There are two main design options for low-pressure turbine blades, thin and solid or thick and hollow. Thin and solid turbine blades are cheaper than thick ones since no core is required for the casting process during production. However thin aerofoils are heavier because the two wall thicknesses of hollow blades can be lighter than the thickness of a thin aerofoil. Thick and hollow turbine blades typically have a shorter pressure side and their loss production is reduced. For the designer a successful balance between cost, weight and loss needs to be found. Although hollow and thick blades minimise the weight and loss, thin and solid blades are usually chosen for cost reasons. Because of their small leading edge radius and because of the low Reynolds Number

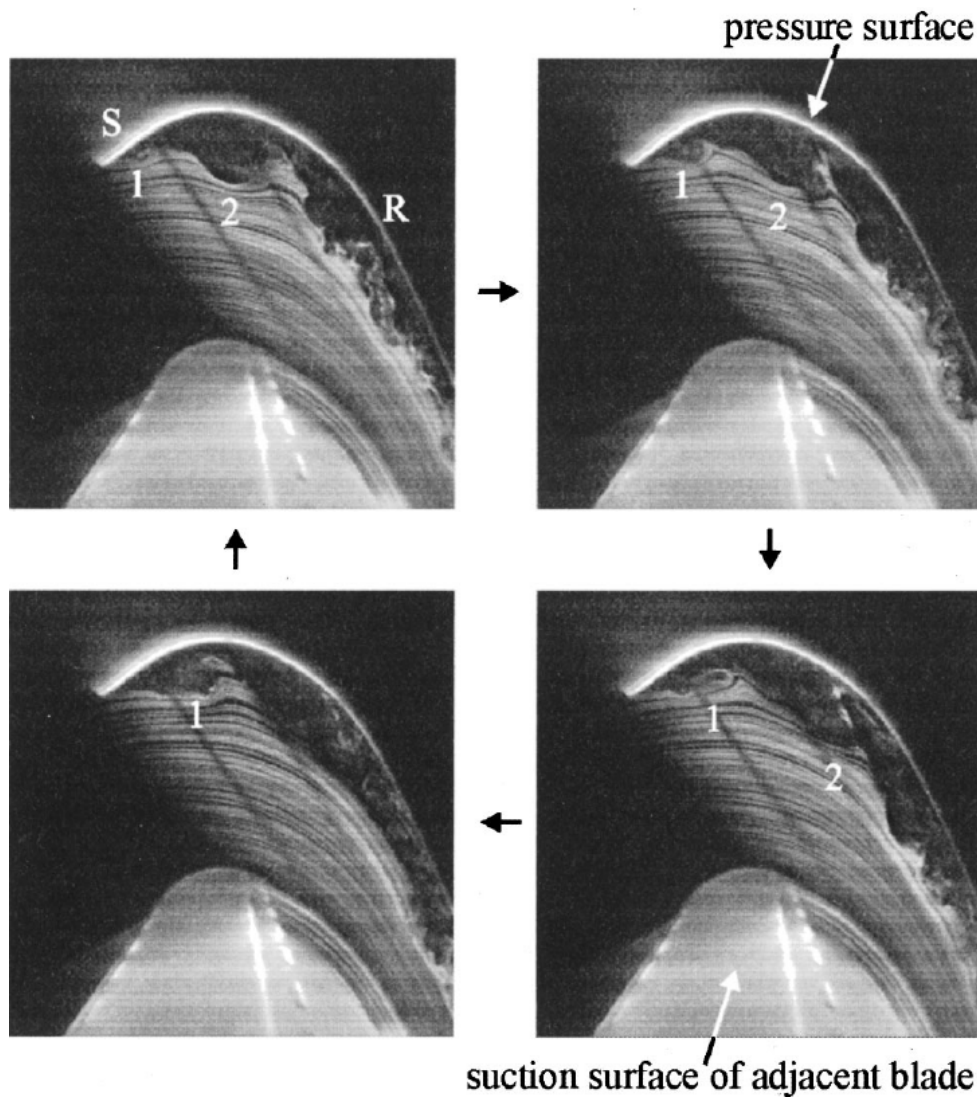


Figure 1.6.: Smoke wire visualisation of pressure side separation by Brear et al. [15].

during operation, low-pressure turbine blades often have separated flow on the pressure side, also at design conditions. Usually the separation occurs close to the leading edge at relatively low radius. The behaviour of the separation bubble is complex, highly unsteady and significantly contributes to the aerodynamic performance of the blade. Brear et al. [15] quantified the loss produced by a pressure side bubble in a linear cascade, showing that it can be a significant contributor to the profile loss. They also found the incidence to be one of the controlling parameter for the characteristics of the pressure side separation. Similar findings were reported by Yamamoto et al. [106] and Hodson et al. [40]. They also found that the unsteady behaviour of the pressure side separation is affected by local centrifugal and radial pressure gradients. The migration process of the separated fluid was first

studied by Brear et al. [14] using experimental and numerical techniques. They found a strong interaction between the separation bubble and the hub secondary flows affecting the strength of the secondary flow and the loss that is created. The available experimental results in the open literature related to the pressure side separation are rare and limited to experiments performed in linear cascades.

### 1.3. Research Objectives

In a perspective to investigate the influence of the end wall profiling on the unsteady interaction mechanisms between the injected rim seal purge flow and the rotor secondary flows in order to mitigate the adverse effects of the purge flow, the following research objectives are formulated. The experimental results measured with three different low-pressure rotor geometries are complemented with corresponding time-accurate numerical simulations.

- Improve the rotor efficiency with the use of profiled hub and shroud end walls in a low-pressure turbine environment and provide a validation for the end wall design methodology.
- Reduce and quantify the sensitivity of different rotor performance parameters to the injected rim seal purge flow using profiled end walls.
- Determine the influence of the end wall profiling on the unsteady interaction mechanisms between the purge flow and the rotor secondary flows with the use of both, time-resolved probe measurements and corresponding CFD simulations.
- Describe the influence of the purge flow and the end wall profiling on the unsteady spatial behaviour of the rotor hub passage vortex.
- Come up with design guide-lines and recommendations for rotor end wall profiling in order to mitigate purge flow losses taking into account the competing economical and engineering interests.

### 1.4. Thesis Outline

**Chapter 1** The introduction, a short literature review and the research objectives are presented in the first chapter. The literature review focuses on the research fields of axial gas turbines related to the presented work,

more precisely secondary flows, loss mechanisms, unsteady flow interaction, pressure side separation, rim seal purge flow, secondary flow control and non-axisymmetric end wall design.

**Chapter 2** In the first part of this chapter the experimental facility and its data acquisition systems are described. Then the different probes and the way they were used in the context of this work are presented. The data reduction section details the probe raw data processing and the most important variables coming out of the post-processing and used when the results are presented. The measurement uncertainties are discussed. In the last chapter a time-accurate numerical model and a particle tracking tool are presented.

**Chapter 3** Unsteady interaction mechanisms between the injected purge flow and the rotor flow field are addressed in this chapter. Three different levels of purge flow are compared for one rotor geometry with profiled end walls, in order to clearly isolate the effect of the purge from geometrical variations. The analysis discusses the purge effects at rotor inlet, at the rim seal cavity exit and at the rotor exit. A method to quantify the losses generated in the rotor hub passage vortex by the purge flow is proposed and discussed.

**Chapter 4** In this chapter the three experimentally investigated rotor geometries are compared with each other at a constant purge flow rate. The presented analysis focuses on the unsteady effects of the profiled end walls at the rotor inlet and exit and also at the NGV2 exit. The benefits of the profiled hub and shroud end walls can be studied independently.

**Chapter 5** Two of the three tested rotor geometries have pressure side separations for the chosen operating point. The unsteady behaviour of this pressure side bubble is studied in this chapter based on time-accurate CFD simulations. The influence of the end wall profiling on the unsteady shape of the bubble and its shedding mechanism are studied, as are the interaction between the purge flow and the pressure side bubble.

**Chapter 6** This chapter focuses on the combined unsteady interaction mechanisms between the elements quasi independently discussed in chapters 3 to 5. For this purpose all nine experimentally investigated test con-

figurations are considered and are mutually compared. In particular, the sensitivity of the efficiency, the turbine reaction and the effects related to the radial migration of the rotor hub passage vortex are studied.

**Chapter 7** The results presented in this chapter aim at studying the unsteady spatial behaviour of the rotor hub passage at the rotor exit caused by the blade row interactions. Particular attention is paid to the influence of varying purge flow on the dynamics of the orbit prescribed by the rotor hub passage vortex.

**Chapter 8** The last chapter offers overall conclusions, a review of the summaries and conclusions of the different chapters and proposals for future work.

## 2. Experimental Methods

### 2.1. Experimental Facility

The experiments were performed using the LISA research turbine facility at the Laboratory for Energy Conversion (LEC) at the Swiss Federal Institute of Technology in Zurich. The facility is designed to accommodate a moderate speed and low-temperature model axial turbine with non-dimensional parameters matching real engine conditions. A schematic view of the experimental facility is given in Figure 2.1.

The air loop of the facility is quasi-closed and includes a radial compressor, a two-stage water to air heat exchanger and a calibrated venturi nozzle for mass flow measurements. At the exit of the turbine test section the air loop opens to atmosphere. The facility extends over three floors. A 750kW radial compressor with a maximum pressure ratio of  $\Pi_{\max} = 1.5$  and a maximum mass flow of approximately 13kg/s compresses the air upstream of the turbine. The pressure ratio and mass flow of the compressor are controlled through variable inlet guide vanes at constant rotational speed. Upstream of the compressor the main mass flow  $\dot{m}_{\text{main}}$  is measured by means of a calibrated venturi nozzle. Downstream of the compressor the air goes through two water to air heat exchangers that control the turbine inlet total temperature  $T_{t,\text{in}}$  to an accuracy of  $\pm 0.3\%$ . Upstream of the turbine section is a 3m flow conditioning stretch to ensure a homogenous flow field at the turbine inlet. Additionally the flow undergoes acceleration ahead of the turbine section in order to reduce the significance of remaining flow non-uniformities from upstream. A DC generator absorbs the turbine power and controls the rotational speed with an accuracy of  $\pm 0.02\%$  ( $\pm 0.5$  rpm). An angular gearbox between the turbine and the generator halves the rotational speed. A torquemeter installed on the vertical shaft between the turbine and the gearbox measures the torque on the rotor shaft. A safety coupling on the vertical shaft decouples the turbine from the gearbox in case of a gearbox failure. A horizontal shaft with a second safety coupling connects the gearbox to the generator.

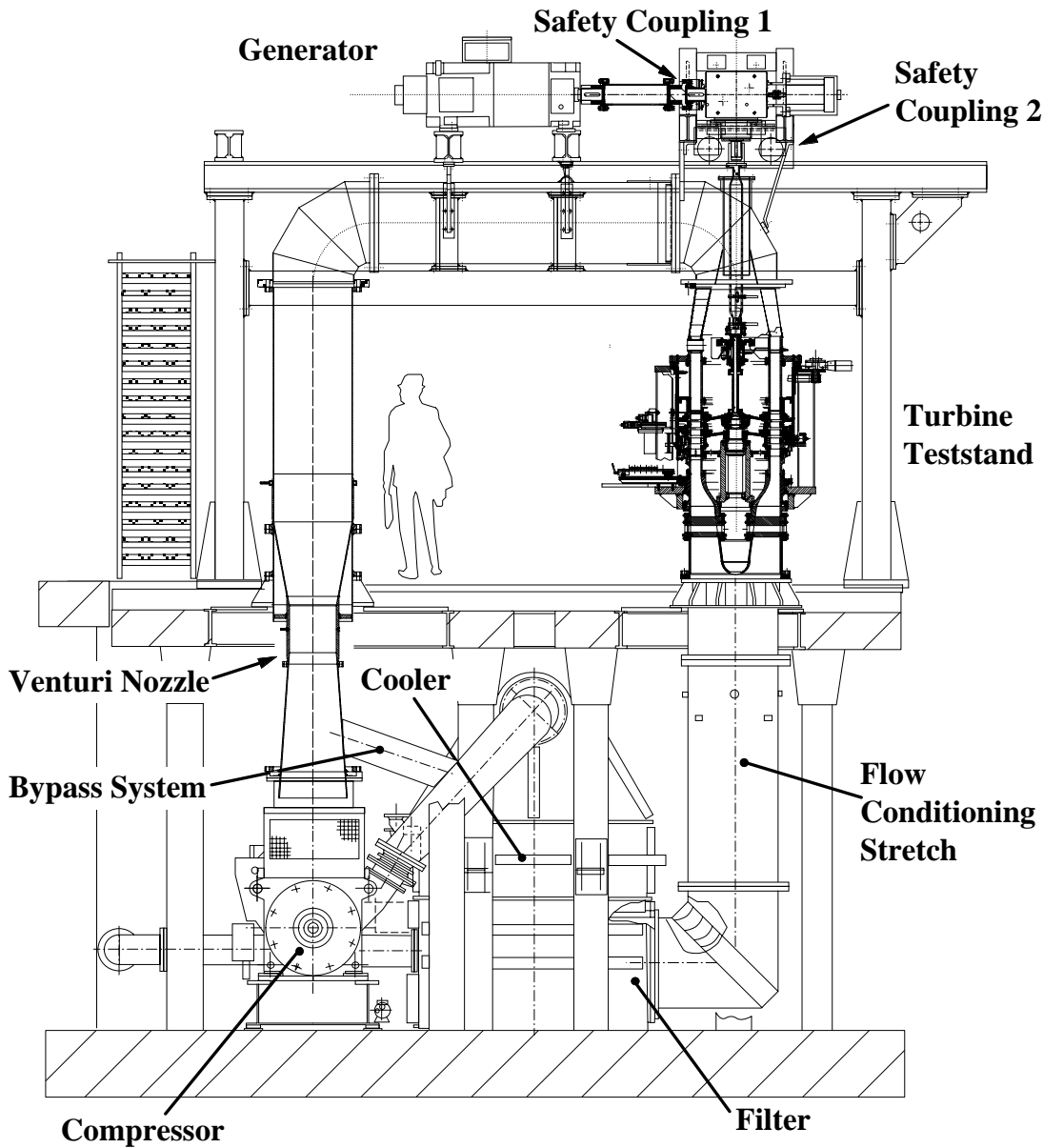


Figure 2.1.: Schematic view of the LISA research turbine test rig.

### 2.1.1. Operating Point

The operating conditions given in Table 2.1 were the same during all the measurements performed in the context of this work. The turbine 1.5 stage total-to-static pressure ratio is kept constant at  $\Pi_{1.5} = 1.65$  and the total turbine entry temperature is kept uniform at  $T_{t,in} = 328\text{K}$ . The total-to-static pressure ratio compares the total pressure at the turbine inlet and the static pressure at the exit of NGV2. With the compressor ratio limited to  $\Pi_{max} = 1.5$  it is necessary to add a tandem de-swirl vane arrangement to recover the static pressure at the exit of the second stator back to the

ambient level, in order to reach the intended turbine total-to-static pressure ratio of  $\Pi_{1.5} = 1.65$ . At the exit of the first nozzle guide vane row the flow is compressible with an exit Mach number of 0.56 in the hub region. These operating conditions are in agreement with measurements previously obtained using this turbine and permit an accurate comparison between all measurements made on different days. In order to account for the change in ambient pressure on different measurement days, the pressures are non-dimensionalised by the respective turbine inlet total pressure.

$\Pi_{1.5}$	$1.65 \pm 0.4\%$
$T_{t,in}$	$328 \pm 0.2 \text{ K}$
$\frac{\dot{m}\sqrt{T_{t,in}}}{P_{t,in}}$	$152 \pm 0.2\% \frac{\text{kg}\sqrt{\text{K}}}{\text{s}\cdot\text{bar}}$
$\frac{\omega}{\sqrt{T_{t,in}}}$	$2.48 \pm 0.05 \frac{\text{rps}}{\sqrt{\text{K}}}$
$M$ (NGV1ex/R1ex/NGV2ex)	0.52/0.28/0.48
$Re$ (NGV1/R1/NGV2)	$7.1/3.8/5.1 \cdot 10^5$

Table 2.1.: Turbine operating conditions.

### 2.1.2. Measurement Planes and Grid

Intrusive probe measurements were performed at three different traversing planes in the turbine test facility. Fig.2.2 shows the blade geometries at mid span and the relative positions of the three traverse planes.

**Measurement plane NGV1ex** The axial chord of the NGV1 is 49.7mm at mid span. The axial gap between the NGV1 and the rotor is 29% of the first nozzle guide vane axial chord. The traversing plane NGV1ex is 15.7% of the NGV1 axial chord downstream of its trailing edge. The axial position of this probe traverse plane makes it possible for the probes to measure in the upper rim seal cavity above the rim seal lip. Including a 1mm safety distance the probes can be used inside the rim seal cavity down to a radius of  $-3\%$  span. The access into the rim seal cavity is possible for the 4-hole, FRAP and FENT probes. The spatial resolution of the measurement grid consisted of 42 radial and 41 equally spaced points in the circumferential direction.

**Measurement plane R1ex** The axial chord of the rotor is 39.9mm at mid span. The axial gap between the rotor and the NGV2 is 55% of the rotor axial chord. The traversing plane R1ex is 38% of the rotor axial chord downstream of its trailing edge. This measurement plane is 14% of the rotor axial chord downstream of the shroud exit cavity. At the hub no rim seal cavity access is possible. The spatial resolution of the measurement grid consisted of 39 radial and 41 equally spaced points in the circumferential direction.

**Measurement plane NGV2ex** The axial chord of the rotor is 72.0mm at mid span. The traversing plane NGV2ex is 12.5% of the second nozzle guide vane axial chord downstream of its trailing edge. The spatial resolution of the measurement grids at the NGV2 exit and the rotor exit are identical.

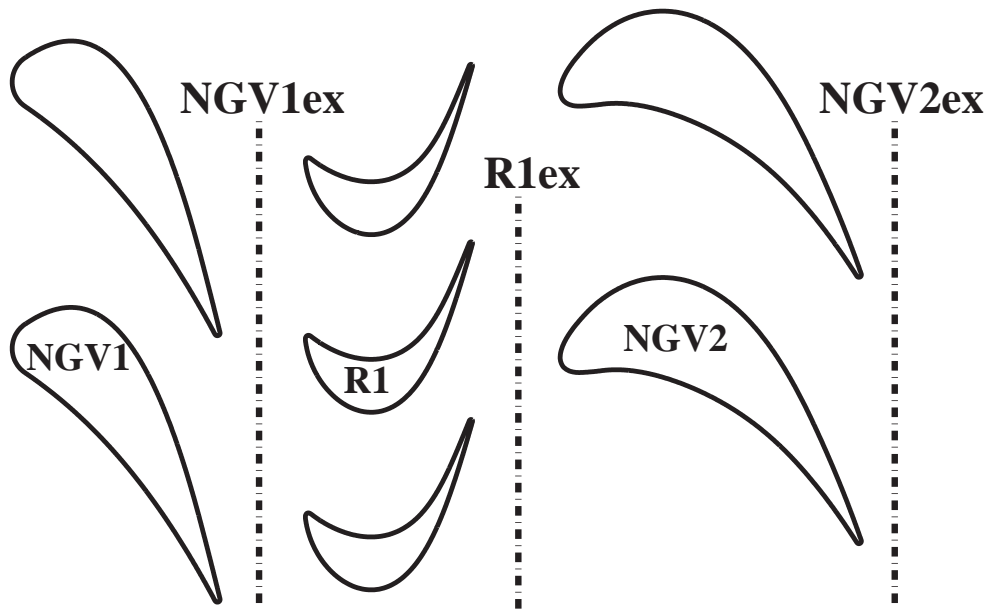


Figure 2.2.: Illustration of geometrical relations and measurement planes.

The measurement grids at all traversing planes cover one stator pitch ( $10^\circ$ , 41 traverses) and show radial clustering near the end walls. In the circumferential direction there is a constant step of  $0.25^\circ$  between two traverses. Table 2.2 gives an overview of the used probe techniques at the different measurement planes and injection rates.

### 2.1.3. Purge Flow Injection System

The air injected through the rim seal between the nozzle guide vane and rotor is bled off the primary air-loop upstream of the main flow conditioning

Measurement Plane	Probes	$IR$
NGV1 exit	4HP, FRAP, FENT	0.4%, 0.8%, 1.2%
Rotor exit	5HP, FRAP, FENT	0.4%, 0.8%, 1.2%
NGV2 exit	5HP, FRAP	0.8%

Table 2.2.: Overview of the measurements performed at the different measurement planes.

stretch. The mass flow of the bypassed air ( $\dot{m}_{\text{bypass}}$ ) is measured by means of a venturi, which is part of the auxiliary air system. After having passed a plenum, the air is fed into the rim seal cavity through 10 tunnels inside the first nozzle guide vanes. Figure 2.3 illustrates the leakage path and the rim seal cavity. From the cavity underneath the nozzle guide vanes there are two leakage paths, which are indicated in Figure 2.3 as dotted arrows. One path is through the upstream rim seal into the main flow,  $\dot{m}_{\text{purge}}$ . The rest of the gas ( $\dot{m}_{\text{drum}}$ ) is ejected through the drum to ambient conditions after being measured in another venturi. The drum pressure level can be controlled by a valve which controls the ejection of the mass flow from the drum to atmosphere. Hence the pressure difference over the labyrinth seal between the downstream rim seal and the drum can be balanced. Under these conditions the net mass flow through the downstream rim seal into the drum is assumed to be zero. Thus the injected purge mass flow can be calculated as the difference between the measured bypass and the drum mass flow.

The purge flow injection rate  $IR$  is defined as the ratio between the injected mass flow and the total turbine mass flow, given by Equation 2.1.

$$IR = \frac{\dot{m}_{\text{purge}}}{\dot{m}_{\text{main}}} = \frac{\dot{m}_{\text{bypass}} - \dot{m}_{\text{drum}}}{\dot{m}_{\text{main}}} \quad (2.1)$$

The measurements were conducted with the following three different injection rates:  $IR = 0.4\%$ ,  $IR = 0.8\%$  and  $IR = 1.2\%$ , which are representative of low, nominal and high injection rates.

### 2.1.4. Data Acquisition Systems

There are three independent main data acquisition chains which were used in the context of the presented work. Each of the data acquisition systems is controlled by a PC, monitoring the operational conditions, the turbine vibrations and the probe measurements.

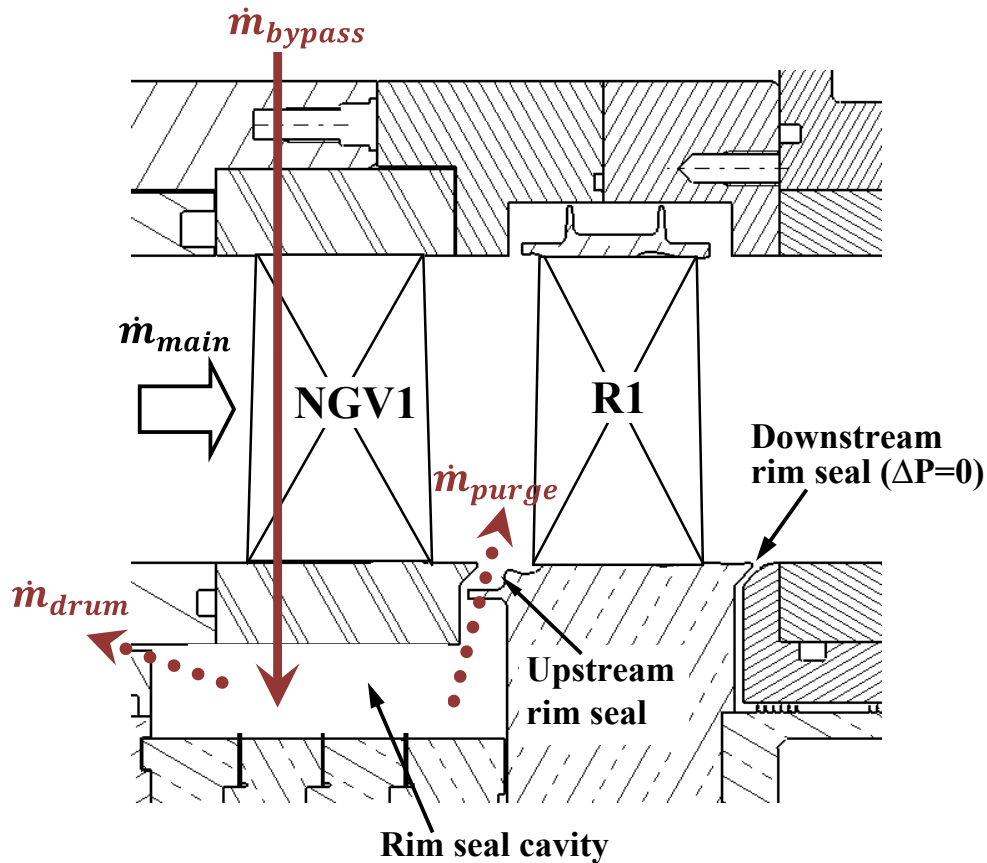


Figure 2.3.: Illustration of leakage path.

#### 2.1.4.1. Operating Conditions

The operating conditions are monitored in real time and are required to start the turbine and to keep the turbine at a constant operating point. The crucial parameters are briefly described and include pressures, torque, rotational speed, temperatures, humidity and mass flow.

**Pressure** Two 16 channel difference pressure PSI modules are measuring the most important operating pressures. This includes the pressures used for the mass flow calculations of the three mass flow measurement devices, the inlet total and static pressures, the ambient pressure and the hub and tip pressure values at exit of each row. The inlet total pressure is measured with a pitot probe mounted at half the channel height on thin struts. These struts are circumferentially displaced relative to the traverse area. All other pressure values are measured with wall pressure tappings of 0.5mm diameter. The ranges of the two modules are  $34.5kPa$  and  $5.0kPa$  respectively.

**Temperature and Humidity** At the turbine inlet and exit four PT<sub>100</sub> resistance thermometers are installed to determine the air temperatures. At the exit of the heat exchanger another PT<sub>100</sub> thermometer measures the outlet temperature, which is the input to the inlet temperature control loop. Additional temperatures are measured at inlet of the mass flow measurement devices as well as inside the cavity underneath the first vane. The temperature measurements in the rim seal cavity are used to determine the temperature of the purge flow. In order to prevent condensation a humidity sensor is installed at the exit of the turbine. Another one is installed at the inlet of the main mass flow device to correct the density value for the actual humidity values.

**Mass Flow Devices** There are three mass flow devices installed in the rig measuring the primary, the bypassed and the drum mass flows.

The primary mass flow is measured with a calibrated Venturi nozzle. Since the upstream length does not conform with the minimum length defined in ISO 5167-3, the Venturi nozzle including the two upstream bends has been calibrated at Delft Hydraulics on a certified calibration rig for flow measurement devices. Now the discharge coefficient of the nozzle can be determined as a function of the Reynolds number. The calculation of the mass flow requires the absolute pressure, temperature and humidity of the flow at the exit of the nozzle as well as the pressure drop across the nozzle contraction.

The air leaving the drum ( $\dot{m}_{\text{drum}}$ , Figure 2.3) is measured with a ISA 1932 standard nozzle. The mass flow calculation applied can be found in ISO 5167-3. The calculation of the mass flow also requires the absolute inlet pressure, temperature and humidity of the flow at the exit of the nozzle and the pressure drop across the nozzle contraction.

The bypassed mass flow ( $\dot{m}_{\text{bypass}}$ ) is measured with a standard Venturi nozzle. The mass flow calculation applied can be found in ISO 5167-3.

**Torque and Rotational Speed** The torquemeter underneath the gearbox was specially designed and calibrated by Torquemeters Ltd and provide accurate measurements of the total rotor shaft torque and rotational speed. By measuring the phase shift of two cogwheels located at both ends of the calibrated torque shafts the angular deflection can be assessed and with it the torque. The shaft ratings of the torquemeter is 1500Nm.

### 2.1.4.2. Vibration Monitoring

For safety reasons the vibrations of the rotating parts are measured by means of 2 displacement and 8 acceleration sensors. The signals are processed and monitored by a Schenk vibration diagnostic module (VibroControl 4000). It indicates the displacement amplitudes and vibration velocities. If the preset limits are exceeded, an emergency shut down of the test rig is automatically initiated. The data is additionally displayed and logged on an independent personal computer which allows one to observe the trends in the long term. Three acceleration sensors monitor the vibrations of the gear box, one is used to measure the generator vibrations. The remaining four are located at the turbine bearings. Two displacement sensor measure the axial displacements of the rotor disk.

### 2.1.4.3. Probe Measurement Chain

The traversing system and the probe are controlled by an independent PC. It automatically moves the probe (3 axis) and saves the measurements performed at each point of the measurement grid. The same system can be used for all types of probes. A detailed description of the system can be found in [51].

## 2.2. Turbine Geometries

Originally the research turbine in the LISA test rig was a two stage axial shrouded turbine, one typical of a steam turbine, Sell et al [95]. The original turbine was redesigned as a one-and-half stage low aspect ratio unshrouded turbine, representative of a high work, cooled, high-pressure gas turbine, featuring compressibility effects. The presence of the second nozzle guide vane results in a representative rotor exit flow field, including the blade row interaction phenomena. Further details of this design are presented by Behr et al. [6], [7]. For the current experimental study, the rotor of the one-and-half stage configuration was replaced by a shrouded rotor with the same blade count but with thinner airfoils more representative of a low-pressure rotor. In this configuration three different rotor geometries were tested and are presented in the next section. Table 2.3 gives the main geometrical parameters of the blade row geometries. The data given in the Table for the rotor is representative for all three tested rotor geometries. The two stationary blade rows and their relative position were identical for

	NGV1	Rotor	NGV2
Blade count	36	54	36
Aspect ratio	0.87	1.42	0.82
Solidity	1.27	0.88	1.34
Turning [°]	71.7	123.8	106.4

Table 2.3.: Geometrical Characteristics of the one-and-half stage turbine at mid span.

all the measurements. The NGV2 has cylindrical end walls whereas the end walls of the NGV1 are shaped. The main features and the methodology of the corresponding end wall design of the NGV1 have been presented by Germain et al. [29]. The primary objectives of the nozzle guide vane end wall optimisation are to reduce secondary kinetic energy and to improve row efficiency. The modified secondary kinetic energy definition used in this context is presented in Germain et al. [29]. Figure 2.4 shows the shape of the NGV1 tip and hub end wall after optimisation.

### 2.2.1. Rotor Designs

In the experimental campaign presented three different shrouded rotor were considered. All three rotors have thin airfoils and are representative of a low-pressure rotor. The salient geometrical parameters can be found in Table 2.3. The differences between the rotors can be found in the end wall and blade design in the hub region:

- **Cylindrical End Walls:** Rotor with axisymmetric end walls at the hub and at the shroud. Blade geometry is typical for a low-pressure turbine and is the result of the redesign of the existing one-and-half stage turbine rotor.
- **1<sup>st</sup> End Wall Design:** Rotor with the same blade geometry as the rotor with cylindrical end walls, but with non-axisymmetric end walls on hub and shroud. The end wall geometry is the result of a optimisation process and methodology described in section 2.2.1.1.
- **2<sup>nd</sup> End Wall Design:** Rotor with thicker airfoils below 50% span and profiled end walls. The shape of the contoured end walls is again the results of an optimisation algorithm, but very similar to the 1<sup>st</sup> end wall design.

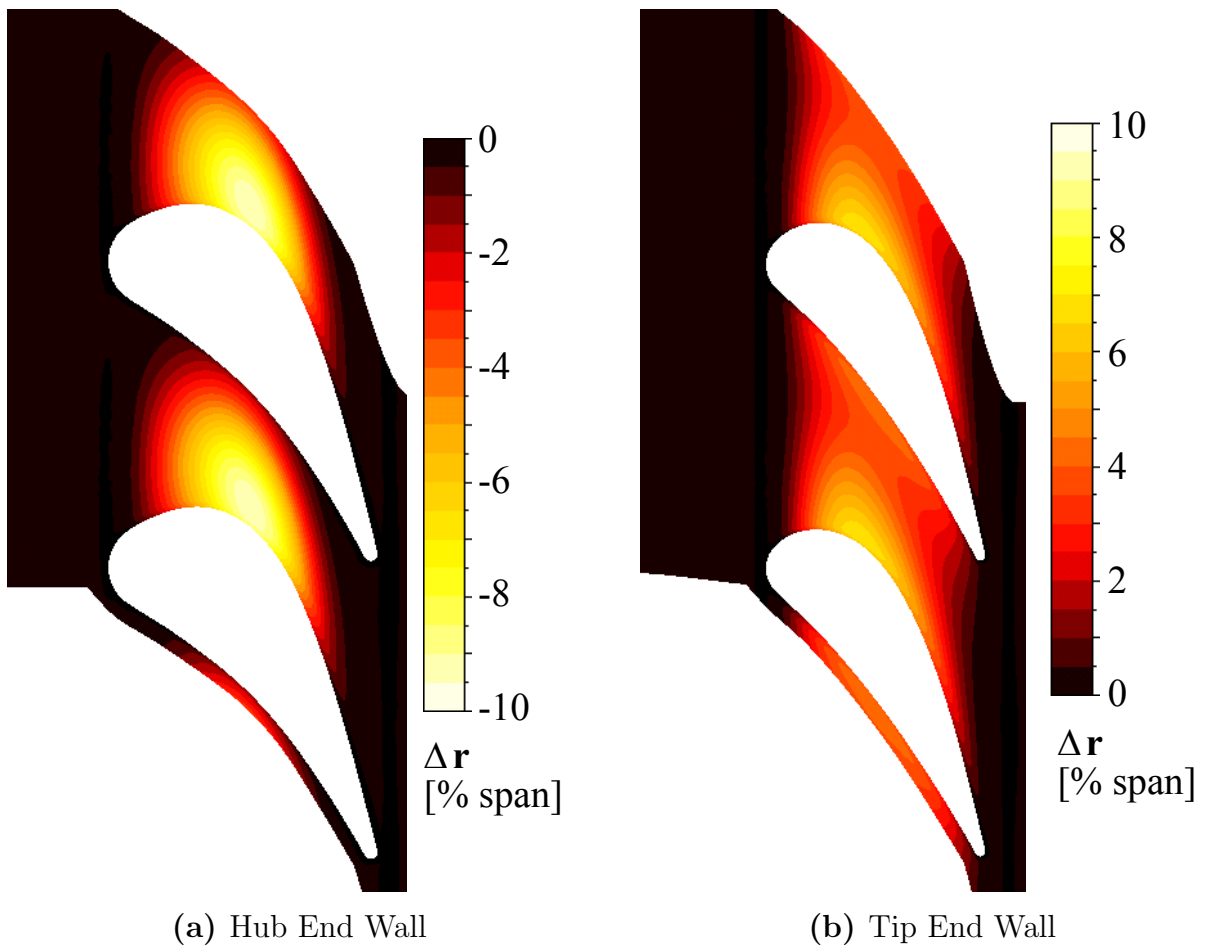


Figure 2.4.: Non-axisymmetric NGV1 end wall shapes from the optimisation.

For the operating point under investigation (Table 2.1) the blades of the rotors with cylindrical and 1<sup>st</sup> end wall design have pressure side separations in the hub region. The modified blade geometry combined with the 2<sup>nd</sup> end wall design suppresses the pressure side bubble.

### 2.2.1.1. End Wall Design Methodology

The rotor end wall contour design is the result of a three-dimensional end wall optimisation algorithm taking into account purge flow as well as the rim seal and the rotor shroud cavity geometries. The optimisation was performed for nominal operating conditions (Table 2.1) with a nominal purge flow rate of 0.8% of the main mass flow. A constant flow capacity was imposed as a boundary condition for the optimiser. Rotor tip and hub end walls have been designed using automatic numerical optimisation by means of a gradient based MTU-in-house optimiser code, the flow being

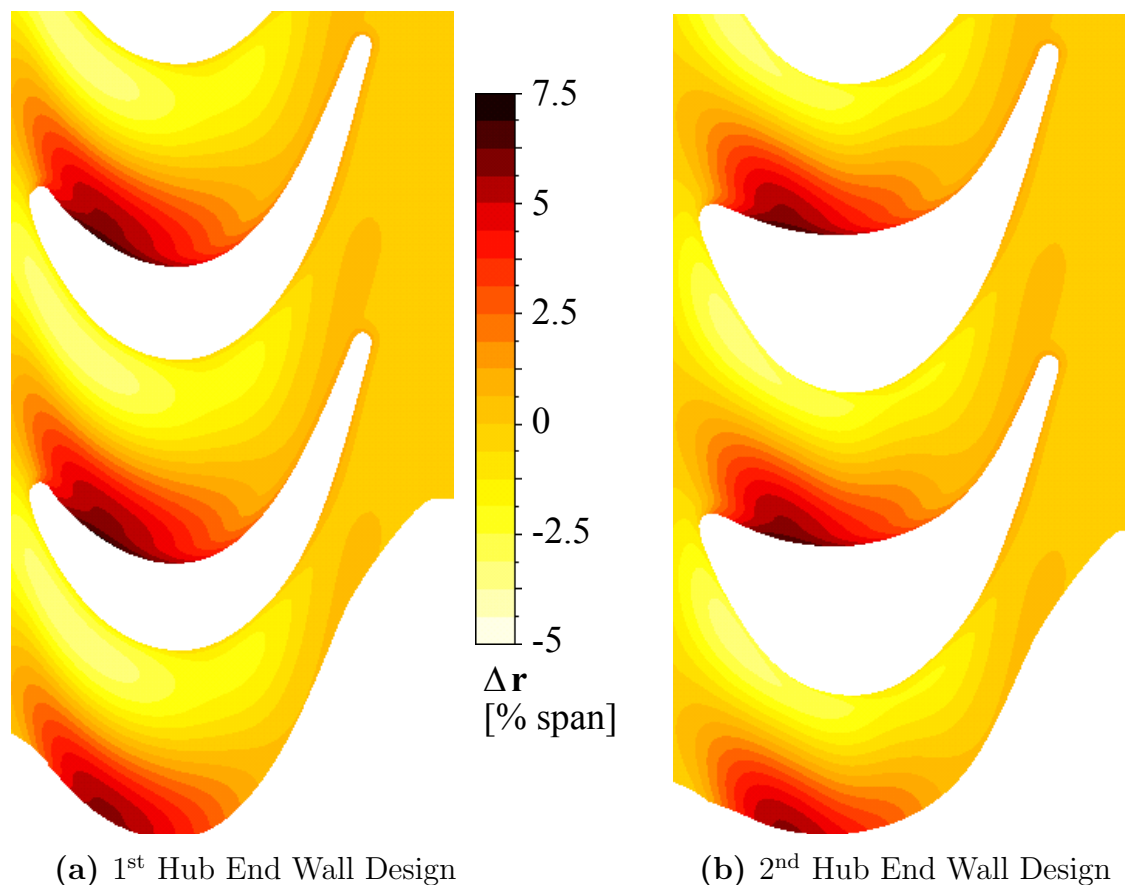


Figure 2.5.: Non-axisymmetric rotor hub end wall shapes from the optimisation.

computed by the steady 3D RANS solver TRACE developed at DLR and MTU. The aim of the rotor end wall design is to mitigate the effect of purge flow and to reduce the secondary losses and secondary kinetic energy generated in the rotor. The optimiser has the freedom to modify the hub end wall shape up to the rotor hub platform leading edge and not only between the leading and trailing edges. This feature is new with regard to the existing rotor hub end wall designs which are typically limited to the region between the blade leading and trailing edges. The results of the end wall profiling optimisation are shown in Figures 2.5 and 2.7 for the rotor hub and shroud end walls. The rotor hub end walls have a typical suction side trough, but smaller amplitudes when compared to the corresponding NGV1 hub end wall design. The amplitudes of the shroud end wall profiling are smaller because they must remain within the thickness of the rotor shroud. The profiling at the rotor hub platform goes up to the leading edge, giving it a wavy shape, Figure 2.6.

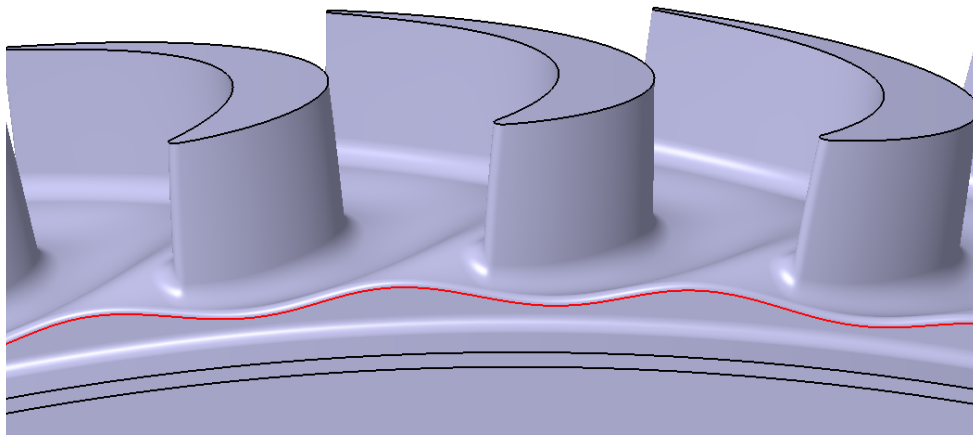


Figure 2.6.: Wavy shape (red line) of rotor hub platform leading edge (1<sup>st</sup> end wall design).

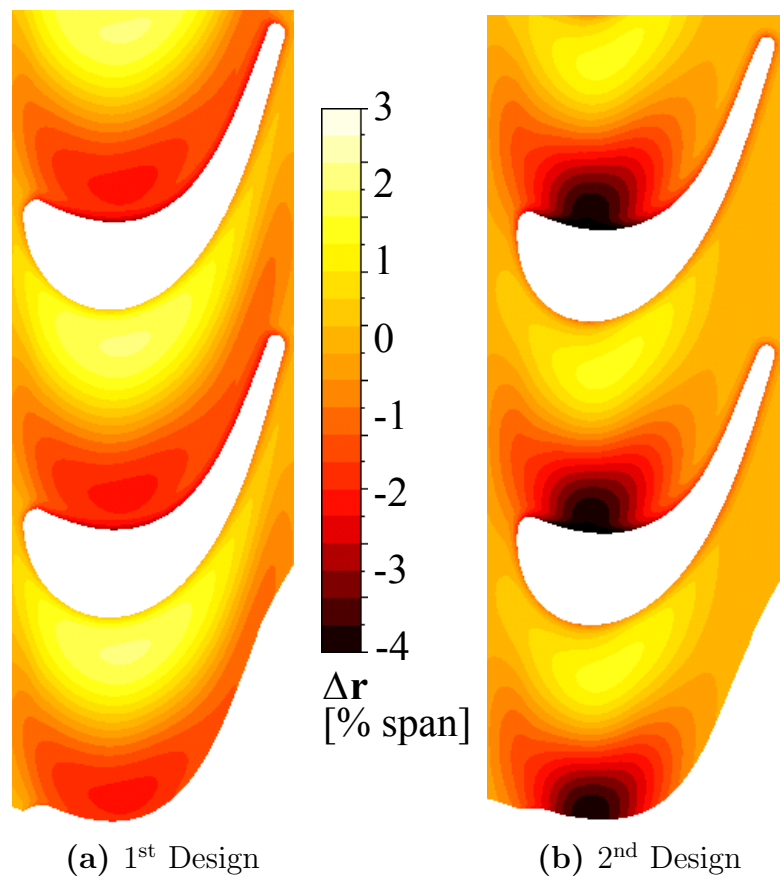


Figure 2.7.: Non-axisymmetric rotor shroud end wall shapes from the optimisation.

### 2.2.2. Blade Root Stress

The three rotor geometries have been meshed and modelled in ANSYS Workbench V13.0. Finite element calculations have been performed in order to assess the mechanical stresses and displacements at the nominal operating point.

All three rotors are made out of the same aluminium alloy (Weldural, HO-GAL2292) with the following mechanical properties:  $Rp_{0.2}=305\text{N/mm}^2$  and  $Rm=415\text{N/mm}^2$ . The FEM analysis was performed at a rotational speed of  $\omega=2700\text{rpm}$  and at a metal temperature of  $T=328\text{K}$  in line with the conditions during the measurements. A zero-displacement boundary condition was set at the cylindrical surface of contact with the rotor disk (indicated by the arrow in Figure 2.8). The meshes for the three rotors have between 1.9 and 3.0 million elements, depending on the rotor geometries. A grid sensitivity study has been performed.

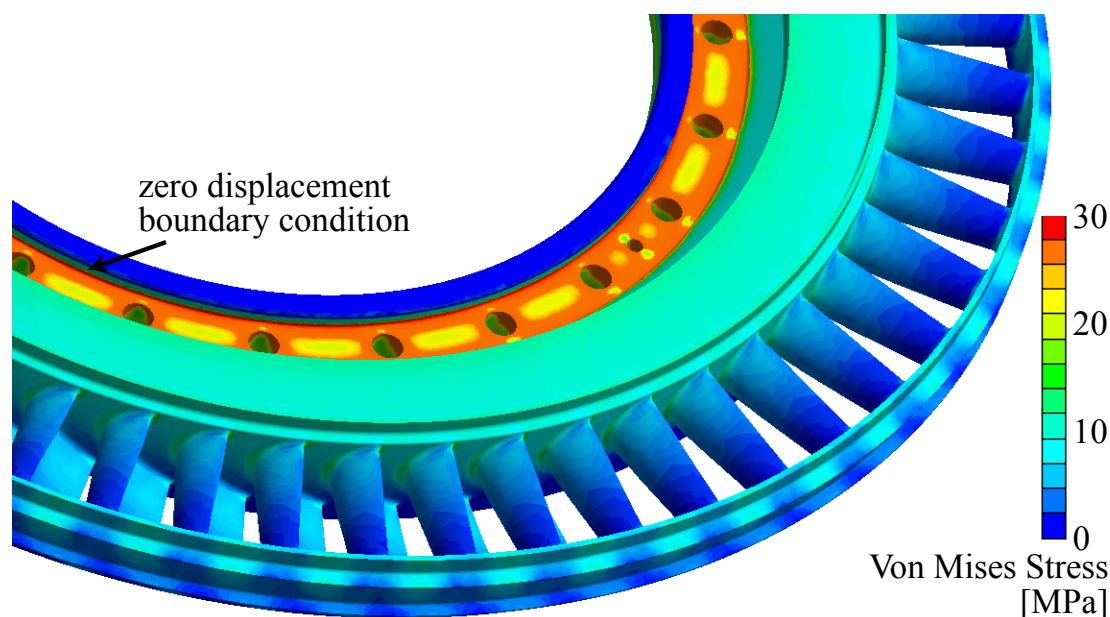


Figure 2.8.: Simulated Von-Mises stress levels in the rotor with cylindrical end walls.

A typical result of the FEM calculations is shown in Figure 2.8 for the rotor with cylindrical end walls. The simulated maximum stresses occur at the inner part of the rotor, where it is connected to the rotor disks. For all rotor geometries the maximum stresses are about 25% of yield stress and below the limit for plastic deformation. In the shroud the stress levels are one order of magnitude lower.

The calculated maximum blade root stresses vary with the end wall and rotor blade geometries. They are 20.1MPa for the rotor with cylindrical end walls, 16.8MPa for the rotor with the 1<sup>st</sup> end wall design and 16.5MPa for the rotor with the 2<sup>nd</sup> end wall design. The end wall profiling appears to reduce the blade root stress by about 15%. The thicker airfoil in blade hub region in combination with the 2<sup>nd</sup> end wall design has a minor effect on the blade root stress levels.

The calculated maximum displacement at the tip of the shroud is insensitive to the rotor blade and end wall geometry and is on the order of 0.05mm.

## 2.3. Probe Technology

Numerous measurement techniques exist to investigate the unsteady and three-dimensional flow field in a turbo-machine. The group of non-intrusive measurement techniques, such as laser Doppler anemometry (LDA) or particle image velocimetry (PIV) have the advantage not to disturb and interact with the flow field under investigation. Although these techniques are successfully used to measure the unsteady velocity vector, they cannot give any information about the local total and static pressure and temperature. The pressure is a relevant measurement that quantifies the thermodynamic state of the flow field. Intrusive probe techniques such as pneumatic x-hole probes, hot wire anemometry and fast response aerodynamic probes are used to measure the local steady and unsteady temperature and pressure in addition to the three-dimensional flow vector.

### 2.3.1. Probe Types

In the context of this work four different intrusive probe technique are used, the 4-hole, 5-hole, FRAP and FENT probes. They are briefly presented in the following sections. The measurement uncertainties for the pressures and derived quantities are listed in Table 2.5.

#### 2.3.1.1. Pneumatic 5-hole Probe

The 5-hole probe has a cobra shaped head with a tip diameter of 0.9mm, Figure 2.9. It consists of a soldered bundle of four miniature tubes arranged around a centre tube. The tip of the probe has the shape of a quadratic pyramid with 45° inclined surfaces and a truncated tip. The main advantage, compared to the other probe types, is the large distance of the probe shaft from the measurement volume at the tip of the probe.

#### 2.3.1.2. Pneumatic 4-hole Probe

The 4-hole probe has a cylindrical probe tip with a rounded surface for the pitch hole, Figure 2.9. The diameter of the tip is 1.8mm and identical to the tip diameter of the FRAP probe. The axial space required by the 4-hole

probe is reduced when compared to the cobra-shaped 5-hole probe. This becomes attractive when performing measurements inside cavities. For this reason only the 4-hole probe could be used at the rotor inlet in order to be able to measure in the rim seal cavity.



(a) 5-hole Probe



(b) 4-hole Probe

Figure 2.9.: Pneumatic probes compared to match for scale comparisons.

### 2.3.1.3. Fast-Response Aerodynamic Probe (FRAP)

The fast response aerodynamic probe technology has been developed over the last two decades at the Laboratory of Energy Conversion (LEC) at ETH Zurich. For details on the fundamentals and first measurements refer

to Gossweiler [31] or for details on further measurements to Kupferschmied [48]. The blockage effects of the probe are minimised as a result of the miniaturisation of the probe head down to a diameter of 1.8mm. The probe head is cylindrical with an inclined, curved tip, Figure 2.10. Schlienger [90] and Pfau et al. [74], [75] further developed the design to a 2-sensor FRAP. The tip is equipped with two complementary single-sensor piezoresistive pressure transducers. The probe is capable of capturing unsteady flow features up to frequencies of 48kHz based on measurements including total and static pressures, flow yaw and pitch angles and Mach number. The frequency bandwidth of the temperature is limited to a frequency of 10Hz. However, the influence of the measured temperature on the velocity is very modest. The 2-sensor FRAP is operated in a virtual-4-sensor mode in order to measure three-dimensional, time-resolved flow properties. The yaw sensitivity is gained from sensor 1 by turning the probe by  $-42^\circ$  and  $+42^\circ$  according to its angular position. Therefore, each radial measurement point consists of 3 different angular positions. As a result of the virtual approach only the periodic part of the time-resolved yaw angle information can be resolved due to phase locking. The pitch sensitivity is the result of the second sensor located below the curved surface. The data is acquired at a sampling rate of 200kHz over a period of two seconds. The FRAP probe allows its use in flow fields up to  $120^\circ\text{C}$ . The recently developed high temperature FRAP probe designed by Lenherr [52] allows measurements to be taken in higher temperature flows  $260^\circ\text{C}$ .

#### 2.3.1.4. Fast Response Entropy Probe (FENT)

Time-resolved temperature measurements were carried out with the fast response entropy probe (FENT probe) designed and developed at the LEC at ETH Zurich by Mansour et al. [54, 55]. The probe has a tip diameter of 1.8mm and is comprised of two parts. Firstly, a miniature silicon piezoresistive chip is glued beneath a pressure tap to measure the unsteady static and total pressures. Secondly, a pair of thin film gauges with a thickness of about 200nm are operated as resistance thermometers at two different film temperatures, and used to measure the unsteady total temperature. The serpentine shaped thin films cover a rectangular area of 1.77mm x 0.85mm, Figure 2.10. The radial distance covered by the serpentine shaped thin-films, representing 2.52% of the turbine passage height in the measurement plane, is the minimum spatial resolution on the measurement grid. The measurements taken with the FENT probe therefore have a radial spacing



(a) FRAP



(b) FENT Probe

Figure 2.10.: Fast response aerodynamic and entropy probes compared to match for scale comparisons.

of 1.125mm in the regions of radial clustering and of 2.25mm elsewhere. In the data processing, coincident phase-locked measurements of  $P_t$  and  $T_t$  are used to determine the unsteady entropy rise. As unsteady temperature and pressure are measured at different locations in the same probe, the data is shifted in the radial direction by the distance between the two measurement holes during the post-processing in order to have both signals from exactly the same location before calculating the entropy. The measurement band-

width is 48kHz, and data are acquired at a sampling frequency of 200kHz over a period of 2 seconds as for the FRAP.

### 2.3.2. Traversing System

The test rig is equipped with a three-axis fully automated traversing system. The radial movement and the turning around the probe axis is enabled by two stepper motors shown in Figure 2.11. The turbine is equipped with 3 movable casing rings, which slide on radial seals. A third motor connected to a Heidenhain encoder enables the circumferential movement of the probe. This design explained in Schlienger [90] minimises the flow disturbances allowing continuous area traversing in one plane with a probe access hole of only 10mm in diameter. The accuracies and ranges of the traversing system components are given in Table 2.4.

	Range	Accuracy
Yaw axis	360°	0.003°
Radial axis	150mm	0.1mm
Circumferential axis	30°	0.002°

Table 2.4.: Range and accuracies of the traversing system.

### 2.3.3. Calibration

Before each measurement campaign all the probes are calibrated against a known reference. The pneumatic probes are aerodynamically calibrated. For the FRAP and FENT probe an aerodynamic and sensor calibration needs to be performed. During the aerodynamic calibration the so-called calibration coefficients are determined. They are required to derive the three-dimensional flow properties in the data reduction. At the LEC there are two facilities dedicated to the probe calibration.

**Freejet Facility** The freejet facility is used for the aerodynamic calibration. All the probes are calibrated for yaw angle, pitch angles and total and static pressures at a given Mach number. The axisymmetric freejet provides a uniform velocity profile at a turbulence level of approximately 0.3%. A detailed description of the facility can be found in Kupferschmied [48]. In the freejet facility the probes can be calibrated for a yaw angle

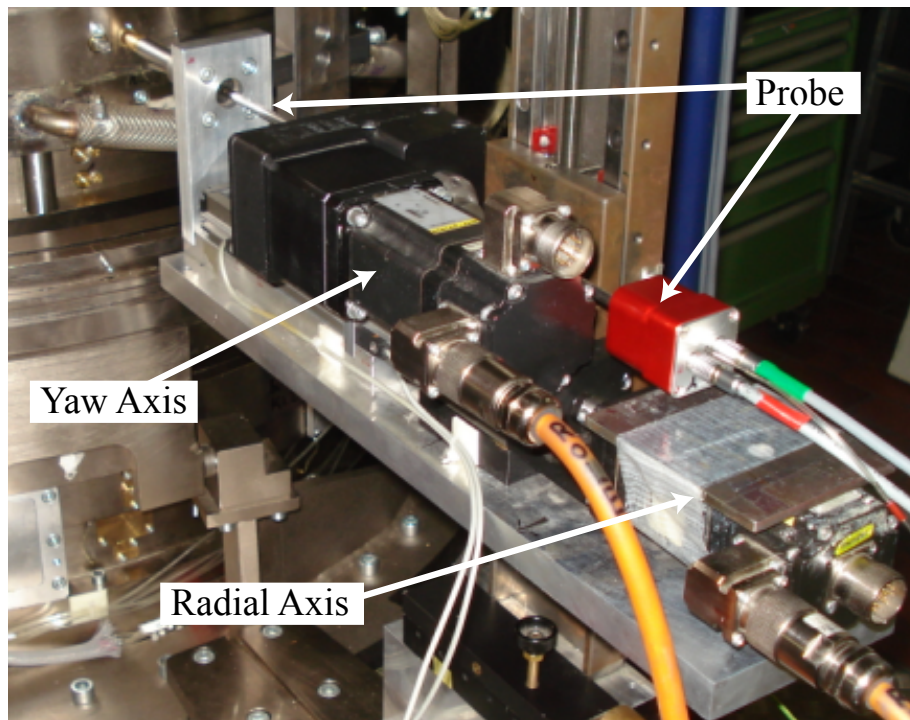


Figure 2.11.: Probe traversing system.

range of  $\pm 180^\circ$  and a pitch angle range of  $\pm 36^\circ$ . The maximum Mach number is around 0.8.

**Sensor Calibration Facility** The pressure sensors of the fast-response aerodynamic and fast entropy probes have to be calibrated for pressure and temperature. For the calibration an oven is used which provides especially accurate and stable temperatures. The calibration is performed at different levels of back pressure applied to the probe cavity and provided by the same accurate pressure source as during the measurements.

### 2.3.3.1. 5-Hole Probe

The pneumatic 5-hole probe has been calibrated for a yaw angle range of  $\pm 30^\circ$  and a pitch angle range of  $\pm 20^\circ$  in steps of  $2^\circ$ . The calibration was performed for  $M=0.3$  and  $M=0.5$ , corresponding to the average Mach numbers at the rotor exit and the NGV2 exit measurement planes where this probe was used. Based on the calibration a set of sensitivity coefficients for the flow angles and total and static pressures is determined. The equations

to evaluate the sensitivity coefficients  $K_i$  are given in Equation 2.2.

$$K_t = \frac{P_t - P_1}{q}, \quad K_s = \frac{P_t - P_s}{q}, \quad K_\varphi = \frac{P_2 - P_3}{q}, \quad K_\gamma = \frac{P_4 - P_5}{q} \quad (2.2)$$

with

$$q = P_1 - \frac{1}{4} \sum_{i=2}^5 P_i$$

### 2.3.3.2. 4-Hole Probe

The pneumatic 4-hole probe has also been calibrated for a yaw angle range of  $\pm 30^\circ$  and a pitch angle range of  $\pm 20^\circ$  in steps of  $2^\circ$ . The calibration was performed for  $M=0.5$ , corresponding to the average Mach numbers at the NGV1 exit measurement plane where this probe was used. Based on the calibration the same set of sensitivity coefficients for the flow angles and total and static pressures as for the 5-hole probe is determined. The corresponding equations to evaluate the sensitivity coefficients  $K_i$  are given in Equation 2.3.

$$K_t = \frac{P_t - P_1}{q}, \quad K_s = \frac{P_t - P_s}{q}, \quad K_\varphi = \frac{P_2 - P_3}{q}, \quad K_\gamma = \frac{P_1 - P_4}{q} \quad (2.3)$$

with

$$q = P_1 - \frac{P_2 + P_3}{2}$$

### 2.3.3.3. FRAP

Before the aerodynamic calibration in the freejet facility can be performed with the FRAP, a sensor calibration is necessary. The sensor calibration was done over a temperature range from  $30^\circ\text{C}$  to  $65^\circ\text{C}$  in steps of  $5^\circ\text{C}$ . This covers the full temperature range the probe experiences when used at the different measurement planes. The pressure sensitivity of the sensors was determined by varying the back pressure from 10mbar to 610mbar. The pressure sensitivity of both sensors is on the order of  $0.1\text{mV/mbar}$ , while the temperature sensitivity is on the order of  $2.5\text{mV}/^\circ\text{C}$ .

Then the FRAP has been aerodynamically calibrated for a yaw angle range of  $\pm 80^\circ$  and a pitch angle range from  $-24^\circ$  to  $-20^\circ$  in steps of  $2^\circ$ . When the probe is operated in the virtual 4-sensor mode where the probe is turned by  $\pm 42^\circ$  for the yaw angle sensitivity, this yaw angle calibration range allows

measurements up to  $\pm 30^\circ$  (theoretically  $38^\circ = 80^\circ - 42^\circ$ ). The sensitivity coefficients for the FRAP are the same as for the pneumatic 4-hole probe, given in Equation 2.3.

### 2.3.3.4. FENT

Like the FRAP the sensor calibration was done before the aerodynamic probe calibration in the freejet. The calibration of the thin film gauges was done over a temperature range from  $30^\circ\text{C}$  to  $130^\circ\text{C}$  in steps of  $10^\circ\text{C}$ . This covers the full temperature range the probe experiences when used at the different measurement planes.

The FENT probe has been aerodynamically calibrated for a yaw angle range of  $\pm 80^\circ$  in steps of  $2^\circ$ . When the probe is operated in the virtual 4-sensor mode where the probe is turned by  $\pm 42^\circ$  for the yaw angle sensitivity, this yaw angle calibration range allows measurements up to  $\pm 30^\circ$ . The probe has no pitch angle sensitivity. The sensitivity coefficients  $K_i$  for the FENT probe are given in Equation 2.4.

$$K_t = \frac{P_t - P_1}{q}, \quad K_s = \frac{P_t - P_s}{q}, \quad K_\varphi = \frac{P_2 - P_3}{q} \quad (2.4)$$

with

$$q = P_1 - \frac{P_2 + P_3}{2}$$

## 2.4. Data Reduction

### 2.4.1. Pneumatic Probes

The pressures measured by the 4-hole or 5-hole probe pressure taps are transformed into flow angles and total and static pressure with the use of the calibration coefficients, determined during the calibration procedure. First the flow angle sensitivity coefficients  $K_\varphi$  and  $K_\gamma$  are determined using Equations 2.2 or 2.3. With the use of the calibration coefficients  $k_{\varphi,ij}$  and  $k_{\gamma,ij}$  the flow yaw and pitch angles are calculated by solving the bivariable polynomials given in Equations 2.5 and 2.6.

$$\varphi = \sum_{i=0}^m \sum_{j=0}^n k_{\varphi,ij} K_\varphi^i K_\gamma^j \quad (2.5)$$

$$\gamma = \sum_{i=0}^m \sum_{j=0}^n k_{\gamma,ij} K_{\varphi}^i K_{\gamma}^j \quad (2.6)$$

The calibration coefficients for the total and static pressures ( $k_{t,ij}$ ,  $k_{s,ij}$ ) and the flow angles  $\varphi$  and  $\gamma$  are used to solve the bivariable polynomials given in Equations 2.7 and 2.8 in order to determine the sensitivity coefficients  $K_t$  and  $K_s$ .

$$K_t = \sum_{i=0}^m \sum_{j=0}^n k_{t,ij} \varphi^i \gamma^j \quad (2.7)$$

$$K_s = \sum_{i=0}^m \sum_{j=0}^n k_{s,ij} \varphi^i \gamma^j \quad (2.8)$$

Finally the total and static pressures are calculating by rearranging the definition of  $K_t$  and  $K_s$  given in Equations 2.2 or 2.3. The coefficients  $m$  and  $n$  in Equations 2.5 to 2.8 represent the order of the polynomial approximation function for the calibration coefficients. Higher order polynomial approximations better fit the calibration data but can lead to a higher error bandwidth in particular at the limits of the calibration range. On the other hand, the use of a lower interpolation polynomial order reduces the accuracy of the model. In the context of this work a 6<sup>th</sup> order polynomial model ( $m=n=6$ ) was used for all probe types.

The determined angles are in the probe relative system. Therefore, the set angles for the traversing system have to be added. The angle convention is as follows: The yaw angle is positive in the rotational direction of the turbine, the pitch angle is positive for fluid moving towards the casing. The yaw angle is given relative to the axial direction. Knowing the flow angles and the total and static pressures, the Mach number  $M$ , the absolute flow velocity  $V$ , the axial  $V_x$ , radial  $V_r$  and circumferential  $V_{\varphi}$  velocity components are calculated as defined in Equations 2.9 to 2.13:

$$M = \sqrt{\frac{2}{\kappa - 1} \left( \left( \frac{P_t}{P} \right)^{\frac{\kappa-1}{\kappa}} - 1 \right)} \quad (2.9)$$

$$V = M \sqrt{\kappa R T_s} \quad (2.10)$$

$$V_x = V \cos \varphi \cos \gamma \quad (2.11)$$

$$V_r = V_x \tan \gamma \quad (2.12)$$

$$V_{\varphi} = V_x \tan \varphi \quad (2.13)$$

For the speed of sound the average static temperature from the corresponding FRAP measurement at the same traversing plane is applied.

## 2.4.2. FRAP and FENT

The time-resolved FRAP and FENT probe measurements are reduced with an in-house software package. A detailed explanation of the program can be found in Schlienger [90]. Generally speaking the data processing of both probes is divided into two steps. Two additional files need to be generated before the raw data pre-processing can be started. The first file contains the point coordinates and the yaw setting angles for the probe of each measurement point. The second file contains the operational data of the turbine during the measurement and used in the second step to calculate the non-dimensional quantities or the turbine efficiency for example.

**Step 1: Raw Data Pre-Processing** In this step the binary raw voltage signals  $U$  and  $U_e$  are read and phase-locked with the use of the optical trigger signal. In this step the amount of data is reduced, only the raw data acquired during the first three rotor blade passages after the trigger signal are kept. With a resolution of 82 samples per blade passage this results in 246 data points. The data is acquired during two seconds corresponding to 90 rotor revolutions at the operating point under investigation, however only the first 85 revolutions are considered. Hence, at each measurement point  $85 \times 246 = 20910$  samples are considered for the processing in the next step. The data is not averaged at this point of the data processing.

**Step 2: Offset Gain Calibration, Evaluation of Flow Quantities** The phase-locked raw voltage data files from the former step are converted into pressure and temperature using the sensor calibration model (bivariable polynomial) given in Equations 2.14 and 2.15.

$$\Delta P = \sum_{i=0}^m \sum_{j=0}^n k_{p,ij} U^i U_e^j \quad (2.14)$$

$$T = \sum_{i=0}^m \sum_{j=0}^n k_{T,ij} U^i U_e^j \quad (2.15)$$

This model applies to both sensors in the FRAP and to the pressure sensor in the FENT probe. The calculation of the unsteady temperature of the

FENT probe, based on the raw voltage signals, is detailed in Mansour [53]. In order to remove the sensor drift effects during the measurement investigated by Kupferschmied [48] an offset-gain calibration is executed before and after each radial traverse. A detailed description can be found in Schlienger [90]. The corresponding offset and gain values are applied to the calculated pressure difference and temperature at each traverse.

In order to further proceed in applying the aerodynamic calibration model and to calculate various flow properties, the absolute sensor pressures are calculated by subtracting the differential pressure  $\Delta P$  from the sum of the atmospheric pressure  $P_{\text{atm}}$  and the sensor reference back pressure  $P_{\text{ref}}$  for each probe sensor, Equation 2.16

$$P = P_{\text{atm}} + P_{\text{ref}} - \Delta P \quad (2.16)$$

Then the flow angles, total and static pressures are calculated in the same procedure as presented for the pneumatic probes and with the use of the aerodynamic calibration coefficients, Equations 2.5 to 2.8 for the FRAP. For the FENT probe these equations are simplified as the probe has no pitch sensitivity, Equations 2.17 to 2.19:

$$\varphi = \sum_{i=0}^m k_{\varphi,i} K_{\varphi}^i \quad (2.17)$$

$$K_t = \sum_{i=0}^m k_{t,i} \varphi^i \quad (2.18)$$

$$K_s = \sum_{i=0}^m k_{s,i} \varphi^i \quad (2.19)$$

A 6<sup>th</sup> order polynomial model was used for both probes. In a next step the measurements are phase-lock averaged over the 85 rotor revolutions available in the reduced data format. Finally the unsteady three-dimensional flow field (Equations 2.9 to 2.13) and other relevant flow quantities are evaluated. The most important are presented in sections 2.4.5 to 2.4.9.

### 2.4.3. Mass- and Area-averaging

Two averaging methods were used to post-process the measurements made with the different probes. Depending on the flow quantity the measurement

results are area- or mass-averaged. The flow quantities can be circumferentially or radially averaged. The average over an entire blade pitch is achieved by a two directional integration. Generally non-convective flow quantities, such as static pressure or static temperature, are expressed as area-averages, while convected quantities, such as total temperature and pressure, are mass-averaged. As the probe measurement grid is discrete, the integration is a numerical one.

**Area Averaging:** The local flow quantity  $\xi$  is cell centred and weighted with the associated local area to calculate the area-averaged quantity  $\bar{\xi}$ . For a structured grid expressed in polar coordinates, the area-weighted integral is given in Equation 2.20

$$\bar{\xi} = \frac{\sum \xi dA}{\sum dA} \quad (2.20)$$

with:

$$dA = r dr d\theta$$

**Mass Averaging:** The local flow quantity  $\xi$  is cell centred and weighted with the associated mass flow through the cell to calculate the mass-averaged quantity  $\bar{\xi}$ . For a structured grid, the mass-weighted integral is given in Equation 2.21

$$\bar{\xi} = \frac{\sum \xi d\dot{m}}{\sum d\dot{m}} \quad (2.21)$$

with:

$$d\dot{m} = \rho V_x dA = \rho V_x r dr d\theta$$

#### 2.4.4. Pressure and Temperature Normalisation

The turbine is open to atmosphere at the exit and the pressure ratio is kept constant during all measurements. Hence the total inlet conditions ( $P_{t,in}$  and  $T_{t,in}$ ) and power of the turbine are not constant for all the measurement days but depend on the daily variations of the atmospheric pressure. Therefore the pressure and temperature measurements have to be corrected for daily variations. Throughout this work only ratios of total and static pressure  $Cp$  and temperature  $Ct$  are used. They are defined in Equation 2.22:

$$Cp = \frac{P}{P_{t,in}} \quad Ct = \frac{T}{T_{t,in}} \quad (2.22)$$

### 2.4.5. Turbine Efficiency

The definition of the total-to-total efficiency  $\eta_{tt}$  accounting for the injection rate  $IR$  used in this study is given in Equation 2.23:

$$\eta_{tt} = \frac{\frac{\omega M}{\dot{m} C_P T_{t,in}}}{1 - (1 - IR) \left( \frac{P_{t,R1ex}}{P_{t,in}} \right)^{\frac{\kappa-1}{\kappa}} - IR \left( \frac{P_{t,R1ex}}{P_{t,cavity}} \right)^{\frac{\kappa-1}{\kappa}}} \quad (2.23)$$

The injection rate is defined in Equation 2.1. The efficiency is calculated at each measurement point at the rotor exit with the current values of  $P_{t,in}$ ,  $T_{t,in}$ ,  $M$ ,  $\dot{m}$ ,  $P_{t,cavity}$  and local  $P_t$ . The total pressure at the rotor exit is provided by the 5-hole probe for all quoted total-to-total efficiencies in this work.

### 2.4.6. Non-deterministic Unsteadiness

An interesting variable to analyse the unsteadiness in the flow field is the experimentally evaluated root mean square values  $rms$  of the total pressure random part. Regions of high  $rms$  are indicative of significant non-deterministic unsteadiness. This may be due to flow instability modes e.g. eddy shedding or transition or may be simply due to high turbulence. Using the triple decomposition of the time-resolved pressure signal as shown in Equation 2.24, the random part  $P'(t)$  can be evaluated as the difference between the raw pressure  $P(t)$  signal of the FRAP probe and the phase-locked averaged pressure  $\bar{P} + \tilde{P}(t)$ . The same approach was used by Porreca et al. [77, 76] to derive turbulent quantities.

$$P(t) = \bar{P} + \tilde{P}(t) + P'(t) \quad (2.24)$$

### 2.4.7. Streamwise Vorticity and Circulation

The streamwise vorticity  $\Omega_S$  is the scalar product of the vorticity vector and the primary flow vector  $\vec{V}$ , Equation 2.25.

$$\Omega_S = \vec{\Omega} \cdot \vec{V} \quad (2.25)$$

The primary flow direction is defined as the measured circumferentially mass-averaged velocity profile. The components of the vorticity vector are given in Equations 2.26 to 2.28 in cylindrical coordinates. The streamwise

vorticity is related to secondary flows as it introduces flow perpendicular to the primary flow direction, defined as the circumferentially mass-averaged velocity profile. Therefore a reduction in streamwise vorticity normally leads to a reduction in secondary loss. To calculate the three dimensional vorticity vector the axial gradients of the radial and circumferential velocity components are needed. In a single axial plane traverse it is not possible to calculate these axial gradients. Therefore the axial gradients are estimated using the time-resolved data, with the assumption that the flow structures are frozen during one time step. The detailed approach and calculation can be found in Schuepbach et al. [92].

$$\Omega_x = \frac{1}{r} \left( \frac{\partial}{\partial r} (rV_\theta) - \frac{\partial V_r}{\partial \theta} \right) \quad (2.26)$$

$$\Omega_r = \frac{1}{r} \frac{\partial V_x}{\partial \theta} - \frac{\partial V_\theta}{\partial x} \quad (2.27)$$

$$\Omega_\theta = \frac{\partial V_r}{\partial x} - \frac{\partial V_x}{\partial r} \quad (2.28)$$

Based on the streamwise vorticity components the circulation  $\Psi$  can be calculated as an area integral of  $\Omega_S$  inside an iso-contour of zero streamwise vorticity, Equation 2.29:

$$\Psi = \int_{\Omega_S \geq 0} \Omega_S dA \quad (2.29)$$

### 2.4.8. Dissipation

The dissipation evaluates the rate at which kinetic energy is irreversibly transformed into thermal energy by viscous forces. The viscous dissipation function  $\Phi$ , is given in cylindrical coordinates in Equation 2.30.

$$\begin{aligned} \Phi = & 2 \left[ \left( \frac{\partial V_r}{\partial r} \right)^2 + \left( \frac{1}{r} \frac{\partial V_\theta}{\partial \theta} + \frac{V_r}{r} \right)^2 + \left( \frac{\partial u_x}{\partial x} \right)^2 \right] \\ & + \left[ r \frac{\partial}{\partial r} \left( \frac{V_\theta}{r} \right) + \frac{1}{r} \frac{\partial V_r}{\partial \theta} \right]^2 + \left[ \frac{1}{r} \frac{\partial V_x}{\partial \theta} + \frac{\partial V_\theta}{\partial x} \right]^2 \\ & + \left[ \frac{\partial V_r}{\partial x} + \frac{\partial V_x}{\partial r} \right]^2 - \frac{2}{3} \left( \nabla \cdot \vec{V} \right)^2 \end{aligned} \quad (2.30)$$

The viscous dissipation function  $\Phi$  multiplied by the laminar viscosity  $\mu$  of

the fluid appears in the energy equation as a source of heat. Equation 2.31 from Schlichting [89] gives the heat generated by the viscous forces in the volume element  $\Delta v$ .

$$dQ_F = dt \cdot \Delta v \cdot \mu \cdot \Phi \quad (2.31)$$

The dissipation function  $\Phi$  can be evaluated based on the FRAP measurements when the required axial gradients are approximated using the frozen flow approach presented by Schuepbach et al. [92]. However the calculated values of the dissipation itself need to be considered with some care. The viscosity, by which the dissipation function is multiplied, is the laminar viscosity. In practice the temporal resolution of the velocity vectors is only deterministic and the spatial resolution is limited by the measurement traverse grid size. For these reasons the calculated dissipation must be regarded with some care as the modest spatial resolution of the measurement grid and the deterministic time signature will result in an underestimate of the real dissipation. In order to evaluate the dissipation correctly one would need the instantaneous velocity vector with its deterministic and turbulent fluctuations on a very fine measurement grid. Having in mind these points, the calculated dissipation appears to be a very sensitive indicator of the local loss generation and the results are valuable.

In order to better quantify the dissipation function, it is normalised by the flux of kinetic energy given in Equation 2.32.

$$\dot{m} \cdot \frac{V^2}{2} = \rho \cdot V_x \cdot A_x \cdot \frac{V^2}{2} \quad (2.32)$$

where

$$V^2 = V_x^2 + V_r^2 + V_\theta^2$$

Hence, the modified dissipation function  $D$  is given in Equation 2.33:

$$D = \frac{\mu \cdot \Phi}{\rho \cdot \frac{V^2}{2}} \quad (2.33)$$

$D$  can be interpreted as the percentage rate at which kinetic energy is converted into heat per second. This is the variable plotted when referred to as dissipation. It should be noted that the dissipation is calculated for only single traverse planes. In order to relate the dissipation to loss, one would need to integrate over the whole volume.

### 2.4.9. Entropy

The FENT probe provides the unsteady total temperature  $T_t$  and the total pressure  $P_t$ . Knowing the total flow conditions the entropy rise compared to the reference conditions can be calculated using Equation 2.34. The total inlet conditions  $T_{t,in}$  and  $P_{t,in}$  are used as reference conditions.

$$\Delta s = C_P \ln \frac{T_t}{T_{t,in}} - R \ln \frac{P_t}{P_{t,in}} \quad (2.34)$$

## 2.5. Measurement Uncertainty

All experimentally acquired results inherently have errors and the true value of a measured variable cannot be exactly known. There are a vast number of error sources related to the instrumentation set-up, the data acquisition and reduction, the facility and the environmental effects. Therefore it is of high importance to have information about the uncertainties when interpreting measurement results, in order to be able to assess whether a measured difference is inside or outside the measurement uncertainty bandwidth. In this section the estimated measurement uncertainties for the probes and the turbine efficiency are summarised.

### 2.5.1. Probes

A probe measurement uncertainty analysis for the 4-hole, 5-hole and FRAP probes using the "Guide of Uncertainty in Measurements" (GUM) [44]. was performed by Lenherr et al. [51]. Mansour [55] did the corresponding analysis for the FENT probe using the same tools. The GUM is a standardised method, which first converts all uncertainty information into probability distributions. In case of correlated parameters, cross-correlation coefficients are needed to evaluate their combined uncertainty contribution. The methods for the evaluation of the uncertainties are defined in DIN 1319-3 section 4.2.

The final statement of the measurement result contains the limits and the distribution of the expected values. Generally a coverage factor of  $k=2$  is used. If the result is normally distributed, this value corresponds to a level of confidence of 95% and is therefore rather conservative. The uncertainties evaluated for all the probes used in the context of this work are presented in Table 2.5. The values for the yaw and pitch angles are given as relative

uncertainties in the calibration range of  $\pm 24^\circ$  in yaw and  $\pm 20^\circ$  in pitch angle. The pressure uncertainties are presented relative to the dynamic head. The pressure uncertainties represent expected uncertainties for real flow angles which are within the inner 85% of the angular pitch calibration range ( $0^\circ$  to  $\pm 17^\circ$ ). The Mach Numbers in Table 2.5 correspond to the conditions at the measurement planes, NGV1 exit ( $M=0.5$ ), rotor exit ( $M=0.25$  to  $0.3$ ) and NGV2 exit ( $M=0.5$ ).

	Parameter	$M = 0.25$	$M = 0.3$	$M = 0.5$
5HP	$\varphi$	$\pm 0.7\%$	—	$\pm 0.5\%$
5HP	$\gamma$	$\pm 1.0\%$	—	$\pm 0.8\%$
5HP	$P_t$	$\pm 1.9\%$	—	$\pm 0.7\%$
5HP	$P_s$	$\pm 2.2\%$	—	$\pm 0.9\%$
4HP	$\varphi$	—	$\pm 0.5\%$	$\pm 0.3\%$
4HP	$\gamma$	—	$\pm 0.7\%$	$\pm 0.5\%$
4HP	$P_t$	—	$\pm 1.5\%$	$\pm 0.8\%$
4HP	$P_s$	—	$\pm 1.6\%$	$\pm 1.1\%$
FRAP	$\varphi$	$\pm 1.3\%$	—	$\pm 0.5\%$
FRAP	$\gamma$	$\pm 1.6\%$	—	$\pm 0.8\%$
FRAP	$P_t$	$\pm 2.8\%$	—	$\pm 1.0\%$
FRAP	$P_s$	$\pm 3.7\%$	—	$\pm 1.2\%$
FENT	$P_t$	—	$\pm 0.1\%$	—
FENT	$T_t$	—	$\pm 2.5\%$	—
FENT	$\Delta s$	—	$\pm 2.51\%$	—

Table 2.5.: Range of expanded uncertainty ( $k=2$ ) of the flow parameters yaw angle  $\varphi$ , pitch angle  $\gamma$ , total pressure  $P_t$ , total temperature  $T_t$ , static pressure  $P_s$  and entropy rise  $\Delta s$  for the pneumatic, FRAP and FENT probe, according to their measurement capabilities.

## 2.5.2. Turbine Efficiency

The expanded uncertainty for the total-to-total turbine efficiency given in Equation 2.23 was estimated by Schuepbach [91]. In this work the same measurement and post-processing devices are used and the results of the uncertainty analysis are summarised.

In order to calculate the expanded uncertainty of the total-to-total efficiency taking into account the purge flow injection, the different input parame-

ters (Equation 2.23) and their related standard uncertainties need to be taken into account. The calculated absolute expanded uncertainty of the total-to-total efficiency is  $\pm 0.37\%$  with a coverage factor of  $k=2$ . The uncertainty of the exit total pressure measured by the 5-hole probe has with 45.8% the largest contribution to the overall uncertainty. The main mass flow and torque measurements are responsible for 29.6% and 17.0% of the total uncertainty respectively. The remaining 7.6% are related to other input quantities. The uncertainty contribution of the secondary mass flows ( $\dot{m}_{\text{bypass}}$  and  $\dot{m}_{\text{drum}}$ ) and the cavity pressure is negligible.

In order to quantify the expanded uncertainty of the delta total-to-total efficiency of two measurements the following assumptions are made. In this work all efficiency measurements were executed with the same probe and the same calibration files. Therefore the uncertainty of the calibration does not need to be taken into account when comparing two efficiency measurements. For relative measurements the contribution of the discharge coefficient on the mass flow uncertainty can also be neglected. The resulting expanded uncertainty ( $k=2$ ) for a change in total-to-total efficiency is  $\pm 0.32\%$ .

## 2.6. Time-Resolved Computational Model

In order to study the combined purge flow and end wall effects at locations inaccessible for the probes, a computational model of the turbine was used. Simulations are performed for all nine experimentally investigated test configurations, three rotor geometries at three different injection rates.

### 2.6.1. Grid and Boundary Conditions

The grids used for the time-resolved simulations are structured and have a total of approximately 18.5 million nodes. As the blade count ratio between stationary and rotating blade rows is two to three, two vane passages of the first and second vane rows as well as three rotor passages are represented in the meshes with periodic boundary conditions in the circumferential direction. In order to have a realistic rim seal flow field the cavity space of the test rig configuration between rotor disk and first vane row is fully modelled with an interface to the first NGV exit hub end wall (Figure 2.3). An overview of the different domains of the meshes is given in Figure 2.12. Three grids for the three different rotor geometries were generated. The inlet, rim seal, NGV1, NGV2, shroud and outlet domains were identical in

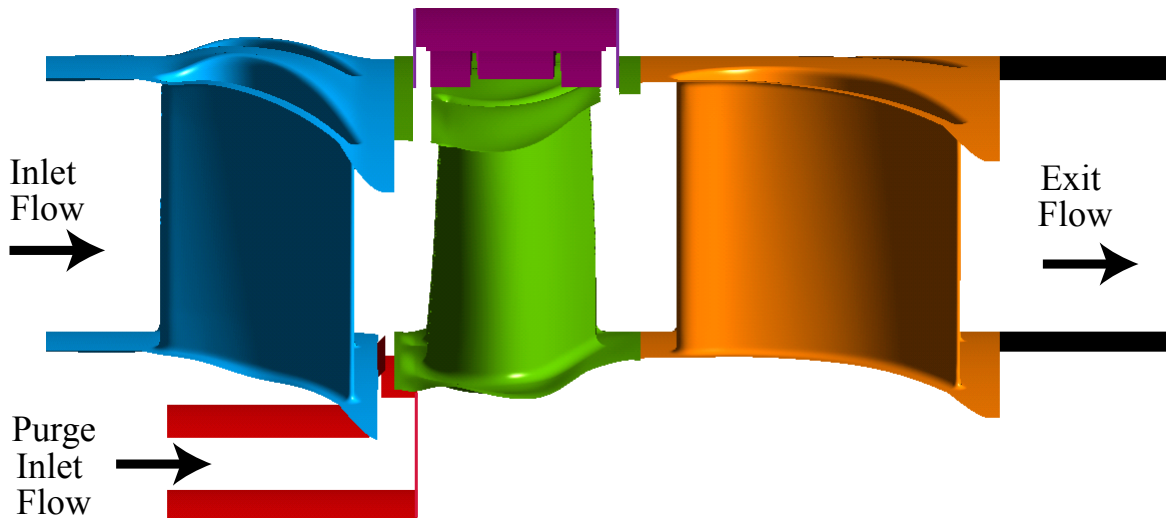


Figure 2.12.: Domains of the CFD mesh.

all three meshes, only the rotor domain is different and is a function of the end wall design.

The non-dimensionalised wall distances on the airfoils and the end walls are on average  $y^+ = 1.5$ . At the inlet of the turbine domain a constant total pressure  $P_{t,in}$  and total temperature  $T_{t,in}$  corresponding to the measured experimental operating conditions were applied. At the exit the measured mass flow  $\dot{m}_{main}$  at these inlet conditions was imposed as a boundary condition. The purge mass flow rate  $\dot{m}_{bypass} - \dot{m}_{drum}$ , measured static pressure  $P_{s,cavity}$  and temperature  $T_{s,cavity}$  were imposed as boundary conditions at the rim seal cavity inlet.

### 2.6.2. Solver

In contrast to the design calculations, the time-resolved results were achieved with the commercial ANSYS CFX Version 12.1 software package. The results of a steady run were used as initial conditions for the time-resolved simulation. The temporal resolution is 80 time steps per period, corresponding to three rotor blade passing events, or a  $0.25^\circ$  shift of the rotor per time step. The shear stress transport (SST) turbulence model without transition modelling was used for the simulations. The maximum residuals were found to be on the order of  $10^{-3}$ , while the mass imbalances were on the order of  $10^{-5}$ . The periodic convergence of the unsteady simulations was judged based on the correlation coefficient of two pressure monitoring points at the rotor exit. Two consecutive vane passage pressure events had to reach a correlation coefficient of over 99%.

### 2.6.3. Validation

In order to validate the computational model the time-averaged results of the unsteady CFD calculation are compared to the experimental results. The validation is done for all the experimentally investigated injection rates and rotor geometries. As an example, Figure 2.13 shows the comparison between the measurement and the numerical prediction of the circumferentially mass and time-averaged radial distribution of the relative flow angle for the nominal injection rate of  $IR = 0.8\%$  and at the exit of the rotor with the 1<sup>st</sup> end wall design. The absolute difference in relative flow angle is within  $-1^\circ$  and  $3^\circ$  between 5% and 95% span. The loss cores are detected at the same radial positions by the CFD simulation and are of a similar shape and strength. The fact that the radial position of the hub loss core is very well captured by the simulation is relevant for the analysis presented.

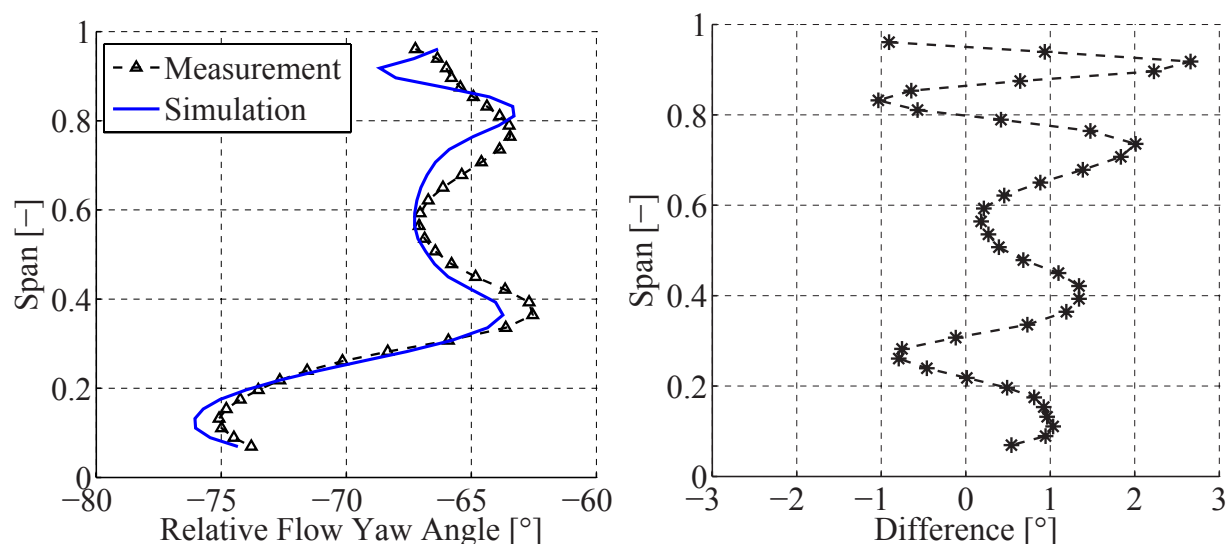


Figure 2.13.: Comparison between measured (5-hole probe) and simulated relative flow yaw angle at the rotor exit (1<sup>st</sup> end wall design) for the nominal injection rate ( $IR = 0.8\%$ ).

Figure 2.14 compares the measured and computed time-averaged normalised total pressure in the rotor frame of reference at the rotor exit with the 2<sup>nd</sup> end wall design. A good qualitative agreement between prediction and measurement was achieved with regard to the shape and the radial position of the zones of low total pressure caused by the hub and tip secondary flows. Generally speaking the CFD simulation appears to over-predict the losses compared to the measurements. In the free-stream region the maximum

relative error of the relative total pressure between simulation and measurement is about 0.5%. The hub passage vortex and rotor wake loss cores are under-predicted by the computation by about 2%. In the tip region over 90% span the relative error reaches about 3%.

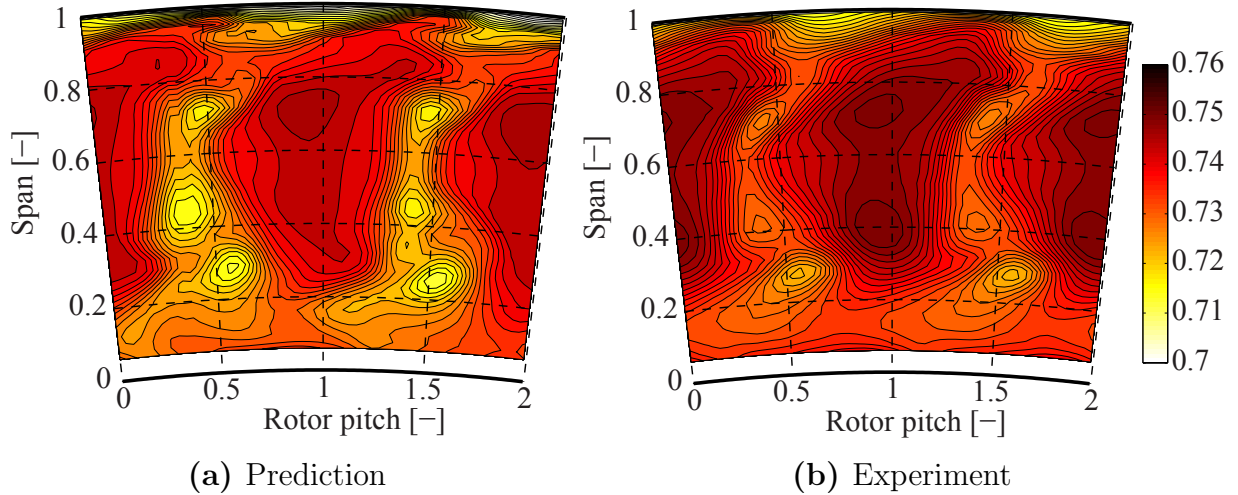


Figure 2.14.: Comparison of normalised total pressure  $Cp_t$  in rotor frame of reference for prediction and experiment at the rotor exit (2<sup>nd</sup> end wall design) at the nominal injection rate ( $IR = 0.8\%$ ).

#### 2.6.4. Particle Tracker

A particle tracking code was implemented as a post-processing tool for the CFX Solver output data. The exported velocity field data at each time step of the numerical simulation is used as an input for the particle tracking tool. The time marching of the particles is based on a 3<sup>rd</sup> order Adams-Bashforth algorithm with 4 sub-iterations [5], Figure 2.15. The algorithm computes the coordinates of the next position  $x_{n+1}$  based on the actual location and the velocity vectors at this actual location and at two former time steps.

$$x_{n+1} = x_n + \frac{\Delta t}{12} (23V_{n,t} - 16V_{n,t-1} + 5V_{n,t-2}) \quad (2.35)$$

The particle tracker is uncoupled and there is no interaction between the particles and the flow field. Hence it can be used as a flow visualisation tool once the numerical simulation is finished.

The particle tracking tool has been validated with streamline calculations provided by the ANSYS CFX software package. Instead of providing the particle tracking tool with the CFD simulation data during one period (80

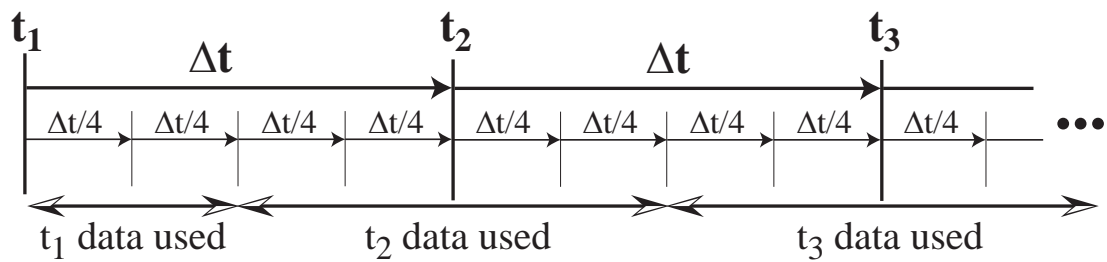


Figure 2.15.: Calculation method of particle tracking tool using a 3<sup>rd</sup> order Adams-Bashforth algorithm with 4 sub-iterations.

time steps), the data at only one single time step was used as an input for the particle tracking tool during the entire calculation and then compared to streamlines provided by CFX for this same transient file. Figure 2.16 shows the comparison between the streamlines (green crosses) exported from the CFX software and the computed streamlines using the particle tracking post-processor tool.

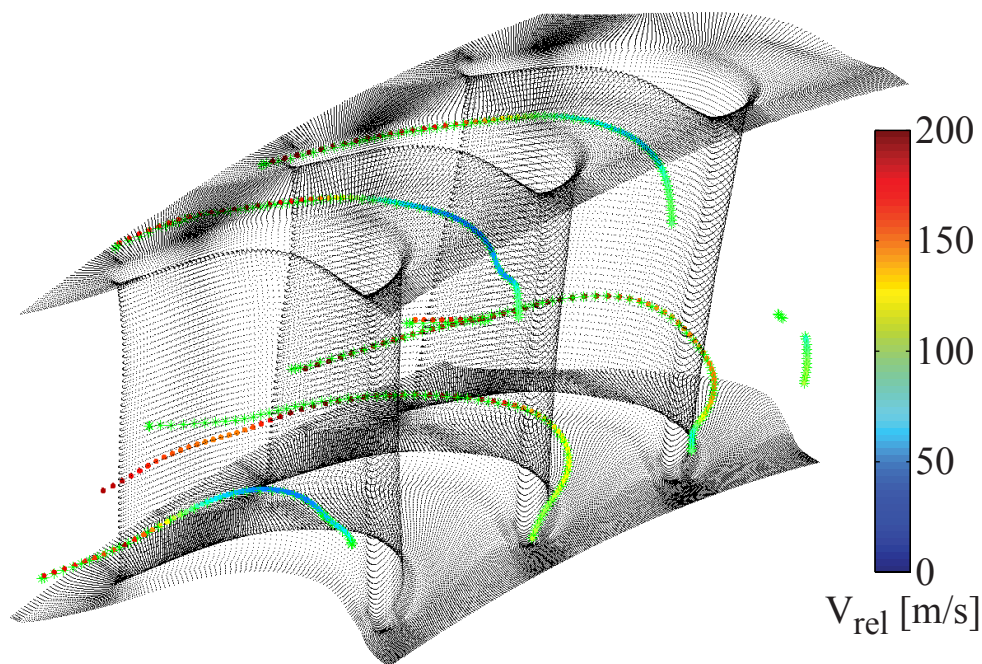


Figure 2.16.: Comparison between CFX stream lines (green crosses) and the streamlines calculated by the particle tracking tool in the relative frame. The exported velocity data from a single time step was used as an input at all time steps in the particle tracking tool.



## 3. Unsteady Purge Flow Migration and Interaction Mechanisms

The purge flow is a secondary cooling mass flow in gas turbines which prevents the ingestion of hot gases into the disk cavities in order to prevent the disk's overheating and to avoid thermal fatigue. The purge flow considered for this investigation is injected at the hub rim seal between the nozzle guide vane and the rotor. The corresponding experimental setup is presented in section 2.1.3. In this chapter three different levels of purge flow are considered,  $IR = 0.4\%$  (low),  $IR = 0.8\%$  (nominal) and  $IR = 1.2\%$  (high). The definition of the injection rate  $IR$  is given in Equation 2.1. Measurements for all three injection rates and at the rotor inlet and exit are analysed and detailed with the use of numerical results. All the presented measurements in this chapter were made with the same rotor having profiled end walls of the 1<sup>st</sup> generation. Based on the available data set a similar analysis could be performed with the other two rotor geometries. The results for the other two rotor geometries are intentionally left out in this chapter in order to isolate the purge flow effects in the absence of geometrical modifications.

### 3.1. Purge Flow Effects at the NGV1 Exit

The axial position of the probe traverse plane at the rotor inlet makes it possible for the probes to measure in the upper rim seal cavity above the rim seal lip. Including the 1mm safety distance the geometrical set-up allows for measurements inside the rim seal cavity down to a radius of  $-3\%$  span. The access into the rim seal cavity is possible for the 4-hole, FRAP and FENT probes. The shape of the rim seal cavity exit requires the use of the 4-hole probe. The cobra shaped head of the 5-hole probe would need more axial space than provided by the rim seal cavity exit. Therefore pneumatic measurements can only be performed with the 4-hole probe at rotor inlet. The access of the 4-hole, FRAP and FENT probes into the rim seal cavity allows them to see the purge flow.

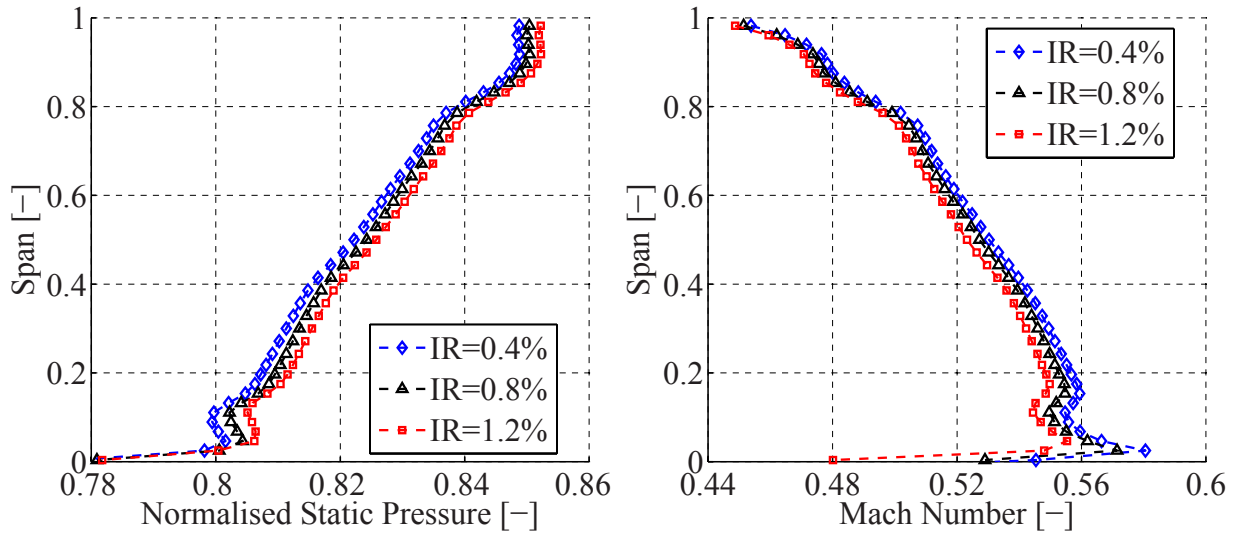


Figure 3.1.: Area and time-averaged measured normalised static pressure  $Cp_s$  and mass-averaged Mach number  $M$  for different injection rates at the rotor inlet (4-hole probe).

Figure 3.1 shows the measured radial distribution of static pressure and Mach number at the rotor inlet. The injected purge flow affects the static pressure and Mach number distributions at all spanwise positions, the injection at the hub is communicated through the subsonic flow up to the turbine casing. The static pressure at rotor inlet increases with increasing injection rate. On average the static pressure at rotor inlet increases by 0.6% per percent of injected purge flow. In the hub region, close to the rim seal exit, the increase is on the order of 1% per percent of injected purge flow. The total pressure above 10% span is not significantly affected by the rim seal purge flow. As a consequence the Mach number at rotor inlet decreases on average by 1.5% per percent of injection rate. Close to the hub rim seal exit, the Mach number decreases by up to 2.5%.

The flow situation between the NGV exit and the rotor can be compared to a balloon with the volume between the NGV throat and the rotor throat. They each have mass flowing through them, but like in a balloon the mass of air in the volume is constant, with increasing amount of purge flow the internal pressure rises. This mechanism causes the measured static pressure to rise. When the purge flow rate is increased, mass flow is added to the main flow in front of the rotor. The fluid has to react to rematch to the new condition with purge flow present. A priori the fluid has two possibilities, either increase the mass flow through the rotor or decrease the mass flow through the NGV. In practice it does both. The measurements show that

the rotor inlet static pressure rises, causing an increase in the relative total pressure into the rotor. At fixed rotor capacity this leads to increased mass flow through the rotor throat. At the chosen operating point the rotor is not choked. But the increased static pressure at the NGV exit also drops the Mach number (Figure 3.1). Since the NGV is not choked it will slightly reduce the NGV mass flow. The inlet total pressure of the NGV is not affected when the amount of purge flow is varied as the test rig is set up to keep the turbine pressure ratio constant. Therefore the effect of the air offtake upstream of the NGV for the additional purge flow itself has no effect on the NGV mass flow.

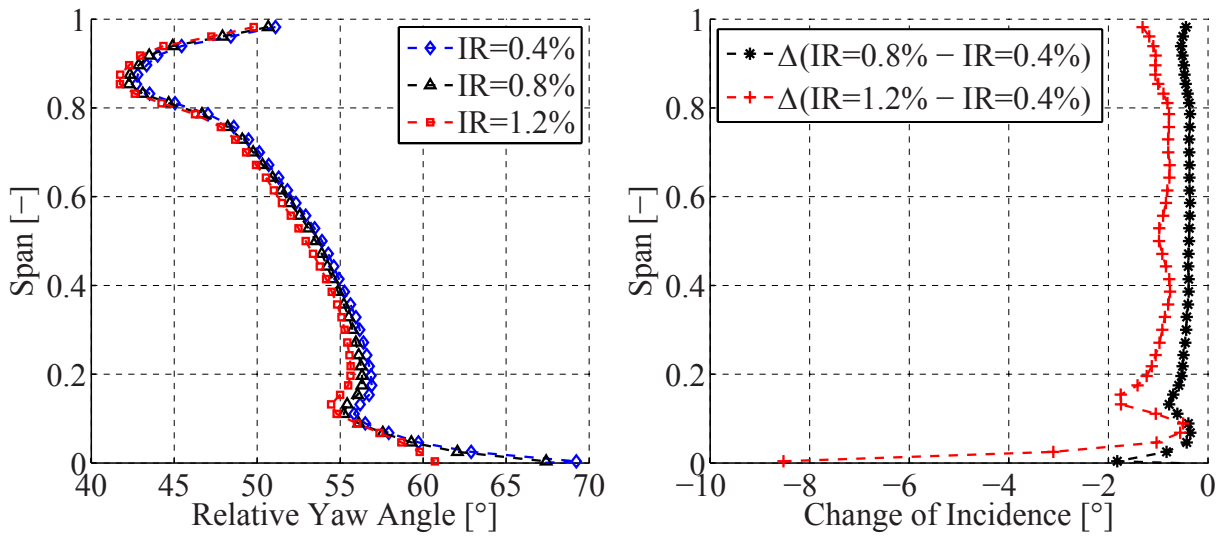


Figure 3.2.: Mass and time-averaged measured relative yaw angle and change of incidence on the rotor between nominal injection rate ( $IR = 0.8\%$ ) and the low injection rate ( $IR = 0.4\%$ ) and the high injection rate ( $IR = 1.2\%$ ) and the low injection rate at the rotor inlet (4-hole probe).

The reduction of the Mach number at rotor inlet with increasing injection rate causes negative incidence on the rotor leading edges. Figure 3.2 shows the circumferentially mass and time-averaged measured relative yaw angle at the rotor inlet and the change of incidence between the nominal and the low injection rates and between the high and the low injection rates. The effect of the injected purge flow on the rotor inlet flow angles is clearly visible. For the higher span-wise positions in the free stream the difference is between  $-1^\circ$  and  $-2^\circ$ . Close to the hub the maximum measured difference of relative flow yaw angle between the lowest and highest injection rate peaks at about  $-9^\circ$ . The missing swirl of the injected purge flow compared to the free stream mainly causes the difference in relative flow yaw angle

close to the hub. This change of incidence has a significant effect on the rotor flow field as described in section 5.2.

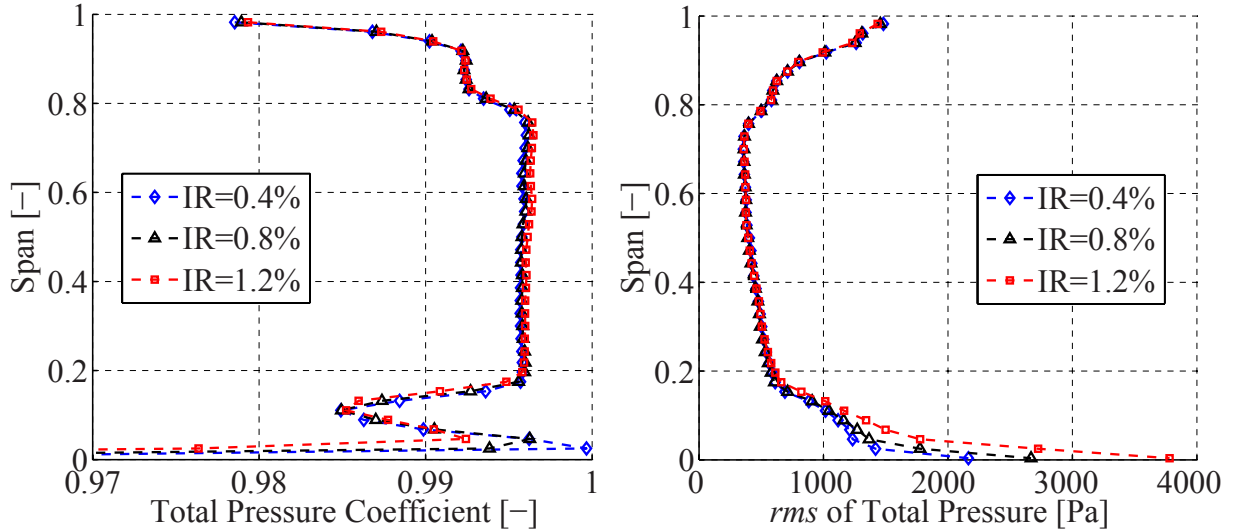


Figure 3.3.: Mass and time-averaged measured total pressure coefficient  $Cp_t$  (4-hole probe) and  $rms$  of the total pressure signal (FRAP) for different injection rates at the rotor inlet.

Beside its effects on the whole rotor inlet flow field, the injected purge flow also significantly affects the rim seal exit flow field. Figure 3.3 shows the radial distributions of the total pressure coefficient  $Cp_t$  and the  $rms$  of the total pressure signal defined in Equation 2.24. The total pressure coefficient is calculated based on the 4-hole probe measurements whereas the time-resolved FRAP data is required to compute the  $rms$  distribution. The two radial profiles in Figure 3.3 are only affected below 20% span by the purge flow. In the rest of the flow field the purge flow has no measurable effect with regard to these two parameters. The total pressure decreases by about 4% per percent of injection rate close to the hub. The measured non-deterministic unsteadiness nearly doubles with the addition of 1% of purge flow.

Figure 3.4 shows two space time plots for the low and high injection rates at the rim seal exit (4% span). The variable is the experimental  $rms$  of the total pressure. The spatial dimension on the x-axis is the circumferential coordinate in the absolute frame of reference. The vertical zone of high  $rms$  between 0.6 and 0.8 stator pitch is the signature of the NGV wake and hub passage vortex. The fact that it is a vertical feature means that it is stationary in space with regard to time. At this spanwise position the potential effect of the passing rotor blades is hardly visible for the low

injection rate. The measurements show no clear interaction, however there are three zones of increased  $rms$  between about 0.8 and 1 stator pitch. The time axis covers three rotor blade passing events, suggesting that these zones are related to one rotor blade each. The comparison of the two space

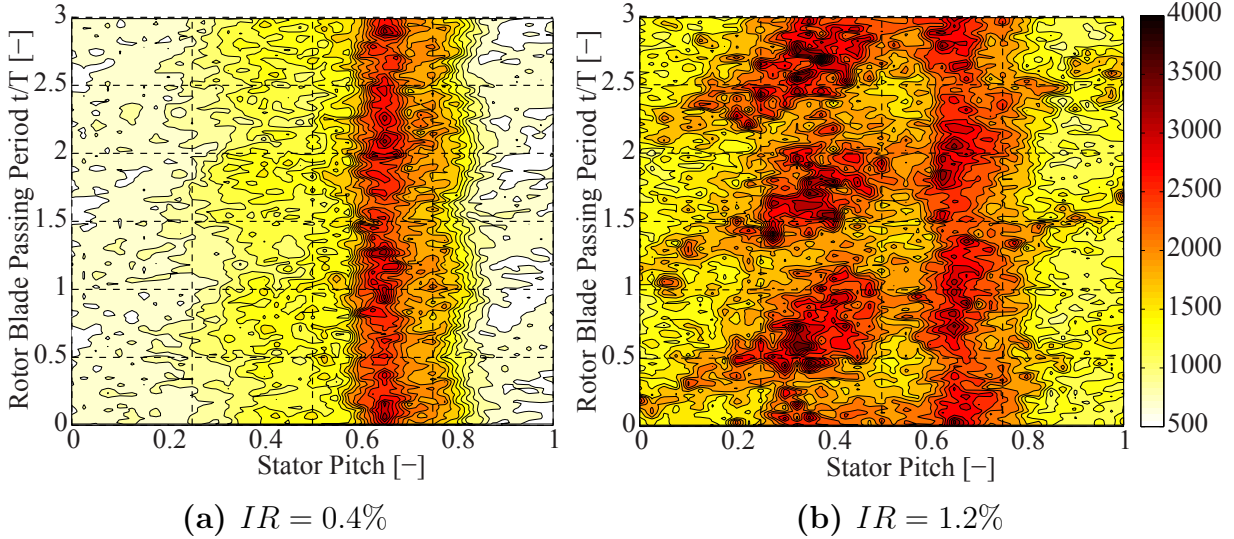


Figure 3.4.: Space time plot in absolute frame of reference of the experimental  $rms$  of the total pressure [Pa] at 4% span for the low and the high injection rates at the rotor inlet (FRAP).

time plots in Figure 3.4 shows that the overall level of unsteadiness at the rim seal exit increases at the higher purge flow injection rate. The increase of the level of turbulence must be caused by the purge flow as this is the only difference between the two space time plots. At the high injection rate the interaction between the additional purge flow and the rotor potential field creates three inclined zones of elevated  $rms$  containing each a patch of strongly increased  $rms$  between 0.2 and 0.4 stator pitch. At this circumferential location the purge flow significantly increases the non-deterministic unsteadiness once per rotor passing event, suggesting that there is one jet of purge flow per rotor passing event. Although the interaction between the purge flow and the rotor increases the  $rms$  for nearly all circumferential locations, it can be seen that most of the purge flow leaves the rim seal cavity between 0.2 and 0.4 stator pitch, causing a much higher increase in  $rms$  in this region compared to the rest of the inclined  $rms$  features. In other words the nozzle guide vane defines where the purge flow is leaving the rim seal cavity and the rotor when. The  $rms$  signature of the NGV wake appears to be insensitive to the amount of purge flow.

Figure 3.5 shows the corresponding space time plots of radial velocity  $V_r$

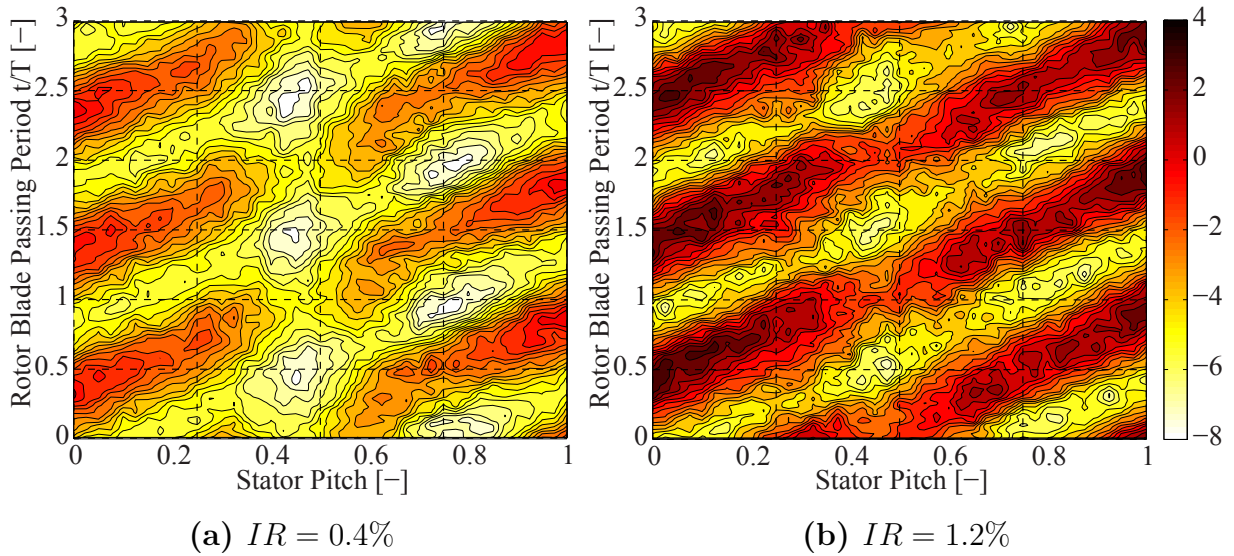


Figure 3.5.: Space time plot in absolute frame of reference of the radial velocity  $V_r$  [m/s] at  $-1\%$  span for the low and the high injection rates at the rotor inlet (FRAP).

at  $-1\%$  span. Investigations performed at the LEC ([28]) have shown that strong radial velocity gradients, present at this spanwise location at the rim seal exit, significantly influence the measurement of the  $V_r$  made by a FRAP. These radial gradients only influence the absolute values of  $V_r$ , therefore the two time space plots in Figure 3.5 can only be interpreted in a relative perspective. Still some effects can be shown. At the low and the high injection rates the distribution of radial velocity is rotor dominated. The inclined red zones show positive radial velocity indicating purge flow radially moving outwards. At the low injection rate there is a vertical zone of negative radial velocity at about 0.45 stator pitch position. This must be a zone of high static pressure caused by the nozzle guide vane. At the high injection rate there are more red zones indicating purge flow leaving the rim seal cavity. This is expected as the amount of purge flow is three times higher compared to the low injection rate. The increased radial velocity of the purge flow at the high injection rate increases the penetration height and the mixing losses generated at the rim seal exit.

The strong dependence of  $V_r$  to the rotor position is not surprising as the static pressure at the rim seal exit is the main parameter deciding when the purge flow is leaving the rim seal cavity. The lower the static pressure of the main flow at the rim seal exit, the faster the purge flow is able to leave the cavity. The increased static pressure upstream of the rotor leading edge prevents the purge flow from leaving the cavity. The purge flow experiences the lowest static pressure upstream of the suction side region of the rotor

blade. This is the moment when most of the purge flow is expected to leave the rim seal cavity. Hence the rotor potential field has a significant effect on the behaviour of the purge flow at the rim seal, as shown in Figure 3.5. Generally speaking these space time plots show that, in the absolute frame, the stationary blade row decides where and the rotor when the purge flow is injected into the main flow. In the rotating frame of reference the two roles are inverted.

## 3.2. Influence of Purge Flow on Rim Seal Exit Cavity Flow

The CFD simulations performed allow one to further detail the flow behaviour in the exit cavity of the rim seal, shown in Figure 2.3. Figure 3.6 shows circumferentially area and time-averaged static pressure coefficient  $Cp_s$ , yaw angle, circumferential velocity  $V_\theta$  and radial velocity  $V_r$  for the three investigated injection rates. The averaging was performed along a cylindrical surface at 0% span. The non-dimensional rim seal axial coordinate indicates the axial position along the rim seal. 0 non-dimensional rim seal axial coordinate indicates the end of the NGV hub platform, 1 the leading edge at the rotor hub platform, as shown in Figure 3.8. The axial dimension of the real rim seal exit in the test rig is approximately 8.5mm. The probe tip diameter is 1.8mm, therefore covering about 20% of the axial extension of the tested rim seal exit geometry. This needs to be kept in mind when interpreting the measurement results in the cavity. The symbols in Figure 3.6 indicate the corresponding circumferentially averaged measured values at 0% span (4-hole probe). The axial position of the tip of the probe when it reaches the rim seal exit at 0% span is not exactly known but the central yaw hole (P1) is estimated to be at around 0.35 non-dimensional axial rim seal coordinate. In order to define the exact axial position of the probe tip, the deflection of the probe caused by the aerodynamic load due to the turbine main flow would be required, but is unknown. The comparison to the measurements of the radial velocity  $V_r$  were intentionally omitted. Investigations performed at the LEC ([28]) have shown that strong radial velocity gradients, present at this spanwise location at the rim seal exit, significantly influence the measurement of the  $V_r$  with a 4-hole probe. All the parameters shown in Figure 3.6 are circumferentially area-averaged (and not mass-averaged) in order to avoid singularities present in the corresponding mass-averaged distributions. The singularities

are caused when the circumferentially summed mass flow crosses the zero line which is the case at two axial positions at the rim seal as shown in Figure 3.7).

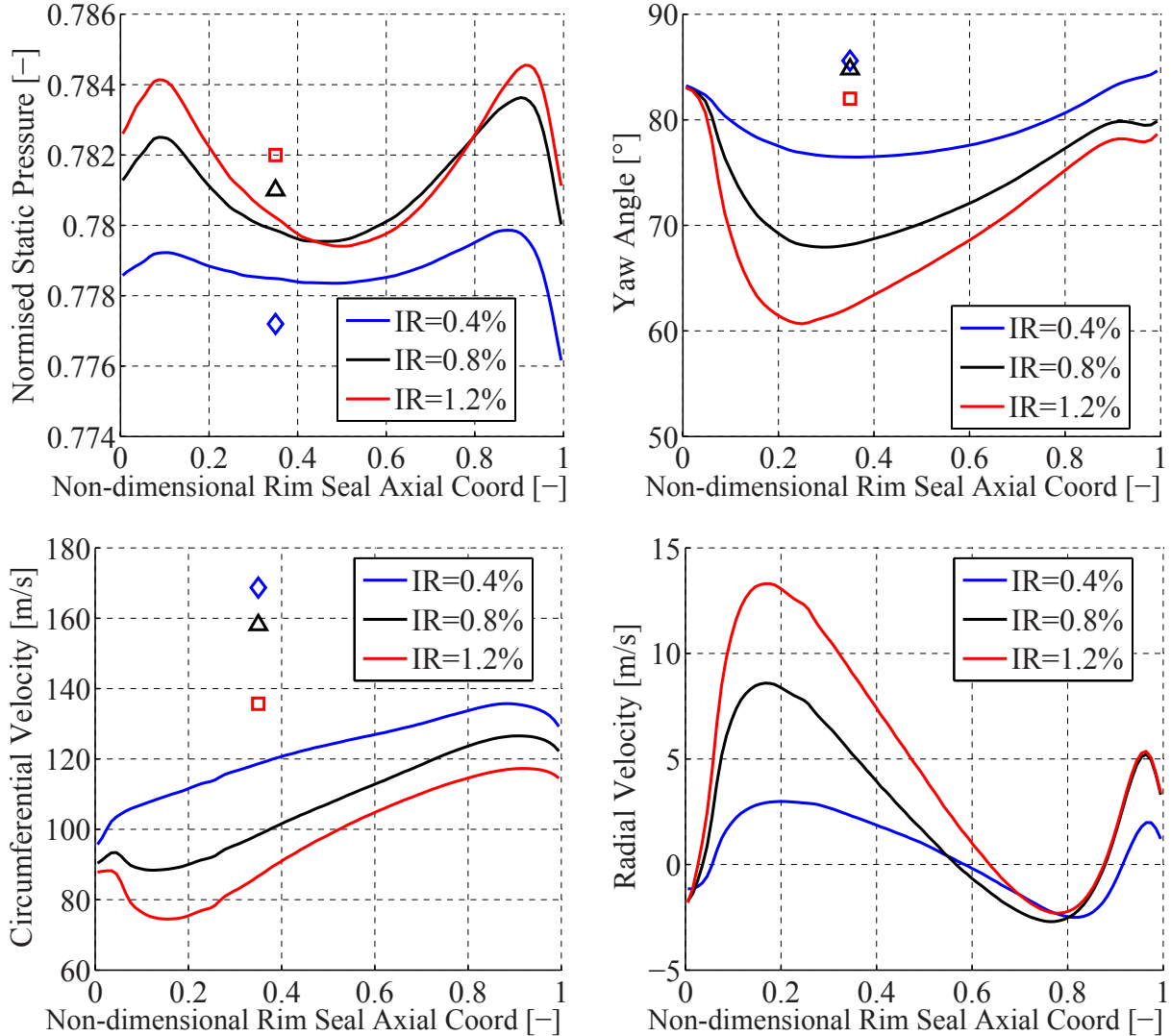


Figure 3.6.: Circumferentially area and time-averaged simulated  $C_{p_s}$ , yaw angle,  $V_\theta$  and  $V_r$  plotted against non-dimensional rim seal axial coordinate at the rim seal exit (0% span) for the three investigated injection rates. Zero corresponds to the end of the NGV hub platform, one to the leading edge at the rotor hub platform. The symbols indicate the corresponding measurements.

The comparison between the measurement and the simulation in Figure 3.6 shows a very good agreement for the static pressure at the rim seal exit. The relative difference in normalised static pressure is less than 0.5%. However the simulation appears to severely underpredict the flow yaw angle and circumferential velocity. The flow yaw angle is underpredicted by approximately 10° to 20°, the circumferential velocity by 30% to 45% percents.

However the difference of these two parameters between measurement and simulation is consistent. For a given net mass flow leaving the rim seal cavity, a lower flow yaw angle in the simulation must correlate with a reduced circumferential velocity, as  $V_\theta$  is the dominant velocity vector component. The simulation shows the same trends caused by increased injected rate as the measurements for the parameters presented in Figure 3.6. Yaw angle and circumferential velocity are decreasing with increasing injection rate. At higher injection rate the flow leaving the rim seal has less circumferential momentum and higher radial velocity. In other words the influence the rotor might have in the cavity is reduced at higher injection rate. The residence time of the flow in the cavity is smaller at higher injection rate and thus the rotor influence can be expected to be reduced. The influence of the rotor can as well be observed when looking at the axial distribution of the circumferential velocity. The closer to the rotor the higher its influence and therefore the higher the  $V_\theta$ . The axial distribution of the yaw angle confirms this behaviour but shows a zone of increased yaw angle at low non-dimensional axial coordinate which cannot be expected like this as the dominate flow yaw angle at NGV1 exit is around  $72^\circ$  (blade metal angle). The radial velocity  $V_r$  is close to zero or negative, indicating that in the time-averaged perspective no purge flow is leaving the cavity in this axial region. The axial distribution of  $V_r$  in Figure 3.6 indicates that there are two axial zones where the purge flow is leaving the rim seal cavity, between 0.05 and 0.6 and between 0.9 and 1 non-dimensional axial rim seal coordinate. The axial distributions of the normalised net mass flow at the rim seal exit shown on the left hand side in Figure 3.7 confirm the trends of the radial velocities, there are two axial zones where the purge flow leaves the rim seal. The normalised mass flow shown in Figure 3.7 is given as a percentage of injection rate per percent of non-dimensional axial coordinate. Or in other words the surface under the different curves is equal to 0.4, 0.8 and 1.2 respectively. With increasing injection rate the radial velocity in the zone between 0.05 and 0.6 axial coordinate increases and so does the normalised mass flow. In this zone the maximum normalised mass flow rate can be observed at about 0.2 non-dimensional axial coordinate. The higher radial velocity at higher injection rate is expected to increase the mixing losses in the main flow. In the second zone where the purge flow leaves the rim seal cavity, between 0.9 and 1 non-dimensional axial rim seal coordinate, there appears to be an increase in mass flow with increasing injection rate, but only until a certain amount, between 0.4% and 0.8% injection rate. In other words once this maximum mass flow is reached

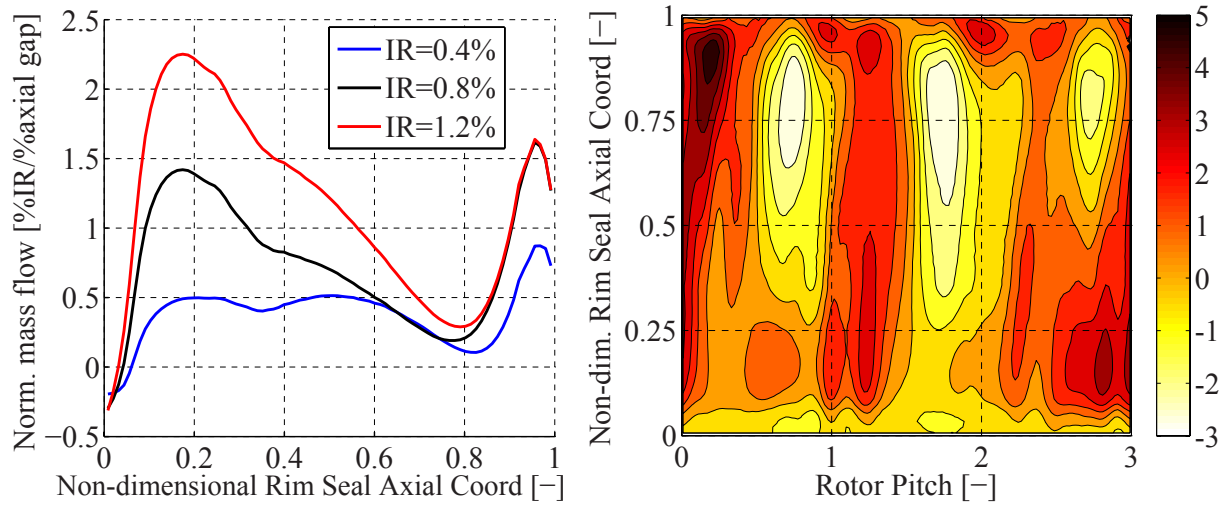


Figure 3.7.: Circumferential integral of the simulated normalised mass flow at the rim seal exit (0% span) for the three investigated purge flow rates on the left hand side. Contour plot of time-averaged normalised mass flow rate [%IR/%rim seal axial gap] at the rim seal exit for the nominal injection rate in the rotor relative frame of reference on the right hand side.

between 0.9 and 1 non-dimensional axial coordinate, the additional mass flow has to leave the rim seal cavity between 0.05 and 0.6 non-dimensional axial coordinate. The mass flow which is leaving the cavity between 0.9 and 1 axial rim seal coordinate is joining the boundary layer of the main mass flow on the contoured rotor hub end wall.

The contour plot on the right hand side in Figure 3.7 shows the time-averaged distribution of the normalised mass flow in the rotor frame of reference at the rim seal exit for the nominal injection rate. At the rotor side of the rim seal (between 0.5 and 1 non-dimensional axial coordinate) the rotor is dominating the mass flow distribution. The rim seal purge flow leaves the rim seal cavity when the static pressure in the main flow is low. The regions of lowest static pressure at the rim seal exit are upstream of the rotor blades suction side. The high flow velocities in these zones cause the static pressure to fall and make it therefore favourable for the purge flow to leave the rim seal cavity. The opposite is the case in the zones upstream of the rotor blades pressure side. This is what can be seen in the contour plot in Figure 3.7. In the rotor relative frame there are three zones of positive mass flow leaving the cavity and three zones of negative mass flow above 0.5 non-dimensional axial rim seal coordinate. These zones correspond to the three rotor blades suction and pressure sides covered by the horizontal axis of the contour plot. The fact that the purge flow leaves the cavity where the

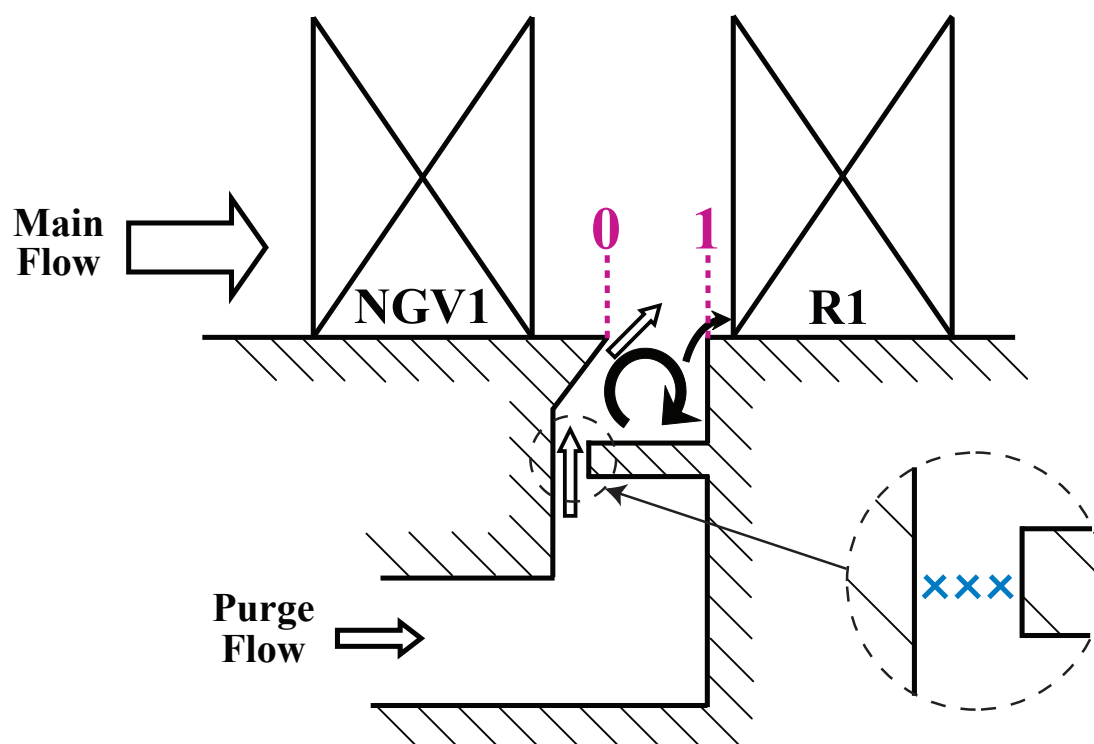


Figure 3.8.: Schematic of the rim seal exit cavity with the simulated flow structures present and the definition of the non-dimensional rim seal axial coordinate. The detail view shows the location where the purge flow particles are injected.

absolute velocity of the main flow is the highest further increases the mixing losses due to the higher velocity mismatches. Although the net mass flow is positive for all axial positions as shown by the line plot in Figure 3.7, there are three regions of negative mass flow upstream of the three rotor blades pressure side. According to the simulation there appear to be regions above 0.5 non-dimensional axial coordinate where portions of air have negative radial velocity and are joining the flow inside the cavity above the rim seal lip. The origin of these portion of air was not investigated. In an ideal case the mass flow entering the cavity in these regions is rim seal purge flow that has left the cavity at an earlier axial position and reenters the cavity in these zone. But the origin could as well be the main mass flow, potential source of thermal problems in the rim seal cavity.

The contour plot in Figure 3.7 shows that the mass flow distribution at the rim seal exit is rotor dominated. However the influence of the rotor is decreasing with increasing distance form the rotor platform. At low axial rim seal coordinates the nozzle guide vane is influencing the normalised mass flow distribution. This is not visible as such in the contour plot in Figure 3.7 because the contour plot shows the normalised mass flow in the

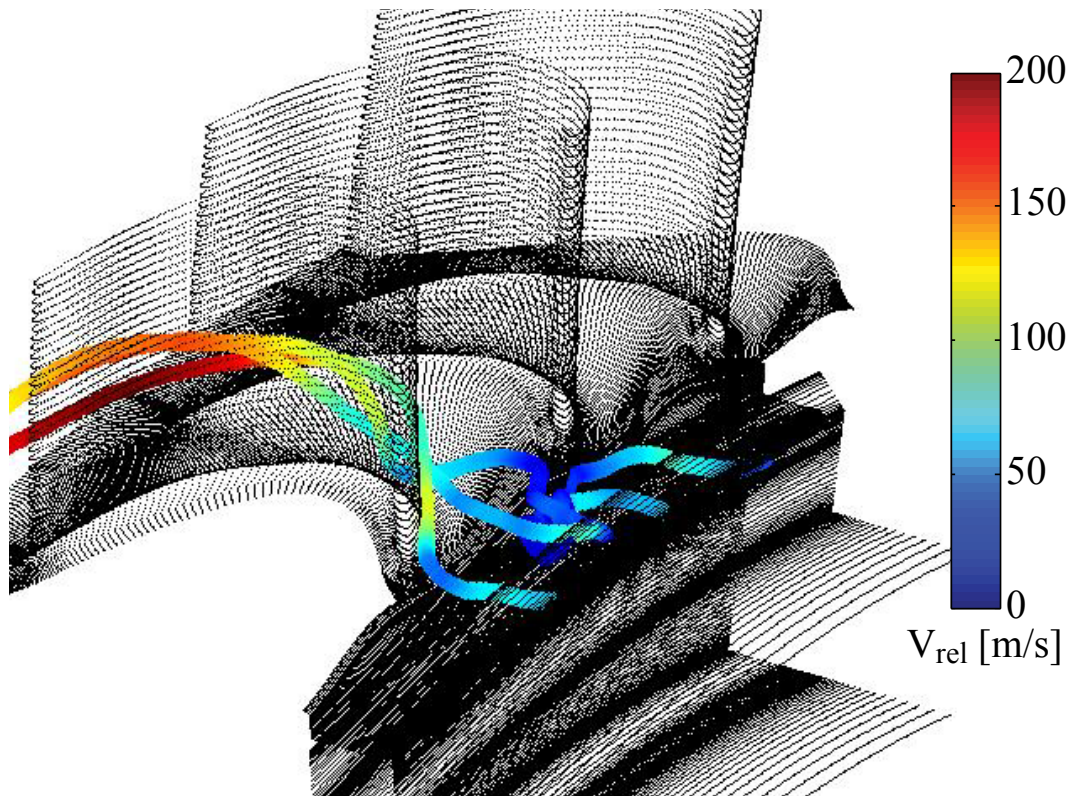


Figure 3.9.: Three typical particle tracks in the relative frame of particles released at the rim seal lip and tracked till the rotor exit,  $IR = 0.8\%$ . Parts of the rotor mesh and the rim seal cavity mesh are represented. These three particle tracks are detailed in Figures 3.10 to 3.13.

relative frame of reference. In the absolute frame the concept is the same, downstream of the nozzle guide vane suction side the static pressure is low because of the high flow velocities. This is therefore a preferred zone for the purge flow to leave the cavity. A contour plot in the absolute frame would therefore be dominated by the effect of the nozzle guide vane, the influence of the rotor would be averaged out. In other words in the absolute frame the nozzle guide vane defines where the purge flow is leaving the cavity and rotor defines when. In the relative frame the rotor defines where and the nozzle guide vane when. The unsteady interaction between the two blade rows defines the time-resolved behaviour of the purge flow at the rim seal exit.

The axial distribution of the mass flow in Figure 3.7 suggests a vortical structure in the volume of the rim seal cavity above the rim seal lip as shown by the schematic in Figure 3.8. Such a vortical structure was also observed by Pfau [73], Porreca et al. [78] and Barmपालias et al. [4] when analysing the unsteady flow in the shroud inlet and exit cavities. In order to further investigate the flow field at the rim seal exit, particles were released

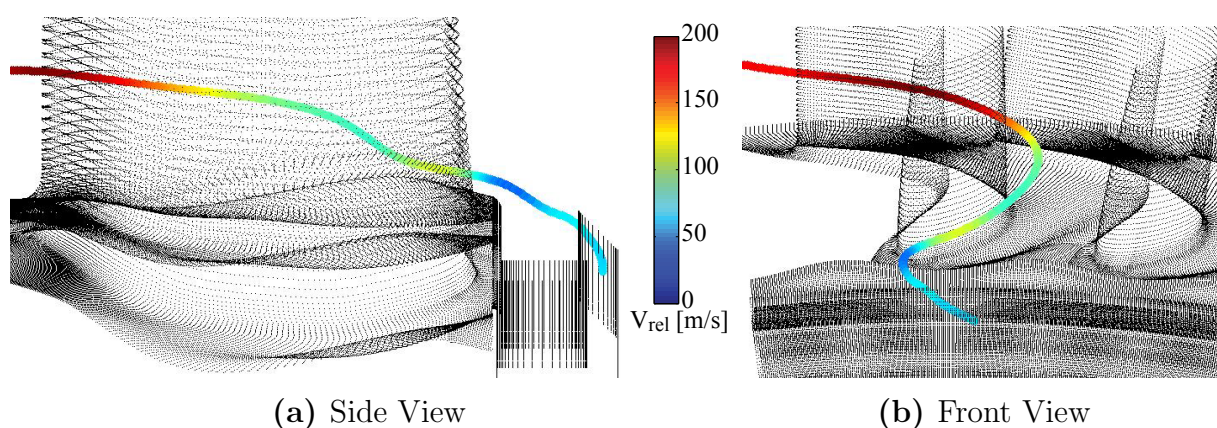


Figure 3.10.: Side and front view of a particle following the typical path **A**.

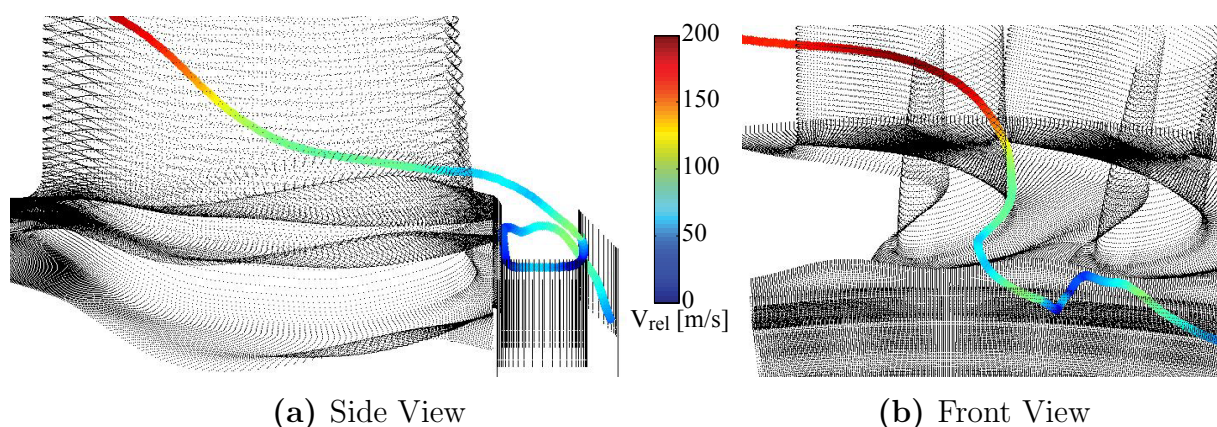


Figure 3.11.: Side and front view of a particle following the typical path **B**.

at the rim seal lip and tracked in order to analyse how, where and when they leave the rim seal cavity. With the use of the CFD simulations 60 uniformly distributed particles were injected at the rim seal (cf. zoom in Figure 3.8) at each of the 80 time steps during one period of the simulation. For each injection rate, these 4800 particles were tracked until the exit of the rotor. The analysis of the particle tracks reveals the existence of a rotating vortical structure in the form of a toroidal vortex inside the rim seal cavity above the rim seal lip, in line with the mass flow distributions at the rim seal exit. The unsteady blade row interaction affects the behaviour of this vortical structure. Depending on the relative position of the stationary and rotating blade rows the vortex is locally tilted, accelerated or insistent. For clarity not all the simulated particles tracks can be presented here. However the analysis of all the calculated particle tracks revealed three typical particle paths which will be further detailed. Figure 3.9 shows a 3d overview of the

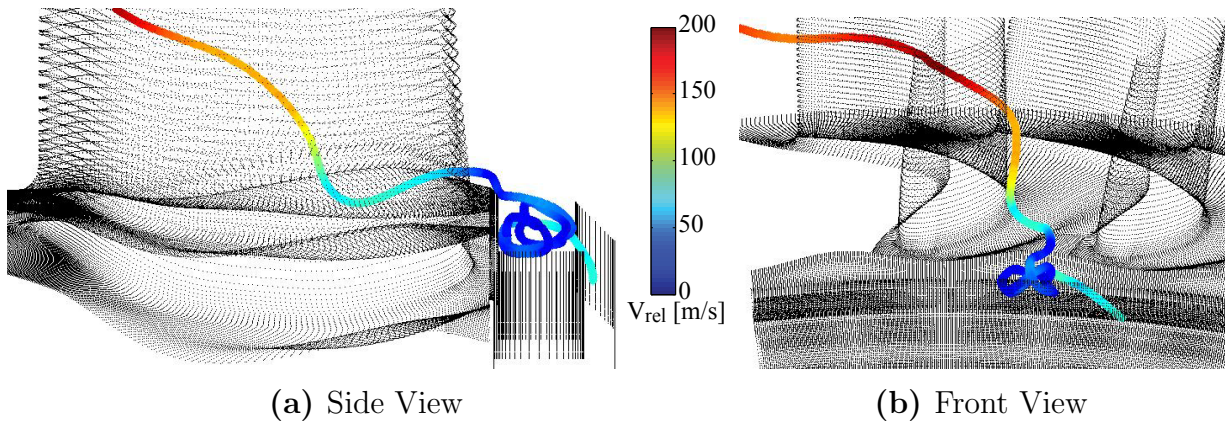


Figure 3.12.: Side and front view of a particle following the typical path C.

three typical particle tracks. Figures 3.10, 3.11 and 3.12 show the side and front views of these tracks:

- Particle path **A**: From the rim seal lip these particles radially migrate outwards and leave the cavity in the zone between 0.05 and 0.60 non-dimensional rim seal axial coordinate. These particles don't get involved with the vortical flow structures in the cavity and have a relatively high radial momentum when they leave the cavity (Figure 3.10).
- Particle path **B**: These particles interact with the vortex in the rim seal cavity once they have passed the rim seal lip. After one or two rotation in the vortical structure they leave the rim seal cavity as well in the zone between 0.05 and 0.6 non-dimensional rim seal axial coordinate (Figure 3.11).
- Particle path **C**: As for the particle path B, these particles get involved with the vortical structure in the cavity before they join the main flow. The interaction with the vortical structure is typically longer. However these particles leave the rim seal cavity in the zone between 0.9 and 1 non-dimensional rim seal axial coordinate. They typically have lower radial momentum and become part of the forming rotor hub boundary layer. (Figure 3.12).

Figure 3.13 further details the three typical particle tracks. The non-dimensional rim seal axial coordinate, the span position and the relative velocity  $V_{rel}$  are given as a function of the normalised particle path. 0 corresponds to the point of injection at the rim seal lip, 1 corresponds to the

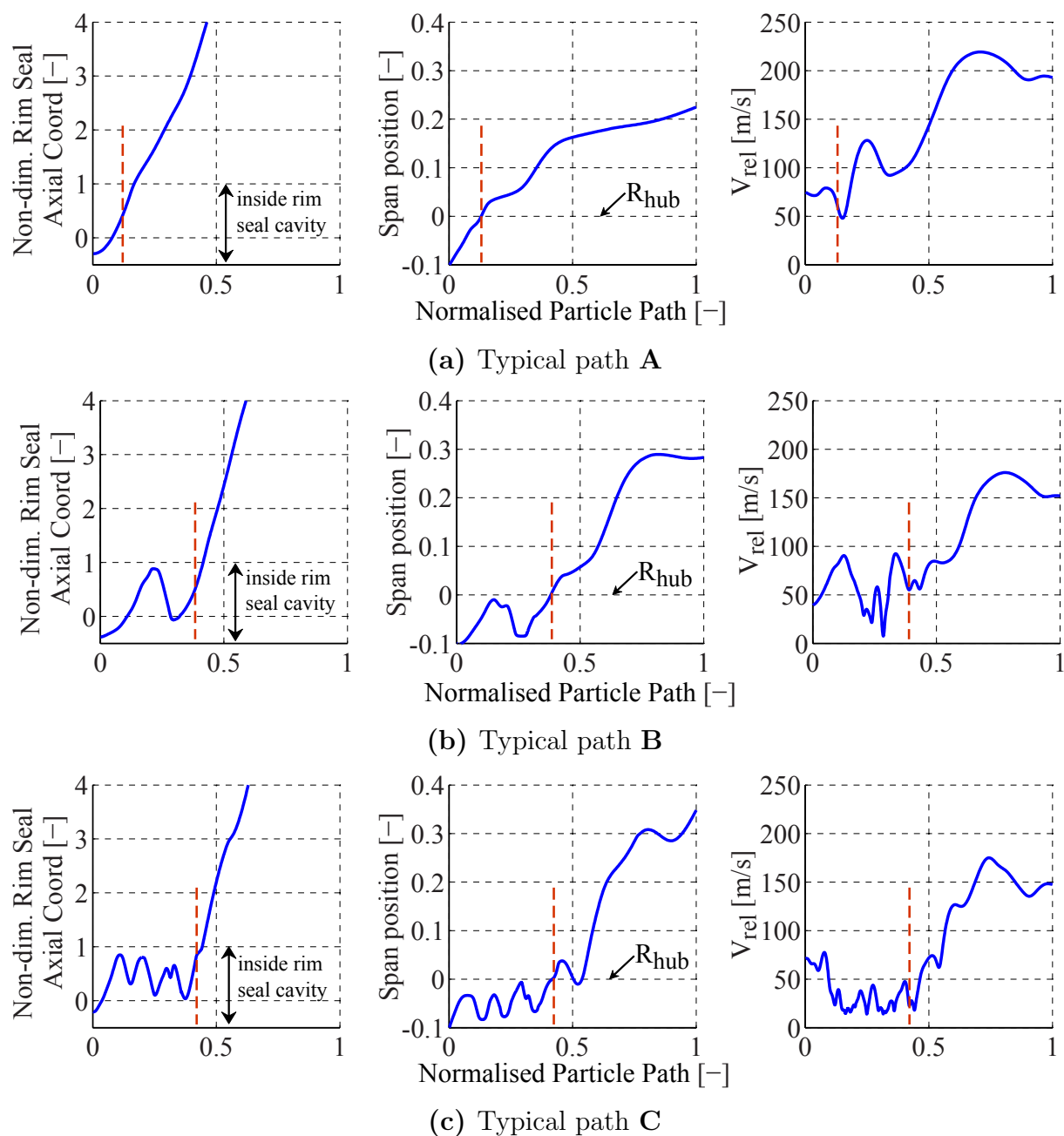


Figure 3.13.: Non-dimensional rim seal axial coordinate, span position and relative velocity of particles as a function of the typical normalised particle paths **A**, **B** and **C**. These 2d plots correspond to the tracks shown in Figures 3.10 to 3.12.

moment when the particle reaches the measurement plane at the rotor exit. For clarity reasons the axis of the non-dimensional rim seal coordinate does not cover the whole particle path till the rotor exit as the zone of interest is at the rim seal between 0 and 1. The point of injection is at negative non-dimensional rim seal axial coordinate as can be seen in Figure 3.8. The dashed red lines indicate the position when the particle leaves the rim seal

cavity. As long as the particle is between 0 and 1 non-dimensional rim seal coordinate and below 0% span (=hub radius), it must be inside the cavity. This is the case only for a relatively short time for the particle path **A**. After its injection the radial coordinate of the particle instantaneously increases and it leaves the cavity before reaching the non-dimensional axial coordinate = 1 corresponding to the rotor hub platform leading edge. Once these particles have left the cavity they are strongly accelerated, in the presented example in Figure 3.13(a) from about 50 m/s to 150 m/s. The particles can be accelerated by friction and by the strong pressure gradients present in this part of the flow field. The CFD simulations indicate a combination of the two mechanism, whereas the pressure gradients are considered to main reason for the strong accelerations. The higher the velocity mismatch between purge flow and main flow the more mixing loss is generated. This topic will be further studied in section 3.4. The particles following track **B** increase and then decreases again their radial and axial coordinates before they leave the cavity, indicating the vortical movement inside the cavity. As for the particles following track **A** these particles first reach the 0% span radius before reaching the axial position of the rotor hub platform, indicating that the particles following track **B** leave the cavity in the same zone as the particles following track **A**. Particles following track **C** do several vortical iterations before they leave the cavity. These particles leave the cavity at a lower speed and close to the rotor hub platform. They have as well less radial momentum. Many of these particles directly join the rotor hub platform boundary layer. The particle track shown in Figure 3.13(c) shows a reduction of the radius to a position below the hub radius once the particle has left the cavity. This is only possible due to the rotor hub end wall profiling, indicating that the particle convects along the hub end wall. Particles following the typical track **C** spend more time in the cavity before they are convected through the rotor, compared to particles following the typical tracks **A** and **B**. Once the particles released at the rim seal lip have left the cavity their trajectory is similar, relative velocity, axial and spanwise coordinates increase after approximately 0.5 normalised particle path. More details on the interaction mechanisms between the purge flow and the rotor flow field can be found in chapters 5 and 6.

### 3.3. Purge Flow Effects at the Rotor Exit

In this section the measured effects of the rim seal purge flow at the rotor exit measurement plane are analysed. Figure 3.14 shows the radial distributions of the circumferentially mass and time-averaged relative flow yaw angle and circumferential velocity  $V_{\theta,rel}$  at the exit of the rotor for the three injection rates investigated. The strong variations of relative yaw angle and relative circumferential velocity between 10% and 50% span are caused by the hub secondary flows. The strong radial gradients of relative yaw angle and  $V_{\theta,rel}$  are indicative of strong axial and streamwise vorticity (Equations 2.26 and 2.25). At the high injection rate the radial gradients of relative yaw angle and  $V_{\theta,rel}$  are more pronounced compared to the low injection rate. The variations are higher within a smaller radial band for the high injection rate. The injected purge flow appears to increase the transported

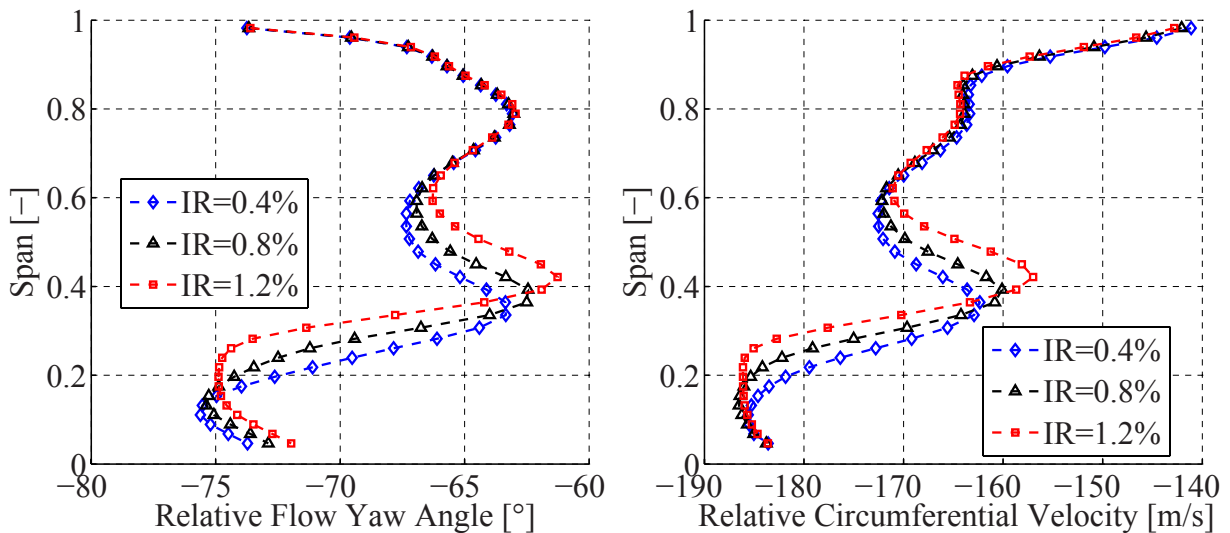


Figure 3.14.: Mass and time-averaged measured relative flow yaw angle and relative circumferential velocity  $V_{\theta,rel}$  for different injection rates at the rotor exit (5-hole probe).

vorticity in the hub passage vortex. The radial distributions in Figure 3.14 show that the measured modifications to the flow field caused by a variation of purge flow only reach a height of about 65% span at the rotor exit. Above this radial height the relative flow yaw angle and  $V_{\theta,rel}$  are unaltered by the purge flow for the turbine configuration tested. The radial distributions in Figure 3.14 show that increased injection flow causes the rotor hub secondary flow structure to radially migrate outwards by about 10% span per percent of injected purge flow. For higher injection rates the

loss core penetrates the free stream region more. Similar findings have been reported by Schuepbach et al. [93] and Ong et al. [69].

Figure 3.15 shows the radial distributions of the circumferentially mass and time-averaged relative Mach number  $M_{rel}$  and normalised relative total pressure  $Cp_{t,rel}$ . Increased injection rate further reduces the measured minimum  $M_{rel}$  in the hub passage vortex. In return the relative Mach number appears to increase in the lower half of the hub passage vortex. The radial distributions of the  $Cp_{t,rel}$  show that the total pressure loss in the hub passage vortex region is higher at higher injection rate. The measured

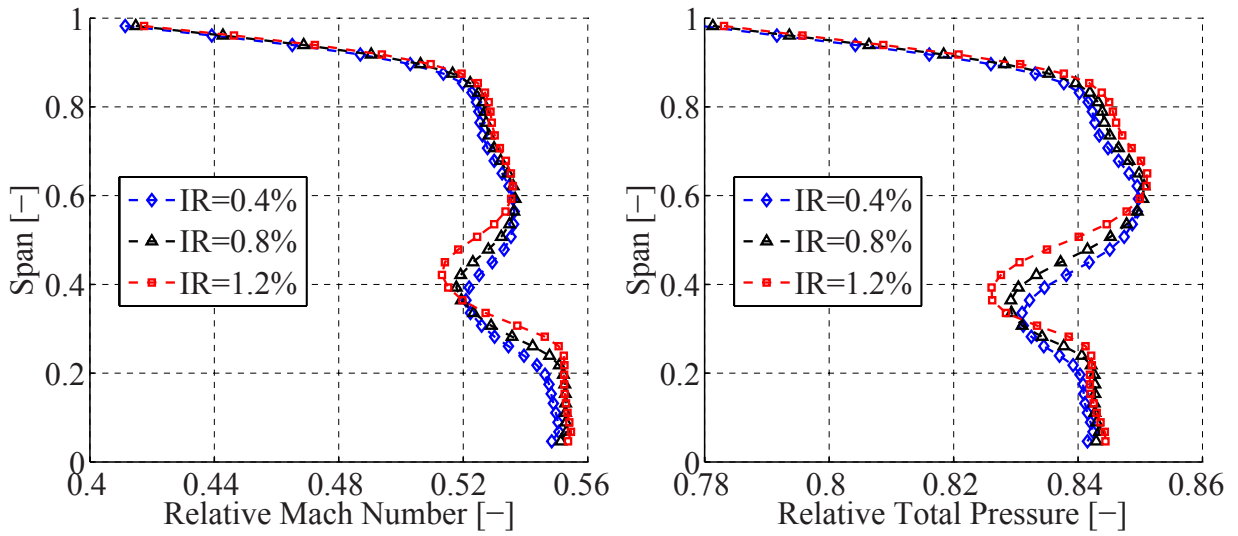


Figure 3.15.: Mass and time-averaged measured relative Mach number  $M_{rel}$  and normalised relative total pressure  $Cp_{t,rel}$  for different injection rates at the rotor exit (5-hole probe).

mass and time-averaged minimum of the relative total pressure in the hub loss core decreases by approximately 0.6% per percent of injected purge flow. The radial migration of the hub loss core under the effect of purge flow observed in Figure 3.14 is confirmed by the radial distributions in Figure 3.15. Assuming the core of the hub passage vortex at the location of the minimum  $Cp_{t,rel}$ , it is located between 30% and 40% span in function of the injection rate. This is at a relatively higher spanwise position compared to measurements performed in former test campaigns. The rotor under investigation has much thinner airfoils compared to the rotors of the former measurement campaigns and therefore enhances the radial migration of the hub passage vortex in the rotor flow field. It is interesting to see that, due to the increase of static pressure at the rotor inlet caused by the additional purge flow, the circumferentially mass and time-averaged

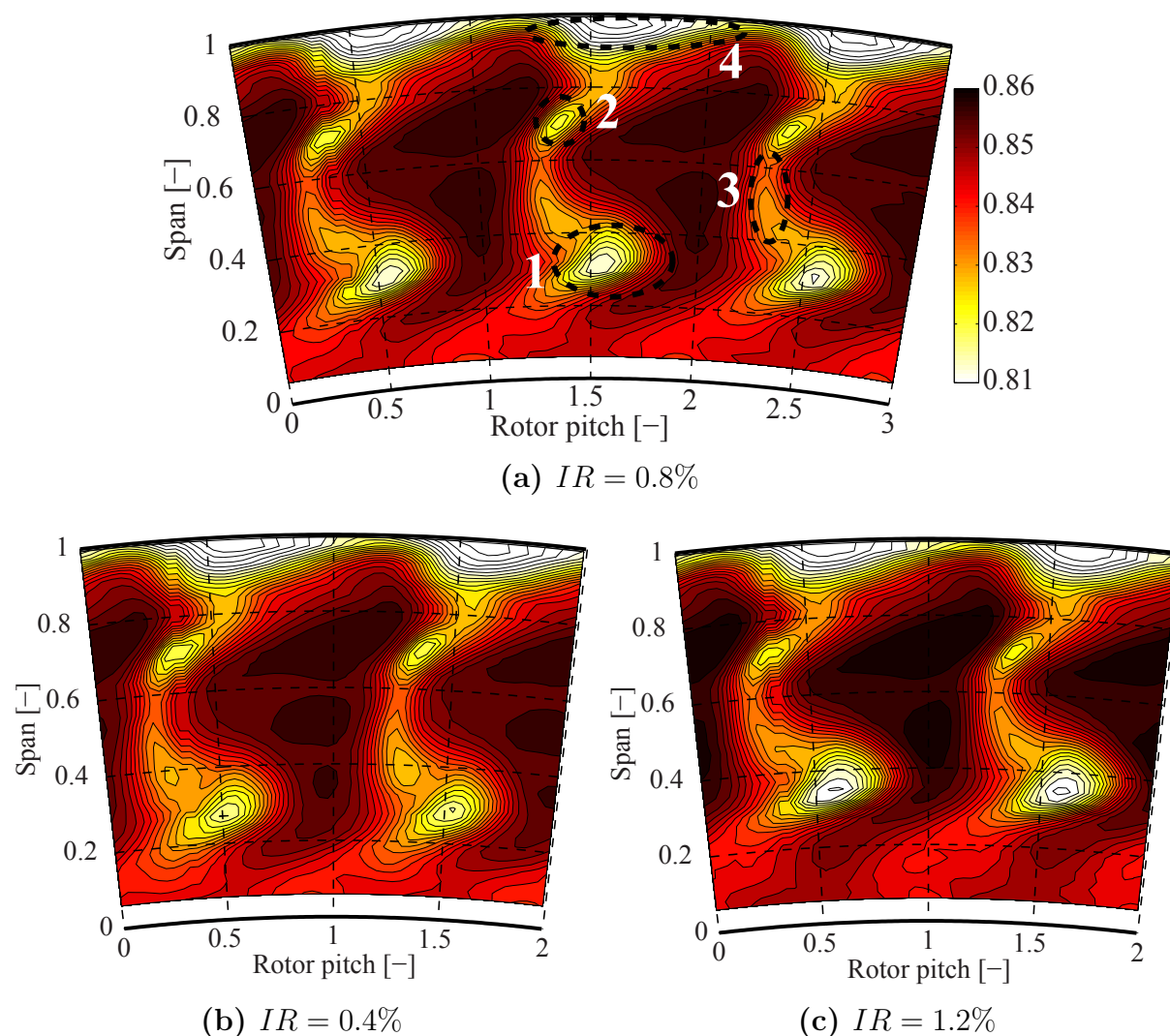


Figure 3.16.: Time-averaged area plots in rotor relative frame of reference at the rotor exit. The parameter is the normalised relative total pressure  $Cp_{t,rel}$  [-] at all investigated injection rates (FRAP).

relative total pressure increases between 60% and 90% span with increased injection rate (Figure 3.15).

The radial distribution of the relative total pressure can be further analysed when considering the corresponding area plots of the relative total pressure in the relative frame shown in Figure 3.16. Time-resolved data is required in order to generate contour plots of any parameter in the relative frame, therefore Figure 3.16 shows FRAP measurements. The significant loss core between 20% and 50% span is the signature of the rotor hub passage vortex (zone 1). The low relative total pressure feature at about 75% span represents the tip passage vortex (zone 2). The zones of reduced  $Cp_{t,rel}$  between the tip passage and hub passage vortex are caused by the rotor wake

(zone 3). The tip region shows zones of low relative total pressure over the whole circumference, an indication of fluid leaving the shroud cavity (zone 4). The measurement plane at the rotor exit is just downstream of the shroud cavity exit. The contour plots of the  $Cp_{t,rel}$  show that the reduction of relative total pressure observed in the radial distributions between 20% and 60% span is due to a reduction of the  $Cp_{t,rel}$  in the centre of the hub passage vortex. Figure 3.17 shows the time-resolved relative total pressure measured by the FRAP at a fixed point in space at the rotor exit. The radial height of the measurement point corresponds to the centre of the hub loss core. The low and the high injection rates are compared with each other and the radial position of the probe adapted in function of the radial migration of the hub loss core due to the variation of purge flow. The three troughs indicated by the dashed lines in Figure 3.17 correspond to the moment when the rotor hub passage vortex passes by the probe. It is only during this time when the relative total pressure decreases at increased purge flow rate. The rest of the period is not significantly affected by the additional purge flow. Hence the purge flow interacts with the rotor hub loss core and causes its relative total pressure to drop at elevated purge flow rate.

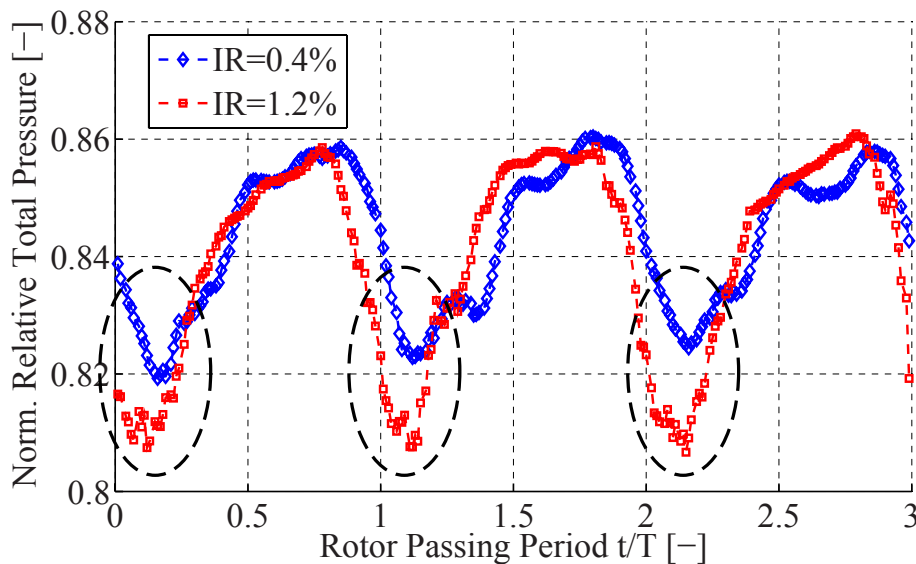


Figure 3.17.: Time-resolved normalised relative total pressure  $Cp_{t,rel}$  at a fixed point in space and at the rotor exit. The radial height of the measurement point corresponds to the centre of the hub loss core (FRAP).

Furthermore, the contour plots of the  $Cp_{t,rel}$  in Figure 3.16 show that the slight increase of the circumferentially averaged relative total pressure between 60% and 90% span is caused by an increase of the relative total

pressure in the free stream between the wakes and the tip vortex. This increase of  $Cp_{t,rel}$  at the rotor exit is due to the increased static pressure, caused by the additional purge flow, at the rotor inlet. Between 0% and 20% span the relative total pressure is more uniformly distributed.

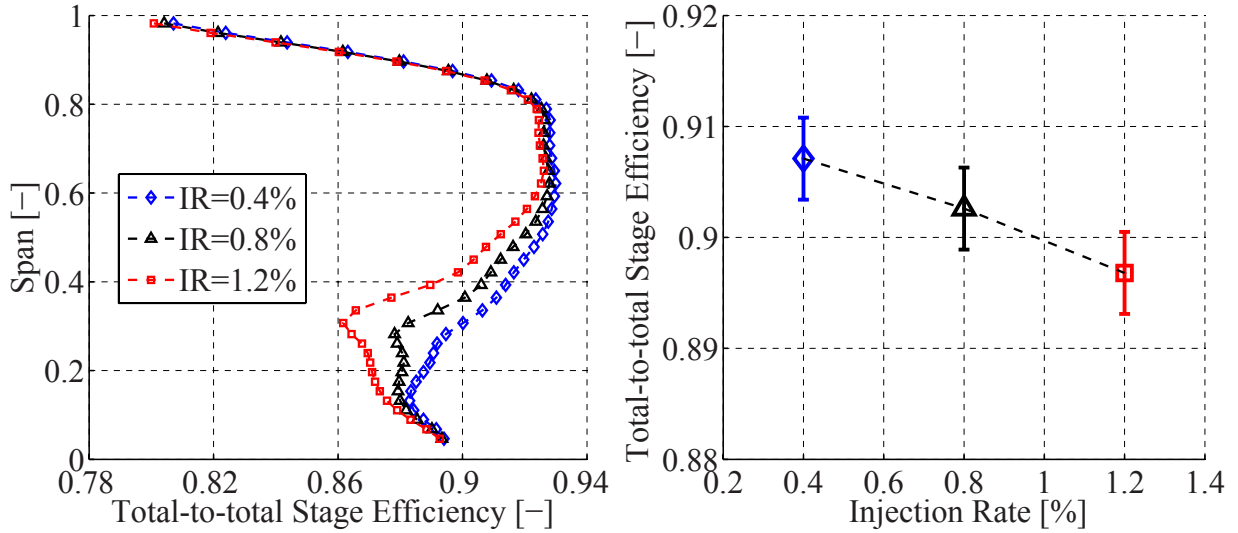


Figure 3.18.: Circumferentially mass and time-averaged (left hand side) and corresponding overall (right hand side) measured total-to-total stage efficiency  $\eta_{tt}$  for different injection rates (5-hole probe).

Figure 3.18 shows the circumferentially mass and time-averaged radial distribution of the total-to-total stage efficiency (5-hole probe) evaluated using Equation 2.23. The corresponding overall efficiencies  $\eta_{tt}$  for the three investigated injection rates are given on the right hand side in Figure 3.18 including an estimate of the measurement uncertainty. The overall efficiency is calculated as the mass weighted integral over one stator pitch of the measured total-to-total stage efficiency. The highest efficiency ( $90.7\% \pm 0.37\%$ ) was measured at the low injection rate, the lowest efficiency for the high injection rate. Within the range of the three investigated injection rates the decrease in efficiency with increasing injection rate is linear. The measured total-to-total efficiency decreases by 1.3% per percent of injected purge flow. Schuepbach et al. [92] reported a 1.2% decrease of total-to-total efficiency per percent of injected fluid using the same NGV as in the present experiment but an unshrouded rotor with high pressure turbine representative airfoils. The efficiency deficit caused due to the additional purge flow at the high injection rate is outside the total-to-total efficiency measurement uncertainty. The radial distributions of  $\eta_{tt}$  show that the main contributor to the total-to-total efficiency deficit at increased injection rate is the ad-

ditional loss in the hub passage vortex. In the same way as for the relative total pressure, the efficiency deficit at increased injection rate is caused by the increased total pressure losses in the core of the hub passage vortex. Contour plots of the total-to-total efficiency in the relative frame of reference are qualitatively identical to the contour plots of  $Cp_{t,rel}$  shown in Figure 3.16. The interaction between the purge flow and the rotor flow field causes the purge flow to significantly reduce the efficiency in the hub passage vortex. However the efficiency is as well negatively influenced by the purge flow at spanwise positions above the rotor hub loss core, in the regions where the relative total pressure was higher at increased injection rate. The increased relative total pressure is not transformed into higher efficiency in this spanwise region.

Figure 3.19 shows the experimental (FRAP) time-averaged *rms* contour plots of the total pressure random part in the rotor frame of reference at the rotor exit for all three investigated injection rates. The calculation of the *rms* is defined in Equation 2.24. The same flow structures that were already defined in Figure 3.16 are present in Figure 3.19, where the relative total pressure is low, the measured *rms* tends to be high. The significant *rms* feature between 20% and 50% span is the signature of the rotor hub passage vortex (zone 1), the elevated *rms* at about 75% span represents the tip passage vortex (zone 2). The zones of increased *rms* between the tip passage and hub passage vortex represent the rotor wake (zone 3). The tip region shows zones of elevated *rms* over the whole circumference, an indication of fluid leaving the shroud cavity (zone 4). The measurement plane at the rotor exit is just downstream of the shroud cavity exit. In contrast to the hub vortices the *rms* signatures of the tip structures are not influenced by the injected purge flow. The free stream region between the rotor wakes and secondary flow structures remains unaffected by the injected purge flow. However the peak *rms* unsteadiness in the hub passage loss core becomes much stronger. The maximum measured *rms* value in the hub passage vortex increases by 30% per percent of injected purge flow. The increased level of *rms* in the loss core at higher injection rate indicates where the injected purge flow migrates to at the rotor exit. The injected fluid interacts with the hub secondary flows, ending up in the hub passage vortex where it increases the unsteadiness. The corresponding radial distributions of circumferentially mass and time-averaged experimental *rms* of the relative total pressure are shown in Figure 3.20. A mass-weighted integral of the *rms* distribution between 10% and 60% span shows a 40% higher value per percent of injected purge flow for the high injection rate

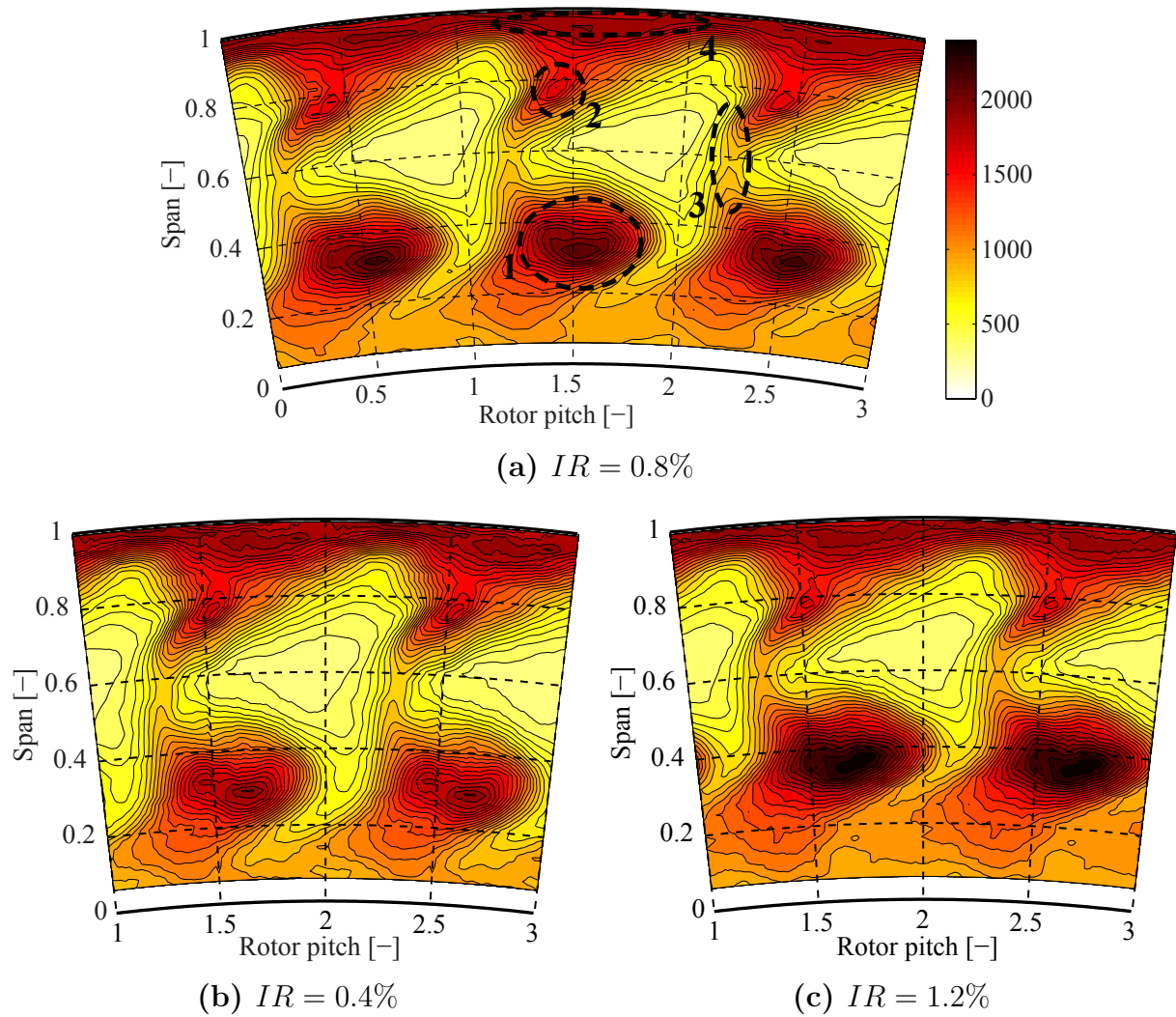


Figure 3.19.: Time-averaged area plots in rotor relative frame of reference at the rotor exit. The parameter is the experimental *rms* of the total pressure [Pa] at all investigated injection rates (FRAP).

than for the low injection rate. Considering an integral over one entire rotor pitch, the overall level of *rms* increases by approximately 20% per percent of injected fluid.

The radial distribution of circumferentially mass and time-averaged measured streamwise vorticity  $\Omega_S$  at the rotor exit for the three tested injection rates is shown in Figure 3.20. The streamwise vorticity was calculated as the scalar product of the vorticity vector and the primary flow vector as defined in Equation 2.25. The radial distributions of *rms* and  $\Omega_S$  in Figure 3.20 confirm two findings already observed based on pneumatic measurements (Figure 3.14). Firstly, the modifications to the flow field caused by a variation of the purge flow only reach a height of about 65% span at the

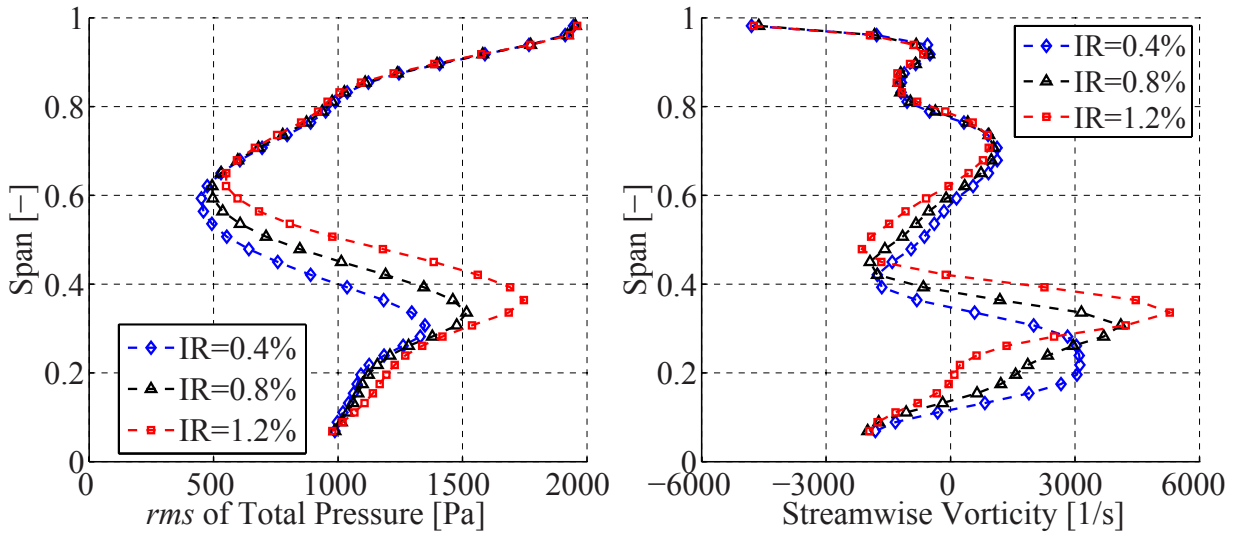


Figure 3.20.: Mass and time-averaged measured *rms* of the relative total pressure and streamwise vorticity  $\Omega_S$  for different injection rates at the rotor exit (FRAP).

rotor exit. Secondly, assuming the centre of the hub loss core to be at the radial location of maximum *rms* or maximum  $\Omega_S$ , the measurements show a radial migration of the hub loss core towards the casing of approximately 10% per percent of injected purge flow.

The circumferentially mass and time-averaged radial distribution of  $\Omega_S$  for the high injection rate shows a concentration of high streamwise vorticity flow at a limited spanwise region compared to the low injection rate. Flow with high streamwise vorticity seems to become concentrated at a higher spanwise position for the high injection rate, whereas the high  $\Omega_S$  fluid is spread over a wider radial range at the low injection rate. Figure 3.21 shows the corresponding time-averaged two-dimensional contour plots of  $\Omega_S$  at the rotor exit in the rotor frame of reference for all tested injection rates. The feature of positive streamwise vorticity at approximately 30% span and labelled **1** is due to the rotor hub passage vortex. The neighbouring negative vorticity in zone **2** can be associated with the hub trailing edge shed vorticity. The negative vorticity feature at about 80% span (zone **3**) is the signature of the tip passage vortex. The tip trailing shed vortex associated with radially outward migration of the suction side boundary layer is labelled **4**. The fluid exiting the tip shroud cavity does not generate significant vorticity. Under the effect of increased purge flow the high vorticity flow of the hub passage vortex (zone **1**) not only concentrates at a higher spanwise position, but also tends to be stretched in the circumferential direction. When comparing Figures 3.19 and 3.21, it can be seen that the

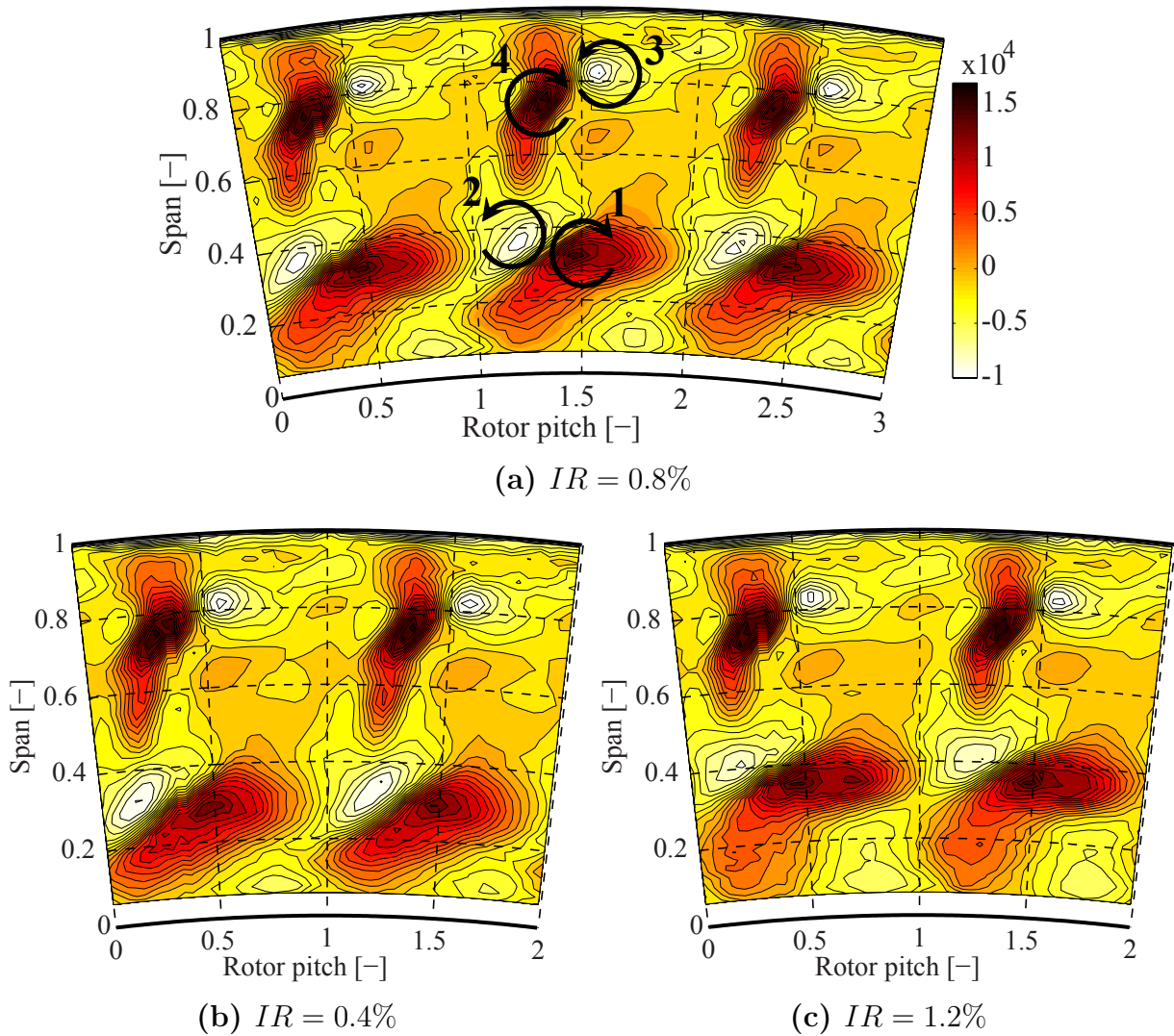


Figure 3.21.: Time-averaged area plots in rotor relative frame of reference at the rotor exit. The parameter is the streamwise vorticity  $\Omega_S$  [1/s] at all investigated injection rates (FRAP).

*rms* distribution in the rotor frame of reference at the rotor exit does not show the same change in shape as the streamwise vorticity does. In order to quantify the strength of the hub passage vortex, its circulation has been calculated as an area integral of  $\Omega_S$  inside an iso-contour of zero streamwise vorticity. The calculated circulation based on the time-averaged streamwise vorticity increases by approximately 10% per percent of injected fluid. The area covered by the hub passage vortex (inside the iso-contour of zero streamwise vorticity) increases by the same amount.

The interaction between the additional purge flow and the rotor hub loss core appears to augment its streamwise vorticity. This is an interesting observation as the purge flow does a priori not have any significant amount

of vorticity when it leaves the rim seal cavity. However, the fact that the purge flow has a different velocity to the free stream means that it is coated in a shear layer of strong vorticity when they meet. The unsteady interaction with the rotor flow field can transform the shear layer vorticity into streamwise vorticity when it is convected through the rotor blade row. Another possible reason for the increase of streamwise vorticity is the fact that the hub loss core radially migrates outwards under the effect of increased injection rate and in so doing gains more rotation. The measured peak streamwise vorticity in the hub loss core also increases by approximately 10% per percent of injected purge flow. In comparison, the purge flow causes the measured level of non-deterministic unsteadiness to increase more significantly (30% per percent of injected purge flow) by causing additional turbulence. Furthermore, the injected purge flow decreases the strength of the streamwise vorticity of the hub trailing shed vortex (zone 2). The minimum measured  $\Omega_s$  in the hub trailing shed vortex reduces by approximately 20% per percent of injected purge flow.

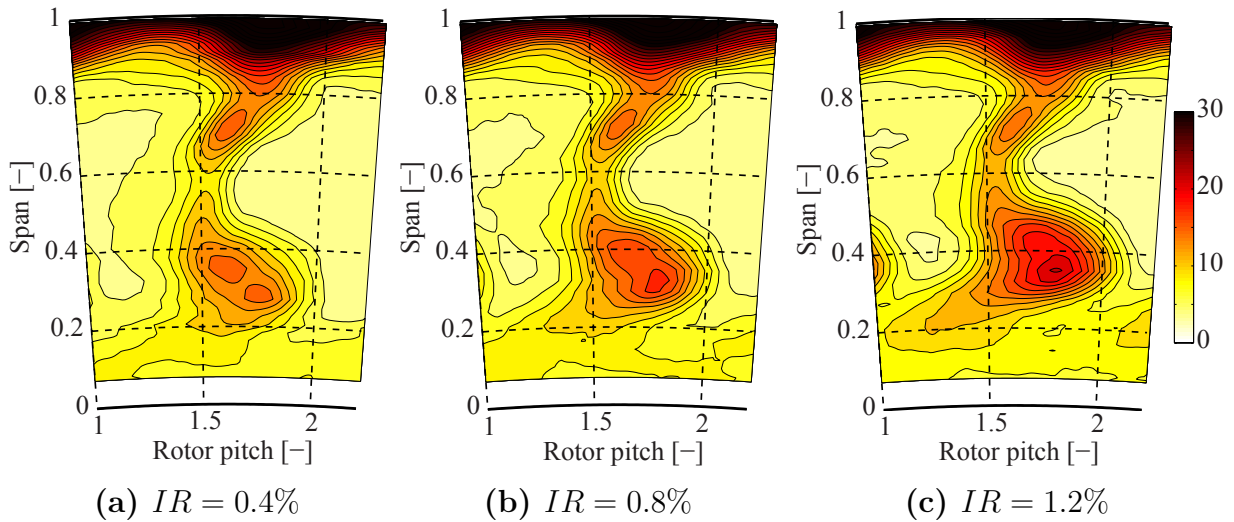


Figure 3.22.: Time-averaged area plots in rotor relative frame of reference at the rotor exit. The parameter is the measured unsteady entropy rise  $\Delta s$  [J/kg/K] at all investigated injection rates (FENT).

Figure 3.22 shows the time-averaged contour plots of the unsteady entropy rise (FENT) in the rotor frame of reference at the rotor exit for all three investigated injection rates. The entropy rise has been calculated using Equation 2.34. The total inlet conditions were chosen as reference conditions. Again only the hub loss core is significantly affected by the additional purge flow. The rest of the rotor exit flow field is unaffected by the purge flow. Beside the non-deterministic unsteadiness the purge flow as well in-

creases the entropy and loss generated in the hub passage vortex. The maximum measured time-averaged entropy rise in the hub loss core increases by 50% per percent of injected purge flow. The two-dimensional shape of the hub passage vortex does not significantly alter with the addition of purge flow. However the entropy signatures tends to be slightly stretched in the circumferential direction combined with the radial migration, in the same manner as the streamwise vorticity, but less pronounced. There is a region of elevated entropy in the tip region over the whole circumference. These increased entropy levels are caused by the fluid leaving the shroud cavity. The air passing through the shroud cavity does no work on the rotor but loses total pressure through friction and viscous dissipation. Its temperature remains therefore higher when it leaves the shroud cavity compared to the main flow (which went through the rotor). The main reason for the increased entropy of the flow leaving the shroud cavity is the elevated temperature combined with a pressure being at a comparable level to the main flow.

A more detailed picture about the purge flow effects can be drawn when considering absolute frame space time diagrams at the rotor exit. Figure 3.23 shows two space time diagrams of the random part of the experimental *rms* signal of the relative total pressure at 60% span at the rotor exit. Figure 3.23(a) gives the lowest injection rate and Figure 3.23(b) the highest. These plots are at the highest spanwise position (60%) to be influenced by the purge flow, at this height the flow is not dominated by the hub loss core. In both diagrams there are a series of rounded high *rms* patches stacked vertically at about -0.15 stator pitch. These are the signature of the upstream NGV1 wake, a stationary feature with regard to space but fluctuating in time. Whereas the inclined high *rms* features are caused by the rotor wakes, as the space time plots are plotted in the absolute frame of reference. The NGV and rotor wakes are very similar in the two space time plots in Figure 3.23, showing that the operating point was very similar. However at about 40% to 50% stator pitch the plot for the higher injection rate shows a region of increased *rms* signal indicated by the dashed ellipse in Figure 3.23. The difference between the two space time plots must be caused by the injected fluid, because this is the only significant change. As the injected fluid is increased, the purge mass flow collects on the rotor suction side, which is what the probe sees first when the rotor blade is passing by. Therefore the increase in *rms* is on the lower side of the rotor wake on the space time plots in Figure 3.23. Furthermore, the high *rms* due to the injected fluid is concentrated around one circumferential region,

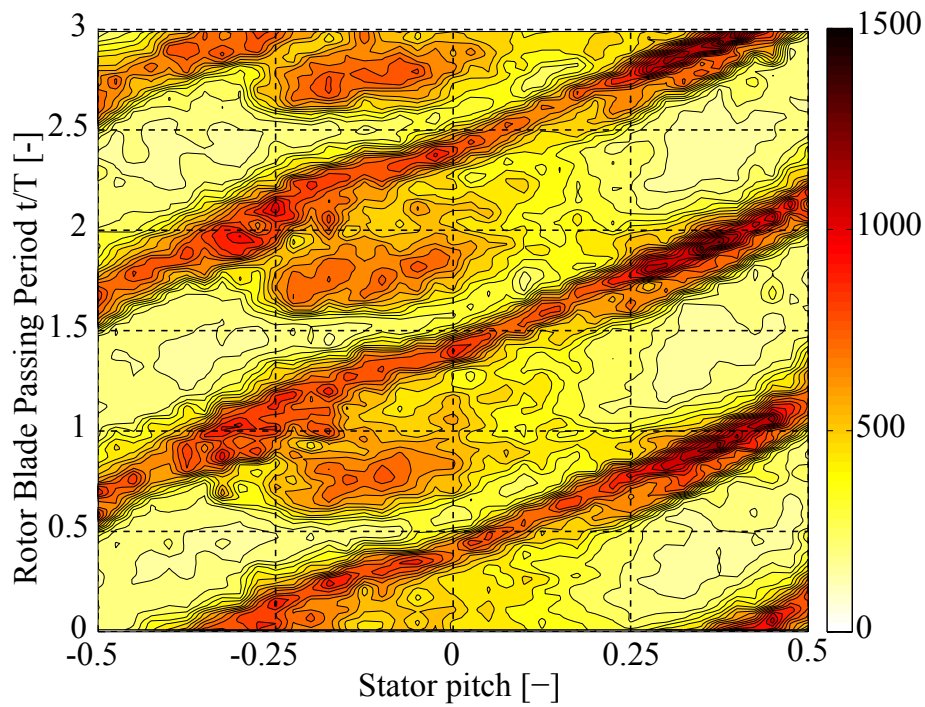
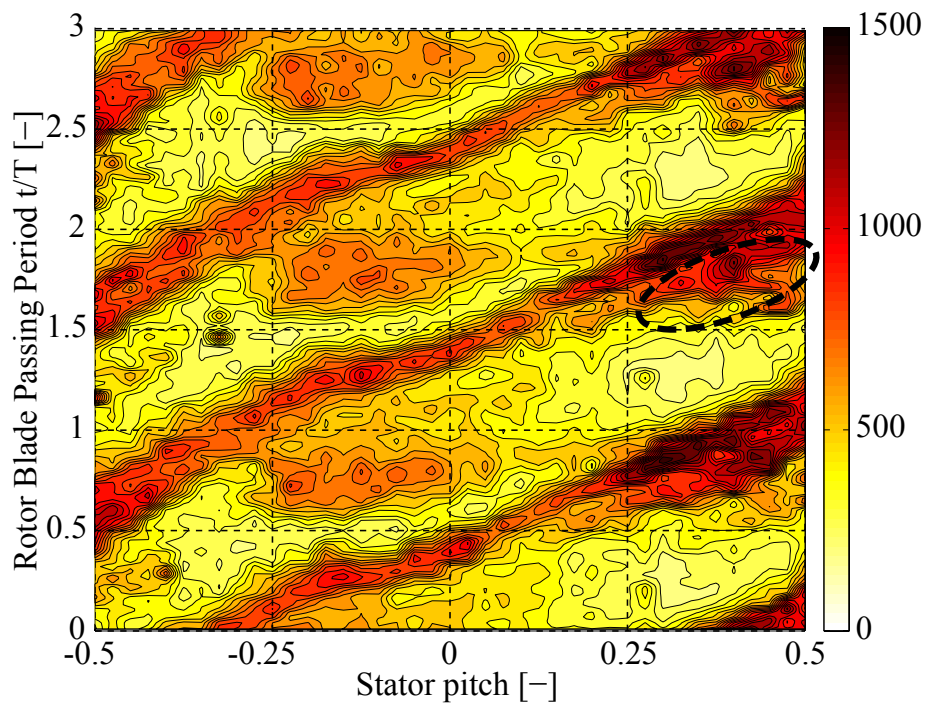
(a)  $IR = 0.4\%$ (b)  $IR = 1.2\%$ 

Figure 3.23.: Space time plots of the experimental *rms* of the relative total pressure [Pa] at 60% span at the rotor exit for the low and the high injection rates (FRAP).

suggesting that the trajectory of the purge fluid is influenced by something stationary - probably the upstream vane. The NGV interaction is causing

the injected fluid to interact with the suction side of the rotor at a fixed point in absolute space. The jet of injected fluid pulsates in the relative frame of reference, one burst of flow per NGV passing event.

Figure 3.24 shows the *rms* of the relative total pressure in the form of time space plots in the absolute frame at the rotor exit. Plots are shown for the low (left column) and the high (right column) injection rates at two different traverses. The circumferential position of the two chosen traverses can be put into context with the help of Figure 3.24. The first traverse at 0.15 stator pitch is between the NGV wake fluid and the location where the purge flow increases the unsteadiness. The second traverse is at the circumferential location where the purge flow was found to increase the unsteadiness on the suction side of the rotor wake. The time axis covers three rotor blade passing events. Therefore the same rotor related flow structures as indicated by the dashed lines in Figures 3.16 and 3.19 can be identified as regions of elevated *rms* three times along the time axis. The hub passage vortex at about 30% span (zone 1), the tip passage vortex at about 75% span (zone 2), the rotor wake between the two passage vortices (zone 3) and the fluid leaving the shroud cavity (zone 4). The experimental *rms* of the flow field at the rotor exit is only affected below 65% span at the rotor exit (Figure 3.20). However when comparing the space time plots at 0.15 and 0.45 stator pitch in Figure 3.24, higher levels of *rms* can be detected above 65% span at 0.45 stator pitch. These variations of *rms* must therefore be related to the downstream second nozzle guide vane. The potential field caused by the NGV2 influences the *rms* distribution. Regions of elevated *rms* are indicative of significant non-deterministic unsteadiness and are typically of low momentum and therefore avoid the static potential field of the downstream stationary blade row. The circumferential coordinate of the NGV2 leading edge can be defined with the space time plot of static pressure shown in Figure 7.2. The maximum potential effect of the NGV2 is observed at approximately 0.05 stator pitch. The time space plots at 0.15 stator pitch in Figure 3.24 are closer to the maximum NGV2 potential effect and therefore show significantly lower levels of *rms* for both injection rates. When looking at time-averaged measurements the effect of the NGV2 on the *rms* distributions is averaged out. When comparing the time space plots of the low and high injection rates in Figure 3.24 the radial migration towards the casing due to increased purge flow is clearly visible at both traverses. Figure 3.23 shows that the purge flow concentrates around one circumferential region (between 0.3 and 0.6 stator pitch). This finding is confirmed when comparing the levels of *rms* for the low and high

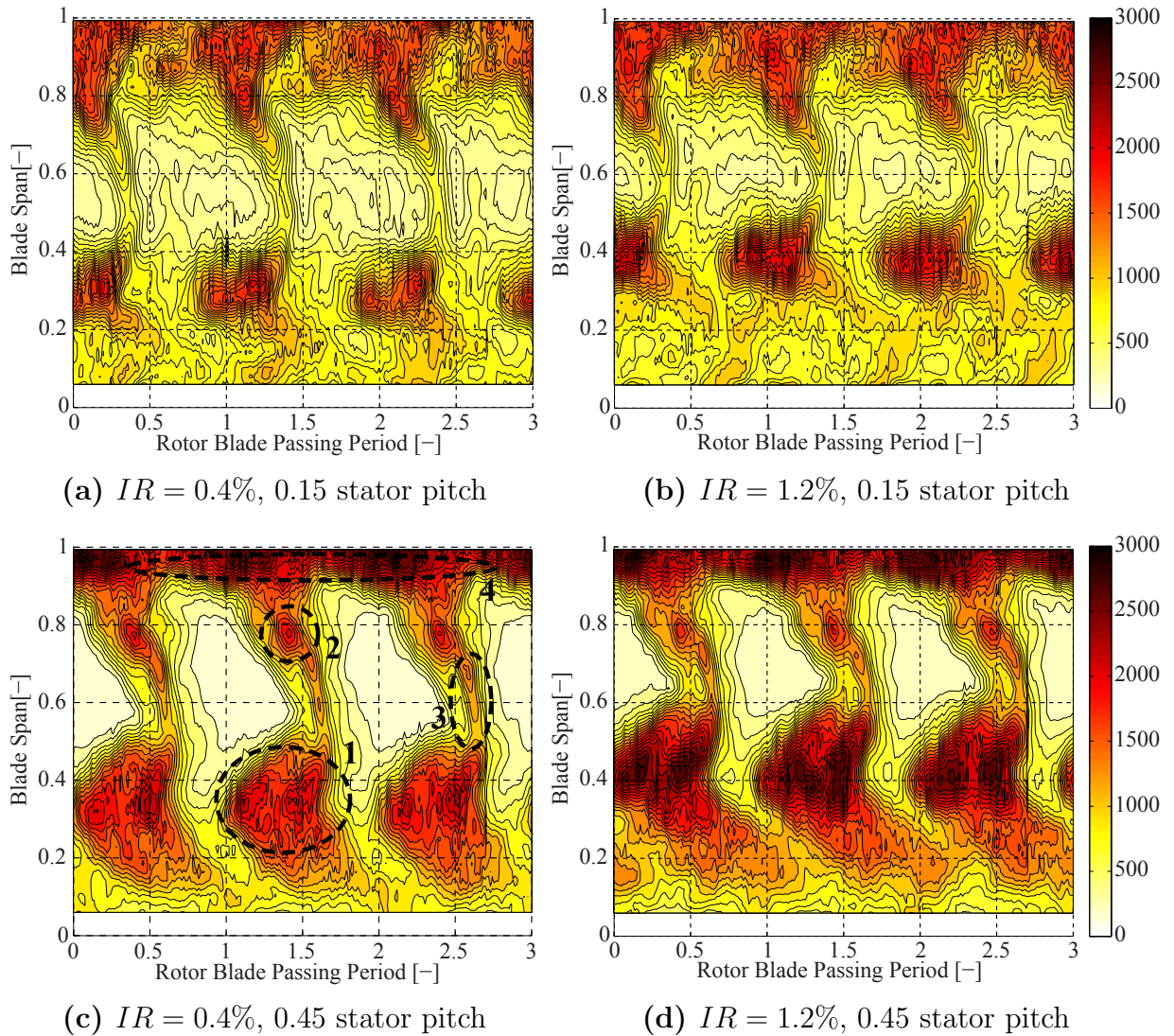


Figure 3.24.: Time space plots of the experimental *rms* of the relative total pressure [Pa] at two circumferential locations (0.15 and 0.45 stator pitch) at the rotor exit for the low and the high injection rates (FRAP).

injection rates at the two traverses. For the traverse at 0.45 stator pitch in the circumferential region where the purge flow accumulates there is a clear increase of *rms* in the hub passage vortex due the increased injection rate. For the traverse at 0.15 stator pitch there is no significant change of *rms* at the high injection rate. For this circumferential region the purge flow appears not to affect the non-deterministic unsteadiness in the hub loss core. The *rms* signature of the hub loss core at the high injection rate and at 0.45 stator pitch shows two separated patches of separated of elevated *rms*. The unsteady rotor hub passage vortex behaviour in the presence of purge flow is discussed in chapter 7.

## 3.4. Purge Flow Losses

In the next section, the additional loss caused by the increased purge flow injection rate is studied and an approach to quantify this loss is proposed. The analysis focuses on the generated losses in the rotor hub passage vortex as this is the only flow structure being significantly affected by the purge flow.

### 3.4.1. Measured Loss in the Rotor Hub Passage Vortex

The variable chosen for the analysis of the additional loss generated in the hub passage vortex at increased injection rate is the experimental unsteady isentropic efficiency  $\eta_{is}$  at the rotor exit. Isentropic efficiency is a non-dimensional number that directly compares the actual work to the ideal work for each fluid particle. When  $\eta_{is}$  is used, two assumptions need to be made: The flow is adiabatic and all the fluid has the same initial conditions. The isentropic efficiency could be artificially increased assuming heat loss in the turbine stage. The actual work would appear to be greater because there is a higher enthalpy change due to this heat loss. The heat loss in the test rig cannot be quantified exactly, but can be assumed to be similar during the measurements at all different injection rates, which allows for relative comparisons. The FENT probe measurements include unsteady total pressure and temperature. Hence, the unsteady isentropic efficiency can be calculated based on the FENT measurements using the local definition in Equation 3.1. The purge flow is not taken into account as for the total-to-total efficiency definition as Equation 3.1 is a local definition.

$$\eta_{is} = \frac{1 - \frac{T_{t,R1ex}}{T_{t,in}}}{1 - \left(\frac{P_{t,R1ex}}{P_{t,in}}\right)^{\frac{\kappa-1}{\kappa}}} \quad (3.1)$$

Figure 3.25 shows the mass and time-averaged radial distributions of  $\eta_{is}$  at the rotor exit for the three investigated injection rates. The corresponding area plots in the rotor frame of reference are shown in Figure 3.26. The deficit of  $\eta_{is}$  present on the radial mass and time-averaged distributions between 20% and 60% span is caused by the additional loss inside the hub passage vortex. The rest of the flow field appears to be much less affected by the different levels of purge flow (Figure 3.26). In order to quantify the significance of the lower efficiency in the hub passage vortex compared

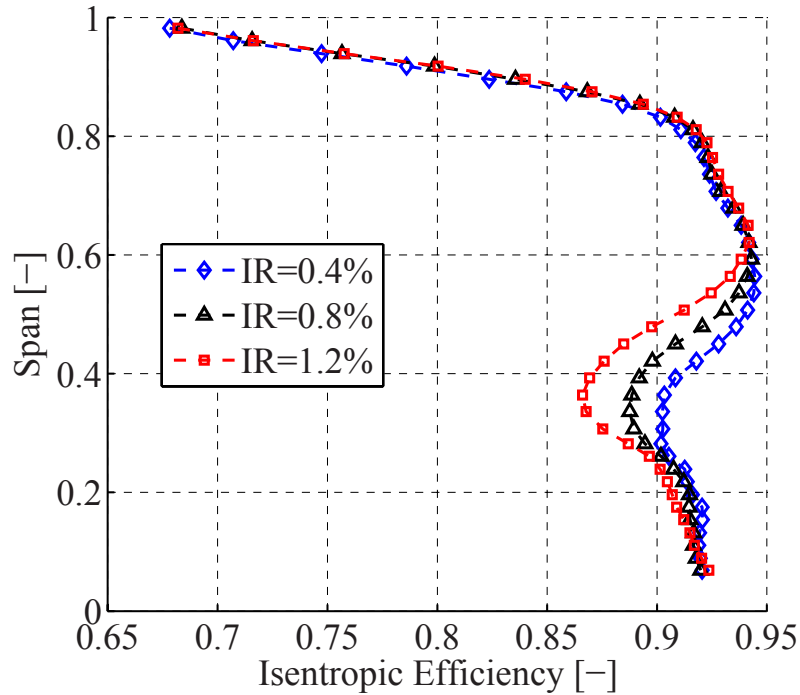


Figure 3.25.: Radial distribution of circumferentially mass and time-averaged isentropic efficiency  $\eta_{is}$  at the rotor exit for the three injection rates investigated (FENT).

to the efficiency of the whole machine, a mass weighted average over one entire rotor pitch is calculated. This mass weighted  $\eta_{is}$  decreases by 1.5% per percent of injected purge flow, whereas a mass-averaged integral of the measured isentropic efficiency in the hub loss core decreases by 4% per percent of injected purge flow. When considering a machine efficiency definition taking into account the effect of the rim seal purge flow, the total-to-total efficiency decreases by 1.3% per % $IR$  for this rotor, which is the one with the 1<sup>st</sup> end wall design (section 6.2.1).

Figure 3.27 shows the mass and time-averaged radial distributions of total pressure and total temperature, the two variables required to calculate  $\eta_{is}$ . It is interesting to note that the effect of the purge flow on the total temperature is at higher radius (between 40% and 60% span), whilst the effect of the total pressure is at lower radius (between 20% and 40% span). Assuming the centre of the vortex to be between 25% and at 35% span, depending on the injection rate, the purge flow causes the temperature to mainly increase in the top part of the vortex and the total pressure to mainly decrease in the lower part of the vortex. The proposed mechanism that causes the total temperature to rise in the top of the vortex is radial migration. At constant rothalpy  $I$  the total temperature  $T_t$  varies with the

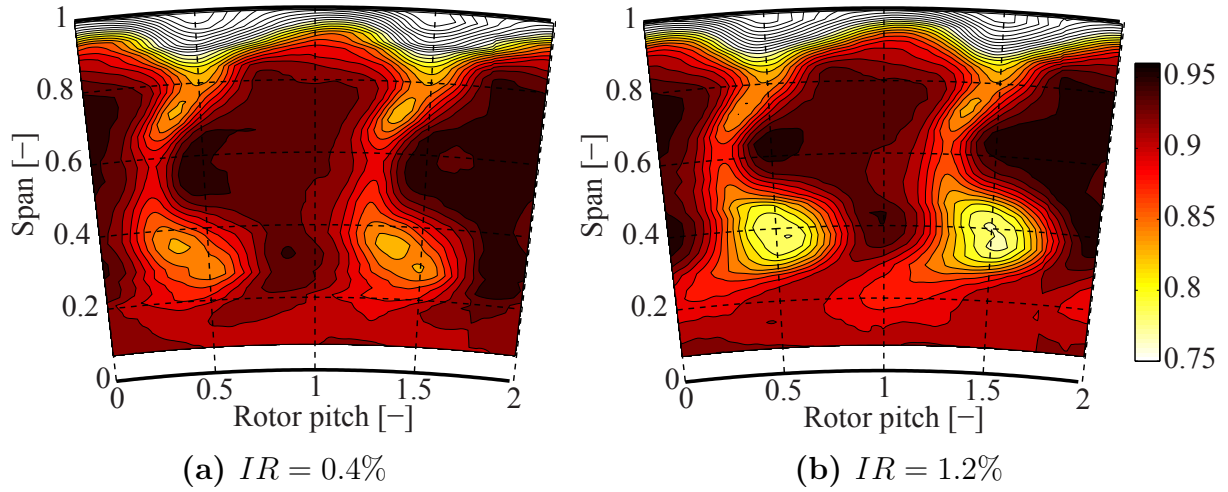


Figure 3.26.: Time-averaged area plots in rotor relative frame of reference at the rotor exit. The parameter is isentropic efficiency  $\eta_{is}$  [-] at low and high injection rates (FENT).

Euler work group  $UV_\theta$ , Equation 3.2:

$$I = h_{t,rel} - \frac{U^2}{2} = h_t - UV_\theta = h_t - C_P T_t \quad (3.2)$$

The blade speed  $U$  increases when the flow radially migrates outwards. Provided that the flow angle and relative Mach number do not significantly change, a radius increase of the flow is a work reduction, hence  $T_t$  increases. The additional purge flow causes radial migration of the hub passage vortex and therefore enforces the increase in the total temperature in the top part of the vortex. The small difference in inlet temperature ( $-2\text{K}$ ) between purge flow and free stream does not explain the changes in the top part of the vortex shown in Figure 3.27. The slight increase in total pressure between 60% and 80% span (Figure 3.27) causes the isentropic efficiency to slightly increase in this part of the flow field (Figure 3.25). Reduced profile loss of the rotor is considered to be one of the reasons for this increase of  $P_t$ , reflected in the slight reduction of isentropic efficiency at higher injection rate at these radial heights (Figure 3.25). Due to the additional purge flow, the rotor sees a slightly higher total to static pressure ratio, which increases the acceleration and hence reduces profile loss. Another reason for the slight increase in total pressure between 60% and 80% span is reduced work. Negative incidence caused by additional purge flow tends to reduce the work. The measured Euler work term decreases by approximately 0.5% per percent of injection rate between 60% and 80% span.

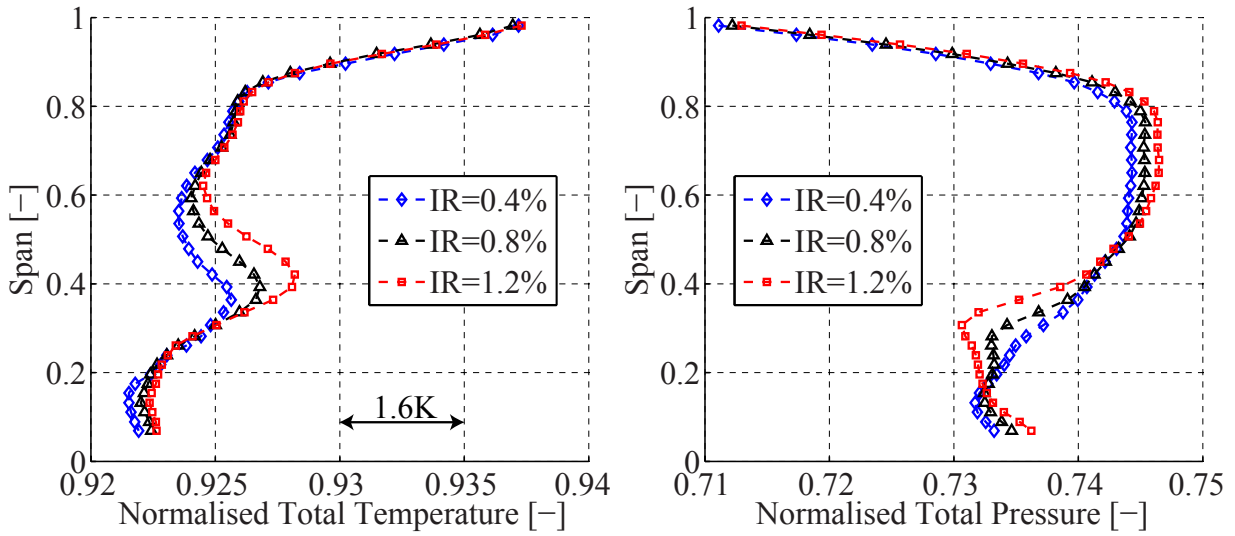


Figure 3.27.: Radial distribution of circumferentially mass and time-averaged normalised total pressure and temperature at the rotor exit for the three investigated injection rates (FENT).

### 3.4.2. Purge Flow Losses: Lagrangian Perspective

The numerical simulations performed in parallel to the measurements were used to detail the flow field in the rotor passage and to further characterise the loss mechanisms caused by the purge flow. For this particles were released at the rim seal lip and tracked to the rotor exit measurement plane as in section 3.1. Figure 3.28 shows the top and side view of a typical particle track of a purge flow particle leaving the rim seal cavity. Figure 3.29 details radial position, circumferential position, relative velocity (kinetic energy) and the Euler work term of the particle track shown in Figure 3.28. The parameters are plotted as a function of the non-dimensionalised axial position. Zero corresponds to the start of the particle at rotor inlet and 1 corresponds to the moment when the particle leaves the rotor domain. For comparison, Figure 3.29 also shows the corresponding track details of a free stream particle leaving the rotor blade row at the same radial position as the particle leaving the rim seal cavity. When the particle leaves the rim seal cavity it has much lower rotor relative velocity compared to the particles leaving the nozzle guide vane. The flow above the rim seal leaving the NGV at low span is expected to have the highest relative velocity. The relative velocity at the rim seal exit (radius equal to rotor hub radius) of the analysed particles in Figures 3.13 and 3.29 are approximately two times lower compared to the free stream particle. The significant velocity mismatch at the exit of the rim seal cavity represents loss generation oppor-

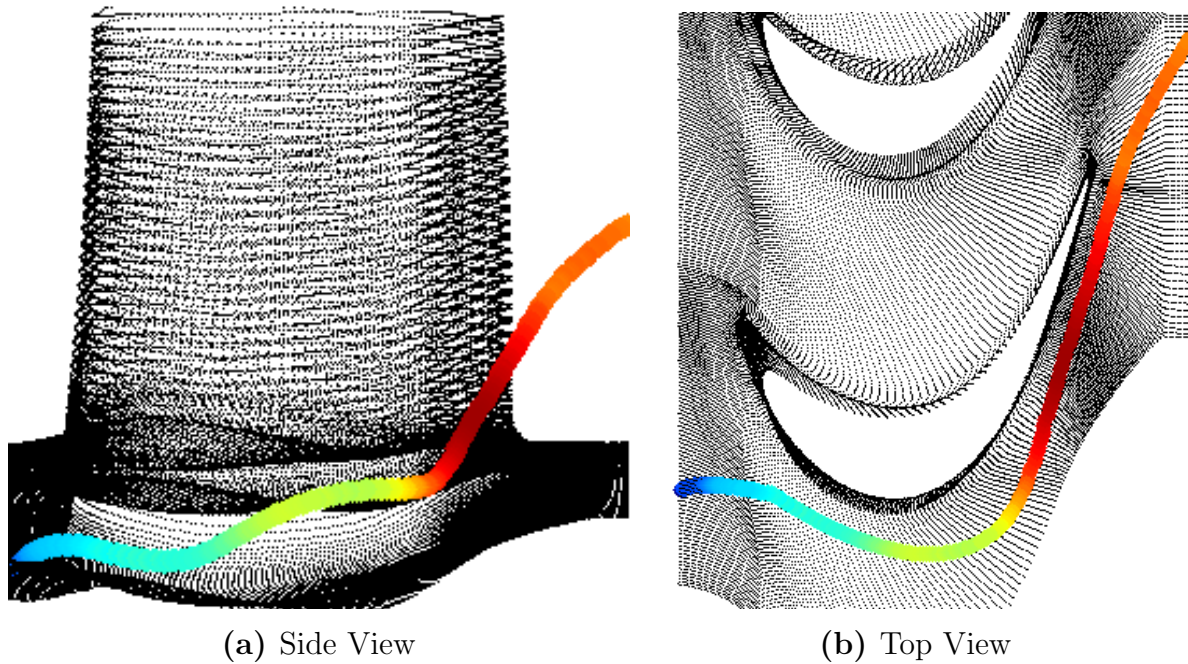


Figure 3.28.: Top and side view of typical particle track of particles leaving the rim seal cavity ( $IR = 0.8\%$ ). The colour of the particles indicates relative velocity.

tunities. It is therefore considered to be one of the reasons for the increased loss and turbulence in the passage vortex, especially at the high injection rate. When the particle has left the cavity it is first strongly accelerated and starts to interact with the hub passage vortex. In the relative frame the particle under investigation in Figure 3.29 is accelerated by a factor of 8 from rotor inlet to rotor outlet. The increasing and decreasing spanwise coordinate in Figure 3.29 indicates a vortical motion during the radial migration of the particle. The particle has become part of the hub passage vortex. Figure 3.29 also shows that the particle leaving the rim seal cavity is accelerated in the circumferential direction in the early rotor passage. As the purge flow fluid enters the rotor it travels directly towards the low pressure of the suction side of the rotor. As it does so, the rotor does work on it with  $UV_\theta$  climbing from  $6000\text{m}^2/\text{s}^2$  to  $11000\text{m}^2/\text{s}^2$ , its enthalpy rises and the turbine rotor locally acts as a compressor. The purge flow particle almost attains the  $UV_\theta$  value of the free stream, but then enters the passage vortex, following an oscillatory path, Figure 3.28. As the particle orbits the vortex it alternately gains and loses enthalpy. When the purge flow particle joins the passage vortex it has a circumferential velocity typical of a free stream particle, but it is joining low momentum fluid. The velocity differences between the purge flow particle and the free stream can be expected to indicate shear stresses and viscous dissipation. The kinetic energy of the

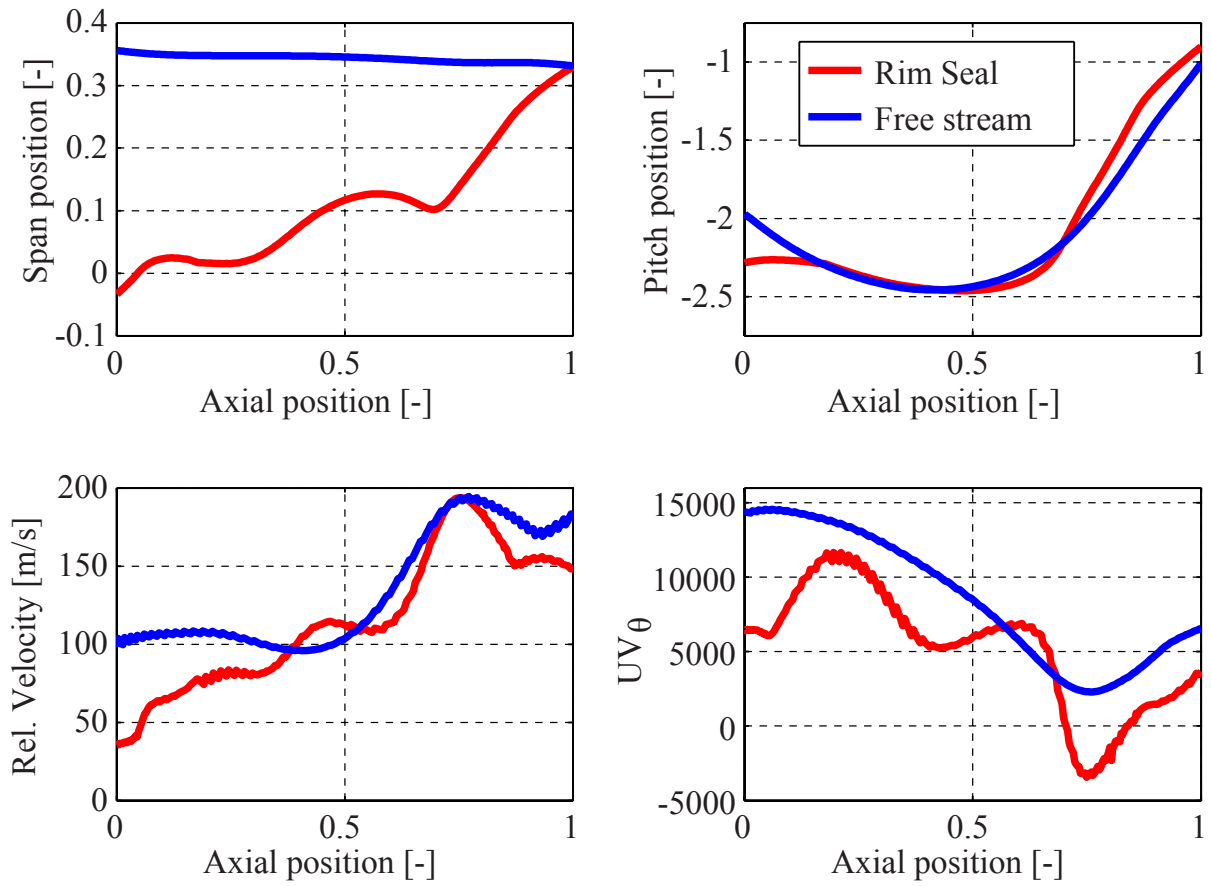


Figure 3.29.: Position, relative velocity and Euler work term of the particle presented in Figure 3.28 and a free stream particle leaving the rotor blade row at the same radius. The parameters are plotted as a function of the non-dimensionalised axial position. Zero corresponds to the start of the particle at rotor inlet and 1 corresponds to the moment when the particle leaves the rotor domain.

purge particle will be viscously destroyed and as a consequence the entropy will rise. Thus the work processes acting on the purge fluid extract energy from the rotor, deliver it to the particle only to be dissipated viscously by friction. This suggests that work processes are a part of the loss mechanisms involved in the hub loss core. The difference in Euler work for the rim seal purge flow particle is approximately  $\Delta UV_{\theta}=3000\text{m}^2/\text{s}^2$ . In comparison, for the free stream particle the corresponding number is  $\Delta UV_{\theta}=7500\text{m}^2/\text{s}^2$ . In other words, the purge flow particle only does about 40% of the work on the rotor compared to the free stream particle. Hence the purge flow fluid reduces the work of the turbine rotor as well as causing additional mixing losses.

### 3.4.3. Flow Structures Involved in the Hub Loss Core

The particle tracking tool was also used to determine which flow structures are predicted to get involved in the rotor hub passage vortex. Particles were released in the hub passage vortex at the rotor exit and tracked in a backward time mode in order to see where they came from and which path they follow in the rotor flow field.

Two injection strategies for the backward tracking of the particles were considered. As a first option, particles were introduced at a different position at each time step as a function of the unsteady spatial movement of the hub passage vortex that has been described in section 7.1. Particles were injected during one period inside a circular cloud around the moving centre of the hub loss core. The centre of the cloud is defined using the maximum value of the Q-criterion (second invariant of the velocity gradient tensor, Hunt et al. [41]) at each time step of the simulation. As a second option, the particles were released at the same coordinates at each time step during one period. Again the particles were released inside a circle whose centre is determined by the minimum time-averaged relative total pressure in the hub passage vortex. Figure 3.30 shows the particle tracks of particles leaving the rotor blade row inside the hub passage vortex. The picture shows the rotor blade row seen from downstream. The colour of the particles indicates their relative velocity. The particles of the hub passage vortex stay at a relatively low radius until they get pulled to higher span positions by the reduced static pressure gradient in the rotor suction side exit region. In this region the reduced static pressure is high at the hub and low at the casing. The reduced static pressure is known from literature (Moore et al. [63], Greitzer et al. [33]).

Classically, the following fluid sources for the rotor hub passage vortex would be expected: rotor end wall boundary layer, radially migrating fluid on the rotor suction side, purge flow out of the rim seal cavity, NGV1 hub end wall boundary layer, NGV1 wakes and hub loss core. For the operating point under investigation, the turbine rotor blades have pressure side separations. For the rotor with the 1<sup>st</sup> end wall design the fluid inside the pressure side bubble leaves the rotor blade row inside the hub passage vortex, as presented in section 5.1.2. The fluid from the listed sources has lower relative momentum than the free stream flow and therefore migrates to the regions of low reduced static pressure in the rotor flow field. Generally speaking, low relative momentum flow from the listed sources migrates radially inwards and towards the suction side of the rotor where it inter-

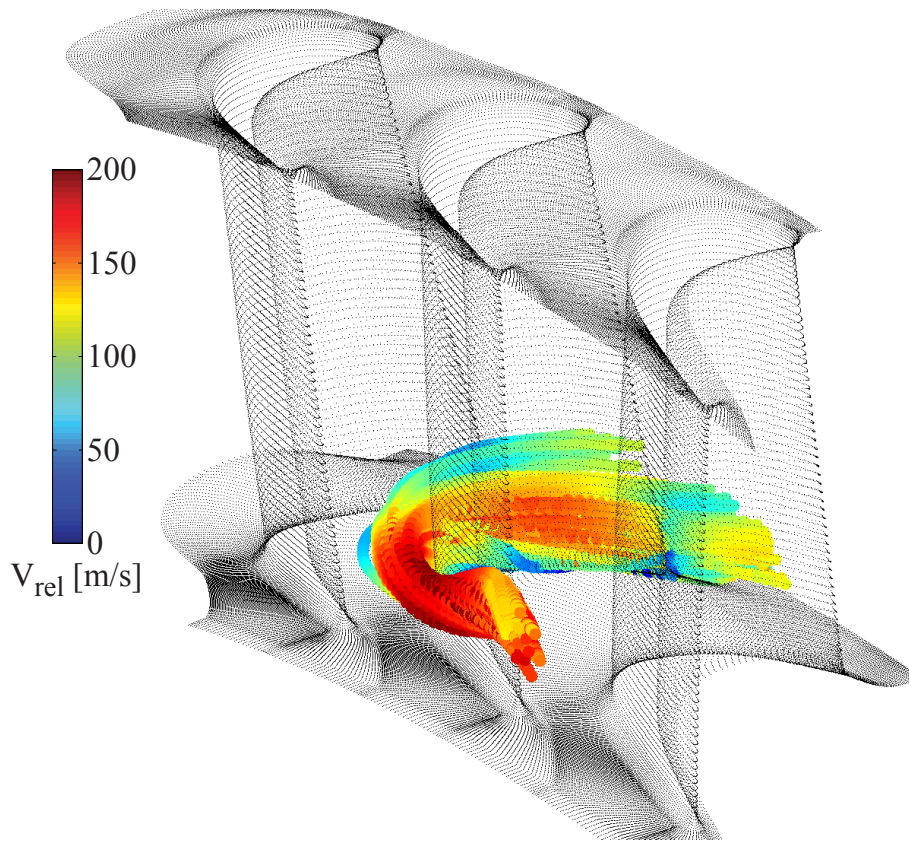


Figure 3.30.: Three-dimensional particle tracks of particles leaving the rotor blade row inside the hub passage vortex ( $IR = 0.8\%$ ). Rotor seen from downstream.

acts with the rotor hub passage vortex. Many of the listed sources include highly complex flow interaction mechanisms and will not be included in this thesis. Typical particle tracks of particles leaving the rim seal cavity are presented and studied in section 3.4.2.

The backwards particle tracking has been used in order to statistically define the percentages of the different flow sources of the hub passage vortex. Thus, for each test case five thousand particles were injected at the rotor exit inside the hub passage vortex using the injection methods described and backtracked to their origin. The results are shown in Table 3.1. At a nominal injection rate approximately 15% of the particles in the hub passage vortex were found to originate from the rim seal cavity. The corresponding approximate percentages at low and high injection rates are 10% and 22%. This relatively small percentage of the hub passage vortex flow causes the 4% increase in loss and the 30% increase in experimental unsteadiness per percent of injected purge flow. Depending on the injection rate, the fluid leaving the pressure side separation was found to represent between 1% and 3% of the total hub passage vortex flow. As described in

section 5.2, the pressure side bubble increases in size with increasing purge flow rate. Hence more flow leaves the pressure side bubble at higher injection rate via the described path. However, the effect of the purge flow on the measured unsteadiness in the hub loss core appears to be one order of magnitude stronger than the effect of the pressure side bubble. Approximately 40% to 50% of the hub passage flow was detected to come from the rotor end wall and blade boundary layers. This number was only slightly affected by the amount of purge flow injected. A particle was considered as boundary layer flow when it was on average closer than 0.5mm to the end wall on its track. The remaining percentage of the hub passage vortex flow is considered to originate from the NGV1 wakes, hub end wall boundary layer and hub passage vortex.

	$IR = 0.4\%$	$IR = 0.8\%$	$IR = 1.2\%$
Rim seal cavity	10%	15%	22%
Pressure side bubble	1%	2%	3%
Boundary layer	35%-50%	35%-50%	35%-50%
NGV1 secondary flows, etc.	30%-45%	30%-45%	30%-45%

Table 3.1.: Statistical composition of the rotor hub loss core.

### 3.5. Summary

The axial position of the probe traverse plane at the rotor inlet makes it possible for the 4-hole probe, FRAP and FENT probe to measure in the upper rim seal cavity above the rim seal lip and to capture the rim seal purge flow effects in this region. The injection of purge flow between the rotor and nozzle guide vane causes the static pressure to rise by 1% and the Mach number to drop by approximately 2.5% per percent of injection rate at the rotor inlet. The reduction of Mach number with increasing injection rate causes negative incidence on the rotor leading edges. Close to the hub the maximum measured change of incidence is  $-9^\circ$ . The time-resolved measurements at rotor inlet show that the injection of the purge flow is determined by the unsteady blade row interaction. In the absolute frame the wake of the nozzle guide vane defines where the purge flow is able to leave the rim seal cavity. The lowest counter pressure for the purge flow can be expected downstream of the nozzle guide vane suction side. The rotor movement is defining the moment when the purge flow is leaving the

cavity. Upstream of the rotor blade suction side shoulder the lowest static pressure at the rim seal exit can be expected. In the relative frame the two roles are inverted, the rotor defines where and the nozzle guide vane when the purge flow is leaving the rim seal cavity.

CFD analysis revealed two axial zones at the rim seal exit where the purge flow is leaving the rim seal cavity, zone 1 between 5% and 60% and zone 2 between 90% and 100% non-dimensional axial rim seal coordinate. Up to a certain injection (smaller than the nominal injection rate) the mass flow increases in both zones. Then the simulations show that when a maximum mass flow is reached in zone 2, all the additional purge flow has to leave the cavity through zone 1. The mass flow distribution at the rim seal exit gives evidence to suggest a toroidal vortex in the rim seal cavity above the rim seal cavity. Particle tracks revealed such a vortical structure. Three typical purge flow particle tracks were analysed.

The purge flow affects the rotor exit flow field only below 65% span and significantly interacts with the hub passage vortex. The injected purge flow causes the hub passage vortex to radially migrate by 10% per percent of injected purge flow. Pneumatic 5-hole probe measurements showed a decrease of the total-to-total efficiency of 1.3% per percent of injected purge flow. The measured maximum non-deterministic unsteadiness in the hub loss core increased by 30% per percent of injected purge flow. A mass-weighted integral of the *rms* distribution between 10% and 60% span shows a 40% higher value per percent of injected purge flow for the high injection rate. The measured streamwise vorticity in the hub passage vortex not only concentrates at a higher spanwise position, but also tends to be stretched in the circumferential direction under the effect of increased purge flow. The circulation of the hub passage vortex increases by 10% per percent of injection rate. The maximum measured unsteady entropy rise in the hub loss core increases by 50% per percent of injection rate. Time-resolved measurements showed that the unsteady rotor flow field causes the purge flow to collect on the rotor airfoil suction side at one circumferential location.

An attempt to quantify the additional loss in the hub loss core caused by the purge flow was presented. A mass-averaged integral of the measured isentropic efficiency in the hub loss core decreases by 4% per percent of injected purge flow. With the use of particle tracks of purge flow and free stream particles two loss mechanisms were identified for particles leaving the rim seal cavity. Firstly, the significant relative velocity mismatch near the rim seal between purge flow and free stream fluid is causing the loss to increase with increasing purge flow rate due to friction and viscous dissipa-

tion. Secondly, the rotor was found to do work on the rim seal purge flow in the early rotor passage by accelerating it in the circumferential direction. These work processes extract energy from the rotor and deliver it to the particle only to be dissipated viscously by friction in the hub loss core. The investigated purge flow particle was found to do 60% less work on the rotor compared to a free stream particle.

Based on a statistical approach using the particle tracking tool the different flow structures involved in the rotor hub passage vortex were numerically weighted. It was found that approximately 10% to 20% of the flow in the hub passage vortex is coming from the rim seal cavity depending on the injection rate. This portion of the flow is responsible for the additional loss caused in the hub passage vortex due to the unsteady interaction mechanisms. The effect of the flow from inside the pressure side separation on the rotor hub passage vortex unsteadiness was found to be an order of magnitude smaller, as it only represents 1% to 3% of the flow in the hub passage vortex, depending on the amount of purge flow.



## 4. Unsteady Effects of Profiled Rotor End Walls

In this chapter the effect of non-axisymmetric rotor end wall contouring in the presence of purge flow is studied. The three experimentally investigated rotors are shrouded and two of them have non-axisymmetric end walls at the hub and on the shroud. The two end wall designs are presented and detailed in section 2.2.1. In this chapter the effects of the hub and shroud end wall profiling are analysed separately.

Measurements made with the rotor with cylindrical end walls and the rotor with the 1<sup>st</sup> non-axisymmetric end wall design are compared with each other in order to study the effect of the hub end wall profiling. Measurements are compared at the exit of the NGV1, the rotor and the NGV2 and CFD simulations are used to further detail the flow field at locations inaccessible for the measurement probes. These two rotors were chosen as they have identical rotor blade geometries and both have separated pressure sides at the operating point under investigation. The comparison to the rotor with the updated blade geometry and the 2<sup>nd</sup> non-axisymmetric end wall design is more complex as two beneficial effects are combined: the end wall design itself and the removal of the pressure side separation. The percentage of the change of the flow field due to the removal of the bubble can not clearly be isolated or quantified against the effect of the end wall profiling.

However on the shroud the effect of both tip end wall designs can be analysed since the pressure side separation has no influence on the flow field in the tip region at the rotor exit. Therefore measurements made with the cylindrical, 1<sup>st</sup> and 2<sup>nd</sup> shroud end wall design will be compared at the rotor exit. The effect of the shroud end wall profiling on the rotor inlet flow field is negligible and is therefore not covered in this chapter.

The analysis in this chapter is performed at the nominal injection rate ( $IR = 0.8\%$ ). The results for the other two injection rates are intentionally left out in order to explicitly isolate the effects caused by the end wall profiling in the absence of purge flow variations. The effects caused by the purge flow are analysed in the chapters 3 and 6.

## 4.1. Upstream Effects at the NGV1 Exit

The influence of the rotor hub and tip end wall profiling on the upstream flow field at the exit of the first nozzle guide vane can be expected to be small. However, as the end wall profiling at the rotor hub reaches up to the platform leading edge giving it a wavy shape (as shown in Figure 2.6), the unsteady interaction between the injected purge flow and the main flow field in this hub region is affected by the end wall profiling. The axial position of the probe traversing plane at NGV1 exit makes it possible for the probes to access into the upper rim seal cavity. Thus the effect of the hub end wall profiling in this region can be captured and will be analysed in this section.

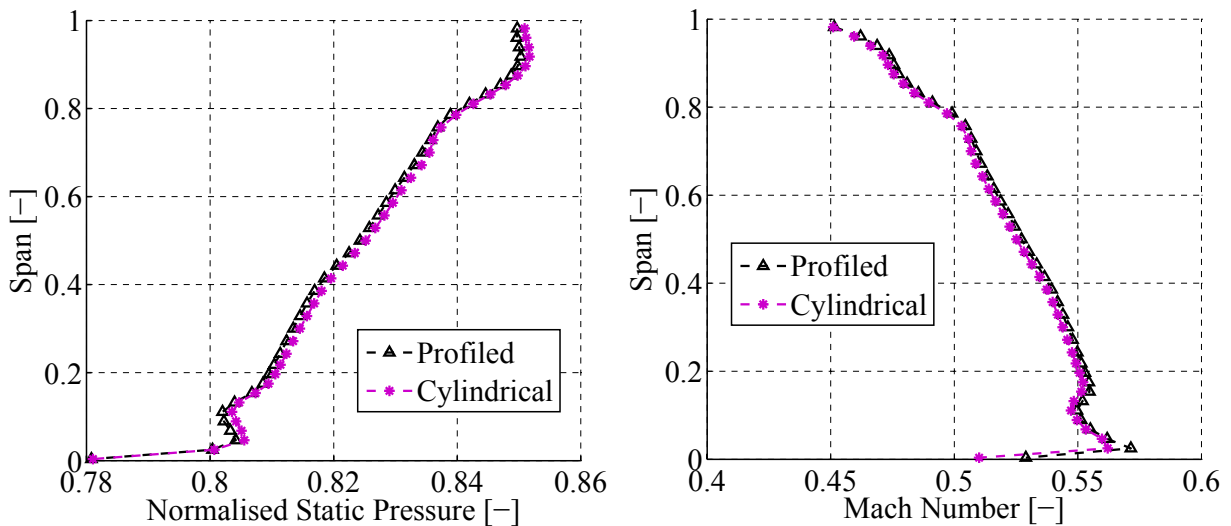


Figure 4.1.: Area and time-averaged measured normalised static pressure  $Cp_s$  and mass-averaged Mach number  $M$  for the nominal injection rate at the rotor inlet ( $IR = 0.8\%$ , 4-hole probe).

Figure 4.1 shows the measured radial distribution of circumferentially mass and time-averaged normalised static pressure and Mach number. The measurements were taken with the 4-hole probe. The measurements taken with two different rotor geometries are very consistent and show that the end wall profiling has no significant influence on the flow field at the rotor inlet. Above 10% span the relative differences of static pressure is below 0.15%. Due to the effect of the rotor hub end wall profiling the relative differences of  $Cp_s$  increase to maximum 0.25% below 10% span. The measurement uncertainty for the static pressure is defined with respect to the dynamic head (Table 2.5). The measured differences correspond to about 0.5% of the dynamic head in the free stream and peak at approximately

1% in the tip (above 90% span) and the hub region (below 10% span) with the rim seal cavity exit. In the free stream the differences are within the measurement uncertainties, in the boundary region they are at the limit of the measurement uncertainties. For the Mach number, the corresponding relative differences in the free stream are about 0.4% and peak at about 0.6% in the secondary flows.

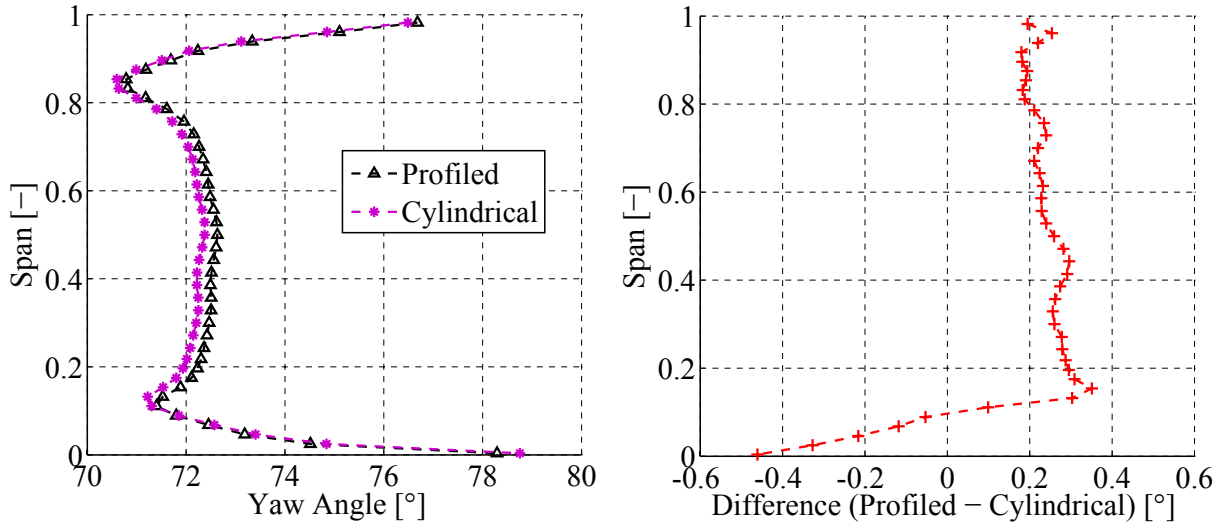


Figure 4.2.: Mass and time-averaged measured yaw angle with and without end wall profiling at the rotor inlet at the nominal injection rate ( $IR = 0.8\%$ , 4-hole probe).

Figure 4.2 compares the mass and time-averaged measured radial distribution of the yaw angle and the change of incidence at the rotor inlet with and without end wall profiling. Above 10% span the measured yaw differ between  $0.2^\circ$  and  $0.3^\circ$ . These numbers correspond to 0.66% and 1% of the yaw angle calibration range of the used 4-hole probe and therefore are slightly above the measurement uncertainty at an average Mach number of 0.5 (Table 2.5). Below 10% span the difference gradually drops by  $1^\circ$  and peaks at  $-0.7^\circ$  inside the rim seal ( $-3\%$  span). This relative change in yaw angle is above the measurement uncertainty. Although the difference in yaw angle appears to be slightly above the measurement uncertainty the rotor end wall profiling is not considered to significantly influence the rotor inlet flow field. One needs to bear in mind that the purge flow injection rate influences the static pressure and yaw angle at rotor inlet, as shown in section 3.1. The uncertainty related to the amount of purge flow injected during the two measurements with the different rotor geometries influences the static pressure at the rotor inlet and therefore needs to be taken into

consideration. Furthermore, the size of the bubble present on the rotor blade pressure sides at the chosen operating point is of smaller size in the presence of non-axisymmetric end walls (cf. chapter 5) and can therefore be expected to have an influence on the flow field at the rotor inlet. A certain part of the already small differences presented in this section are due to the variation of injected purge flow and the pressure side bubble size. Nevertheless, the measured effect of the end wall profiling at the rotor inlet stays within or very close to the measurement uncertainty bandwidth, except at very low spanwise positions where the end wall profiling interacts with the injected purge flow. The consistency in static pressure, Mach number and flow angle shows that the design of the non-axisymmetric end walls did not significantly change the rotor capacity. Thus the rest of this section will focus on the flow field at the exit of the rim seal.

## 4.2. Influence on Rim Seal Exit Cavity Flow

The influence of the rotor hub end wall profiling on the flow field in the cavity at the rim seal exit is analysed based on the time-accurate numerical predictions. Figure 4.3 shows the circumferentially area and time-averaged static pressure coefficient  $Cp_s$ , yaw angle, the circumferential velocity  $V_\theta$  and radial velocity  $V_r$  for the rotors with and without end wall profiling at the nominal injection rate ( $IR = 0.8\%$ ). The area-averaging was performed along a cylindrical surface at 0% span. The non-dimensional rim seal axial coordinate indicates the axial position along the rim seal. 0 non-dimensional rim seal axial coordinate indicates the end of the NGV hub platform, 1 the leading edge at the rotor hub platform, as defined in Figure 3.8. The symbols indicate the corresponding circumferentially averaged measured values at 0% span (4-hole probe). The exact axial position of the probe tip during the measurements at the cavity exit is not exactly known and estimated to be at 0.35 non-dimensional rim seal axial coordinate. The comparison to the measurements of the radial velocity  $V_r$  were intentionally omitted for the same reasons described in section 3.2. The data shown in Figure 4.3 was generated in the same manner as the data shown in Figure 3.6. Additional information about the data shown in Figure 4.3 and the related post-processing can be found in the corresponding section and is not repeated here.

The comparison between the circumferentially area averaged measurement and the simulation in Figure 4.3 shows a good agreement for the static

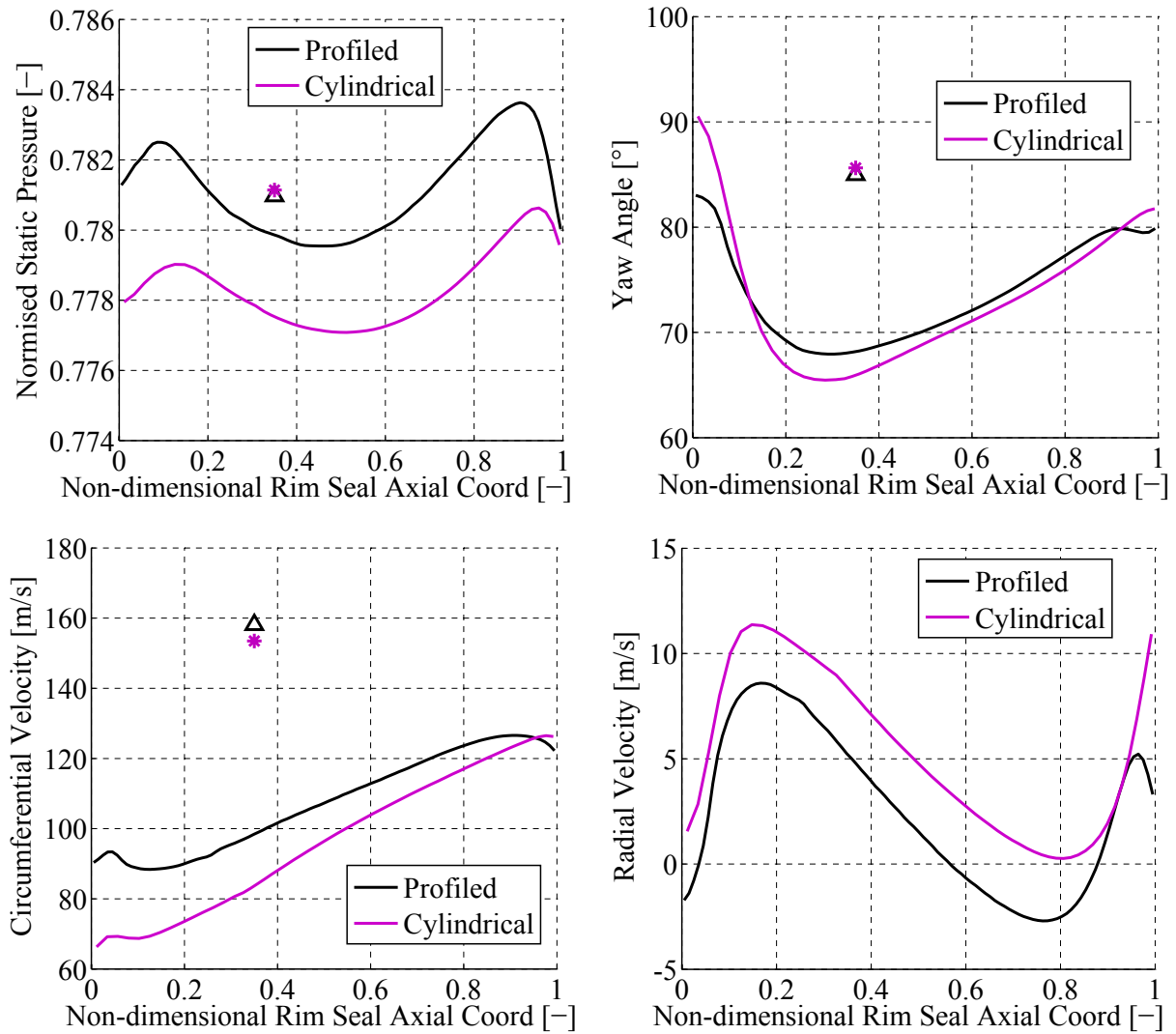


Figure 4.3.: Circumferentially area and time-averaged simulated  $Cp_s$ , yaw angle,  $V_\theta$  and  $V_r$  plotted against non-dimensional rim seal axial coordinate at the rim seal exit (0% span) with and without end wall profiling. Zero corresponds to the end of the NGV hub platform, one to the leading edge at the rotor hub platform. The symbols indicate the corresponding measurements. All the data shows the situation at the nominal injection rate ( $IR = 0.8\%$ ).

pressure at the rim seal exit in terms of absolute value. The simulation appears to underpredict the flow yaw angle and circumferential velocity. The flow yaw angle is underpredicted by approximately  $15^\circ$  to  $20^\circ$ , the circumferential velocity by 40% to 50% percents. However the difference of these two parameters between measurement and simulation is consistent. For a given net mass flow leaving the rim seal cavity, a lower flow yaw angle in the simulation must correlate with a reduced circumferential velocity, as  $V_\theta$  is the dominant velocity vector component. The simulation

with end wall profiling shows a bigger influence on the flow field than the corresponding measurements. Whilst the measurements show very low sensitivity to the end wall profiling, the simulations detect a more significant difference between the two end wall designs. Two zones are distinguished for the analysis, from 0 to 0.9 (zone 1) and between 0.9 and 1 (zone 2) non-dimensional rim seal axial coordinate.

In zone 1 the simulated trends of the plotted variables are very similar with and without end wall profiling, suggesting that the basic structures of the flow field are the same in both cases. More precisely, for the rotor with end wall profiling the simulation predicts a 0.25% higher static pressure, 2-3 m/s lower  $V_r$ , an increased  $V_\theta$  especially on the side closer to the NGV1 and slightly higher yaw angles in most of zone 1. For a given injected mass flow, the combination of higher radial velocity and lower circumferential velocity is consistent and indicates that the purge flow has more radial momentum when leaving the rim seal cavity in the absence of profiled end walls. From this point of view the end wall profiling positively reduces the loss generation opportunities and the radial momentum of the purge flow. The influence of the rotor can also be observed when looking at the axial distribution of the circumferential velocity. The closer to the rotor the higher its influence and therefore the higher the  $V_\theta$ .

In zone 2 the end wall profiling has a much higher influence on the flow field due to the proximity of the rotor. In this zone the end wall profiling appears to reduce yaw angle, static pressure and circumferential velocity more significantly compared to the axisymmetric case. The impact of the end wall profiling on the radial velocity can be clearly seen, the simulated  $V_r$  is halved in zone 2 in the presence of end wall profiling. The end wall profiling enables the purge flow to leave the rim seal cavity in a more axial direction at lower spanwise position and along the hub end wall. As a consequence the radial velocity of the purge flow in zone 2 and the resulting mixing losses in the main flow can be reduced. It is interesting to note that with cylindrical end walls the radial velocity distribution along the rim seal exit never falls below zero. In the time-averaged view there must always be a net mass flow leaving the rim seal cavity. For both rotor geometries the axial distribution of  $V_r$  in Figure 4.3 indicates that there are two axial zones where the purge flow is leaving the rim seal cavity, between 0.05 and 0.6 and between 0.9 and 1 non-dimensional axial rim seal coordinate.

The axial distributions of the normalised net mass flow at the rim seal exit for the two rotor geometries shown in Figure 4.4 confirm the trends of the radial velocities. The normalised mass flow shown in Figure 4.4 is

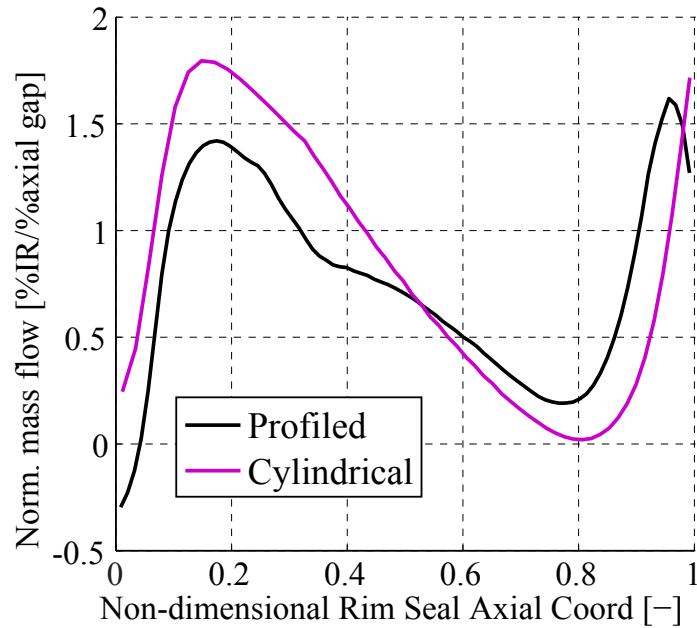


Figure 4.4.: Circumferential integral of the simulated normalised mass flow at the rim seal exit (0% span) with and without end wall profiling ( $IR = 0.8\%$ ).

given as a percentage of injection rate per percent of non-dimensional axial coordinate. In other words the surface under the two curves is equal to 0.8. As investigated in section 3.1 there is a toroidal vortex present in the rim seal cavity above the rim seal lip, shown by the schematic in Figure 3.8. With cylindrical end walls the peak in normalised mass flow between 0.05 and 0.6 non-dimensional axial coordinate is approximately 30% higher. The minimum mass flow at about 0.8 non-dimensional axial rim seal coordinate reaches zero net mass flow for the axisymmetric case, but stays at about 0.25 for the non-axisymmetric case. Due to the area-averaging procedure the negative circumferentially area and time-averaged radial velocity between 0.55 and 0.85 non-dimensional axial coordinate with end wall profiling (Figure 4.3) does not conflict with the positive net mass flow in this region (Figure 4.4). If the radial velocity was circumferentially mass-averaged, it could not become negative. The area-averaging procedure is required for the reasons described in section 3.2. When considering the net mass flow distribution at the rim seal exit, the end wall profiling appears to reduce the strength of the toroidal vortex in the rim seal cavity. Furthermore, the wavy shape of the rotor hub platform leading edge due to the end wall profiling enables a larger amount of purge flow to leave the cavity between 0.9 and 1 non-dimensional axial rim seal coordinate, but at a lower radial velocity and increased axial velocity.

A more detailed picture can be gained when considering the time-resolved

measurements at the cavity exit provided by the FRAP. Figure 4.5 shows two space time plots at 1% span for the rotors with cylindrical and profiled end walls at the nominal injection rate. The variable is the experimental *rms* of the total pressure, as defined in Equation 2.24. The spatial dimension on the x-axis is the circumferential coordinate in the absolute frame of reference. The vertical zone of high *rms* between 0.6 and 0.8 stator pitch is the signature of the NGV wake and hub passage vortex, as already observed in Figure 3.4. The interaction between the injected purge flow and the rotor potential field creates three inclined zones of elevated *rms* containing each a patch of strongly increased *rms* between 0.2 and 0.4 stator pitch. This is the circumferential region where most of the purge flow leaves the rim seal cavity, triggered by the rotor movement as observed in section 3.1. The inclined zones of elevated *rms* must be related to the rotor as they are changing circumferential coordinate with time. The time axis covers three rotor blade passing events, suggesting that these zones are related to one rotor blade each.

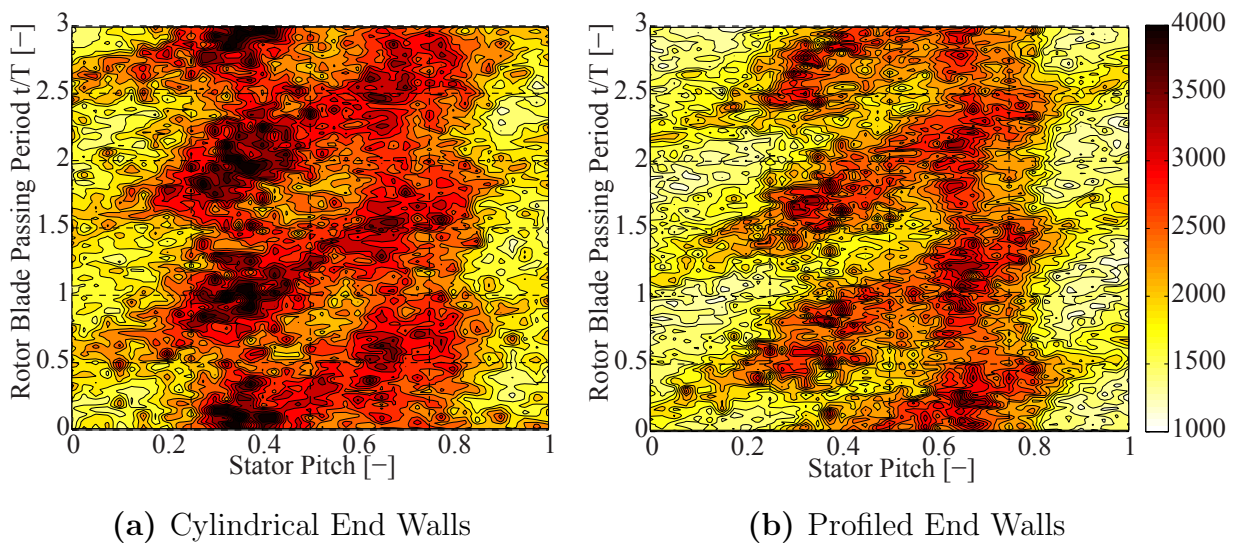


Figure 4.5.: Space time plot in absolute frame of reference of the experimental *rms* of the total pressure [Pa] at 1% span with and without end wall profiling at the rotor inlet ( $IR = 0.8\%$ , FRAP).

The comparison of the two space time plots in Figure 4.5 shows that the overall level of unsteadiness at the rim seal exit decreases in the presence of profiled rotor end walls. With cylindrical end walls the unsteadiness is significantly higher in the vertically stacked patches of increased *rms* between 0.2 and 0.4 stator pitch. With profiled end walls the purge flow appears to create less turbulence and loss at the cavity exit when injected into the

main flow. These findings are confirmed by the space time plots at 1% span of the normalised total pressure  $Cp_t$  shown in Figure 4.6. The vertical low total pressure feature between 0.7 and 0.8 stator pitch is caused by the wake of the nozzle guide vane and is not affected by the end wall profiling. As for the space time plots of the experimental *rms* of the total pressure, there are inclined region of reduced total pressure caused by the interaction of the rotor and the purge flow. When comparing Figures 4.5 and 4.6 one can see that the zones of increased *rms* between 0.2 and 0.4 stator pitch with cylindrical end walls are correlated with the zones of reduced normalised total pressure. The end wall profiling successfully reduces the total pressure deficit and the unsteadiness at the rim seal cavity exit when the purge flow is injected and therefore has a positive effect on how the purge flow joins the main flow.

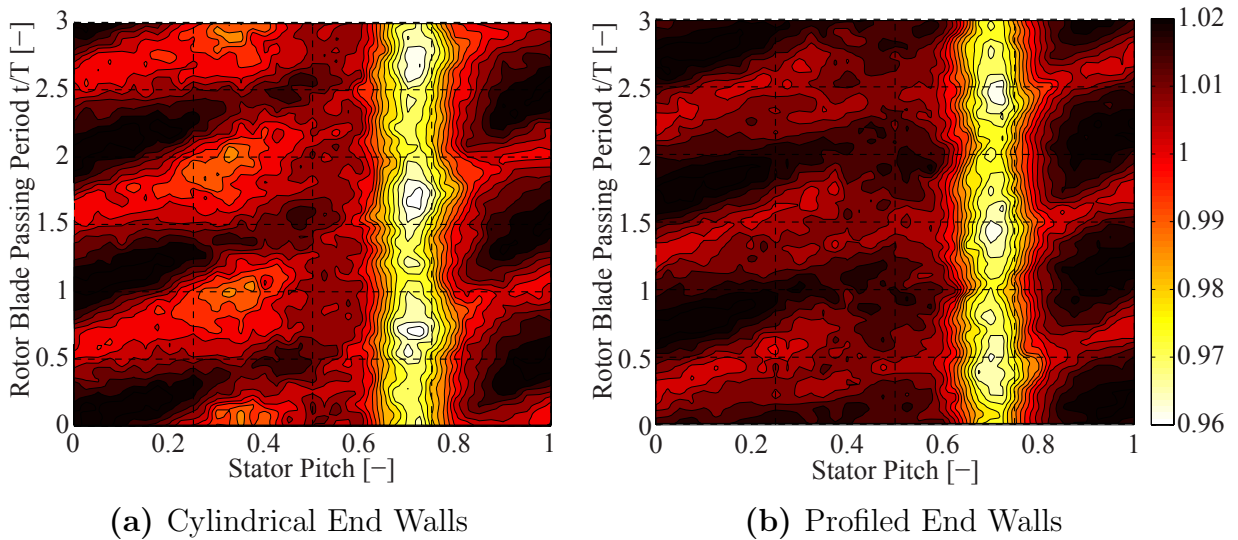


Figure 4.6.: Space time plot in absolute frame of reference of the normalised total pressure  $Cp_t$  [-] at 1% span with and without end wall profiling at the rotor inlet ( $IR = 0.8\%$ , FRAP).

### 4.3. Effects of Profiled Hub End Wall at the Rotor Exit

The effect of the end wall profiling of the flow field at the rotor exit is studied in this section. In a first part the effect of the non-axisymmetric end walls at the hub end wall are analysed. The measurements made with cylindrical end walls are compared to the 1<sup>st</sup> design of shaped end walls.

Figure 4.7 shows the radial distributions of the circumferentially mass and time-averaged relative flow yaw angle and circumferential velocity  $V_{\theta,rel}$  at the exit of the rotor at nominal injection rate with and without end wall profiling. The strong radial gradients of relative yaw angle and  $V_{\theta,rel}$  between 10% and 60% span are indicative of strong axial and streamwise vorticity (Equations 2.26 and 2.25). The strong variations of relative yaw angle and circumferential velocity are caused by the rotor hub passage vortex which is dominating the flow field at these spanwise regions. Firstly the rotor end wall profiling successfully reduces these radial gradients and resulting vorticity in the rotor hub passage vortex. The difference between measured maximum and minimum time-averaged relative flow yaw angle decreases by  $5^\circ$ , from  $18^\circ$  to  $13^\circ$ , in the presence of non-axisymmetric end walls. In terms of relative circumferential velocity the corresponding difference reduces by 25%. Secondly, the end wall profiling reduces the radial

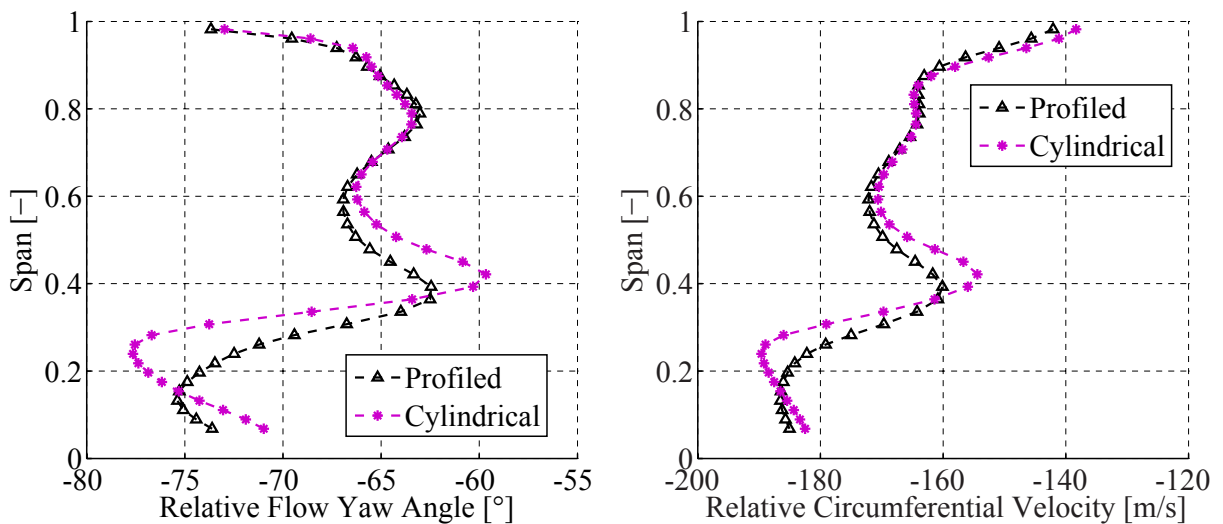


Figure 4.7.: Mass and time-averaged measured relative flow yaw angle and and relative circumferential velocity  $V_{\theta,rel}$  with and without end wall profiling at the rotor exit ( $IR = 0.8\%$ , 5-hole probe).

migration of the hub loss core. Assuming the centre of the hub loss core in the middle between the maximum and minimum relative flow yaw angle, the radial height of the rotor hub passage vortex decreases by approximately 5% span under the effects of the rotor end wall profiling. The mass and time-averaged radial distributions in Figure 4.7 show that the rotor hub end wall profiling causes modifications to the measured flow field up to approximately 65% span. The purge flow was found to influence the flow field at the rotor exit (section 3.3) up to the same spanwise position. Above

this radial height the relative flow yaw angle and  $V_{\theta,rel}$  is not significantly affected by the non-axisymmetric end wall profiling. However the relative circumferential velocity slightly reduces above 90% span in the presence of the end wall profiling on the shroud. The effect of the end wall profiling on the shroud is discussed in section 4.4.

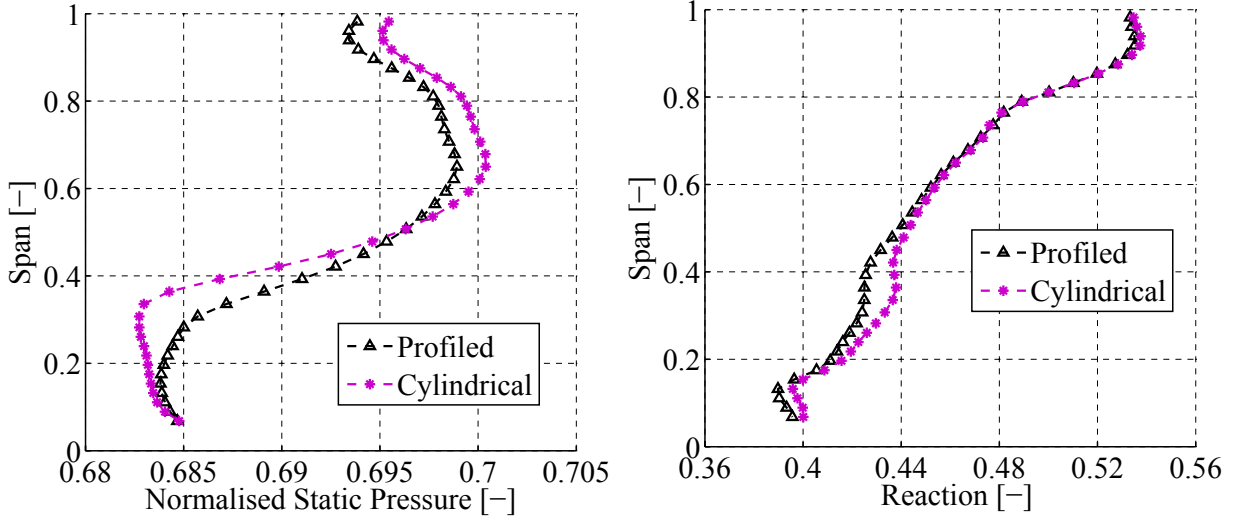


Figure 4.8.: Mass and time-averaged measured normalised static pressure  $Cp_s$  and reaction  $R$  with and without end wall profiling at the rotor exit ( $IR = 0.8\%$ , 5-hole probe).

Figure 4.8 compares the circumferentially area and time-averaged static pressure  $Cp_s$  and the reaction with and without end wall profiling. The measurements were made at the nominal injection rate with the 5-hole probe. The reaction  $R$  is calculated based on the pressure measurements at turbine inlet, NGV1 exit and rotor exit, given in Equation 4.1:

$$R = \frac{P_{s,NGV1ex} - P_{s,R1ex}}{P_{s,Inlet} - P_{s,R1ex}} = \frac{Cp_{s,NGV1ex} - Cp_{s,R1ex}}{\frac{P_{s,Inlet}}{P_{t,Inlet}} - Cp_{s,R1ex}} \quad (4.1)$$

The radial distribution of  $Cp_{s,NGV1ex}$  is shown in Figure 4.1, the radial distribution of  $Cp_{s,R1ex}$  in Figure 4.8. As the turbine pressure ratio was constant during all the measurements, the ratio of static and total inlet pressure in Equation 4.1 is a constant. The measurements show that the end wall profiling has no significant influence on the reaction above 50% span ( $<0.2\%$ ). Below this radial height the end wall profiling slightly reduces the reaction. The maximum measured absolute difference is  $-1.3\%$  at 36% span. The average reaction of all measured radial positions reduces by  $0.4\%$  (abs.) in the presence of end wall profiling. When comparing the

radial distributions of static pressure at rotor inlet (Figure 4.1) and rotor exit (Figure 4.8), one can see that the difference in reaction is driven by the change of static pressure at the rotor exit. With profiled rotor end walls the static pressure decreases for positions above 50% span, but increases in the loss core region below 50% span, slightly reducing the reaction for these spanwise positions containing the rotor hub secondary flows. Given the facts that the end wall profiling does not change the capacity (cf. section 4.1) of the turbine, only slightly reduces the overall reaction at the chosen operating point and the turbine pressure ratio is constant, the measured efficiency variations can be considered as relevant.

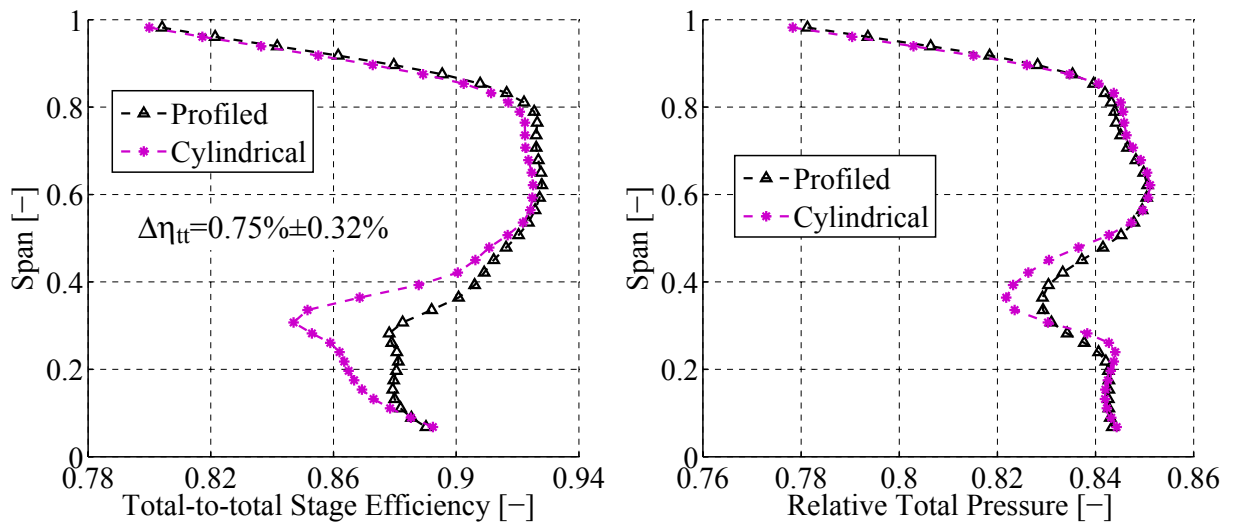


Figure 4.9.: Mass and time-averaged measured total-to-total stage efficiency  $\eta_{tt}$  and normalised relative total pressure  $Cp_{t,rel}$  with and without end wall profiling at the rotor exit ( $IR = 0.8\%$ , 5-hole probe).

Figure 4.9 details the impact of the end wall profiling on the radial distributions of the circumferentially mass and time-averaged total-to-total stage efficiency  $\eta_{tt}$  at the rotor exit (5-hole probe). The definition of the  $\eta_{tt}$  is given in Equation 2.23. The end wall profiling increases the efficiency at nearly all spanwise positions. However the significant efficiency improvement is located between 10% span and 50% span. In the presence of non-axisymmetric end walls the negative impact of the rotor hub passage vortex on the efficiency is significantly reduced. At 36% span the absolute efficiency difference peaks at 4%. At nominal injection rate a mass weighted integral over one stator pitch of the total-to-total stage efficiency increases by  $0.75\% \pm 0.32\%$  in the presence of end wall profiling. The effect of the end wall profiling on the sensitivity of the  $\eta_{tt}$  to purge flow is analysed in

chapter 6. The reduced loss in the hub passage vortex is clearly the main reason for this significant efficiency improvement. The positive effect of the rotor end wall profiling is also reflected in the radial distribution of the time and mass-averaged normalised relative total pressure  $Cp_{t,rel}$  shown in Figure 4.9. The minimum mass and time-averaged relative total pressure in the trough caused by the rotor hub loss core reduces by approximately 1% due to the beneficial effect of the end wall profiling. The radial distribution of  $Cp_{t,rel}$  confirms the reduced radial migration of the hub loss core due to the end wall profiling, as already shown by the radial distributions of relative flow angle and circumferential velocity.

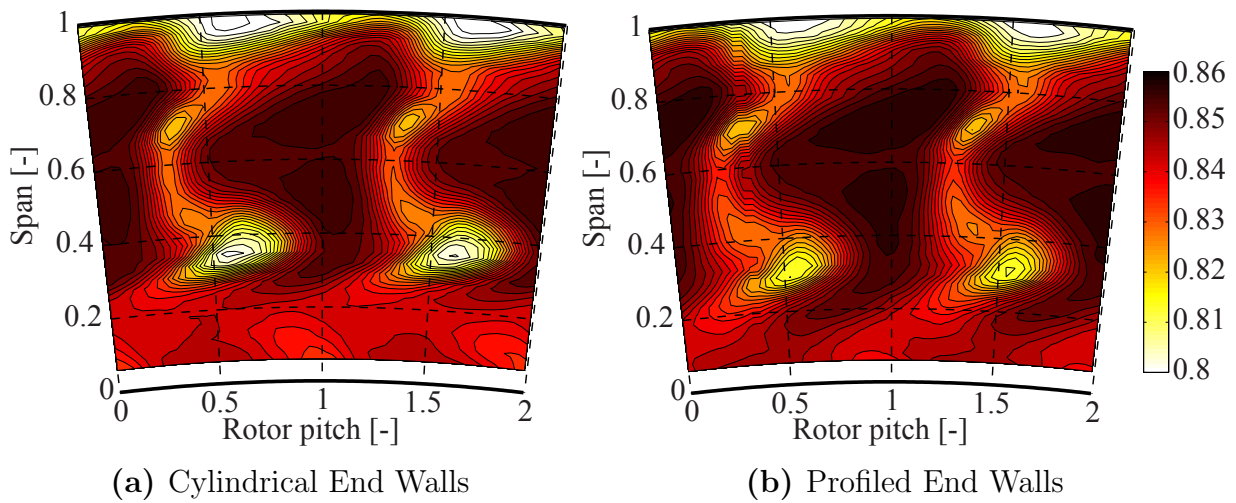


Figure 4.10.: Time-averaged area plots in rotor relative frame of reference at the rotor exit. The parameter is the normalised relative total pressure  $Cp_{t,rel}$  [-] at the nominal injection rate ( $IR = 0.8\%$ , FRAP).

The radial distribution of the relative total pressure can be analysed more precisely when considering the corresponding area plots in the rotor frame of reference shown in Figure 4.10. Time-resolved data is required in order to generate contour plots of any parameter in the relative frame, therefore Figure 4.10 shows FRAP measurements. The salient flow features present in these two area plots are described in the text related to Figure 3.16. The contour plots of the  $Cp_{t,rel}$  show that the reduction of relative total pressure observed in the radial distributions between 20% and 50% span is due to a significant reduction of the  $Cp_{t,rel}$  in the centre of the hub passage vortex. The hub end wall profiling successfully limits the total pressure loss in the core of the hub passage vortex. The end wall profiling is assumed to influence the formation of the hub passage vortex within the rotor blade row in a beneficial manner. Furthermore, the  $Cp_{t,rel}$  in the free stream region

between the rotor wakes is slightly higher with profiled end walls, explaining the slight increase of relative total pressure between 60% and 90% span in the corresponding radial distribution. For the rotor with cylindrical end walls there is a zone of relatively uniform relative total pressure below the hub loss cores. In the presence of profiled end walls this zone below 20% span becomes more structured by the rotor hub secondary flows.

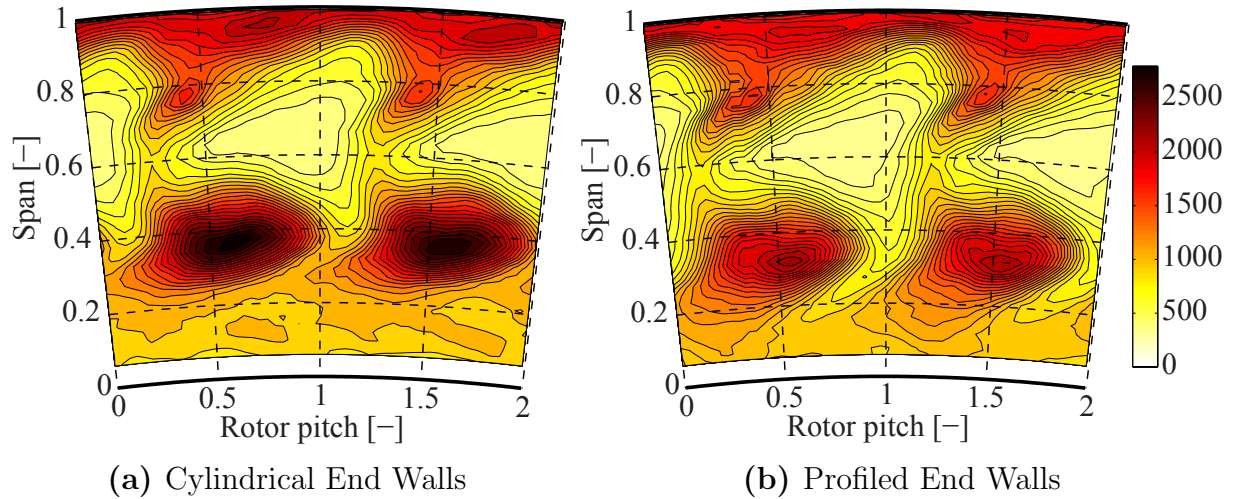


Figure 4.11.: Time-averaged area plots in rotor relative frame of reference at the rotor exit. The parameter is the  $rms$  of the relative total pressure [Pa] at the nominal injection rate ( $IR = 0.8\%$ , FRAP).

Figure 4.11 shows the effect of the end wall profiling on the experimental (FRAP)  $rms$  of the relative total pressure random part in terms of time-averaged contour plots in the rotor frame of reference at the rotor exit. The  $rms$  is evaluated according to Equation 2.24. The salient secondary flow structures in Figure 4.11 are identified and described in the context of Figure 3.16. Regions of low relative total pressure correlate with regions of elevated  $rms$ . The reduction of the non-deterministic unsteadiness in the rotor hub passage vortex due to the end wall profiling is obvious and significant. At the nominal injection rate the maximum measured  $rms$  value in the hub passage vortex reduces by 25% in the presence of profiled end walls. A mass-weighted integral of the  $rms$  distribution between 25% and 60% span decrease by 30% due to the end wall profiling. Considering an integral over one entire rotor pitch and hub to casing, the overall level of  $rms$  decreases by approximately 12%. The underlying mechanisms reducing the non-deterministic unsteadiness in the rotor hub loss core are complex and are thought to be partially related with the reduced radial migration and vorticity of the hub loss core caused by the end wall profiling. In contrast

to the hub vorticies the *rms* signatures of the free stream region, the rotor wakes and the tip passage vortex remain unaffected by the end wall profiling. However the end wall profiling at the shroud has a slight positive effect on the unsteadiness in the tip region. The circumferentially mass and time-averaged experimental *rms* of the relative total pressure shown in Figure 4.12 reduces above 90% span due to the non-axisymmetric shroud end wall. The effect of the shroud end wall profiling is further detailed in section 4.4. The radial distribution of the experimental *rms* reveals that the unsteadiness of the hub loss core is mainly reduced in the upper part of the hub passage vortex. It is interesting to observe that the circumferentially time-averaged level of *rms* below the rotor hub loss core (below 20% span) remains nearly unaffected by the end wall profiling, despite the spatial proximity to the rotor hub end wall profiling.

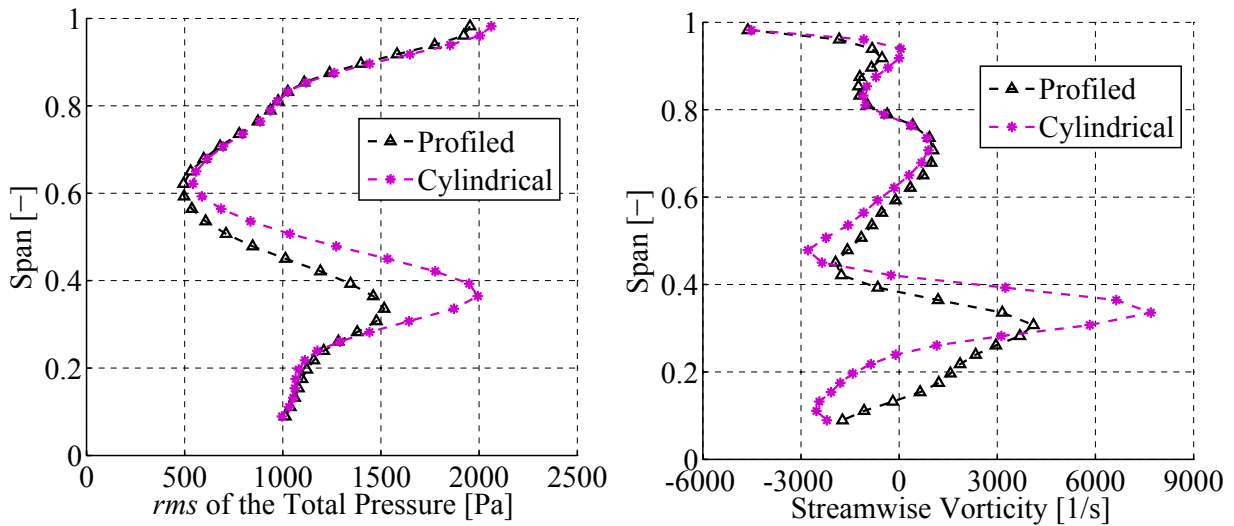


Figure 4.12.: Mass and time-averaged measured *rms* of the relative total pressure and the streamwise vorticity  $\Omega_S$  with and without end wall profiling at the rotor exit ( $IR = 0.8\%$ , FRAP).

The radial distribution of circumferentially mass and time-averaged streamwise vorticity  $\Omega_S$  measured at the exit of the rotors with and without end wall profiling is shown in Figure 4.12. The streamwise vorticity was calculated as the scalar product of the primary flow vector and the vorticity vector whose components are given in Equation 2.25. The  $\Omega_S$  for the rotor with cylindrical end walls is clearly higher when compared to the rotor with profiled end walls. The high streamwise vorticity flow appears to be concentrated in a limited spanwise region at a higher radial position. The maximum circumferentially mass and time-averaged streamwise vorticity

nearly doubles in the absence of end wall profiling. Assuming the centre of the hub loss core to be at the spanwise position of maximum streamwise vorticity, the end wall profiling reduces its measured radial migration by 5% span. The analysis of the relative flow yaw angle and circumferential velocity (Figure 4.7) based on pneumatic 5-hole probe measurements led to the same finding. Figure 4.13 adds the second dimension to the radial distribu-

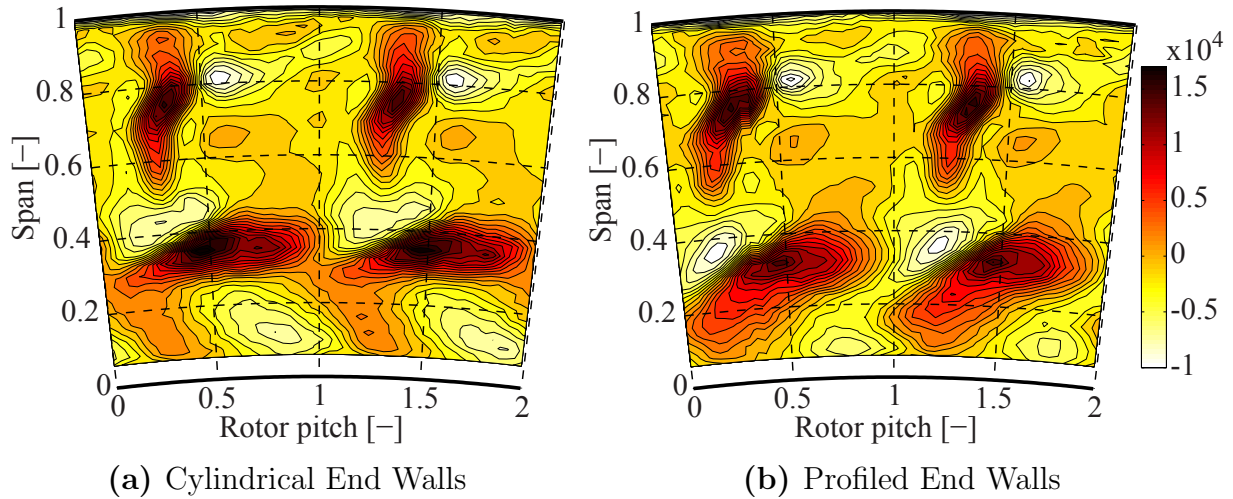


Figure 4.13.: Time-averaged area plots in rotor relative frame of reference at the rotor exit. The parameter is the streamwise vorticity [1/s] at the nominal injection rate ( $IR = 0.8\%$ , FRAP).

tions and shows the corresponding time-averaged two-dimensional contour plots of  $\Omega_S$  at the rotor exit in the rotor frame of reference. The high and low streamwise vorticity features in Figure 4.13 are related to the rotor exit secondary flow and have been described in the text related to Figure 3.21. In the presence of end wall profiling the vorticity transported in the rotor hub passage vortex not only concentrates in a limited spanwise region but also becomes stretched in the circumferential direction. The elevated  $\Omega_S$  is confined in a smaller region with an oval shape. The higher concentration of streamwise vorticity with cylindrical end walls considerably pushes up the maximum vorticity in the core. Consequently, the hub passage vortex rotates faster thereby creating increased loss and increased unsteadiness as shown in Figure 4.11. The static pressure in the core of the vortex has to drop in order to hold this vortical structure together. Thus the rotor hub passage vortex attracts and concentrates in its core more low momentum fluid from its vicinity with cylindrical end walls. The streamwise vorticity variations related to the other secondary flow structures at the rotor exit do not appear to be significantly affected by the end wall profiling. Only

the negative streamwise vorticity associated with the hub trailing edge shed vorticity further decreases in the presence of end wall profiling. In order to quantify the strength of the hub passage vortex, its circulation has been evaluated as an area integral of  $\Omega_S$  inside an iso-contour of zero streamwise vorticity as defined in Equation 2.29. The calculated circulation based on the time-averaged streamwise vorticity decreases by approximately 4% in the presence of non-axisymmetric end walls. The comparison of this value to the decrease of maximum streamwise vorticity enforces the conclusion that the streamwise vorticity is more concentrated with cylindrical end walls. The end wall profiling redistributes the hub loss core vorticity but does not significantly reduce its strength.

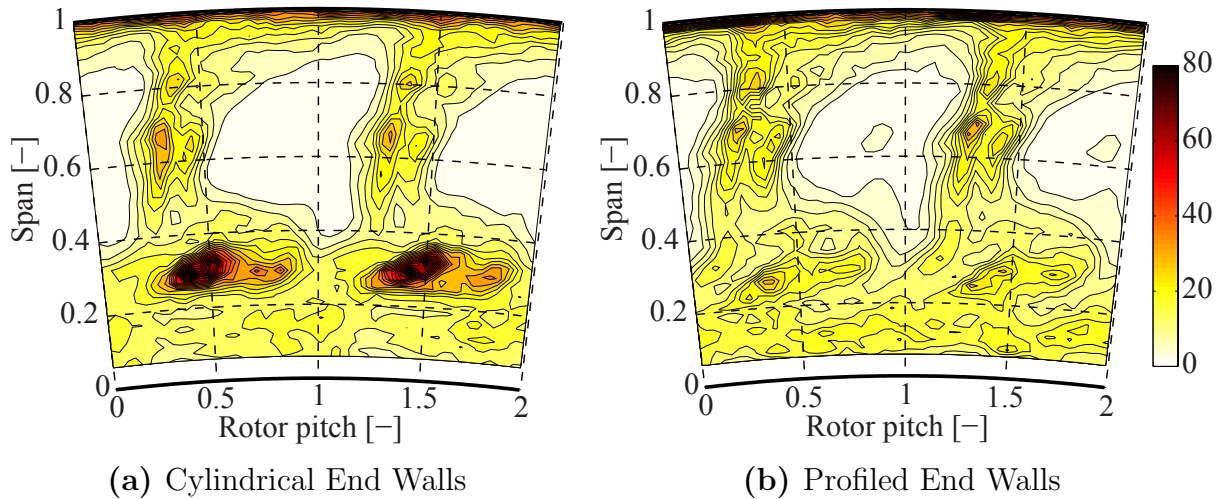


Figure 4.14.: Time-averaged area plots in rotor relative frame of reference at the rotor exit. The parameter is the dissipation [%/s] at the nominal injection rate ( $IR = 0.8\%$ , FRAP).

An interesting variable to consider when analysing the effects of the end wall profiling is the dissipation. Figure 4.14 shows the effect of the end wall profiling on the dissipation in terms of time-averaged contour plots in the rotor frame of reference at the rotor exit. The dissipation function has been evaluated using Equation 2.30 and can be interpreted as the percentage rate at which kinetic energy is converted into heat per second. The assumptions made during the calculation of the dissipation function and the carefulness required when interpreting the variable are presented and discussed in section 2.4.8. The non-axisymmetric rotor end wall profiling considerably reduces the dissipation function in the rotor hub loss core, a good indication for loss reduction. With profiled end walls the maximum measured dissipation in the core of the hub passage vortex is approximately

2-3 times lower. The end wall profiling successfully reduces the dissipation in the hub loss core to approximately the same level as in the rotor wake and tip passage vortices, the rest of the flow field being unaffected. The high dissipation region confined to the casing is expected to be mainly caused by the flow leaving the shroud cavity, a potentially beneficial effect from the shroud end wall profiling disappears. The considerable reduction of dissipa-

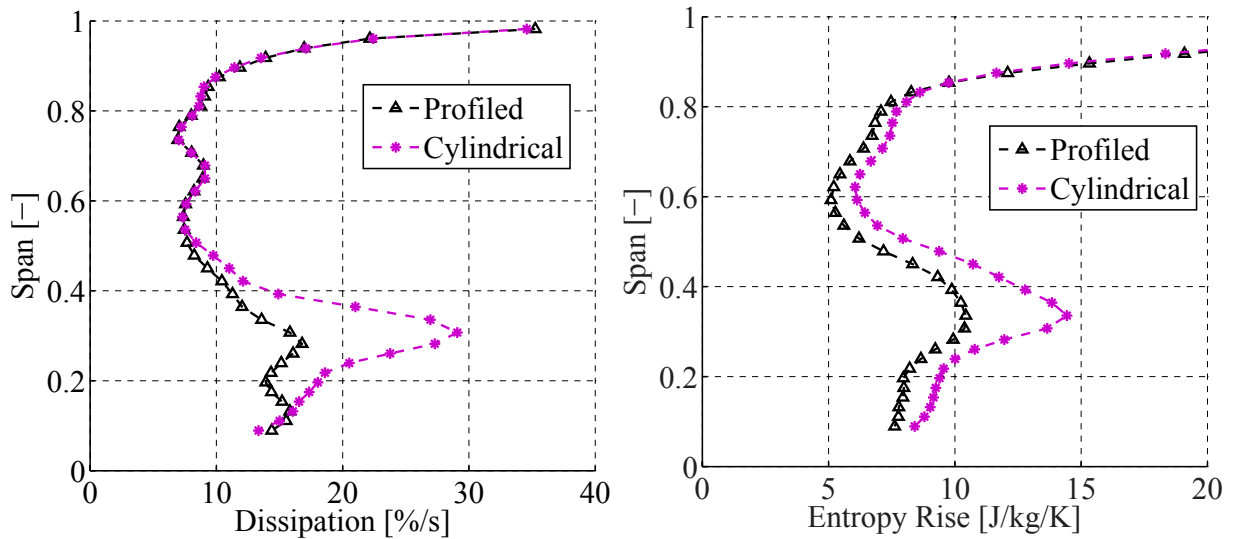


Figure 4.15.: Mass and time-averaged measured dissipation (FRAP) and entropy rise (FENT) with and without end wall profiling at the rotor exit ( $IR = 0.8\%$ ).

tion in the hub loss core due to non-axisymmetric end walls is also reflected in the radial distribution of circumferentially mass and time-averaged dissipation function shown in Figure 4.15. A mass weighted integral between 10% and 50% span decreases by 25% in the presence of profiled end walls. The circumferentially mass and time-averaged radial distribution of entropy rise provided by the FENT probe is also shown in Figure 4.15. The entropy rise was evaluated as defined in Equation 2.34 using the total turbine inlet conditions as reference conditions. Unlike for other flow parameters the effect of the shaped end walls affects the entropy at all spanwise positions. The entropy is reduced from the casing up to spanwise positions of 85% span, whereas the flow parameters investigated so far typically only significantly influence the hub loss core regions between 20% and 60% span. A mass weighted integral of the entropy between 60% and 85% span or between the casing and 20% span decreases by 10% and 12% respectively with profiled rotor end walls. When considering the corresponding time-averaged area plots of entropy in the rotor frame of reference shown in Figure 4.16, it can be seen that the increase of entropy in the regions between the casing

and 20% span and between 60% and 80% span occurs for all circumferential coordinates. The free stream entropy level is also slightly reduced by the end wall profiling. In the rotor hub loss core the end wall profiling

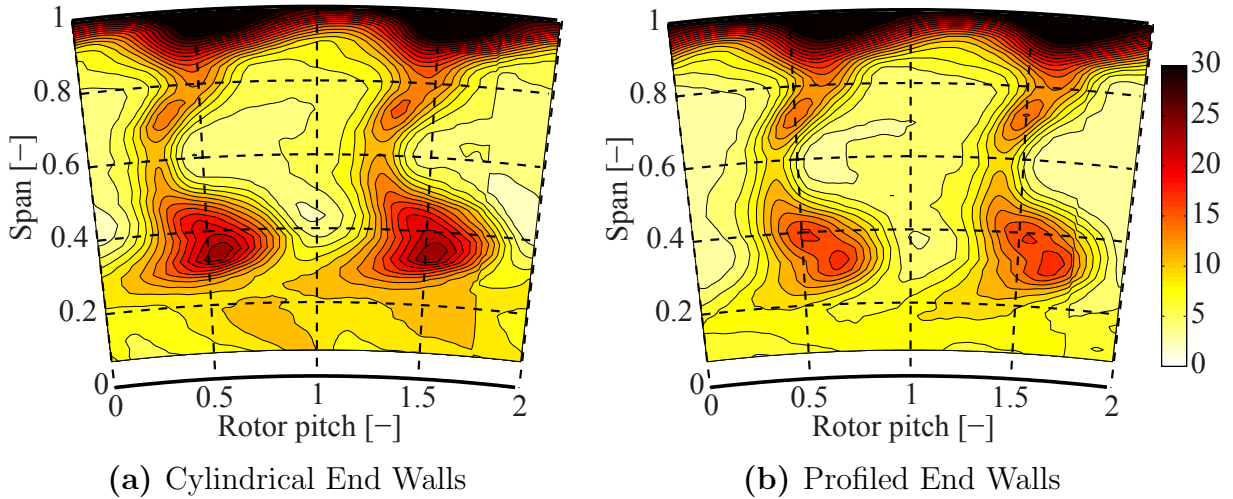


Figure 4.16.: Time-averaged area plots in rotor relative frame of reference at the rotor exit. The parameter is the entropy rise [J/kg/K] compared to the total inlet conditions at the nominal injection rate ( $IR = 0.8\%$ , FENT).

successfully reduces the generated entropy. The maximum measured time-averaged entropy in the rotor hub passage vortex decreases by nearly 30% in the presence of end wall profiling. The entropy reduction in the region between 60% and 80% span due to the profiled end walls can be further investigated when space time plots are considered. Figure 4.17 compares two space time plots of the unsteady entropy rise at 64% span with and without end wall profiling. This spanwise position is chosen in order to cut through the rotor wakes between the hub and tip passage vortices without being influenced by them (cf. Figure 4.16). The inclined high entropy zones are the signature of the rotor wakes, a moving flow element in the stationary frame of reference. The vertically stacked zones of elevated entropy between  $-0.1$  and  $0.25$  stator pitch are caused by the wakes of the first nozzle guide vane, a stationary object with regard to time. When considering the non-deterministic unsteadiness of the relative total pressure, the wake flow from the first nozzle guide vane crosses the measurement plane at the rotor exit between  $-0.25$  and  $0$  stator pitch, as shown in Figure 3.23. The circumferential coordinate of the NGV2 leading edge can be defined when considering the space time plot of static pressure shown in Figure 7.2. The maximum potential effect of the NGV2 is observed at approximately  $0.05$  stator pitch. The elevated entropy zones in Figure 4.17 appear to be the

result of the interaction between the wake of the first nozzle guide and the potential field of the second nozzle guide vane.

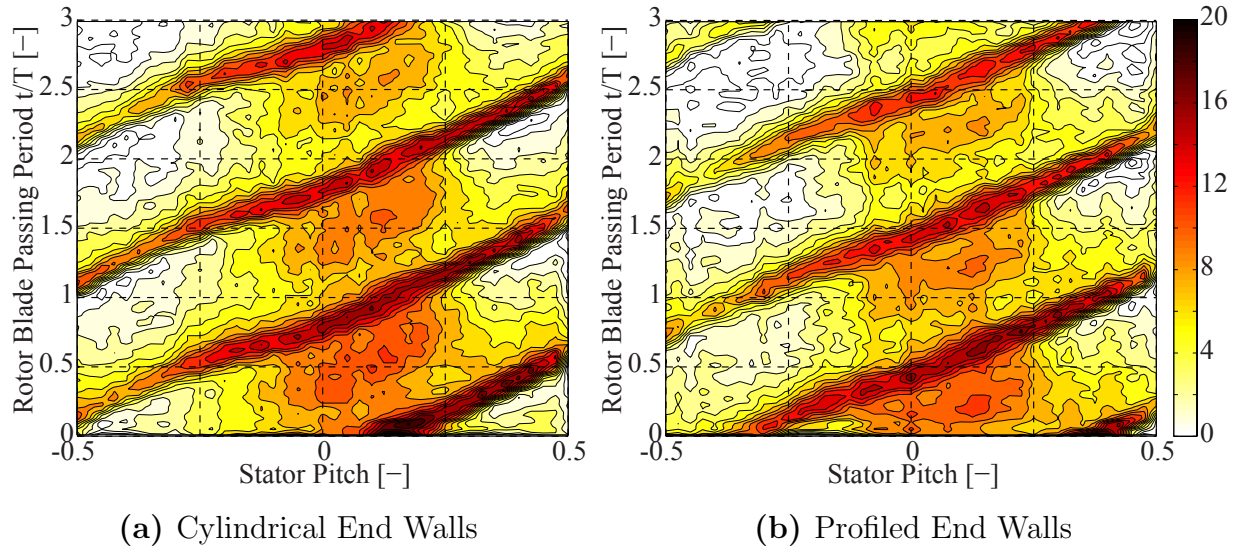


Figure 4.17.: Space time plot in absolute frame of reference of the measured unsteady entropy rise [J/kg/K] at 64% span with and without end wall profiling at the rotor exit ( $IR = 0.8\%$ , FENT).

The direct comparison of the two space time plots in Figure 4.16 does not indicate a clear region or flow feature causing the difference in measured entropy at this spanwise position. The end wall profiling appears to reduce the entropy level mainly in the rotor wakes and the free stream region between the wakes. The signature of the downstream nozzle guide vane is less affected by the end wall profiling. Especially the free stream region between  $-0.5$  and  $-0.1$  stator pitch shows a reduction in entropy rise. Furthermore, the entropy in the rotor wake between  $0.25$  and  $0.5$  stator pitch is reduced in the presence of shaped end walls. The combination of these different improvements in terms of entropy results in the mass and time-averaged entropy reduction at 64% span shown in Figure 4.15. The gradient of the inclined high entropy features in the time space plot corresponds to the circumferential velocity of the rotor wake. A steeper gradient corresponds to slower circumferential velocity (less distance per time). Without cylindrical end walls the rotor wakes have a kink at about  $-0.2$  stator pitch and on either side of the kink the gradient is different. Therefore the circumferential velocity of the rotor wake is not constant indicating varying lift on the rotor airfoil at this spanwise position. The end wall profiling appears to reduce this effect that occurs at the same circumferential location for all the rotor wakes.

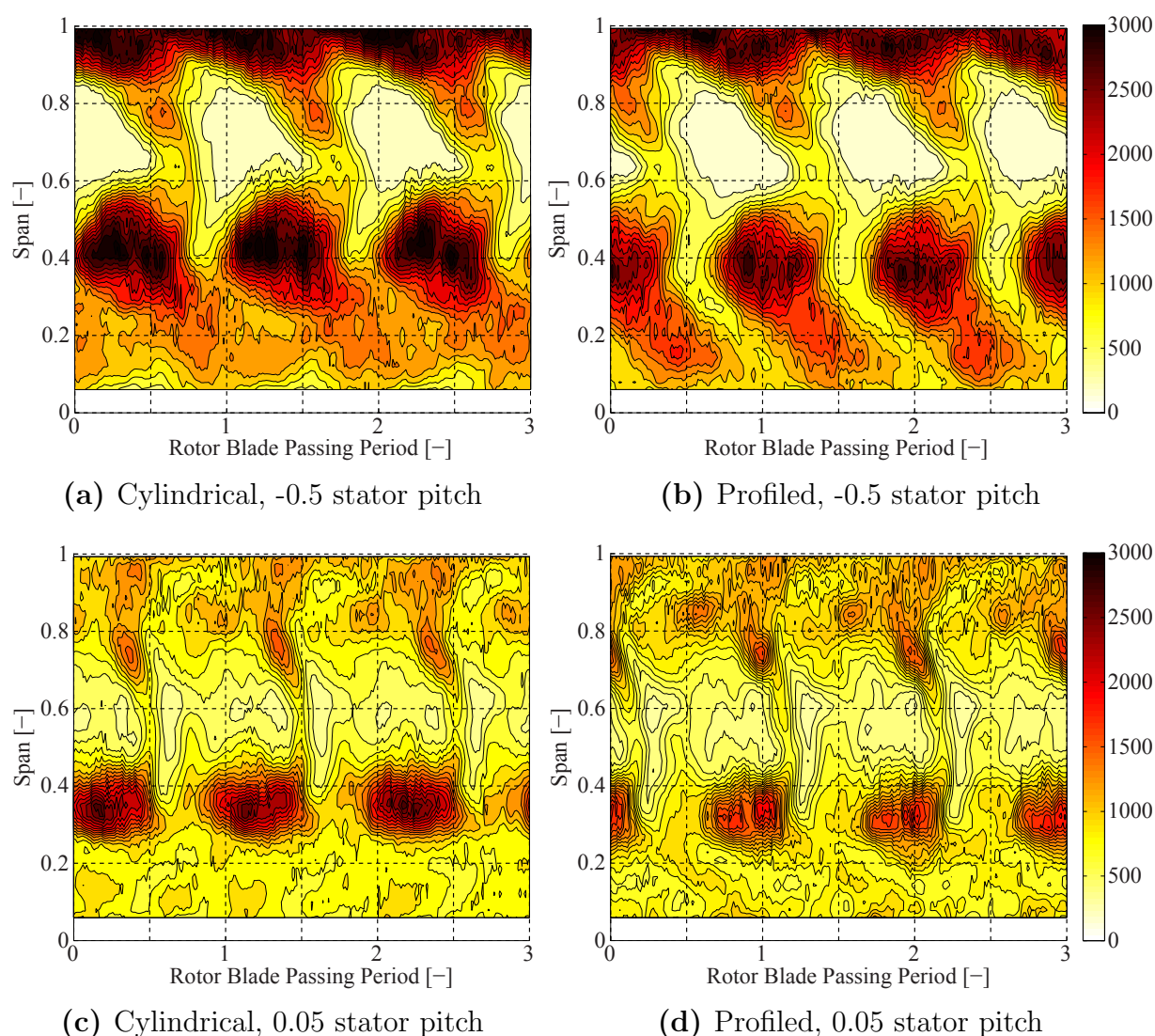


Figure 4.18.: Time space plots of the experimental *rms* of the relative total pressure [Pa] at two circumferential locations (-0.5 and 0.05 stator pitch) at the rotor exit with and without end wall profiling ( $IR = 0.8\%$ , FRAP).

Figure 4.18 shows the *rms* of the relative total pressure in the form of time space plots in the absolute frame at the rotor exit. Measurements made at -0.5 and 0.05 stator pitch with cylindrical (left column) and profiled (right column) end walls are shown. The circumferential position of the two chosen traverses can be put into context with the help of Figures 4.18 and 3.23. The traverse at -0.5 stator pitch is at a circumferential location which is not affected by the NGV1 wake fluid nor by the NGV2 potential field. The second traverse at 0.05 stator pitch is at the circumferential location where the maximum potential effect of the NGV2 is observed and can therefore be assumed to be approximately upstream of the second nozzle

guide vane leading edge, in the region of elevated entropy. The time axis covers three rotor blade passing events, the y-axis the blade span. The same rotor related secondary flow structures as described in the text related to Figure 3.16 can be identified as regions of elevated *rms*.

At both circumferential positions the time space plots in Figure 4.18 confirm the reduction of the unsteadiness (by 25%) and of the radial height (by 5%) of the hub loss core due to the end wall profiling. This behaviour has already been observed in the context of Figures 4.11 and 4.12. Furthermore, in the rest of the flow field the non-deterministic unsteadiness is not significantly affected by the end wall profiling, as well in a time-resolved perspective given in Figure 4.18. When comparing the measurements at the two different circumferential locations one can see that the radial height of the hub passage vortex varies under the effect of the second nozzle guide vane potential field. Upstream of the second nozzle guide vane, at 0.05 stator pitch, the centre of the hub loss core is at approximately 10% lower radial coordinate compared to the situation at -0.5 stator pitch. The loss core appears to radially oscillate under the effect of the second nozzle guide vane. The unsteady rotor hub passage vortex behaviour in the presence of purge flow is discussed in chapter 7. When comparing the space time plots at -0.5 and 0.05 stator pitch in Figure 4.18, significantly higher levels of *rms* can be detected also outside of the hub loss core region at -0.5 stator pitch. This mainly applies to the regions below 30% span and above 80% span. These variations of *rms* must be related to the downstream second nozzle guide vane located at 0.05 stator pitch. The potential field caused by the NGV2 influences the *rms* distribution. Regions of elevated *rms* indicate regions of significant non-deterministic unsteadiness and are typically of low momentum and therefore do not have enough energy to travel to regions of high static pressure caused by the downstream stationary blade row. Therefore the overall *rms* level shown in the time space plots at 0.05 stator pitch is significantly lower compared to the situation at -0.5 stator pitch. These findings are not influenced by the end wall profiling.

#### 4.4. Effects of Shroud End Wall Profiling at the Rotor Exit

In the next section the effect of the end wall profiling on the rotor shroud is analysed. The 1<sup>st</sup> and 2<sup>nd</sup> end wall designs are compared to the axisymmetric case. The shroud thickness limits the design freedom in terms of the

maximum allowable  $\Delta r$ . At the measurement plane at the rotor exit the measurable modification to the flow are limited to radial heights between 80% span and the casing.

Figure 4.19 shows time-averaged contour plots in the rotor relative frame of FRAP measurements made with all three rotor shroud end wall geometries at the rotor exit. The contours indicate the normalised relative total pressure  $Cp_{t,rel}$  in the tip region at the nominal injection rate. The effect of both non-axisymmetric end wall designs compared to the cylindrical baseline is relatively small and limited to the rotor tip secondary flow interaction region above the rotor wake. The time-averaged minimum relative total pressure in this region increases by 0.4% and 0.5% on average due to the 1<sup>st</sup> and 2<sup>nd</sup> shroud end wall designs. These differences are just above the FRAP measurement uncertainty bandwidth. However the 2<sup>nd</sup> end wall design increases the measured minimum relative total pressure in the tip region by nearly 1%. Figure 4.20 shows the corresponding circumferentially mass weighted integral of the  $Cp_{t,rel}$  between 80% and 100% span. Compared to the cylindrical shroud, the radial distribution above 80% span shows an increase of approximately 0.6% of the relative total pressure due to the 2<sup>nd</sup> shroud end wall design. This increase of relative total pressure is not within the measurement uncertainties of the FRAP probe, hence the beneficial effect of the profiled shroud is measurable and on the order of half a percent close to the casing in terms of relative total pressure.

Equation 4.2 gives the definition for the relative total pressure loss coefficient  $Y_{rel}$ . It is calculated using the mass-averaged rotor inlet and exit relative total pressure values at the same radial height.

$$Y_{rel} = \frac{P_{t,rel,NGV1ex} - P_{t,rel,R1ex}}{P_{t,rel,R1ex} - P_{s,R1ex}} \quad (4.2)$$

In Figure 4.20 the mass and time-averaged radial distribution of  $Y_{rel}$  is given for all three shroud geometries. The 1<sup>st</sup> shroud end wall design reduces a mass-weighted integral of the relative total pressure loss by 7% above 80% span. The 2<sup>nd</sup> shroud design further reduces the  $Y_{rel}$  by another 13% resulting in an overall reduction of 19% compared to the cylindrical shroud. The 2<sup>nd</sup> shroud end wall design especially performs well above 95% radial height compared to the 1<sup>st</sup> shroud design and the cylindrical shroud. Above 95% span a mass weighted integral of the  $Y_{rel}$  reduces by nearly 30% compared to the cylindrical case.

The Euler work term for the rotor  $\Delta(UC_{\theta}) = UC_{\theta,NGV1ex} - UC_{\theta,R1ex}$  can be evaluated using the mass-averaged rotor inlet and exit circumferential

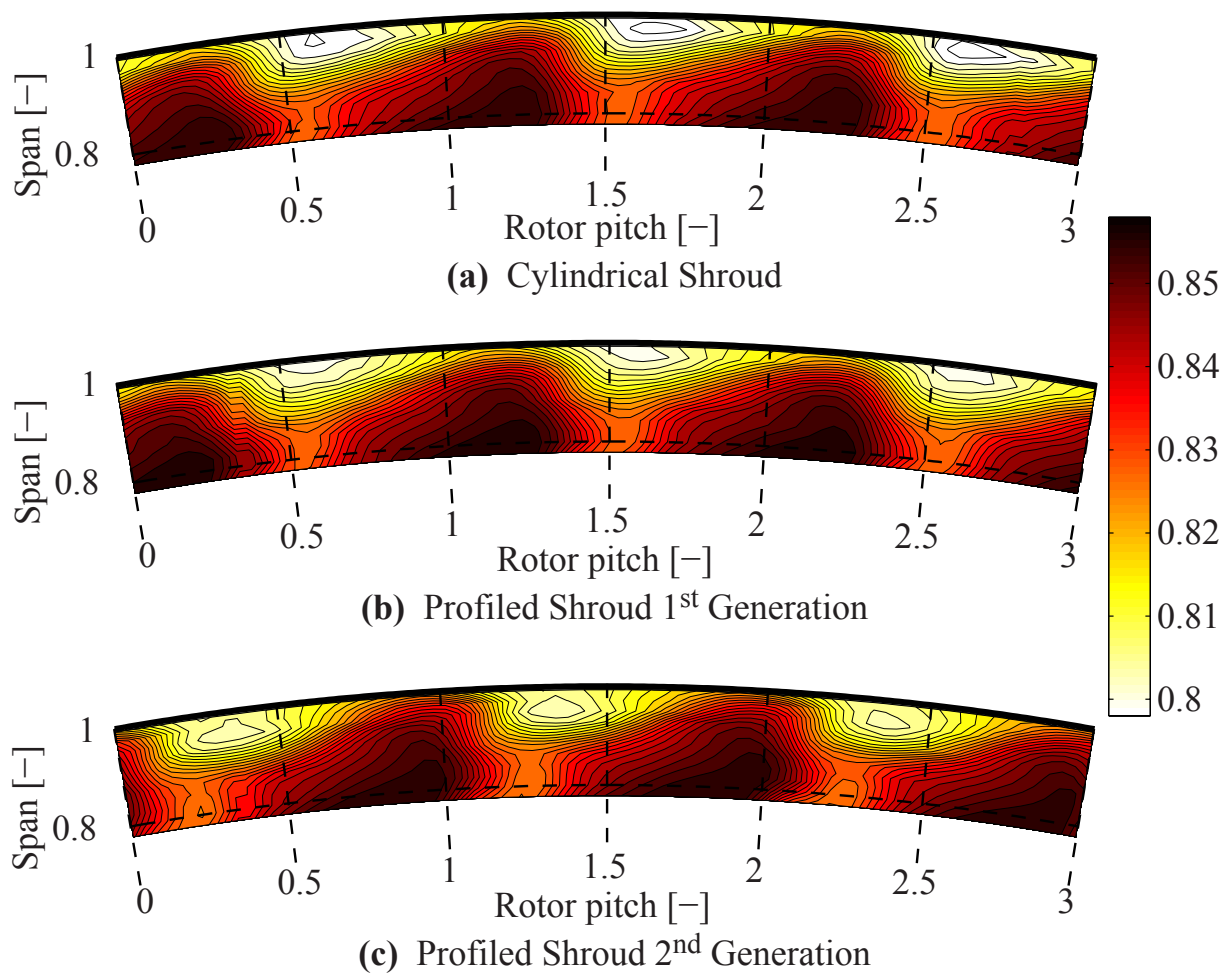


Figure 4.19.: Time-averaged area plots in rotor relative frame of measurements made with all three rotor shroud end wall geometries at the rotor exit. The parameter is the normalised relative total pressure  $C_{p_{t,rel}}$  [-] at the nominal injection rate ( $IR = 0.8\%$ , FRAP).

velocities at the same radial height. The corresponding time-averaged radial distributions are given in Figure 4.21. Between 85% and 93% radial height both shroud end wall designs increase the time-averaged Euler work by about the same amount, by 2% on average. Above 95% span the 2<sup>nd</sup> shroud end wall design further increases the work by up to 6% compared to the cylindrical shroud. This is the region where the 2<sup>nd</sup> shroud end wall design also further reduces the relative total pressure loss compared to the 1<sup>st</sup> shroud design. The average total temperature drop over the rotor is approximately  $\Delta T_t = 25\text{K}$ . Thus the 6% work increase at the casing corresponds to an additional 1.5K temperature drop in the tip region at the rotor exit in the presence of shroud end wall profiling.

The effect of the shroud end wall profiling on mass and time-averaged radial distribution of the entropy rise  $\Delta s$  (FENT) above 80% span is also given on

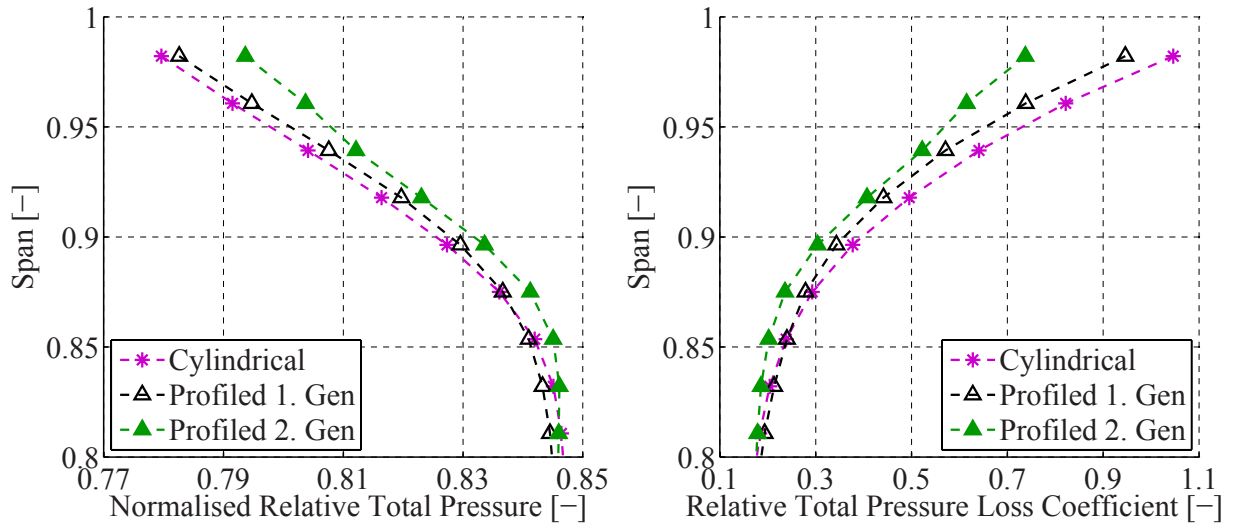


Figure 4.20.: Mass and time-averaged measured normalised relative total pressure  $Cp_{t,rel}$  and relative total pressure loss coefficient  $Y_{t,rel}$  with and without end wall profiling at the rotor exit ( $IR = 0.8\%$ , pneumatic probes).

the right hand side in Figure 4.21. The reference conditions are the total turbine inlet temperature and pressure. The 1<sup>st</sup> shroud end wall design appears to only slightly reduce the measured entropy rise above 80% radial height, between 2% to 4% on average. This decrease is just outside of the uncertainty range of the FENT probe (Table 2.5). However the 2<sup>nd</sup> shroud end wall design reduces the generated entropy in the tip region more significantly. At the casing the entropy reduction peaks at 15%, a mass weighted integral between 80% and 100% span decreases by 5% in the presence of the 2<sup>nd</sup> end wall design.

Time-resolved measurements of the *rms* of the relative total pressure in the form of a space time plot at 99% span are shown in Figure 4.22 for all three experimentally investigated shroud geometries. The space time plots are dominated by the vertical zone of reduced *rms* between -0.2 and 0.15 stator pitch. This region is not significantly influenced by the shroud end wall profiling. In this zone the inclined elevated *rms* signature of the rotor wake nearly entirely disappears. Flow of high *rms* avoids regions of increased static pressure caused by the NGV2 located at 0.05 stator pitch. This also has been observed in the context of Figures 4.18 and 3.23. Outside of low *rms* region both shroud end wall profiling designs reduces in the same manner the non-deterministic unsteadiness mainly in the inclined rotor wake regions between 0.3 and 0.5 stator pitch. The 2<sup>nd</sup> shroud end wall design further reduces the non-deterministic unsteadiness compared to the 1<sup>st</sup> shroud end wall design. The increase of the non-deterministic

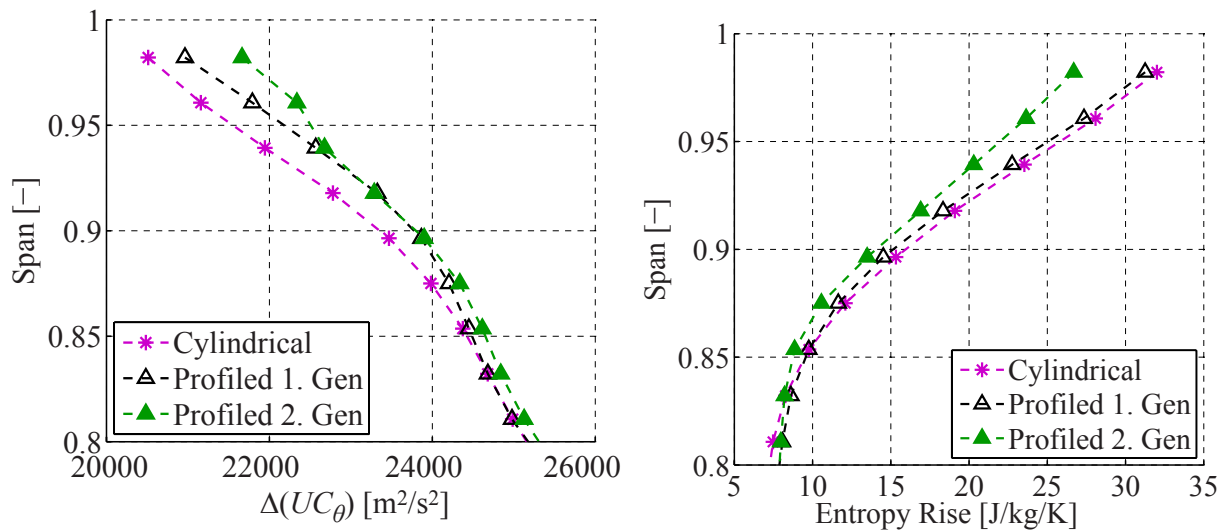


Figure 4.21.: Mass and time-averaged measured Euler work term  $\Delta(UC_\theta)$  and entropy rise  $\Delta s$  with cylindrical and profiled (1<sup>st</sup> and 2<sup>nd</sup> generation) shroud end walls ( $IR = 0.8\%$ , pneumatic probes, FENT).

unsteadiness at the casing is caused by rotor related flow structures. The rotor tip secondary flows can be expected to be involved in this unsteady process. The measurement plane at the rotor exit is downstream of the shroud exit cavity. Unsteady interaction mechanisms between the rotor tip secondary flows and the flow leaving the shroud cavity are considered to be improved by both end wall profiling designs.

In terms of total-to-total stage efficiency both shroud end wall designs have a beneficial effect in the tip region. Figure 4.23 gives the mass and time-averaged radial distribution of the  $\eta_{tt}$  for all three shroud geometries. On average the 1<sup>st</sup> shroud end wall design increases the total-to-total efficiency by  $0.5\% \pm 0.32\%$  (abs.) above 85% span, the 2<sup>nd</sup> shroud end wall design by  $1.2\% \pm 0.32\%$  (abs.) compared to the cylindrical shroud. A mass weighted integral between 85% and the casing increases by 0.7% and 1.1% in the presence of the 1<sup>st</sup> and 2<sup>nd</sup> shroud end wall designs.

Based on these numbers it is difficult to assess the fraction of the overall efficiency improvement due to the beneficial effect of the shroud end wall profiling. An approach is proposed where three mass and time-averaged radial distributions of  $\eta_{tt}$  are considered which are composed of two parts. Below 80% span they all have the total-to-total efficiency distribution measured in the presence of cylindrical end walls. Above 80% span the efficiency distribution corresponds to the measurements made with the 1<sup>st</sup> and 2<sup>nd</sup> shroud end wall designs. These three artificially assembled radial distributions of measured total-to-total efficiency correspond to three imaginary

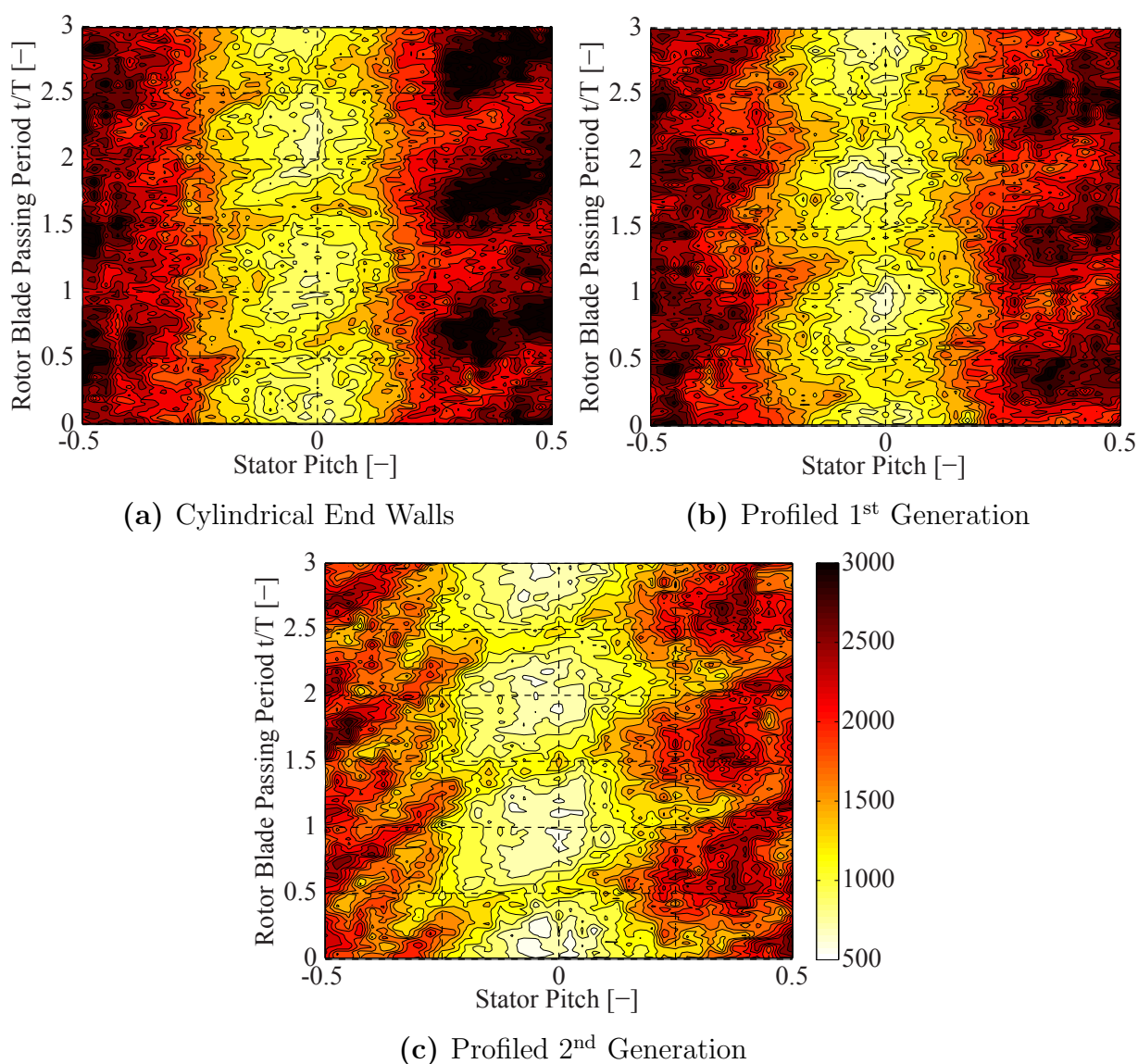


Figure 4.22.: Space time plot in absolute frame of reference of the experimental *rms* of the total pressure [Pa] at 99% span with 1<sup>st</sup> generation, 2<sup>nd</sup> generation and without shroud end wall profiling. The plots show measurements made at the rotor exit at the nominal injection rate ( $IR = 0.8\%$ , FRAP).

rotors which all have a cylindrical hub end wall combined with a varying geometry (cylindrical, 1<sup>st</sup> and 2<sup>nd</sup> end wall design) only at the shroud. This model allows the isolation of the shroud end wall profiling effect which then can be compared to the overall  $\eta_{tt}$  improvement. In this rotor configuration the overall stage efficiency increases by  $0.15\% \pm 0.32\%$  and  $0.25\% \pm 0.32\%$  in the presence of the 1<sup>st</sup> and 2<sup>nd</sup> end wall design at the shroud only. When these numbers are compared to the average overall efficiency improvements listed in Table 6.1, it can be seen that approximately 20% to 25% of the

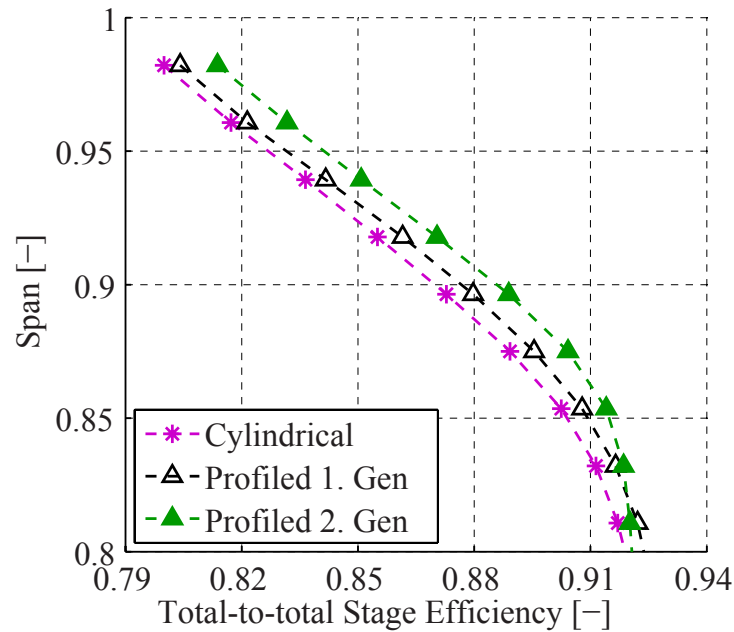


Figure 4.23.: Mass and time-averaged measured total-to-total stage efficiency  $\eta_{tt}$  in the tip region with cylindrical and profiled (1<sup>st</sup> and 2<sup>nd</sup> generation) shroud end walls ( $IR = 0.8\%$ , 5-hole probe).

overall  $\eta_{tt}$  benefit comes from the shroud end wall profiling. These efficiency numbers confirm that the 2<sup>nd</sup> shroud end wall design performs significantly better compared to the 1<sup>st</sup> design, as already observed in Figures 4.20 and 4.21.

Part of the reason for the smaller contribution of the shroud end wall profiling to the overall stage efficiency benefit is related to the amplitude of the radial variations within the end wall profiling. The radial variations of the shroud end wall profiling need to stay within the thickness of the shroud and are smaller compared to the radial variations at the rotor hub.

## 4.5. End Wall Effects at the NGV2 Exit

At the NGV2 exit measurements were performed with the 5-hole probe and the FRAP. The effects of the rotor end wall profiling can also be captured at this measurement plane. At the NGV2 only the effects of the 1<sup>st</sup> end wall design are considered for the same reason as in the hub region at the rotor exit. The second nozzle guide vane has cylindrical end walls. Figure 4.24 gives the mass and time-averaged radial distribution of total-to-total 1.5 stage efficiency. The rotor end wall profiling reduces the total pressure loss and increases the total-to-total efficiency as well at NGV2 exit. The

overall mass weighted  $\eta_{tt,1.5}$  increases by  $0.8\% \pm 0.32\%$  in the presence of the non-axisymmetric rotor end walls. This number is slightly higher than the efficiency improvement measured at the rotor exit ( $\eta_{tt} = 0.75\% \pm 0.32\%$ ). Hence the efficiency of the second nozzle guide vane appears to also improve by a small amount due to its improved inlet conditions. Due to the reduced unsteadiness at the rotor exit in the presence of profiled end walls, reduced mixing losses can be expected in the second nozzle guide vane. When considering the radial distributions the efficiency deficit without profiled end walls mainly occurs in two regions: between 35% and 85% and below 18% span. The end wall profiling does not improve the efficiency for all spanwise positions at the NGV2 exit, between 35% and 50% span there is a region of lower efficiency.

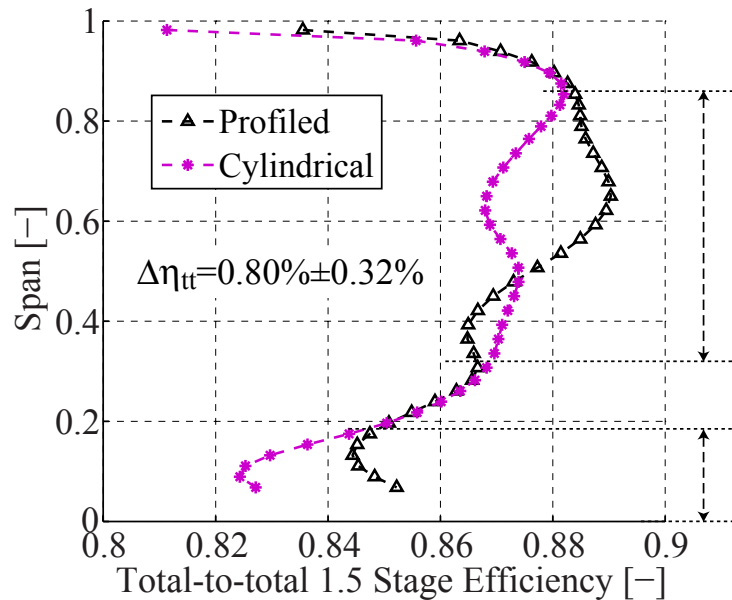


Figure 4.24.: Mass and time-averaged measured total-to-total stage efficiency  $\eta_{tt}$  with and without rotor end wall profiling at the NGV2 exit ( $IR = 0.8\%$ , 5-hole probe).

Figure 4.25 compares the radial distributions of the *rms* of the total pressure measured with and without end wall profiling at the rotor and NGV2 exit. When comparing Figures 4.24 and 4.25 it can be seen that there is a certain correlation between regions of increased  $\eta_{tt,1.5}$  and increased *rms* at the NGV2 exit. Between 50% and 80% span the non-deterministic unsteadiness is 10% higher with cylindrical end walls, below 20% span the *rms* is up to 20% higher at the NGV2 exit. A mass-weighted integral of the *rms* over one stator pitch decreases by 7% in the presence of the end wall profiling. The regions positively affected by the end wall profiling in terms of *rms* are regions of relatively high overall *rms*. At the rotor exit

the reduction of  $rms$  due to the end wall profiling also affects the regions of overall high non-deterministic unsteadiness between 25% and 60% span and above 90% span. The dashed arrows in Figure 4.25 indicate possible migration scenarios of the high  $rms$  fluid between the second nozzle guide vane inlet and exit. Regions of elevated  $rms$  indicate regions of significant non-deterministic unsteadiness. These parts of the flow are typically of low momentum and therefore are attracted by the lower static pressure in the hub region of a stationary blade row. Hence any radial migration of elevated  $rms$  fluid in the second nozzle guide vane towards the hub can be expected. Such a migration pattern would explain the elevated  $rms$  region below 20% span at the NGV2 exit, but cannot explain the extended high  $rms$  region between 50% and 80% span. The reduction of  $rms$  above 90% span at the rotor exit is unlikely to be the reason for the extended elevated  $rms$  region above 50% at the NGV2 exit. As indicated by the dashed arrow in the middle, the measurements suggest a radial migration of the high  $rms$  fluid from the hub loss core to higher radial heights.

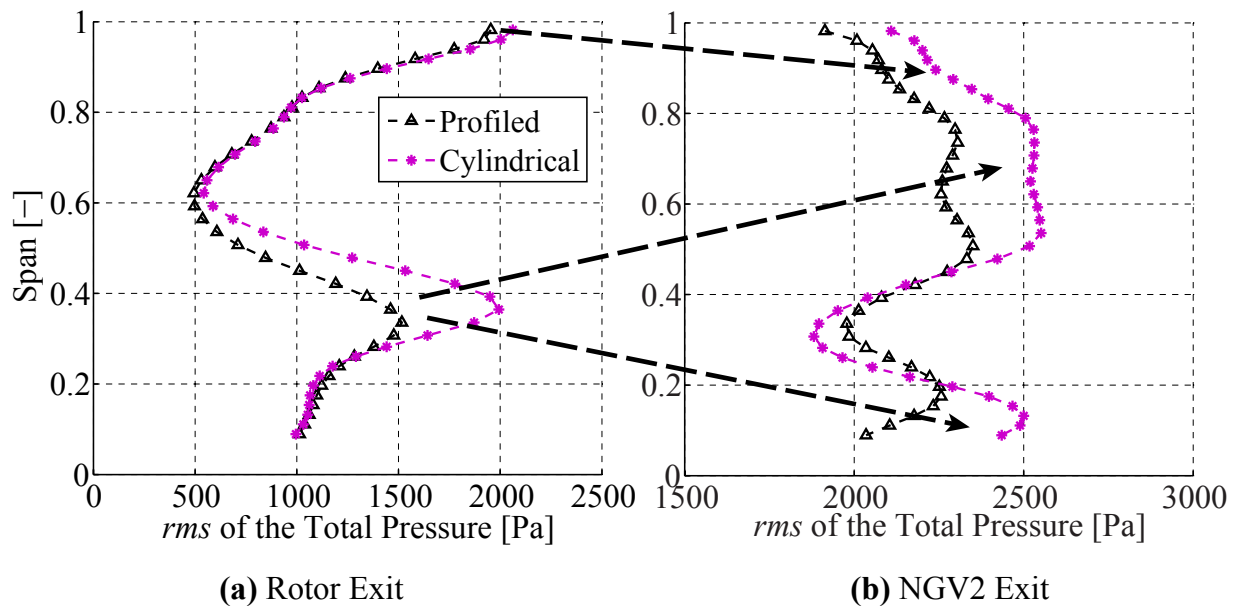
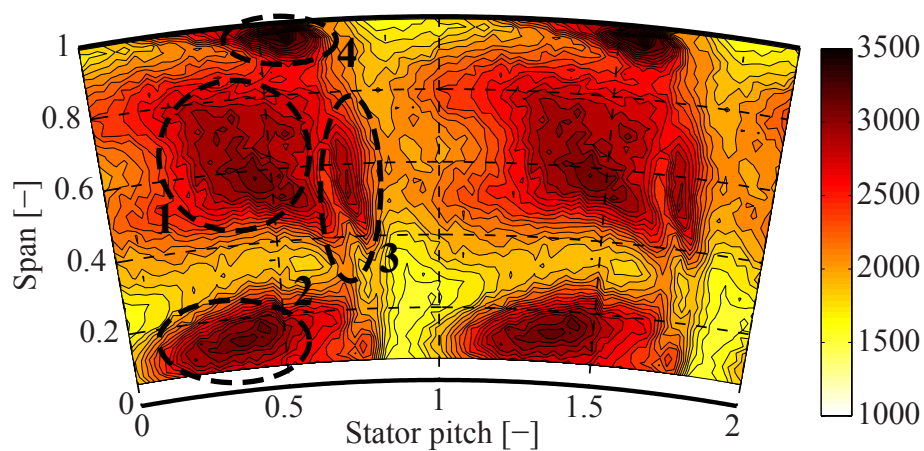


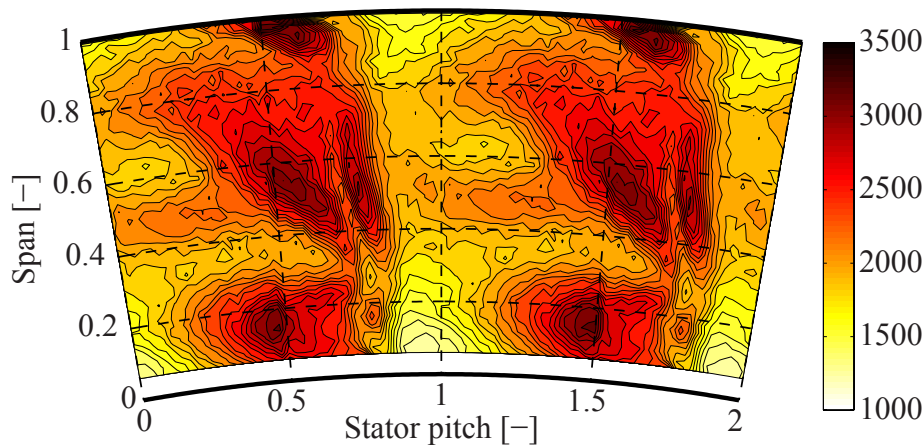
Figure 4.25.: Mass and time-averaged measured  $rms$  of the relative total pressure signal at the rotor exit and NGV2 exit ( $IR = 0.8\%$ , FRAP).

The corresponding contour plots of the  $rms$  of the total pressure measured with and without end wall profiling at the NGV2 exit are shown in Figure 4.26. The regions causing increased  $rms$  are divided into 4 zones indicated by the dashed lines. The following flow structures are considered to contribute to the elevated unsteadiness in zones 1 to 4:

- Zone 1: NGV2 tip passage vortex, shroud cavity tip leakage flow, rotor tip secondary flows and rotor hub loss core
- Zone 2: NGV2 hub passage vortex and rotor hub loss core
- Zone 3: NGV2 wake
- Zone 4: NGV2 secondary end wall feature often referred to as the corner vortex.



(a) Cylindrical End Walls

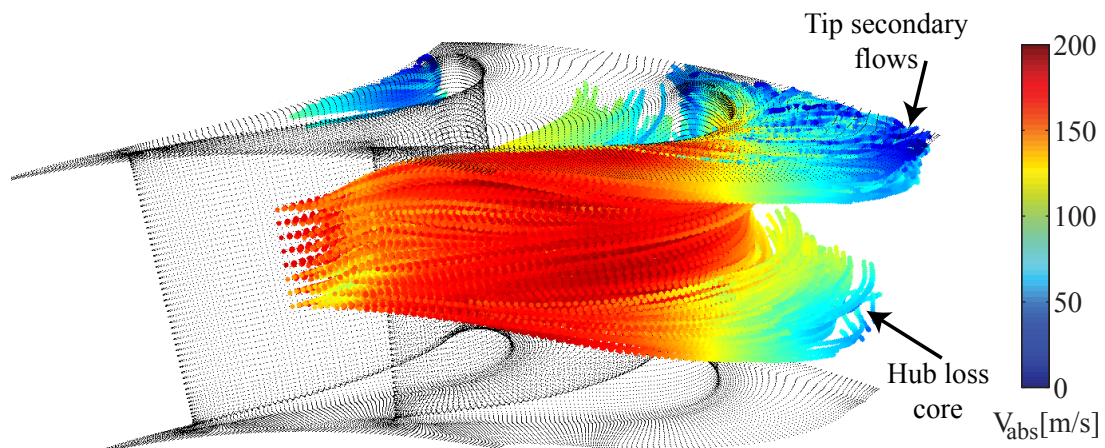


(b) Profiled Rotor End Walls

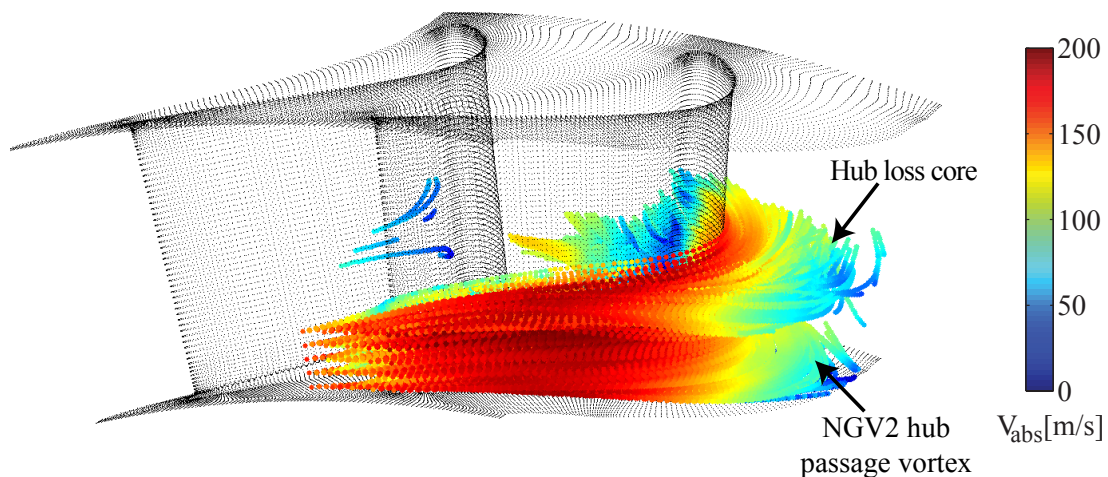
Figure 4.26.: Time-averaged area plots at the NGV2 exit. The parameter is the *rms* of the total pressure [Pa] at the nominal injection rate ( $IR = 0.8\%$ , FRAP).

The rotor end wall profiling reduces the *rms* of the total pressure in zones 1, 2 and 4. These zones contain rotor secondary flow structures that were convected through the second nozzle guide vane.

Firstly, the maximum unsteadiness in these zones is reduced by the end wall profiling. Secondly, the area of these secondary flow structures is bigger with cylindrical rotor end walls, especially in zones 2 and 4. The reduction of unsteadiness in these zones is the consequence of reduced unsteadiness at the rotor exit in the presence of non-axisymmetric end walls. The additional unsteadiness created due to fact that flow at elevated  $rms$  enters the second nozzle guide vane is one order of magnitude smaller. This is also reflected in the moderate additional efficiency increase when the  $\eta_{tt,1.5}=0.8\%$  and  $\eta_{tt}=0.75\%$  are compared. The unsteadiness in the NGV2 wake appears to be only slightly influenced by the end wall profiling.



(a) Particles released in zone 1 between 45% and 80% span.



(b) Particles released in zone 2 between 5% and 25% span.

Figure 4.27.: Particle tracks based on the CFD simulation with profiled end walls at the nominal injection rate. Particles were injected at the NGV2 exit during half a period and tracked in a backward time mode ( $IR = 0.8\%$ ).

The proposed compositions of the four zones of elevated  $rms$  at the NGV2 exit are verified with the use of the particle tracking tool based on the time-accurate CFD calculations performed in the context of this work. For this purpose particles were released inside zones 1 and 2 at the NGV2 exit and then tracked in a backward time mode in order to see where they come from and which path they follow in the second nozzle guide vane flow field. Figure 4.27 shows the particle tracks of particles released in zones 1 and 2 defined in Figure 4.26. The particles shown were injected at the NGV2 exit during half a period. The colour indicates their velocity. The particle tracks show that the high  $rms$  flow in zone 1 is composed by fluid originating from the rotor and NGV2 tip secondary flows, suction side boundary layer and also rotor hub loss core. Indeed, part of the rotor hub loss core particles have the energy to migrate radially outwards, as proposed in the context of Figures 4.25 and 4.26. The rest of the rotor hub passage vortex flow can be found in zone 2, as indicated by the particle tracks in Figure 4.27(b). Therefore the increased  $rms$  in zone 2 is caused by the rotor hub loss core and the NGV2 hub secondary flows.

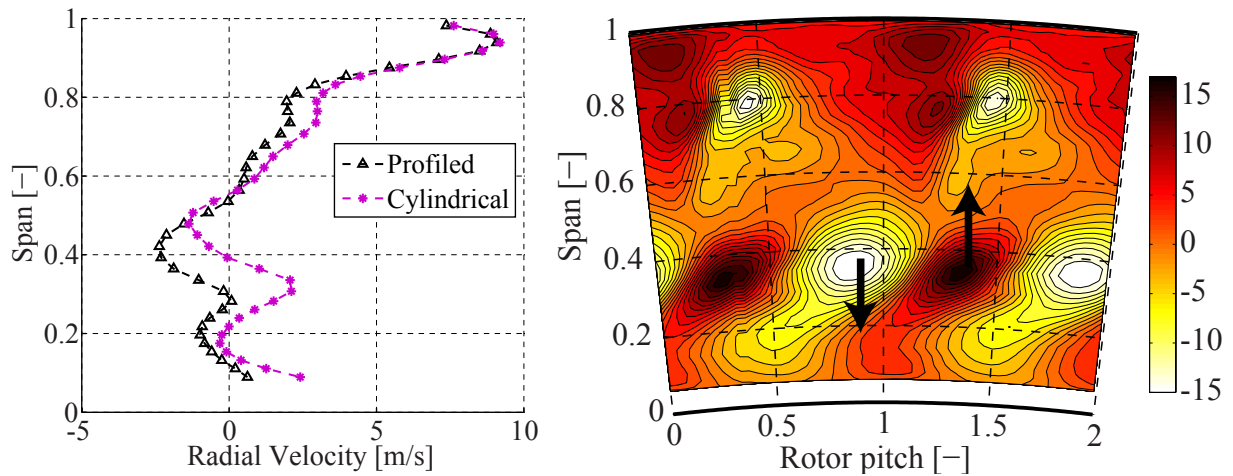


Figure 4.28.: Mass and time-averaged radial velocity  $V_r$  [m/s] with and without end wall profiling and corresponding area plot in the relative frame of reference at the rotor exit ( $IR = 0.8\%$ , FRAP).

Although the particle tracks have shown that part of the unsteadiness in zone 1 at the NGV2 exit is coming from the rotor hub loss core, the increased unsteadiness in the rotor hub loss core with cylindrical end walls not necessarily means increased unsteadiness in zone 1 at the NGV exit. On the contrary, an increased level of unsteadiness theoretically enhances radial migration towards lower radial heights. However the measurement show a reduction of the  $rms$  level in zone 1 in the presence of non-axisymmetric

end walls. Hence the high loss fluid in the hub loss core with cylindrical end walls needs more momentum in order to be able to radially migrate towards the casing. A parameter to consider in this context is the dynamic head  $\rho V_{\text{abs}}^2$  of increased *rms* fluid in the hub loss core and how it gets influenced by the end wall profiling. Figures 4.28 and 4.29 show the radial and absolute flow velocities at the exit of the rotor with and without end wall profiling. The circumferentially mass and time-averaged radial distribution of  $V_r$  indicates an increased radial velocity towards the casing in the rotor hub loss core region. On average the high loss fluid in the hub passage vortex has more radial momentum and leaves the rotor blade row at a higher spanwise position with cylindrical end walls. The corresponding area plot shows a region at about 0.25 or 1.25 rotor pitch of increased positive radial velocity. Furthermore, Figure 4.29 shows a higher absolute flow velocity  $V_{\text{abs}}$  in the core of the hub passage vortex with cylindrical end walls. The end wall profiling reduces the time-averaged maximum dynamic head  $\rho V_{\text{abs}}^2$  in the rotor hub loss core by 12.5%. The combination of the increased radial velocity and increased dynamic head in the absence of profiled end walls suggests that the high *rms* fluid in the hub loss core has enough or more momentum to radially migrate towards the casing and significantly increase the unsteadiness in zone 1, and not only in zone 2.

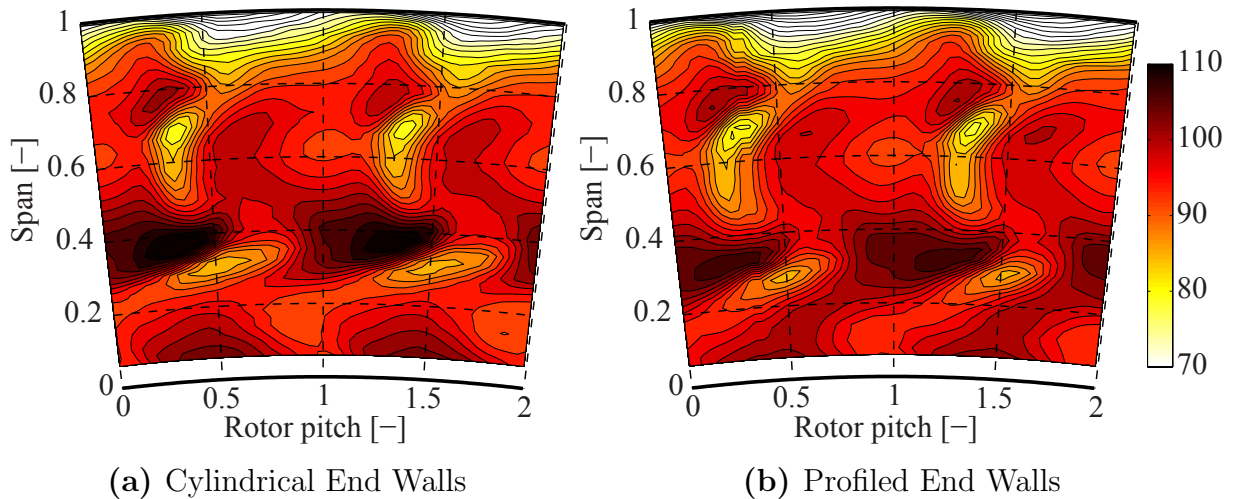


Figure 4.29.: Time-averaged area plots in rotor relative frame of reference at the rotor exit. The parameter is the absolute flow velocity  $V_{\text{abs}}$  [m/s] at the nominal injection rate ( $IR = 0.8\%$ , FRAP).

## 4.6. Summary

In this chapter the effects of the rotor end wall profiling on the flow field are analysed. Probe measurements at NGV1, rotor and NGV2 exit are analysed and complemented by corresponding unsteady CFD simulations at the nominal injection rate.

Apart from the rim seal exit region, the flow field at the rotor inlet is not significantly affected by the rotor end wall profiling. The measured differences are within measurement uncertainties indicating a constant rotor capacity and confirming an end wall design condition. As observed when analysing different purge flow rates, the rim seal exit flow field is dominated by a toroidal vortex and two zones of positive mass flow along the axial rim seal gap. However the end wall profiling successfully reduces the maximum radial velocity at the rim seal exit by up to 50% close to the rotor disk. The wavy shape of the rotor hub platform leading edge due to the end wall profiling enables more purge flow to leave the rim seal cavity in a more axial direction at lower spanwise position along the hub end wall. These mechanisms can be expected to reduce the radial migration of the hub loss core and the loss generation opportunities at the exit of the rim seal cavity. The non-axisymmetric rotor hub end walls reduce the non-deterministic unsteadiness caused by the rotor interaction at the rim seal exit.

The measurements at the rotor exit show that the rotor hub end wall profiling only significantly influences the unsteady behaviour of the rotor hub passage vortex. The reaction was found to decrease by 0.3% on average in the presence of the 1<sup>st</sup> end wall design, due to modifications of the static pressure in the hub loss core region at the rotor exit. The measured total-to-total stage efficiency increased by  $0.75\% \pm 0.32\%$  due to the 1<sup>st</sup> end wall design. The main reason for this efficiency benefit comes from the significantly higher efficiency in the hub loss core region which peaks at 4% (abs.). Given the facts that the end wall profiling does not change the capacity of the turbine and only slightly reduces the overall reaction at the chosen operating point, the measured efficiency improvement can be considered to be relevant. Furthermore, the end wall profiling reduces the average radial coordinate of the hub passage vortex by 5% span. The time-resolved measurements show a reduction of the unsteadiness by 25% in the hub loss core. The streamwise vorticity in the hub loss core was found to be much more concentrated and stretched in the circumferential direction with cylindrical end walls. The peak streamwise vorticity nearly doubles in the absence of profiled end walls. Thus, the flow is spinning at higher

velocity and therefore creating more loss and reduced relative total pressure ( $-1\%$ ). The dissipation function in the hub loss core reduces by a factor 2-3 in the presence of rotor end wall profiling. The hub loss core was found to oscillate in the radial direction by 10% span and to change its overall level of unsteadiness under the effect of the downstream NGV2 leading edge. Only the 1<sup>st</sup> hub end wall design is considered when studying the unsteady effects of the hub end wall profiling on the hub loss core region. The 2<sup>nd</sup> hub end wall was optimised and designed for a thicker blade in the hub region which also removes the pressure side separation present for the 1<sup>st</sup> end wall design. The improvements due to the removal of the bubble and due to the successful 2<sup>nd</sup> end wall design are difficult to distinguish.

However both shroud end wall designs can be analysed and compared to each other as the bubble does not affect the flow field influenced by the shroud end wall profiling (above 80% span). The beneficial contribution of the shroud end wall design to the overall stage efficiency improvement is approximately five times lower compared to the overall stage efficiency improvement. The beneficial effects caused by the 2<sup>nd</sup> shroud end wall design were found to be nearly twice as high compared to the 1<sup>st</sup> shroud design. The 2<sup>nd</sup> shroud end wall especially performs better above 95% span. The minimum time-averaged relative total pressure increases by 1%, the Euler work term by 6%, the entropy rise by 15% and the non-deterministic unsteadiness by 5% above 90% span and in the presence of the 2<sup>nd</sup> shroud end wall design. The change in *rms* of the relative total pressure occurs within a limited circumferential region and in the unsteady interaction zone between the rotor tip passage vortex and the shroud leakage flow.

The measured 1.5-stage efficiency improvement due to the 1<sup>st</sup> end wall design is  $0.8\% \pm 0.32\%$  and slightly higher compared to the 1-stage efficiency. Hence, the rotor end wall profiling also tends to increase the efficiency of the second nozzle guide vane. The regions between 35% and 85% span and below 18% span at the NGV2 exit were identified to have increased total-to-total efficiency and reduced non-deterministic unsteadiness (by 10% and 20% respectively) in the presence of profiled rotor end walls. Part of the elevated *rms* flow transported in the hub passage vortex has the energy to migrate radially outwards and increase the non-deterministic unsteadiness between 35% and 85% span. With cylindrical rotor end walls the maximum dynamic head and radial velocity in the rotor hub loss core at the rotor exit are 12.5% higher compared to the non-axisymmetric case and therefore enhance the radial outwards migration of high *rms* flow in the second stator blade row.

## 5. Unsteady Pressure Side Bubble Behaviour

Two of the three tested rotor geometries have pressure side separations for the chosen operating point in the context of this work. The unsteady behaviour of this pressure side bubble is studied in this chapter. Since the probes cannot be used to perform measurements in the rotating blade row and the rotor blades are not instrumented, the unsteady behaviour of the pressure side bubble is studied based on time-accurate CFD simulations. Probe measurements at the rotor inlet and exit are used to validate the CFD simulations (section 2.6.3) and to analyse the effects of the pressure side bubble at the rotor inlet and outlet.

The unsteady behaviour of the pressure side separations presented in this chapter relies entirely on unsteady CFD simulations and therefore needs to be considered with some care. The pressure side separation is visualised as a bubble with fluid inside an iso-surface of zero velocity. In reality bubbles are four-dimensional flow features including rolling sets of eddies migrating along the blade surface (Figure 1.6) that is strongly influenced by the radial velocity and transition effects. The prediction of the behaviour of the pressure side separation and of the underlying shear stresses strongly depends on the transition and the turbulence models of the CFD code used in the context of this work. Direct numerical simulation would be required to predict and understand the involved flow mechanisms in greater detail. In a first part the effect of the rotor hub end wall profiling on the dynamic of the bubble is investigated at a constant purge flow injection rate. The analysis focuses on the unsteady three dimensional shape and size of the pressure side separation and on the bubble shedding mechanism caused by the unsteady blade row interaction. For this purpose the time-resolved CFD data obtained for the rotor with cylindrical end walls are compared to the data for the rotor with the same blade geometry but non-axisymmetric end walls (1<sup>st</sup> generation). In a second part the influence of the injected rim seal purge flow on the unsteady behaviour of the pressure side bubble for a given rotor geometry is analysed based on both, the time-resolved CFD data and

the probe measurement results at the rotor inlet and exit. In a third part the rotor with thicker airfoils and the adapted 2<sup>nd</sup> end wall design, which has successfully removed the pressure side separations, is compared to the rotor with the 1<sup>st</sup> end wall design operating with separated pressure sides. The effect of the 2<sup>nd</sup> shroud end wall design is studied in section 4.4. Based on the probe measurements the effects on the rotor exit flow field caused by separated pressure sides can hereby be studied.

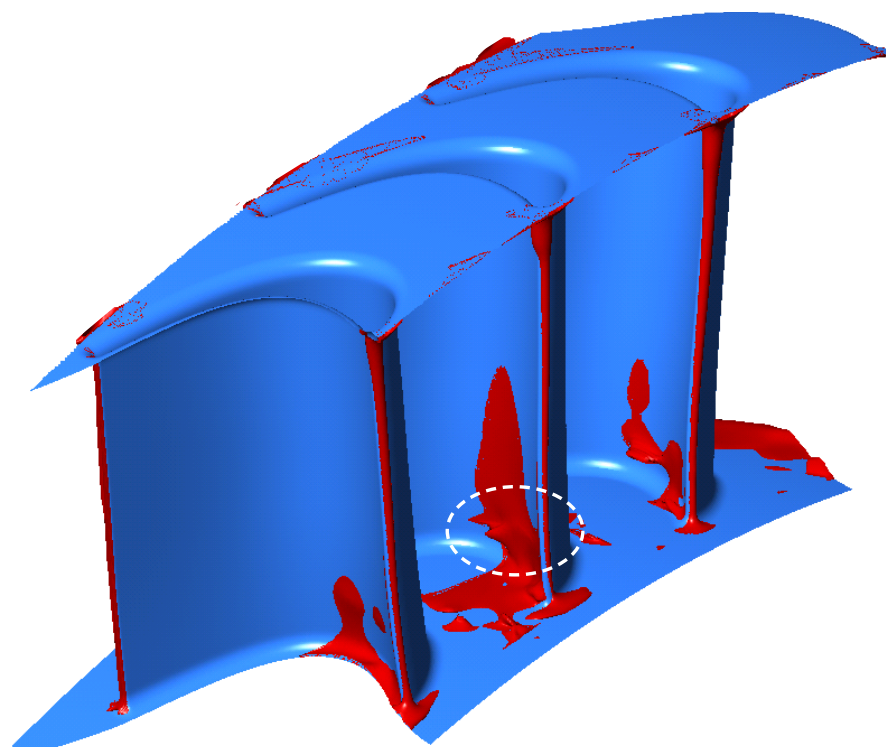
## 5.1. Effect of End Wall Profiling on Pressure Side Bubble

The airfoils of the rotors with cylindrical end walls and with the 1<sup>st</sup> end wall design are identical and feature a small leading edge radius and very high turning and loading. At the chosen operating point of the turbine the time-resolved CFD simulations clearly detect a separation bubble in the hub region close to the leading edge on the rotor pressure side.

### 5.1.1. Unsteady Size and Shape of Bubble

Figure 5.1 shows iso-surfaces of zero axial velocity on the rotor blade pressure side at a fixed point in time ( $t/T = 0$ ) for the rotors with cylindrical and 1<sup>st</sup> generation end walls. Three adjacent rotor blades are represented. When comparing the pressure side separations on the rotor blade in the middle in Figure 5.1, one can see that the end wall profiling successfully reduces the size and volume of the bubble, especially in the region close to and on the hub end wall. With cylindrical end walls the bubble has a more three dimensional shape in the region indicated by the white dashed lines at a radial height of approximately 15% to 20%. With non-axisymmetric end walls the bubble is more confined to the end wall and has less volume. For both rotor geometries the shape and size of the pressure side separation is different on the three adjacent rotor blades represented in Figure 5.1. Thus the relative position of the rotating and stationary blade rows seems to influence the unsteady behaviour of the bubble.

Figure 5.2 shows iso-surfaces of zero axial velocity on the rotor blade pressure side of the rotor with non-axisymmetric end walls for 11 equally spaced snapshots during one period  $T$ . Due to the 2 to 3 blade count between the NGV1 and the rotor, one period corresponds to the duration the rotor needs to travel the distance of two nozzle guide vane pitches. Therefore each rotor



(a) Cylindrical End Walls

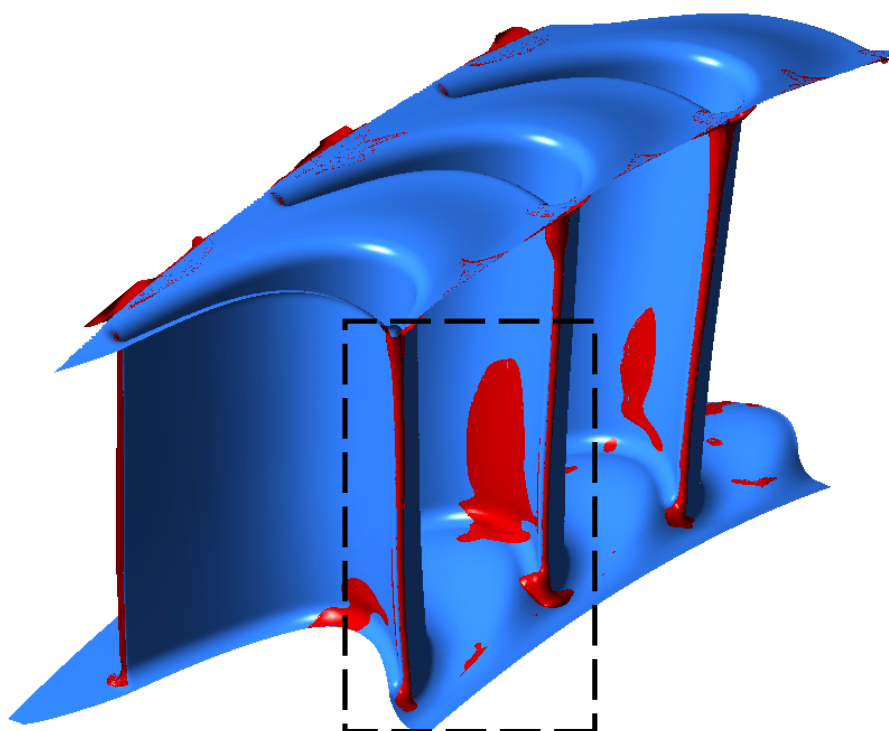
(b) Profiled 1<sup>st</sup> Generation

Figure 5.1.: Iso-surfaces of zero axial velocity on the rotor pressure side with and without end wall profiling at the time step  $t/T = 0$  ( $IR = 0.8\%$ ).

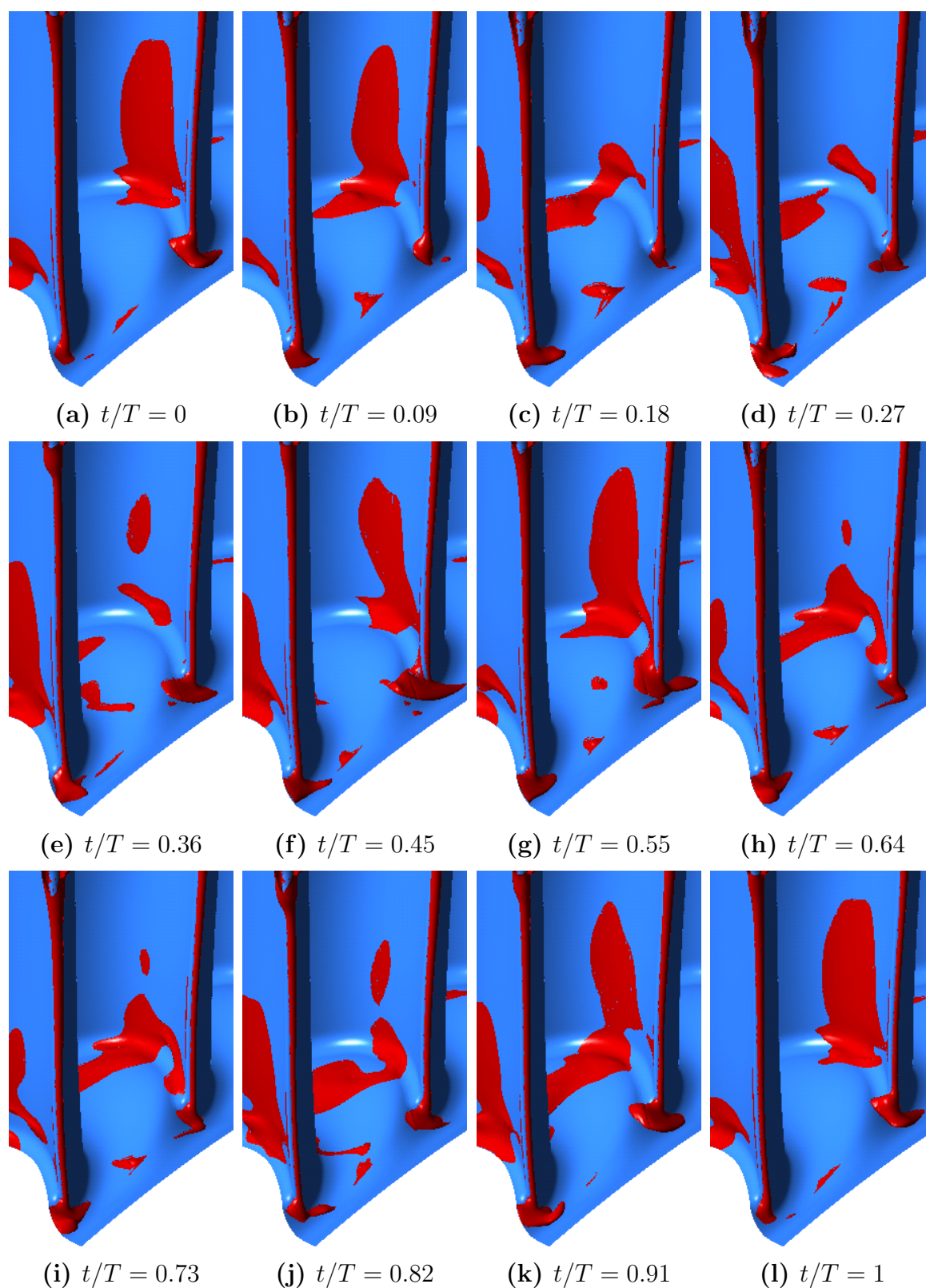


Figure 5.2.: Iso-surfaces of zero axial velocity on the rotor pressure side during one period  $T$  corresponding to two stator pitches. The black rectangle in Figure 5.1 defines the view of each subfigure.

blade interacts with two NGV1 wakes during one period and the potential field interaction also goes through two cycles. The size and shape of the pressure side separation shows a very unsteady behaviour due to the blade row interaction. During one period the bubble disappears twice and builds up again after having disappeared. During one period the NGV1 wake hits the rotor blade row twice, therefore there may be a link between the two elements. The iso-surfaces not only reveal a bubble on the pressure side, but also a vortical structure on the hub end wall. This vortical structure can be described as an unsteady end wall separation and it acts like a tube draining the fluid periodically from the pressure side separation.

The size of this structure on the hub end wall seems to be related to the size of the pressure separation. When the pressure side bubble decreases in size the structure on the hub end wall is very big (time step  $t/T = 0.18$  or  $t/T = 0.73$  in Figure 5.2) and disappears when the pressure side bubble grows again ( $t/T = 0.45$  or  $t/T = 1$ ). The pressure side bubble seems to get purged through this vortical structure on the hub end wall once per nozzle guide vane passing event.

### 5.1.2. Bubble Shedding Mechanism

The unsteady blade row interaction causes the pressure side separations to change in size and shape. With and without end wall profiling the bubble collapses and nearly disappears twice during one period. Hence the amount of fluid inside the bubble is varying and portions of the pressure side separation are shed into the free stream. In order to get a more detailed view of the flow physics related to the unsteady behaviour of the separation bubble and its shedding mechanism, the particle tracker was used. For this purpose massless particles are released inside the pressure side separation during one period and then tracked until they leave the rotor domain. The location where the particles are injected is kept constant, but particles are only released when the axial velocity is negative at the point of injection for a given point in time. Figure 5.3 shows the isometric and top view of the computed tracks of four particles that were released at one specific point in time inside the pressure side bubble of the rotor with cylindrical end walls. The CFD simulations at the nominal injection rate were used and the colour of the particles indicates the relative velocity of the particles. Figure 5.4 shows the corresponding tracks of 4 particles released at the same location as the particles shown in Figure 5.3 but inside of the pressure side separation of the rotor with non-axisymmetric end walls (1<sup>st</sup> generation).

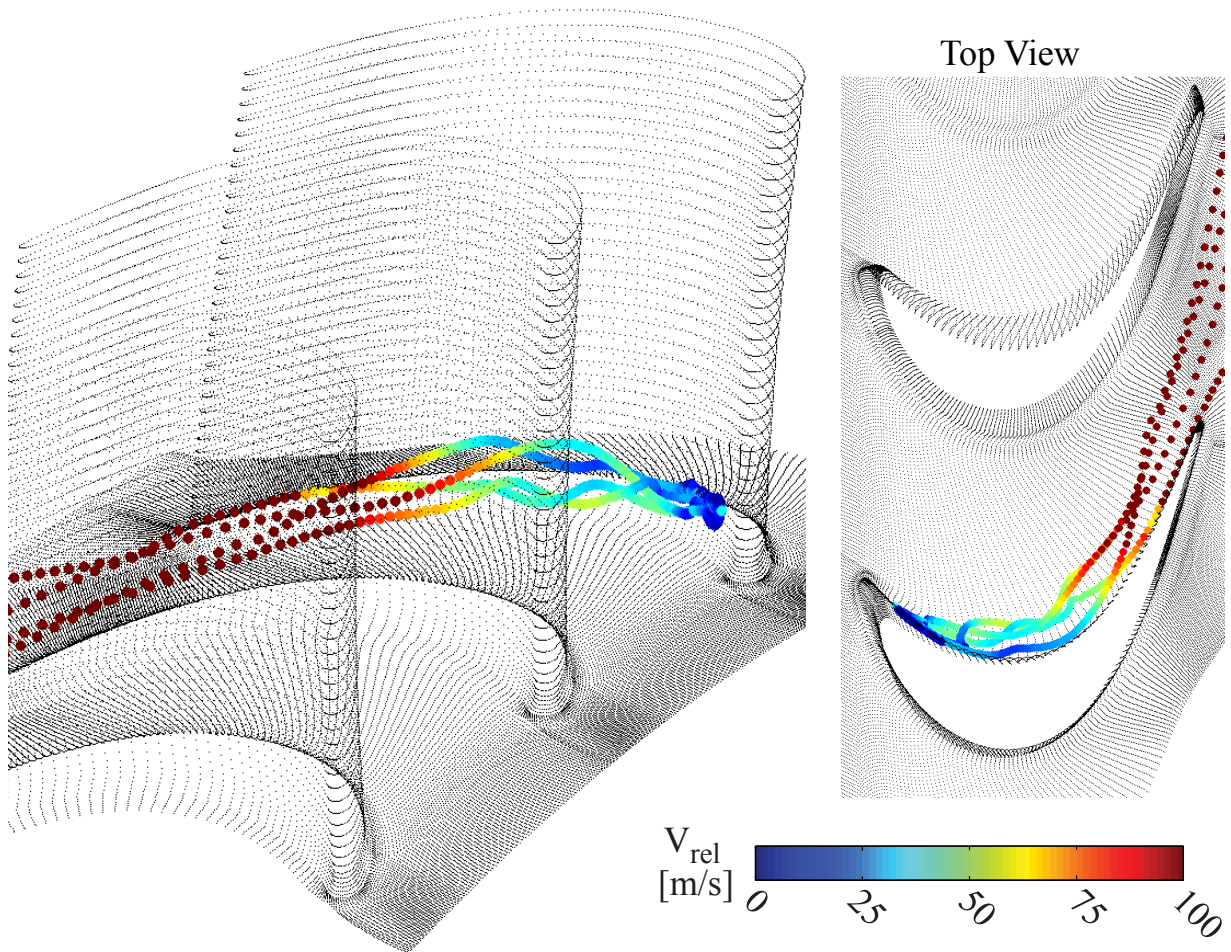


Figure 5.3.: Particle tracks of particles released inside the pressure side bubble of the rotor with cylindrical end walls,  $IR = 0.8\%$ .

The particles were injected at a different point in time but at the same purge flow injection rate. Figure 5.5 gives the spanwise and rotor pitch position of a typical track of a particle released at negative axial velocity inside the pressure side separations present on the rotors with cylindrical and non-axisymmetric (1<sup>st</sup> generation) end walls. The tracks which are detailed in Figure 5.5 correspond to one of the four tracks shown in the isometric and top views shown in Figures 5.3 and 5.4 respectively. The span and rotor pitch positions are plotted as a function of the non-dimensional axial coordinate. Zero corresponds to the point where the particles are injected (inside the bubble) and 1 corresponds to the moment when the particle leaves the rotor domain. Both particles were injected at the same location but at a different time step of the simulation.

The particle tracks shown in Figures 5.3, 5.4 and 5.5 indicate that the bubble shedding mechanism is significantly modified in the presence of profiled end walls. With cylindrical end walls the particles leave the pressure side

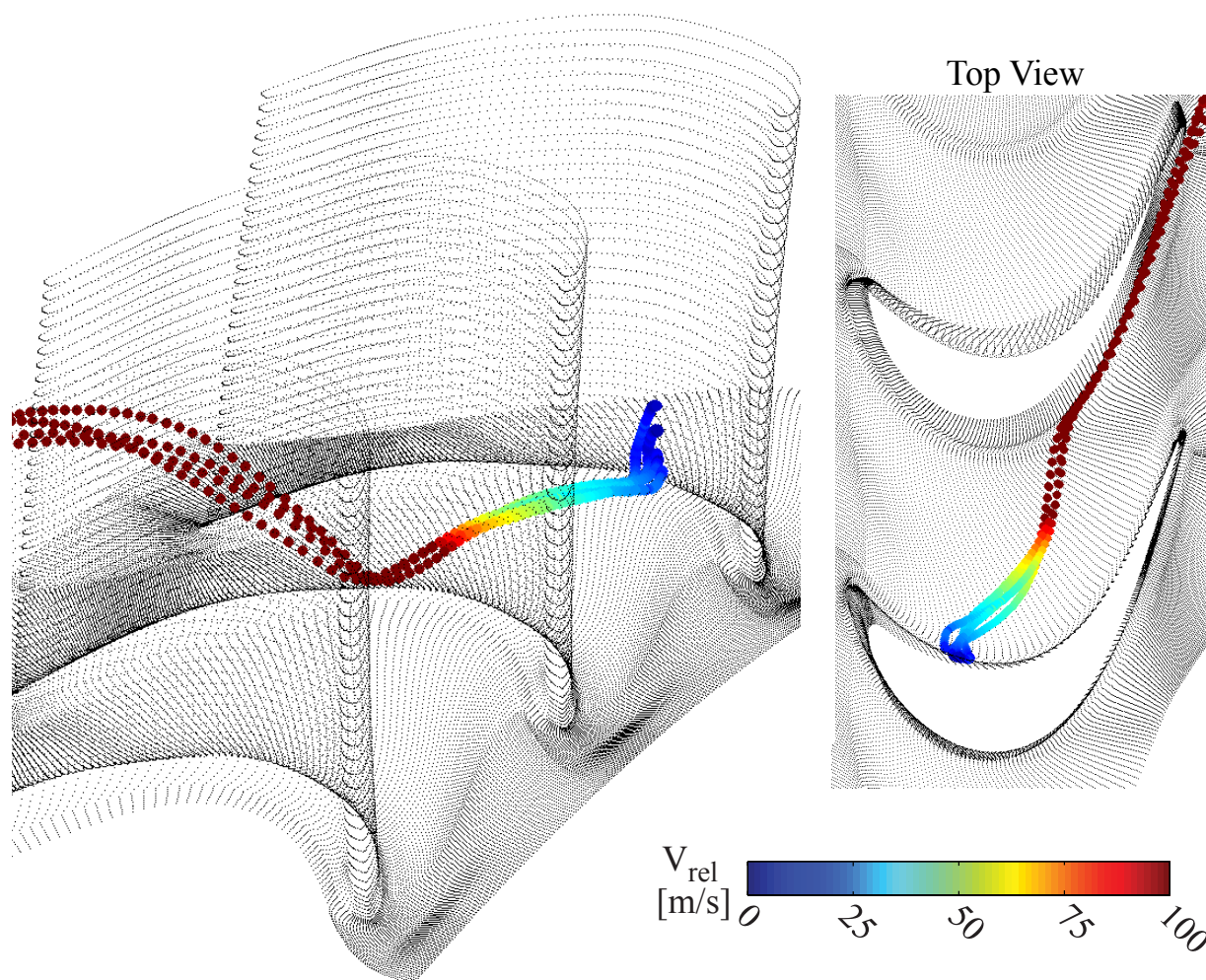


Figure 5.4.: Particle tracks of particles released inside the pressure side bubble of the rotor with non-axisymmetric (1<sup>st</sup> generation) end walls,  $IR = 0.8\%$ .

bubble at about 10% span and join the free stream inside a vortical structure. This can be seen by the oscillating nature of the radial height when the particle has left the bubble as shown in Figure 5.5. Inside this vortical structure the particles are strongly accelerated by the free stream through viscous forces; work from the free stream needs to be transferred to the bubble fluid. The significant velocity mismatch between the fluid leaving the pressure side separation and the free stream is considered to generate loss in the rotor flow field. Once the particles have left the bubble, they stay in a first phase close to the pressure side as shown by the pitch position in Figure 5.5 for cylindrical end walls. Only in approximately the last third of the rotor blade chord the particles start migrating towards the suction side. With cylindrical end walls the particles remain at low radial height until they leave the rotor domain.

In the presence of profiled end walls the bubble shedding mechanism changes.

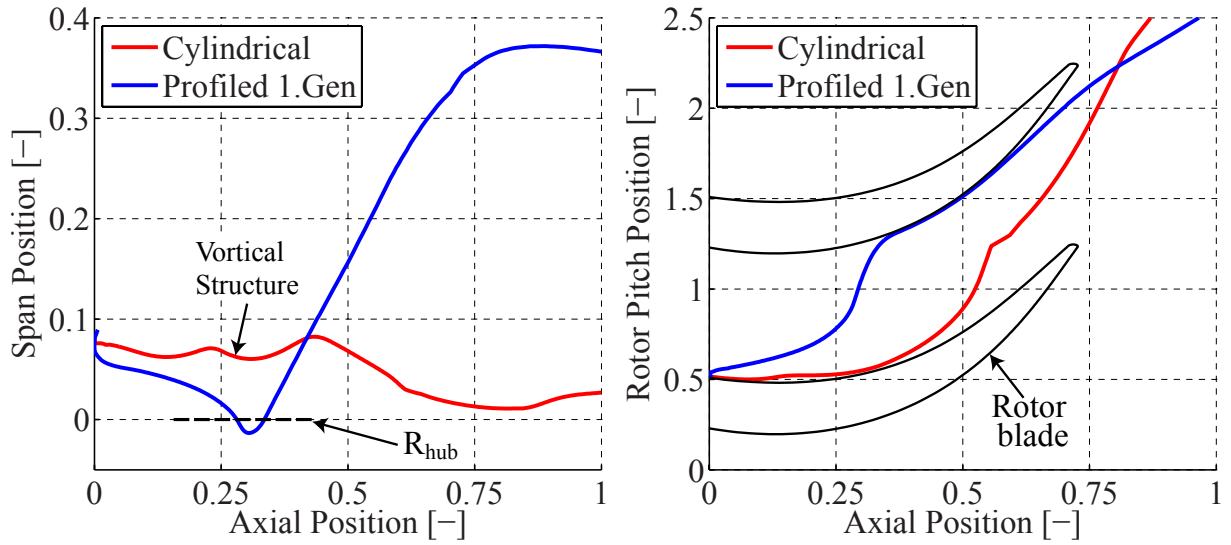


Figure 5.5.: Span and pitch position of two typical particles released inside the pressure side separation of the rotor with cylindrical and 1<sup>st</sup> generation end wall profiling ( $IR = 0.8\%$ ). The corresponding three dimensional views are shown in Figures 5.3 and 5.4. The parameters are plotted as a function of the non-dimensional axial coordinate. Zero corresponds to the point where the particles are injected inside the bubble and 1 corresponds to the moment when the particle leaves the rotor domain. The rotor blade geometry at 7% span is given in the plot on the right hand side.

The particles released inside the pressure bubble migrate slowly and radially towards the hub, as shown in Figure 5.4. The pressure side bubble fluid is of low relative momentum and therefore skews towards the region of low reduced static pressure in rotating systems. The reduced static pressure is known from literature (Moore et al. [63], Greitzer et al. [33]), and is defined in Equation 5.1:

$$P_{red} = P_s \left( \frac{2C_P T_s + (V_{rel}^2 - U^2)}{2C_P T_s + V_{rel}^2} \right)^{\frac{\kappa}{\kappa-1}} \quad (5.1)$$

On the rotor blades and end walls the relative velocity is zero ( $V_{rel} = 0$ ). Equation 5.1 can therefore be rewritten as

$$P_{red} = P_s \left( 1 - \frac{U^2}{2C_P T_s} \right)^{\frac{\kappa}{\kappa-1}} \quad (5.2)$$

Figure 5.6 shows the contour plots of computed reduced static pressure on the rotor pressure side for one specific time step. It can be seen that the

radial gradient of the reduced static pressure is outwards at the hub on the third rotor blade. This drives the stagnant bubble fluid radially inwards. Particles on the pressure side above the region of maximum reduced static pressure experience an opposite gradient and migrate towards the tip. It is also important to note that this radial gradient is not steadily present. It is a function of the relative position of the stationary and rotating blade rows. The reduced static pressure that drives the bubble migration is set up by the bubble itself, its size and shape depends on the distribution of reduced static pressure (Figure 5.2). A feedback mechanism seems to exist and the bubble blockage changes the reduced static pressure which causes the bubble fluid to migrate.

Once the particles arrive at the profiled hub end wall they start to migrate across the passage until they reach the metal of the suction side of the adjacent rotor blade, as shown in Figure 5.5(b). The particles migrate across the passage to the suction along the hub end wall. The radial coordinate of the typical particle track shown in Figure 5.5 falls below 0% span. This is only possible due to the dip in the profiled hub end wall in the region close to the rotor suction side. The vortical structure on the hub end wall shown in Figure 5.2 forms a tunnel for the pressure side separation bubble particles to travel across the passage. As the pressure side separation fluid has low momentum it responds to the cross passage pressure gradient. Once the particles arrive at the suction side they interact with the suction side secondary flows and get rolled up. In consequence they undergo a significant radial migration along the rotor suction side. The particle following the typical path presented in Figure 5.5 climbs up to 35% span and becomes part of the hub loss core. The main flow has to transfer work to these particles in order to accelerate them, creating loss to the flow. A similar mechanism has been presented by Brear et al. [14] for low pressure turbine blades in a linear cascade.

Due to the different migration pattern of the particles released inside the pressure side bubble, the radial height at which the bubble fluid leaves the rotor is significantly different between the two rotor designs. Table 5.1 gives the mean spanwise position at the rotor domain exit of the particles released inside the pressure side separation of the rotor with cylindrical and non-axisymmetric end walls for the three experimentally investigated injection rates. With cylindrical end walls the mean radial height of the bubble fluid at the rotor exit is at approximately 6% span and insensitive to the injection rate. With profiled end walls the pressure side separation particles become part of the rotor suction side passage vortex and therefore leave the

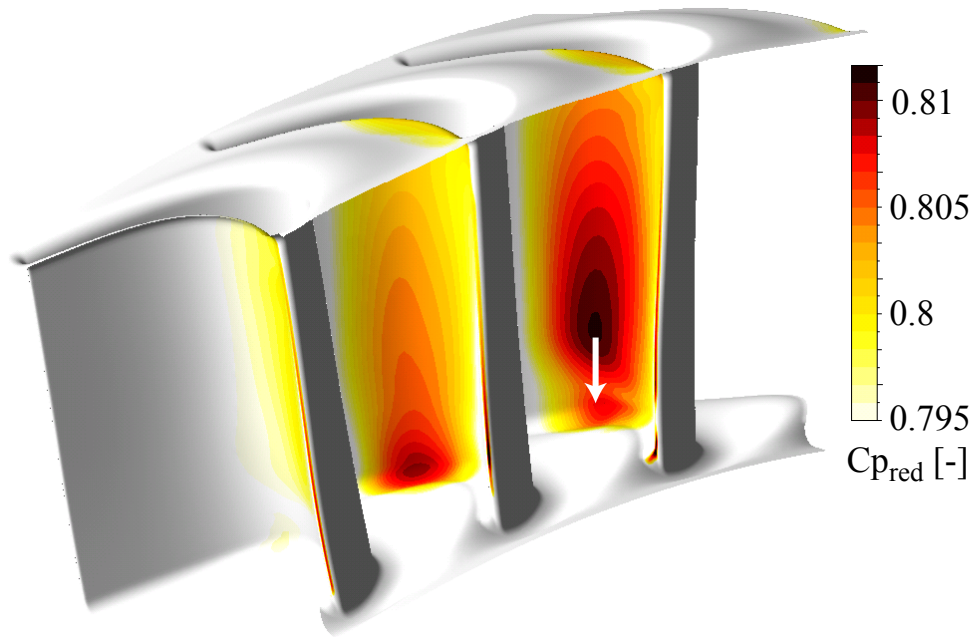


Figure 5.6.: Contour plot of normalised reduced static pressure  $Cp_{red} = P_{red}/P_{t,in}$  on the rotor blade for nominal injection rate. The white arrow indicates the gradient spatial gradient in the hub region on the rotor pressure side.

rotor at radial heights between 34% and 40%, depending on the amount of injected purge flow. The purge flow affects the radial height of the rotor hub passage vortex, as described in section 3.3. Hence the sensitivity of the radial height of the bubble fluid at the rotor exit to the purge flow injection rate is not surprising, as the bubble fluid gets rolled up in the rotor hub passage vortex in the presence of profiled end walls. However the trend has an opposite sign. Whereas the radial height of the hub passage vortex increases with increasing injection rate, the mean spanwise position of the pressure side separation fluid at the rotor exit does the opposite.

	$IR = 0.4\%$	$IR = 0.8\%$	$IR = 1.2\%$
Cylindrical	6.3%	6.4%	6.4%
Profiled 1 <sup>st</sup> Gen.	40%	39%	34%

Table 5.1.: Mean radial height (% span) at the rotor exit of the particles released inside the pressure side separation.

The geometry of the non-axisymmetric hub end wall close to the pressure side causes the change in bubble shedding mechanism. The end wall profiling introduces a convex region of curvature near the pressure side end wall corner. This is a feature that is typically present in successful non-

axisymmetric end wall profiling in this part of the passage. The effect is to reduce the static pressure in this region - tending to reduce the cross-passage pressure gradient and in consequence the amount of fluid which gets rolled up in the rotor suction side secondary flows. This effect also acts to attract the pressure side separation fluid down the blade and onto the end wall. In consequence the bubble fluid is not shed into the free stream. In the absence of a convex region of curvature near the pressure side end wall corner, the NGV1 hub secondary flows are thought to be part of the reason for the difference in bubble fluid migration. The NGV1 hub passage vortex, when it hits the rotor leading edges, causes more positive incidence between 0% and 10% span. This could be the mechanism that closes the bubble at these spanwise positions and forces it to shed at a higher radial coordinate.

Given the improved efficiency and reduced loss at the rotor exit in the presence of the 1<sup>st</sup> generation end wall profiling (section 3.3), convecting the low momentum pressure side bubble fluid inside of rotor secondary flows (along the hub end wall and then inside the hub passage vortex) out of the rotor blade row is more advantageous in terms of loss generation, than shedding it directly into the free stream. The very high velocity gradients that occur when the bubble fluid is shed into the free stream are expected to be a major reason for the increased loss generation in the presence of cylindrical end walls.

## 5.2. Purge Flow Interaction with Pressure Side Separation

Beside the relative position of the blade rows, the size and shape of the pressure side separation also depends on the amount of injected fluid. The unsteady behaviour between the separated pressure side and the injected purge flow is analysed next. Figure 5.7 shows the computed iso-surface of zero axial velocity on the rotor pressure side of the rotor with profiled end walls (1<sup>st</sup> generation) for the three different levels of injection investigated but at the same phase in the cycle. The influence of the purge flow on the bubble size as shown in Figure 5.7 is intrinsically similar for the rotor with cylindrical end walls. Generally speaking, the bubble grows with increasing rate of injection for both rotor geometries.

Rebholz et al. [80] analysed the pressure side bubble dimension by tracking its border during one cycle. The maximum axial and radial dimensions

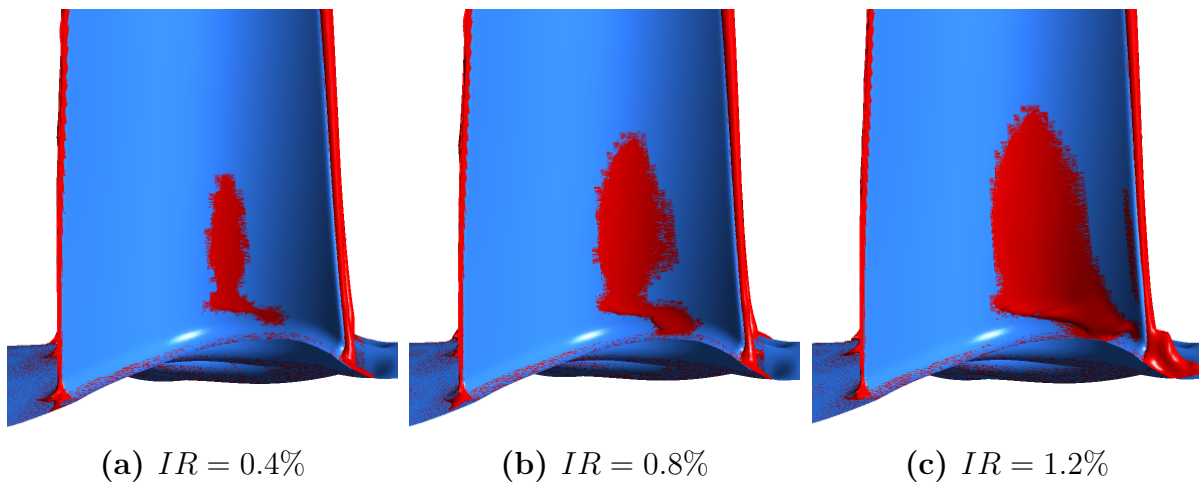


Figure 5.7.: Iso-surfaces of zero axial velocity on the rotor blade pressure side of the rotor with the 1<sup>st</sup> end wall design for three different injection levels but at the same phase in the cycle.

of the pressure side bubble during one cycle for both rotor geometries are shown in Figure 5.8. The analysis of the dimension of the pressure side bubble shows a relatively linear correlation between the maximum radial and axial dimensions and the injection rate. With cylindrical end walls the bubble is slightly larger for all injection rates, but its size is less sensitive to the purge flow injection rate. With cylindrical end walls the maximum radial amplitude increases by 8%, in the presence of profiled end walls by 17% per percent of injected purge flow. For the axial amplitude the sensitivities are 12% and 17% per percent of injected purge flow, respectively. The profiled rotor has lower radial but bigger axial amplitudes. This may be related to increased lift at the end wall in the presence of profiled end walls.

When the data shown in Figure 5.8 is extrapolated to zero injection rate the maximum bubble dimension does not become zero. This has been numerically verified. The CFD simulations also predicts a separated pressure side with and without end wall profiling when no purge flow is injected. The CFD simulations performed for the rotor with the 2<sup>nd</sup> end wall design in combination with thicker airfoils in the hub region did not detect a separated rotor pressure sides. Rebholz et al. did numerical investigations at injection rates up to  $IR = 3\%$  for the rotor with the 2<sup>nd</sup> end wall design. This corresponds to two and half times more purge flow than at the highest experimentally investigated injection rate. They found that even at this purge flow rate the simulations did not detect a pressure side bubble. Hence, based on the performed numerical simulations, the rotor blade and

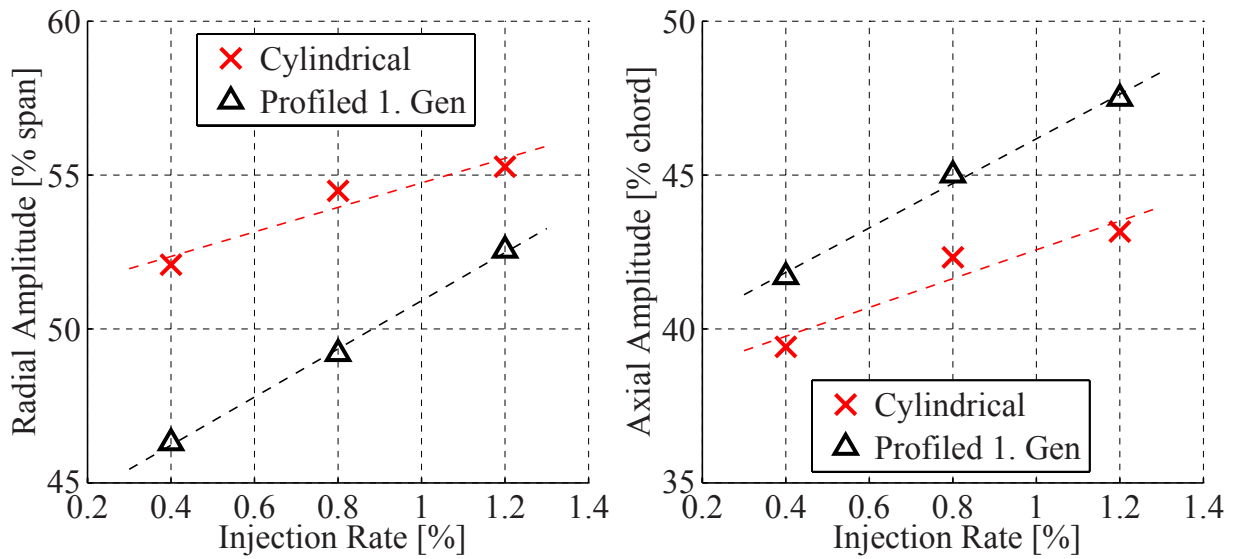


Figure 5.8.: Maximum radial and axial dimension of the pressure side bubble during one period. The rotor with cylindrical end walls is compared to the rotor with profiled end walls at the three experimentally investigated purge flow injection rate.

end wall design seems to be the element that causes the flow to separate on the rotor pressure side, and not the purge flow itself. For none of the numerically studied rotor geometries the pressure side separation occurs only above a critical limit of purge flow. The injection flow rate was numerically varied from 0% to 3%. However, if the airfoil and end wall design accommodates a pressure side separation, the rim seal purge flow interacts with it and negatively affects its volume and shape.

The pneumatic probe measurements at the NGV1 exit show an increase of static pressure of approximately 1% per percent of injected purge flow. The underlying flow mechanisms causing this increase of static pressure are discussed in section 3.1. Figure 5.9 shows this increase in static pressure for higher injection rates based on the measurement results at rotor inlet. If the static pressure increases at rotor inlet, the absolute and relative Mach numbers decrease. The reduction of the Mach number at the rotor inlet with increasing injection rate affects the relative flow yaw angle and causes negative incidence on the rotor leading edge. Figure 5.9 shows the circumferentially area and time-averaged measured change of incidence at the rotor inlet between the nominal injection rate ( $IR = 0.8\%$ ) and the lowest injection rate ( $IR = 0.4\%$ ) and the maximum injection rate ( $IR = 1.2\%$ ) and the lowest injection rate. For the higher span-wise positions in the free stream the difference is between  $-1^\circ$  and  $-2^\circ$ . Close to the hub

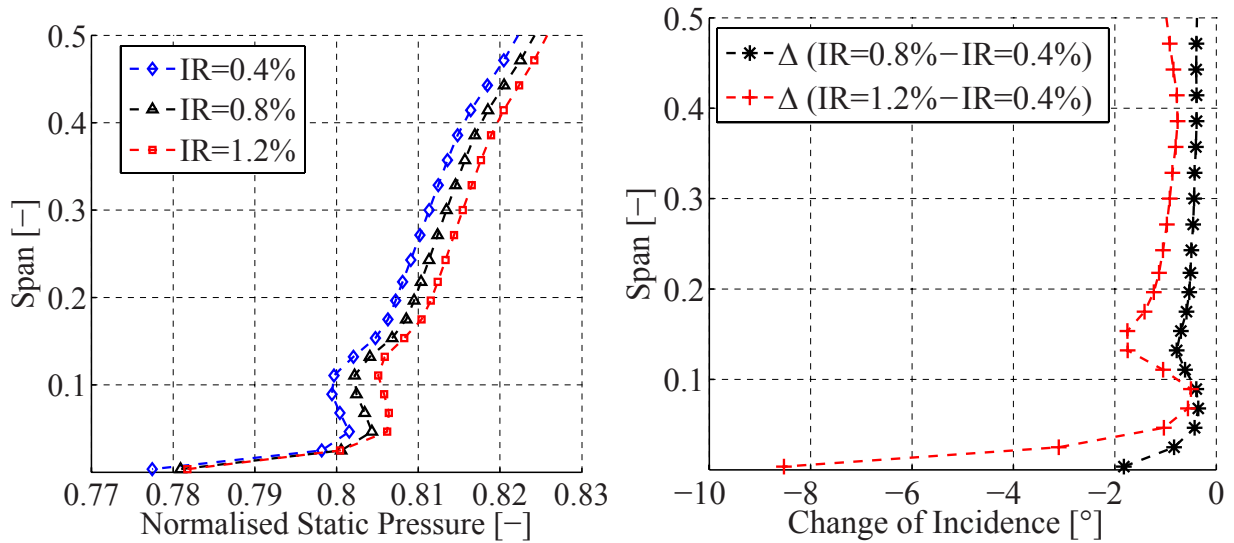


Figure 5.9.: Circumferentially area and time-averaged measured normalised static pressure  $Cp_s$  and change of incidence between nominal injection rate ( $IR = 0.8\%$ ) and the lowest injection rate ( $IR = 0.4\%$ ) and the maximum injection rate ( $IR = 1.2\%$ ) and the lowest injection rate at rotor inlet (4-hole probe).

the maximum measured difference of relative flow yaw angle between the lowest and highest injection rate peaks at about  $-9^\circ$ . The missing swirl of the injected purge flow compared to the free stream mainly causes the difference in relative flow yaw angle close to the hub. The relatively thin rotor blade profiles do not tolerate a negative change in incidence well and as a consequence the pressure side bubble becomes bigger. The strong dependence of the pressure side separation behaviour on the flow incidence angle is well known [106], [40].

### 5.3. Influence of Bubble on Rotor Exit Flow Field

In this section the measurements made in the presence of the 1<sup>st</sup> and 2<sup>nd</sup> rotor end wall design are compared with each other in order to analyse the influence of the pressure side separation on the rotor exit flow field. Some caution is required when the 1<sup>st</sup> and 2<sup>nd</sup> end wall designs are compared. Although their general hub end wall topology consists of the same main features and has similar maximum and minimum radial amplitudes, the 2<sup>nd</sup> design is the result of an optimisation with thicker airfoils in the 2<sup>nd</sup> hub region. Due to the thicker airfoils the flow remains attached to the blade on the pressure side. Therefore the measured differences in the rotor

exit flow field are not exclusively caused by the absence of the pressure side bubble, but may also be related to the slightly adapted hub end wall design. Contour plots of the variation of the hub radius are plotted in section 2.2.1. Therefore only a limited number of variables aiming to outline the combined effects of the removal of the pressure side separation and the 2<sup>nd</sup> end wall design will be presented in this section. The study will focus on the hub loss core and the region below the hub loss core as this is the region where the blade has been thickened. The particle tracking has shown that the bubble fluid can be expected to leave the rotor domain inside the hub passage vortex. Complementary results can be found in section 6.2.

The modifications caused to the flow field at the NGV1 exit due to the updated end wall profiling and blade geometry are very small and within the measurement uncertainties and will therefore not be studied here. This is also valid for the flow field at the rim seal exit. The end wall profiling upstream of the rotor leading edges at the hub platform leading edge (wavy shape) is very similar for the 1<sup>st</sup> and 2<sup>nd</sup> end wall designs.

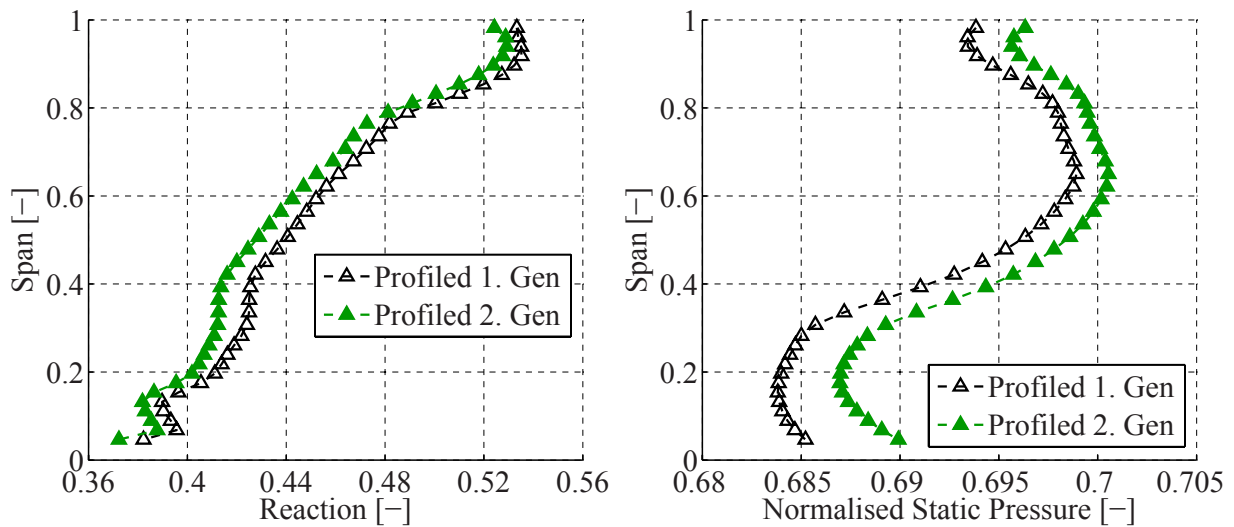


Figure 5.10.: Mass and time-averaged measured reaction  $R$  and area-averaged normalised static pressure  $Cp_s$  for the 1<sup>st</sup> and the 2<sup>nd</sup> end wall designs at the rotor exit ( $IR = 0.8\%$ , pneumatic probes).

Figure 5.10 shows the mass and time-averaged normalised static pressure at the rotor exit and reaction for the nominal injection rate for the two end wall designs. The reaction  $R$  is calculated based on the pneumatic pressure measurements using Equation 4.1. The measured mass-weighted reaction of the rotor with pressure side separation and the 1<sup>st</sup> end wall design is 44.7% at the nominal injection rate. The rotor with thicker airfoils and 2<sup>nd</sup> end wall design reduces the reaction by 0.9% (abs.) on average.

The radial distribution of the reaction shows a decrease in reaction for all radial heights, however with slightly bigger differences between 20% and 60% span, the region influenced by the hub passage vortex. The maximum reduction of the reaction (1.25%, abs.) occurs at 36% span. The turbine and rotor inlet static pressure distributions required for the evaluation of the reaction are identical for both end wall designs. Hence the difference in reaction must be caused by the difference in static pressure at the rotor exit. The corresponding radial distribution of area-averaged normalised static pressure is given on the right hand side in Figure 5.10. The radial trend of the static pressure is not modified by the removal of the pressure side separation. However the thicker airfoil and 2<sup>nd</sup> end wall design increase the static pressure by 0.2% to 0.35% above 50% span and by 0.35% to 0.65% in the other half of the span.

Figure 5.11 shows the mass and time-averaged measured total-to-total stage efficiency  $\eta_{tt}$  and normalised relative total pressure  $Cp_{t,rel}$  for the 1<sup>st</sup> and the 2<sup>nd</sup> end wall designs at the rotor exit. The 2<sup>nd</sup> end wall design improves the overall total-to-total efficiency by  $0.30\% \pm 0.32\%$ . The removal of the pressure side separation improves the  $\eta_{tt}$  at all radial heights, except between 70% and 82% span. Three main regions of efficiency improvement are proposed: Above 80% span the efficiency improves by up to  $1.0\% \pm 0.32\%$ . The hub end wall profiling does not influence the rotor exit flow field at these spanwise positions (cf. section 4.3), these improvements are related the modified shroud end wall profiling. The effects of the profiled shroud are studied in section 4.4. The efficiency improvement between 25% and 65% has to be related with an improvement within the hub loss core, present at these spanwise positions. The pressure side bubble fluid was found to leave the rotor blade row as part of the hub passage vortex (cf. section 5.1.2). The absence of the pressure side bubble fluid inside the hub passage vortex is supposed to be a factor for the  $\eta_{tt}$  improvement in this region. Finally the total-to-total efficiency continuously improves below the hub passage vortex (below 20% span) reaching a maximum of  $1.3\% \pm 0.32\%$  at the hub. Hence the thicker airfoil at these spanwise positions appears to improve the efficiency.

The radial distribution of normalised relative total pressure reflects the three regions of improved total-to-total efficiency as regions of increased  $Cp_{t,rel}$ . Assuming the centre of the hub passage vortex to be at the radial height of minimum relative total pressure, the removal of the pressure side separation has further reduced the radial height of the hub loss core by approximately 2% to 3% at the nominal injection rate.

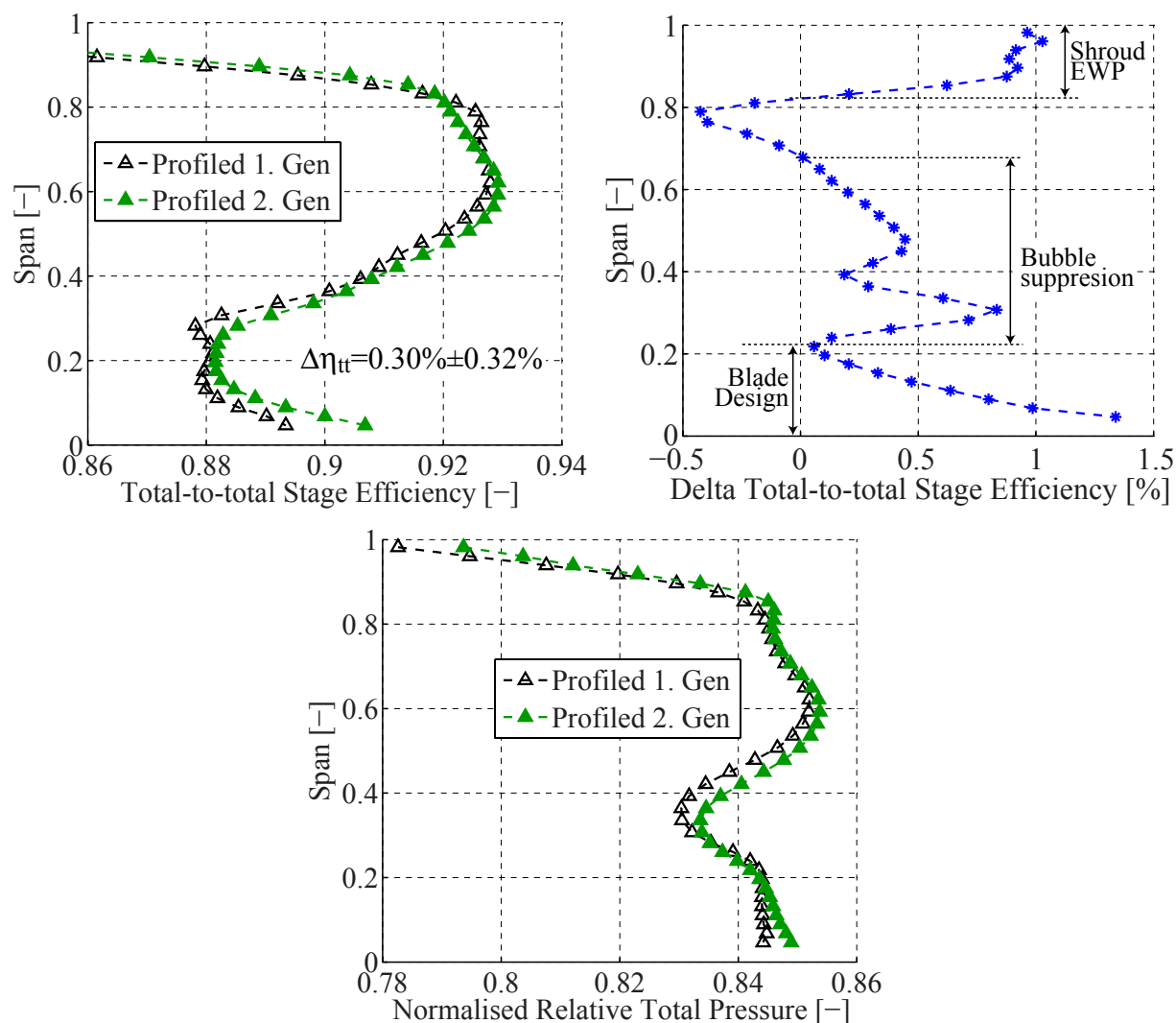


Figure 5.11.: Mass and time-averaged measured total-to-total stage efficiency  $\eta_{tt}$ , absolute difference and normalised relative total pressure  $Cp_{t,rel}$  for the 1<sup>st</sup> and the 2<sup>nd</sup> end wall designs at the rotor exit ( $IR = 0.8\%$ , 5-hole probe).

## 5.4. Summary

In this chapter the unsteady behaviour of the pressure side bubble is studied based on time-accurate CFD simulations. The analysis relies entirely on unsteady CFD simulations and therefore needs to be considered with some care. The prediction of the behaviour of the pressure side separation and of the underlying shear stresses strongly depends on the transition and the turbulence models of the CFD code used in the context of this work. Direct numerical simulation would be required to predict and understand the involved flow mechanisms in greater detail.

Time-accurate CFD simulations showed a strong interaction between the

size and shape of the pressure side bubble and the nozzle guide vane wake when it is convected through the rotor. Depending on the relative position of the blade rows the bubble can nearly disappear for a limited period of time. During one period the bubble was found to disappear twice and build up again after having disappeared. During one period the NGV wake hits the rotor twice, therefore there may be a link between the two elements. The 1<sup>st</sup> end wall design successfully reduces the volume and maximum size of the pressure side separation but does not appear to influence the described unsteady behaviour.

However the non-axisymmetric hub end wall influences the shedding mechanism for the fluid inside the bubble when it collapses. In the presence of profiled hub end walls particle tracking calculation showed that the pressure side bubble fluid migrates radially towards the hub under the effect of the rotor flow field and then across the passage inside a vortical structure attached to the profiled hub end wall. Once the fluid arrives on the rotor suction side shoulder it gets rolled up in the rotor suction side hub passage vortex and finally convected out of the rotor blade row as part of the vortex. With cylindrical end walls the pressure side bubble fluid is directly shed into the free stream at approximately 10% span and then leaves the rotor blade row underneath the hub passage vortex at low radial height. The high velocity mismatch compared to the free stream is pushing up the mixing loss.

For both end wall geometries (cylindrical and 1<sup>st</sup> generation) the rim seal purge flow was found to have a strong negative effect on the size of the pressure side bubble as it increases the static pressure by 1% per percent of injected purge flow at the rotor inlet. As a consequence, the relative Mach number and flow yaw angle decrease causing negative incidence on the airfoil stimulating the separation process. Furthermore, based on the CFD simulations the maximum axial and radial extension of the bubble increases with increasing amount of injected purge flow in a relatively linearly manner.

The rotor with the 2<sup>nd</sup> end wall design combined with the thicker rotor blades in the hub region does not show separated pressure sides. Even at injection rates reaching 3% no pressure side separations were detected by the numerical prediction. Hence the purge flow does not appear to be the flow structure causing a pressure side separation, but strongly interacts in a negative way if a bubble is present for a given blade geometry.

Measurements performed at the rotor exit showed a  $0.30\% \pm 0.32\%$  total-to-total stage efficiency increase due to removal of the pressure side bubble.

---

The efficiency was found to increase at low spanwise positions below the hub passage vortex, in the hub passage vortex region and above 80% span. On average, the thicker airfoils and 2<sup>nd</sup> end wall design have decreased the reaction by 0.9% (abs.) in the form of a nearly constant offset for all spanwise positions. The radial coordinate of the hub passage vortex is further reduced by 2% to 3% (abs.) in the presence of the 2<sup>nd</sup> end wall design.



## 6. Combined Effects of Profiled End Walls and Purge Flow

After having studied the unsteady effects of purge flow (chapter 3), the non-axisymmetric (chapter 4) end wall contouring and the behaviour of the pressure side bubble (chapter 5) in an isolated manner, this chapter focuses on the combined unsteady interaction mechanisms. All nine investigated test cases during the entire measurement campaign are considered and mutually compared. Measurements were performed at three different injection rates ( $IR = 0.4\%$ ,  $0.8\%$  and  $1.2\%$ ) for each of the three rotor geometries (with cylindrical, 1<sup>st</sup> and 2<sup>nd</sup> end wall design) associated with three different pressure side bubble sizes. The measurements provide a consistent data set in the form of 3x3 matrix at NGV1 exit, rotor exit and NGV2 exit.

So far the effects along separated lines or columns of this 3x3 data matrix have been analysed, whereas in this chapter the corners of the matrix will also be considered, where the interaction effects are often most clearly seen. The numerous unsteady interaction mechanisms among all the nine investigated test cases are chosen not to be analysed with the same rigor as in the former chapters given the extensive amount of data and the involved complexity, especially with regard to the time domain. The underlying unsteady mechanisms are detailed and analysed in the corresponding chapters 3 and 4. In the present chapter the matrix data will typically be presented as solid bar charts in 3d perspective view in order to easily see the time-averaged trends in both variables. The data is normalised with the best efficiency case which is the rotor with 2<sup>nd</sup> generation end wall profiling at the low injection rate. A few selected time-averaged radial distributions and area traverse plots will be used to illustrate selected trends and mechanisms. This chapter only presents probe traverse measurement results at the NGV1 exit and rotor exit knowing that the unsteady CFD simulations were required in order to detect and analyse the separated pressure sides present for the rotors with cylindrical and 1<sup>st</sup> generation non-axisymmetric end walls.

## 6.1. Combined Interaction Mechanisms at the NGV1 Exit

The effects of the purge flow and the rotor end wall profiling at the NGV1 exit can mainly be found in the cavity exit region at very low or negative spanwise position with limited probe access and are of an unsteady nature. The variations in the main NGV1 exit flow field caused by the purge flow and the rotor geometry are of small amplitude and typically not far beyond the measurement uncertainty. However when the extreme case scenarios are compared caused effects are clearly outside the measurement uncertainty bandwidth allowing for relative comparison. Furthermore, the results from all nine test cases show a high level of consistency with regard to the observed trends caused by the purge flow or the rotor design also enhancing their reliability. Figure 6.1 shows the area and time-averaged

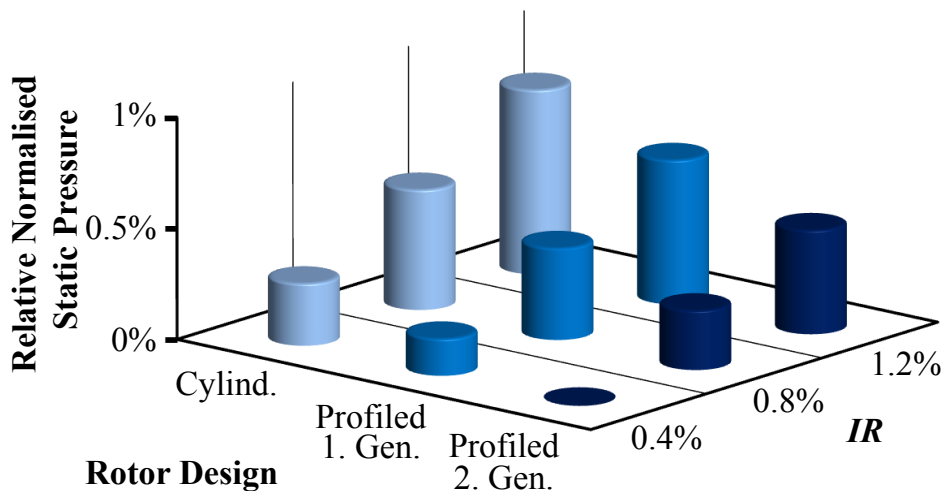


Figure 6.1.: Area and time-averaged normalised static pressure  $Cp_s$  at the NGV1 exit for all nine test cases. The values are presented relative to the reference case: the rotor with 2<sup>nd</sup> generation end wall profiling and rotor blade geometry at the low injection rate (4-hole probe).

normalised static pressure  $Cp_s$  at the NGV1 exit for all nine test cases. The area weighted integral was performed over one NGV1 pitch. The normalised pressure values are presented relative to the reference case which is the measurement with the rotor equipped with 2<sup>nd</sup> generation end wall profiling and rotor blade geometry at the low injection rate. The area-averaged static pressure linearly increases by 0.8% per percent of injected purge flow for all rotor geometries as observed in section 3.1 when studying the rotor with 1<sup>st</sup> generation end wall profiling. The highest overall levels of static pressure are measured in the presence of cylindrical rotor end

walls. This is the rotor with the biggest pressure side bubble size. The static pressure is lowest at the inlet of the rotor with the 2<sup>nd</sup> generation of profiled end walls and in the absence of a pressure side bubble. The effects of the rotor design on the static pressure at rotor inlet are identical for all investigated injection rates. The 1<sup>st</sup> and 2<sup>nd</sup> end wall design both reduce the time-averaged static pressure at the rotor inlet by 0.15% on average at all purge flow injection rates.

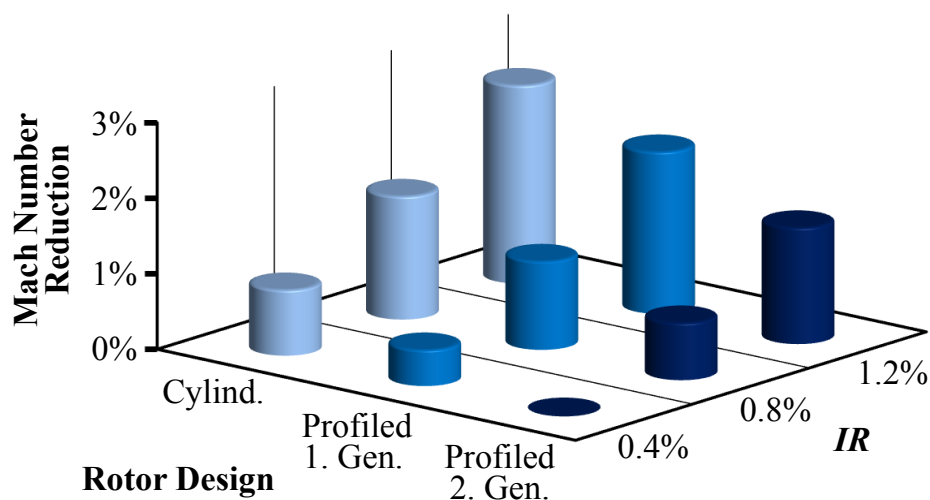


Figure 6.2.: Mass and time-averaged Mach number  $M$  at the NGV1 exit for all nine test cases. The values are presented as a Mach number reduction relative to the reference case (4-hole probe).

The corresponding variations of Mach number are shown in Figure 6.2 for all the nine investigated test cases. The mass and time-averaged Mach numbers are evaluated using the same calculation methods as for the normalised static pressure and show the decrease of Mach number relative to the best efficiency reference case. The overall trends observed for the  $Cp_s$  are confirmed by the Mach number, at an exchange rate of about 1 to  $-3$ . Or in other words, when the static pressure increases by 1%, the Mach number drops by approximately 3%. When comparing the influence of the rotor design and the injection rate on the rotor inlet flow field at the Mach number of interest, one can see that the flow modifications caused by the variation of purge flow are slightly more pronounced than the modifications caused by the end wall profiling and the bubble size. The underlying unsteady mechanisms are detailed and analysed in chapters 3 and 4.

## 6.2. Combined Interaction Mechanisms at the Rotor Exit

The combined effects of the non-axisymmetric end walls and the purge flow rate in the rotor exit flow field are studied next. The analysis will focus on the sensitivity of total-to-total efficiency to purge flow, the turbine reaction and the combined effects in the hub loss core region. At the rotor exit the effects of the shroud end wall profiling do not interact with the purge flow.

### 6.2.1. Sensitivity of Efficiency to Purge Flow

In this section the measured total-to-total efficiency is studied for all nine test cases. Pneumatic 5-hole probe measurements at the rotor exit are considered. The definition of the total-to-total efficiency  $\eta_{tt}$  accounting for the injected purge flow used for this study is given in Equation 2.23. Figure

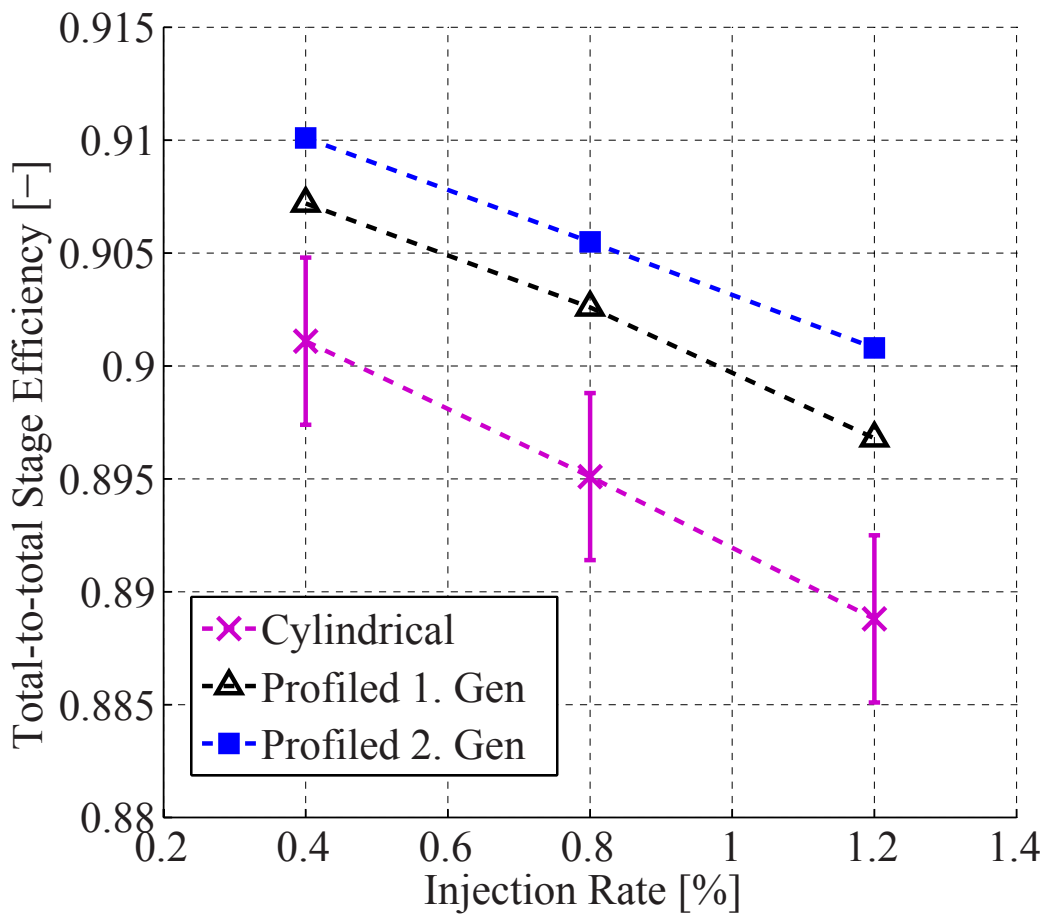


Figure 6.3.: Mass and time-averaged overall measured total-to-total stage efficiency  $\eta_{tt}$  for all nine test cases (5-hole probe).

6.3 shows the measured total-to-total efficiencies as a function of injected purge flow for the three investigated rotor geometries. The absolute expanded uncertainty of  $\pm 0.37\%$  for the total-to-total efficiency is drawn as error bars for the rotor with cylindrical end walls in Figure 6.3. The absolute expanded uncertainty bandwidth is the same for all test cases. The highest total-to-total stage efficiency ( $\eta_{tt} = 91.0\% \pm 0.37\%$ ) is measured with the 2<sup>nd</sup> generation end wall profiling on the rotor at the low injection rate. The lowest efficiency ( $\eta_{tt} = 88.9\% \pm 0.37\%$ ) was measured with cylindrical end walls at the highest injection rate. Table 6.1 shows the measured  $\eta_{tt}$  improvements between the three rotor geometries for the three injection rates. Due to the beneficial effect of the 1<sup>st</sup> shaped rotor end wall design, the measured total-to-total efficiency has increased by  $0.75\% \pm 0.32\%$  for the nominal injection rate on an absolute scale compared to the rotor with the same blade geometry but cylindrical end walls. Schuepbach et al. [94] reported a  $0.3\% \pm 0.32\%$  total-to-total efficiency increase due to successful rotor end wall contouring using the same NGV as in the present experiment but an unshrouded rotor with high pressure turbine representative airfoils. The thicker airfoils in the hub region of the rotor with the 2<sup>nd</sup> generation end wall profiling removes the pressure side bubble and further improves the total-to-total efficiency by  $0.33\% \pm 0.32\%$  on average resulting in a total average efficiency benefit of  $1.05\% \pm 0.32\%$  compared to the rotor with cylindrical end walls.

	$\Delta\eta_{tt}$ (1 <sup>st</sup> Gen. – Cylindrical)	$\Delta\eta_{tt}$ (2 <sup>nd</sup> Gen. – Cylindrical)	$\Delta\eta_{tt}$ (2 <sup>nd</sup> Gen. – 1 <sup>st</sup> Gen.)
$IR = 0.4\%$	$0.61\% \pm 0.32\%$	$0.90\% \pm 0.32\%$	$0.29\% \pm 0.32\%$
$IR = 0.8\%$	$0.75\% \pm 0.32\%$	$1.04\% \pm 0.32\%$	$0.30\% \pm 0.32\%$
$IR = 1.2\%$	$0.81\% \pm 0.32\%$	$1.20\% \pm 0.32\%$	$0.40\% \pm 0.32\%$
Average	$0.72\% \pm 0.32\%$	$1.05\% \pm 0.32\%$	$0.33\% \pm 0.32\%$

Table 6.1.: Measured total-to-total efficiency  $\eta_{tt}$  improvements between the three rotor designs for the three investigated purge flow injection rates.

The effect of injected purge flow on the efficiency is given for the three rotor geometries in Table 6.2. The decrease in efficiency with increasing  $IR$  appears to be linear for all three measured rotor geometries. Neither the end wall profiling design nor the presence of the pressure side separation have an influence on the linear behaviour of the sensitivity to purge flow. The rotor with thicker airfoils in the hub region combined with the 2<sup>nd</sup>

profiled end wall design has the lowest sensitivity to purge flow, its total-to-total stage efficiency decreases by 1.17% per percent of injected purge flow. This 2<sup>nd</sup> generation rotor design has not only successfully improved the overall efficiency, but also reduced the sensitivity to purge flow, in line with the design intent. Compared to the rotor with the 1<sup>st</sup> generation end wall design with the pressure side bubble the sensitivity to purge flow is reduced by 10%. Furthermore, if the end wall profiling is removed at constant blade geometry, the sensitivity is increased by another 20% to 1.54%  $\eta_{tt}$  reduction per percent of injected purge flow, resulting in an overall increase of the sensitivity to purge flow of about 30% between the best and worst case. Schuepbach et al. [92] reported a 1.2% decrease of total-to-total efficiency per percent of injected fluid. They also reported similar trends for the sensitivity reduction of efficiency to purge flow. In terms of exchange rates the end wall profiling alone can bring back the efficiency deficit of about 0.6% of additional purge flow. The combined effects of pressure side bubble suppression and end wall profiling account for about 0.8% of injected purge flow.

	$\% \eta_{tt}$ per $\% IR$	$\eta_{tt}$ at $IR=0$
Cylindrical	-1.541	90.7%
Profiled 1 <sup>st</sup> Gen.	-1.296	91.3%
Profiled 2 <sup>nd</sup> Gen.	-1.170	91.5%

Table 6.2.: Interpolated sensitivities of total-to-total stage efficiency for the three rotor geometries shown in Figure 6.3.

In order to further analyse the efficiency improvements and sensitivity reductions, Figure 6.4 shows the radial distributions of total-to-total efficiency as a function of injection rate for the three different rotor designs. These radial distributions of  $\eta_{tt}$  show that the purge flow mainly deteriorates the efficiency in the hub passage vortex region for all tested rotor geometries. The underlying unsteady mechanisms have been discussed in section 3.3 for the rotor with the 1<sup>st</sup> generation end walls. Furthermore, the profiled end wall improves the efficiency in this same region as analysed in section 4.3. The offsets between two corresponding radial distributions of  $\eta_{tt}$  cause the absolute improvements in efficiency listed in Table 6.1. The differences between the curves at the low and the high injection rates for different rotor geometries partially explain the different sensitivities to purge flow listed in Table 6.2. The 1<sup>st</sup> generation end wall profiling reduces the difference between the radial distribution at the low and the high injection rates for

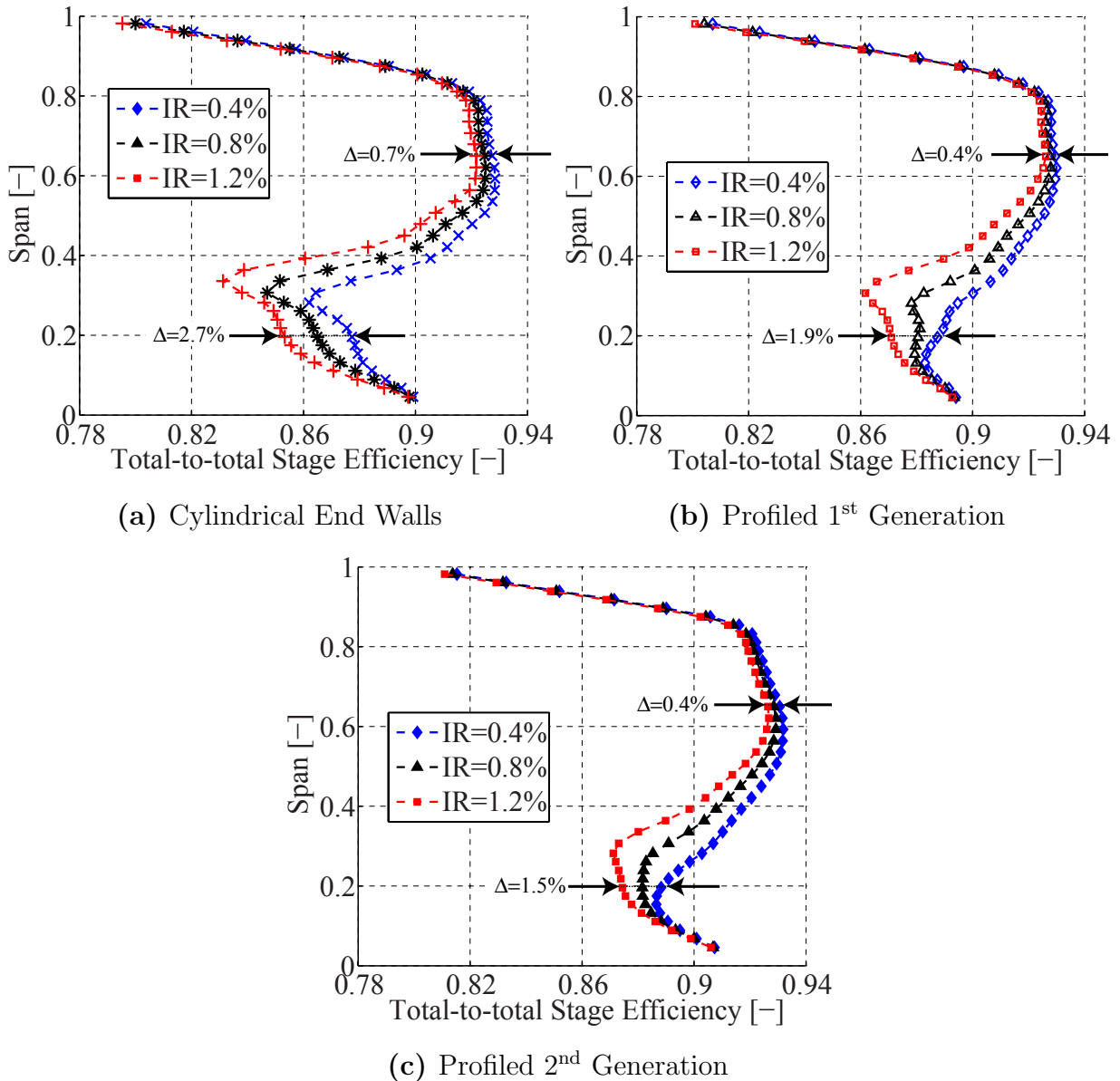


Figure 6.4.: Radial distribution of mass and time-averaged overall measured total-to-total stage efficiency  $\eta_{tt}$  as a function of the injection rate for the three tested rotor designs (5-hole probe).

nearly all spanwise positions including the free stream region between 60% and 85% span. This is indicated by the arrows in Figures 6.4(a) and 6.4(b) and illustrates the 20% lower sensitivity to purge flow. The 2<sup>nd</sup> generation end wall profiling does not significantly affect the sensitivity in the free stream region at the rotor exit, but mainly decreases the offset between the low and high injection rate distributions below the hub loss core at radial heights between 10% and 25% span, as indicated by the arrows in Figure 6.4.

## 6.2.2. Turbine Reaction

Figure 6.5 shows the measured turbine reaction for the nine experimentally investigated configurations. The reaction  $R$  is calculated based on the pneumatic pressure measurements at rotor inlet and exit using Equation 4.1. For all three rotor geometries the purge flow increases the reaction by approximately 1.6% to 1.8% per percent of injected purge flow. Probe measurements at the rotor inlet show a 1% increase of the static pressure per percent of injection rate (cf. section 3.1). The static pressure term in Equation 4.1 increases the reaction at higher injection rate. In section

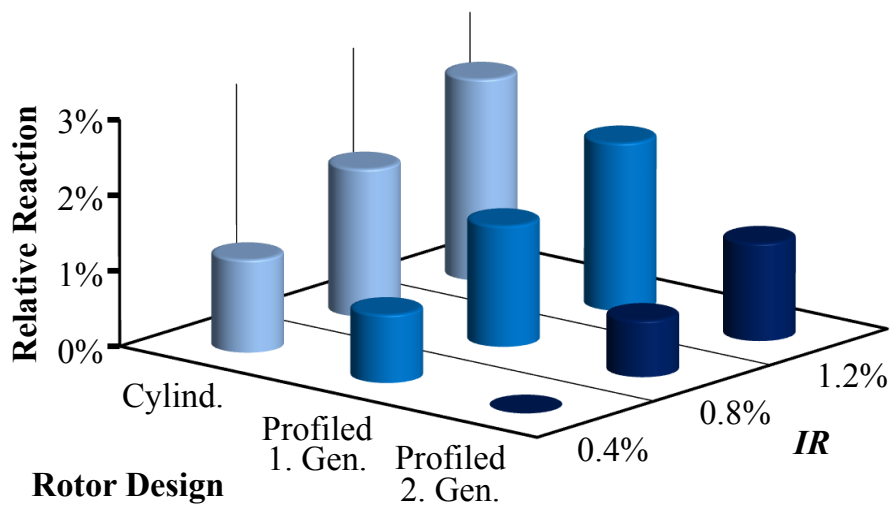


Figure 6.5.: Area and time-averaged relative turbine reaction for all nine test cases. The reaction is presented as an increase of reaction (absolute percentage) relative to the reference case (pneumatic probes).

4.3 the reaction was found to decrease by 0.3% (abs.) on average in the presence of end wall profiling (1<sup>st</sup> generation) at the nominal injection rate. Figure 6.5 shows that the 1<sup>st</sup> end wall design reduces the reaction by the same amount at all investigated injection rates. The slight reduction of the overall reaction is caused by an increase of the static pressure in the hub loss core region (between 20% and 50% span) at the rotor exit. Outside of this limited region the change of the reaction was within the measurement uncertainties and the end wall design intent achieved. However the thicker airfoil and 2<sup>nd</sup> end wall design involve an average reduction of the reaction by 0.8% (abs.) for all spanwise positions. A shift of the static pressure at the rotor exit in the presence of the 2<sup>nd</sup> end wall design for all radial heights (cf. Figure 5.10) causes the reduction of reaction. Again this behaviour is insensitive to the purge flow rate.

### 6.2.3. Impact on Rotor Hub Loss Core

The rotor hub passage is the secondary flow feature which shows a strong reaction to the variation of the purge flow rate and the rotor hub end wall geometry. The involved combined interaction mechanisms are studied next, starting with the relative flow yaw angle. Figure 6.6 shows the circumferentially mass and time-averaged relative flow yaw angle at the exit of the three tested rotor geometries at the low and the high injection rates. The strong radial gradients of flow yaw angle between 10% and 60% span are caused by the rotor hub passage vortex and indicate streamwise vorticity (Equation 2.25). Generally speaking and based on the radial distributions of relative flow yaw angle two things can be observed. Firstly the injection

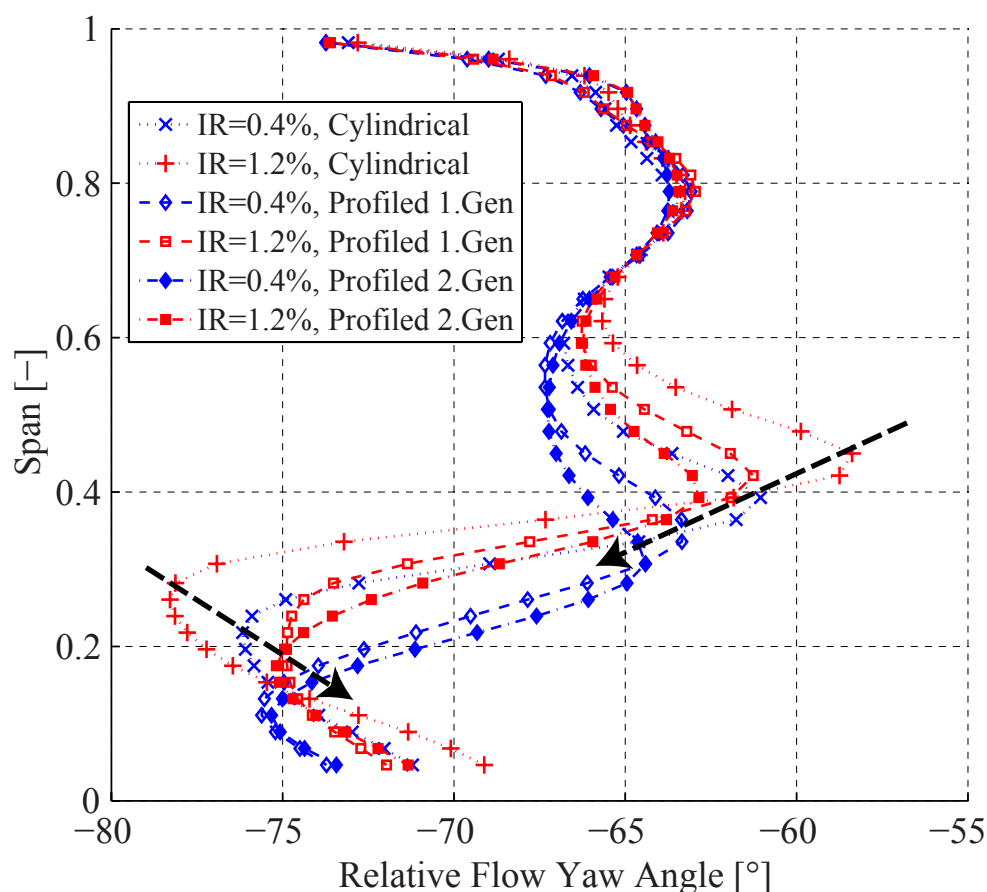


Figure 6.6.: Mass and time-averaged relative yaw angle for the three tested rotor geometries at the low and the high injection rates (5-hole probe).

rate increases both, the radial height and the strength of the hub passage vortex for all the tested rotor geometries. In other words the average radial position of the maximum and minimum relative yaw angles and the difference between the maximum and minimum yaw angles increases at higher

purge flow rate. The radial coordinate of the hub loss core is further analysed in the context of Figure 6.9. Secondly both end wall designs have similar effects as described at all the investigated injection rates. The 2<sup>nd</sup> generation of profiled end walls with thicker airfoils in the hub region further amplifies the positive effects achieved with the 1<sup>st</sup> generation of profiled end walls in terms of a reduction of the radial height and strength (difference between maximum and minimum relative yaw angle) of the hub loss core at a given injection rate. For example, this difference of relative flow yaw angle between the maximum and minimum increases from 15° at the low injection rate to 20° at the high injection rate for the rotor with cylindrical end walls. In the case of the rotor with the 2<sup>nd</sup> generation of profiled end walls the difference increases from 11° to 12.5° under the effect of increased purge flow rate. The combination of the two mentioned effects reveals that the end wall profiling also reduces the sensitivity of the strength of the hub loss core to the injection rate. 0.8% of additional purge mass flow increases the difference between maximum and minimum relative flow yaw angle by 5° for the rotor with cylindrical end walls. This difference is reduced to 1.5° in the presence of the 1<sup>st</sup> or 2<sup>nd</sup> end wall design. Hence, the 2<sup>nd</sup> end wall design does not further significantly reduce the strength of the rotor hub passage vortex, but does reduce the radial height.

Furthermore it can be seen in Figure 6.6 that both, the rotor hub end wall profiling and the purge flow only have an influence on the rotor exit flow field at the traverse plane below 65% spanwise position. The shroud end wall profiling appears to slightly influence the rotor exit flow field above 75% span. The measured differences are outside of the probe uncertainty bandwidth. However at this radial heights the injection rate does not have any influence and the caused variations must be related with the geometrical modifications on the shroud end wall.

An interesting parameter to analyse in this context is the experimentally evaluated root mean square values (*rms*) of the random part of the total pressure signal. The unsteady pressure signal provided by the FRAP is considered. The calculation of the *rms* is defined in Equation 2.24. Regions of high *rms* are indicative of significant non-deterministic unsteadiness. Area traverse plots in the relative frame at the rotor exit of the *rms* are given in Figures 4.11 and 3.19 and are representative of all the nine test cases. In the context of these two Figures the influence of the purge flow and the end wall profiling on the non-deterministic unsteadiness in the hub passage vortex has been analysed. Other secondary flow structures transporting high *rms* fluid have been identified and are found not to be

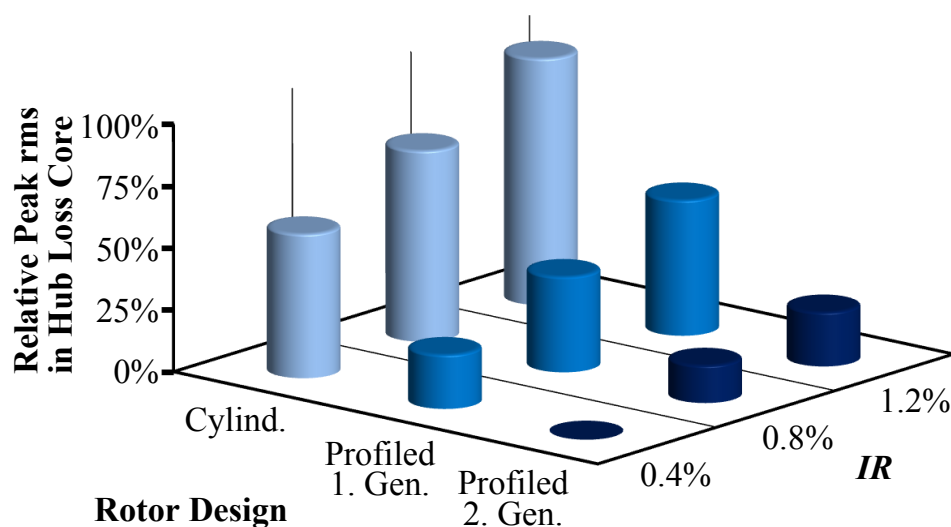


Figure 6.7.: Relative increase of the peak *rms* of the rotor relative total pressure  $P_{t,rel}$  in the rotor hub passage vortex for all nine test cases. The values are presented relative to the reference case: the rotor with 2<sup>nd</sup> generation end wall profiling and rotor blade geometry at the low injection rate (FRAP).

significantly affected by the purge flow and the end wall profiling. Figure 6.7 compares the measured peak *rms* of the  $P_{t,rel}$  in the hub loss core at the rotor exit for all test cases investigated. The rotor with the 2<sup>nd</sup> generation end walls shows the lowest non-deterministic unsteadiness (1650 Pa at  $IR = 0.4\%$ ) in the hub passage vortex core for all injection rates when compared to the other two rotor end wall designs and is therefore used to non-dimensionalise the other values. The pressure side separation present for the rotor with the 1<sup>st</sup> generation end wall profiling increases the maximum experimental *rms* by an average of 25% compared to the 2<sup>nd</sup> generation end walls. With cylindrical end walls the peak *rms* increases by 60% compared to the rotor with cylindrical end walls and by 30% compared to the rotor with the 1<sup>st</sup> end wall design. In other words, the beneficial effects of the end wall profiling and the removal of the bubble have about the same positive impact on experimental peak *rms* in the hub loss core for all measured injection rates.

The measured effect of injected purge flow on the rotor exit flow is intrinsically similar for all rotor geometries. The purge flow appears to increase the maximum non-deterministic unsteadiness in the hub passage vortex in a relatively linear manner. For instance, the measured peak *rms* value in the hub passage vortex increases by about 40% per percent of injected purge flow for the rotor with the 1<sup>st</sup> generation end wall profiling. However, the sensitivity to purge flow is different between the rotor geometries.

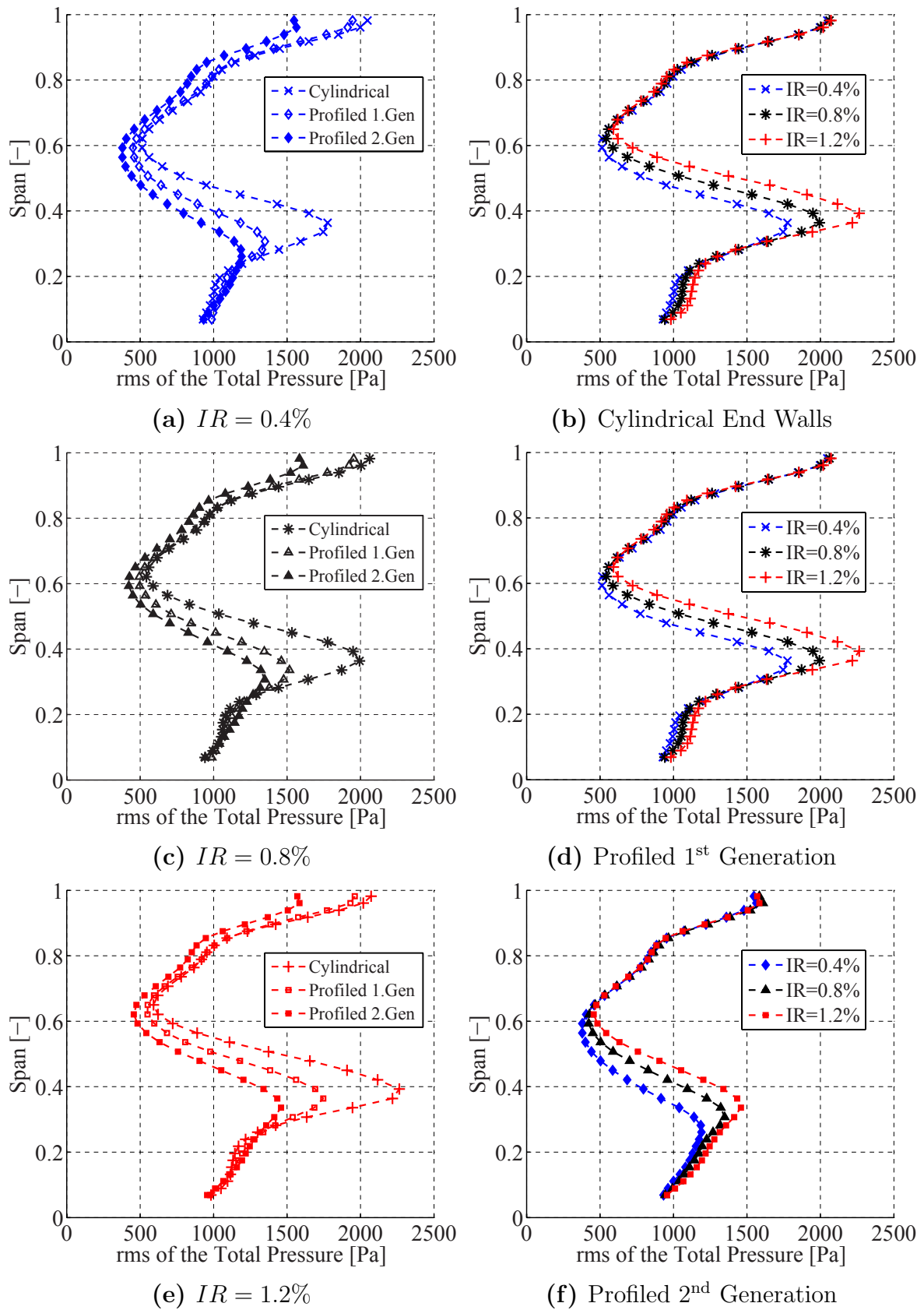


Figure 6.8.: Radial distributions of mass and time-averaged measured *rms* of the relative total pressure for all nine cases at the rotor exit (FRAP).

With cylindrical end walls the increase of peak *rms* between the low and the high injection rate is twice as high (60% per %*IR*) compared to the rotor with 2<sup>nd</sup> generation end walls (30% per %*IR*). The presence of end wall profiling and the suppression of the pressure side separation both clearly reduce the sensitivity of hub passage vortex unsteadiness to purge flow. These results are in line with the sensitivities found for the total-to-total efficiency (Figure 6.3).

A more detailed picture can be drawn when considering the circumferentially mass and time-averaged measured *rms* of the rotor relative total pressure. Figure 6.8 compares this parameter at the rotor exit for all nine investigated test configurations. The plots in the column on the left hand side in Figure 6.8 compare the radial distributions of *rms* between the different rotor geometries at a constant injection rate. The plot on the right hand side present the effect of varying purge flow rate for a given rotor geometry. As there are nine test cases, every curve is presented twice. Generally speaking the radial distributions confirm the trends found for the maximum *rms* values. However, the reduction of the radial *rms* distribution around the hub loss core when going from cylindrical to profiled (1<sup>st</sup> generation) end walls is more significant than the reduction caused by the improved blade and end wall design implying the removal of the pressure side bubble, as shown in Figures 6.8(a), 6.8(c) and 6.8(e). Numerically, a mass-weighted integral of the *rms* distribution between 25% and 60% span shows an average 30% reduction for all injection rates when the end walls become non-axisymmetric. The improved end wall design (2<sup>nd</sup> generation) reduces the mass-weighted integral by another 15%. The benefit in the *rms* of mass-weighted *rms* in the region of the hub passage vortex due to end wall profiling is about twice as big as the benefit gained when the bubble is suppressed. This trend appears to be insensitive to the amount of injected purge flow. The mass-weighted integral of the experimental *rms* between 25% and 60% span reduces by 50% when both beneficial effects are combined. When considering an integral over one entire rotor pitch, the overall level of *rms* increases by 27% at the nominal injection rate between the rotors with axisymmetric and 2<sup>nd</sup> generation end wall profiling.

The effects of increased injection rate on the radial distributions of circumferentially mass and time-averaged experimental *rms* of the relative total pressure has the same nature for all rotor geometries, as shown in Figures 6.8(b), 6.8(d) and 6.8(f). Compared to the sensitivity to geometrical variation of the rotor, the reduction of the radial *rms* distribution around the hub loss core with increasing injection rate appears to be more linear. A

mass-weighted integral of the *rms* distribution between 25% and 60% span shows a 20% increase between the low and the nominal and between the nominal and the high injection rates for all tested rotor geometries. The mass-weighted integrals reflect the linear trends with regard to injection rate already observed in the context of the experimental peak *rms* in the loss core. When considering an integral over one entire rotor pitch, the overall level of *rms* increases by 20% per percent of injected purge flow.

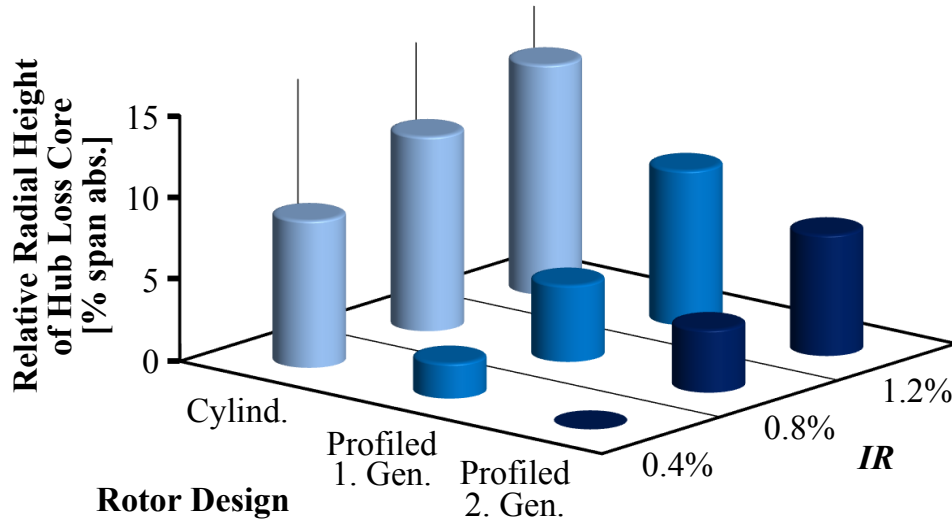


Figure 6.9.: Relative radial height of the centre of the hub passage vortex at the rotor exit for all nine test cases. The values are presented as an absolute percentage relative to the reference case (FRAP).

Considering the combined effects of injection rate and rotor geometry on the unsteadiness in the hub loss core shows that the beneficial effect of the end wall profiling (1<sup>st</sup> generation) can compensate for the increase of *rms* in the hub loss core due to 0.8% additional purge flow (Figure 6.7). The suppression of the pressure side bubble due to the improved blade and end wall design (2<sup>nd</sup> generation) again accounts for about 0.8% injected purge flow.

In Figure 6.8 it can be seen that the measured modifications to the flow field caused by a variation of purge flow only reach a height of about 65% span at the rotor exit. On the other hand the 2<sup>nd</sup> end wall design reduces the *rms* from hub to tip, whereas the 1<sup>st</sup> generation end wall profiling appears to leave the *rms* distribution unaltered between 60% and 90% span for all investigated injection rates. The decrease of *rms* over the whole span which looks like a small offset could be related to the probe measurement technique which was improved between the two corresponding measurement campaigns.

The overview over all test cases given in Figure 6.8 shows the radial migration of the hub loss core due to both the rotor geometry and the purge flow injection rate. On the one hand the loss core penetrates the free stream region more for increased injection rate. On the other hand both end wall profiling designs appear to reduce the radial coordinate of the hub loss core. Assuming the centre of the hub passage vortex close to the location of maximum unsteadiness, Figure 6.9 shows the relative radial height of the centre of the hub passage vortex as a function of injection rate and rotor geometry. The reference is the loss core at the lowest radial position (21% span), which is measured in the absence of a pressure side bubble for the rotor with the 2<sup>nd</sup> generation end wall profiling and at the minimum injection rate. For all tested geometries the loss core migrates in a relatively linear manner with regard to increasing purge flow rate. However the sensitivity of the radial height to the injection rate appears to be higher in the presence of profiled end walls, approximately 10% in span-wise direction per percent of injected purge flow for the two rotors with non-axisymmetric end walls. With cylindrical end walls the sensitivity of radial migration to injected purge flow appears to be reduced to 7% span per percent of injected purge flow, however at a much higher overall span-wise position. The absence of end wall profiling increases the radial penetration of the hub passage vortex by about 6% span for all experimentally investigated injection rates compared to the rotor with the 1<sup>st</sup> end wall design. The suppression of the pressure side separation due to the improved blade and end wall design further reduces the radial coordinate of the hub loss core by about 2% for all three levels of purge flow.

Figure 6.10 compares the minimum relative total pressure in the rotor hub passage vortex at the rotor exit. The values are presented as a decrease in relative total pressure relative to the best efficiency case. The best efficiency reference case shows the highest minimum relative total pressure ( $Cp_{t,rel} = 0.810$ ). Figure 6.10 shows that both end wall designs significantly reduce the minimum relative total pressure in the rotor hub passage vortex. The minimum  $Cp_{t,rel}$  in the loss core at the highest injection rate for the rotor with cylindrical end walls is approximately 3% lower compared to the reference case. The minimum relative total pressure in the hub loss core at the high injection rate for both rotors with non-axisymmetric end wall profiling is still higher compared to minimum the  $Cp_{t,rel}$  for the rotor with cylindrical end walls at the low injection rate. Furthermore, the rotors with profiled end walls show a lower sensitivity to the purge flow in terms of minimum relative total pressure in the hub loss core. For the rotor with

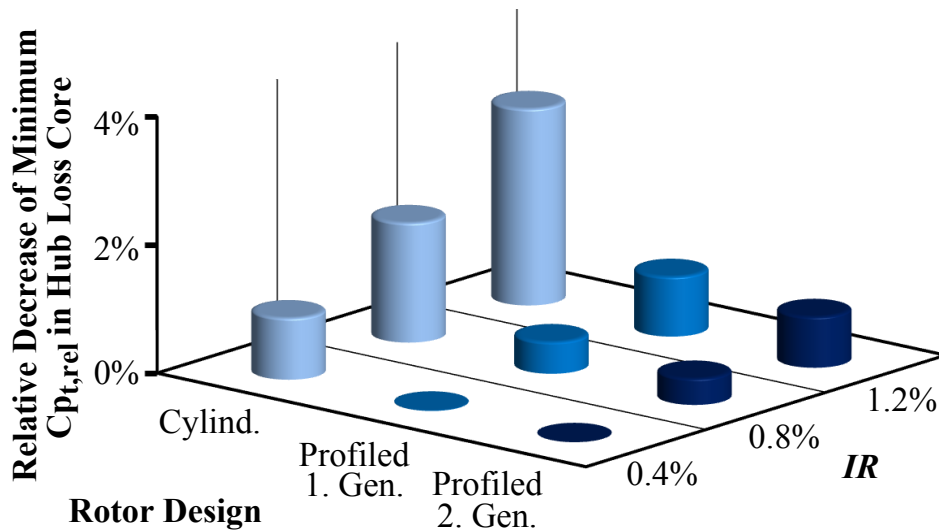


Figure 6.10.: The bars indicate minimum relative total pressure in the rotor hub loss core for all nine test cases at the rotor exit. The values are presented as decrease of minimum  $C_{p_{t,rel}}$  relative to the reference case which has the highest minimum  $C_{p_{t,rel}}$  (FRAP).

cylindrical end wall profiling the minimum  $C_{p_{t,rel}}$  reduces by approximately 2.5% per percent of injected purge flow. This sensitivity is halved in the presence of both end wall design. Both end wall designs show the same absolute levels and sensitivity of the minimum relative total pressure in the hub loss core with regard to the injection rate. Although the maximum unsteadiness is further reduced and the efficiency further increased by the 2<sup>nd</sup> end wall design, the relative total pressure in the rotor hub loss core appears to be unaffected.

Figures 3.21 and 4.13 show the time-averaged streamwise vorticity  $\Omega_s$  at the rotor exit in the rotor frame of reference for different test cases. The prominent vortical structures in the secondary flows are presented in the context of Figure 3.21. As for the relative total pressure *rms* distributions the main difference in streamwise vorticity between the nine investigated test cases is found in the hub loss core. The vorticity distributions in the rest of the measured flow field appear to be little affected by the level of purge flow and the rotor geometry. In order to compare the hub passage vortical structures for different injection rates, the circulation has been calculated by integrating the streamwise vorticity over the area affected by the hub passage loss core. The streamwise vorticity inside an iso-contour of zero vorticity has been considered. Figure 6.11 compares the circulation of the hub passage vortex among all the test cases, based on measurements. For all geometries the addition of purge flow increases the circulation in the hub

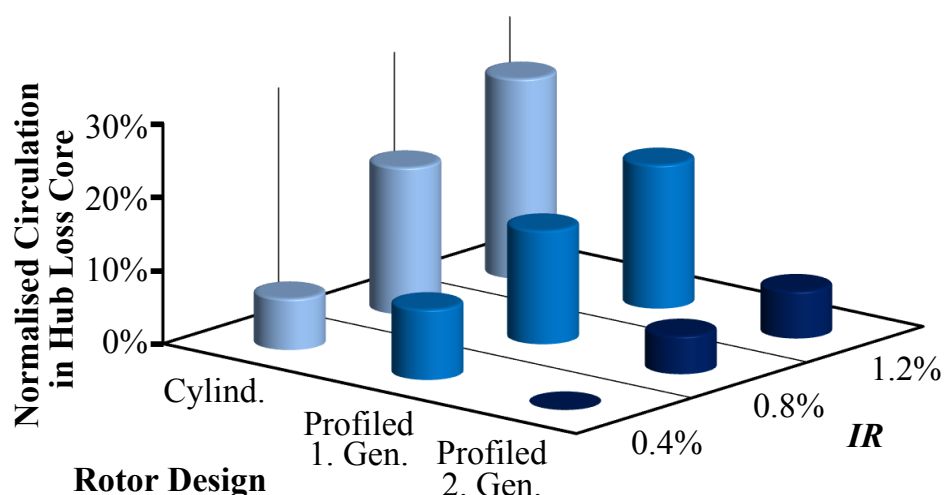


Figure 6.11.: The bars indicate the circulation of the rotor hub loss core for all nine test cases at the rotor exit. The values are presented relative to the reference case (FRAP).

loss core. The lowest values for the circulation integral were found for the best efficiency case with 2<sup>nd</sup> generation end wall profiling at the minimum injection rate ( $7.3 \text{ m}^2/\text{s}$ ). Experimentally, the rotor with axisymmetric end walls shows a 30% higher value at the high injection rate compared to the best efficiency case at the low injection rate, which was chosen as a reference in Figure 6.11. Both, the end wall profiling and removal of a pressure side separation decrease the level of the circulation in the hub passage vortex, especially at higher injection rates. At the lowest injection rate the measured circulation is lower with cylindrical end walls compared to the 1<sup>st</sup> end wall design. The end wall profiling was designed at the nominal injection rate, but appears to have an adverse effect at lower injection rates than assumed in the design. The sensitivity of the circulation to purge flow for the rotor with cylindrical end walls is about twice as high (20% per percent of injected purge flow) as for the rotors with non-axisymmetric end walls. The underlying unsteady interaction mechanisms affecting the streamwise vorticity and circulation of the hub passage vortex which are caused by increased purge flow rate and the end wall profiling are discussed in sections 4.3 and 3.3.

When comparing Figures 6.7 and 6.9 a correlation between the radial height and the peak unsteadiness of the rotor hub passage vortex can be identified. The same statement can be made when comparing Figures 6.9 and 6.11. The measured non-deterministic unsteadiness and the circulation of the hub loss core appear to scale with its radial coordinate. Figure 6.12 shows

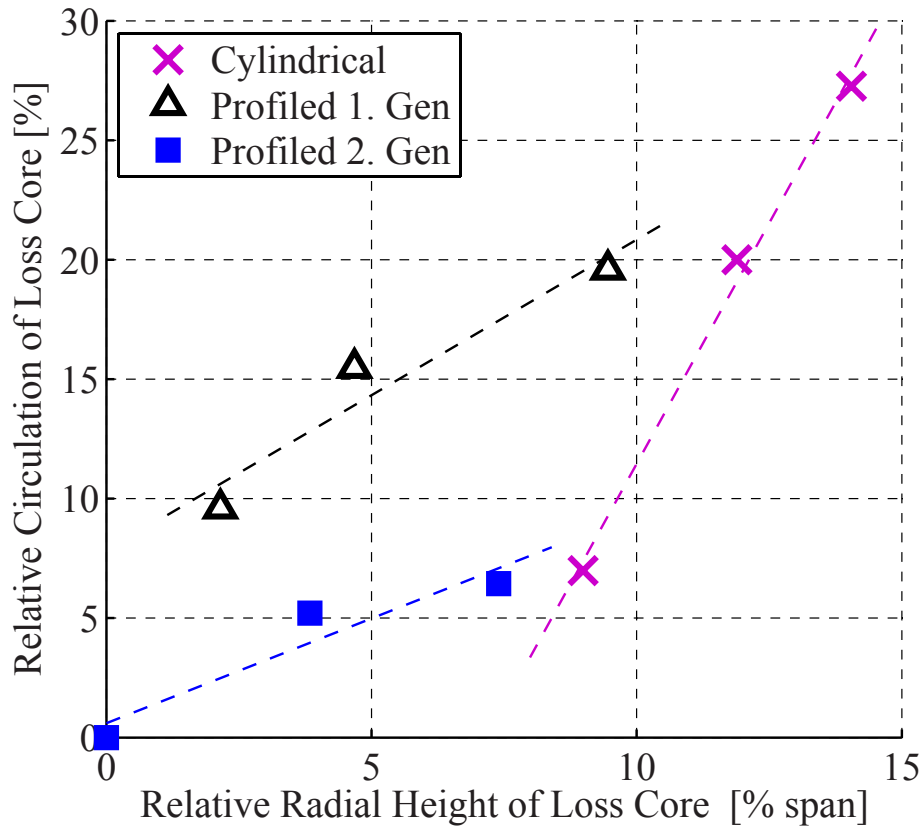


Figure 6.12.: Circulation of the rotor hub passage vortex as a function of its radial height for all nine test cases. The values are presented relative to the best efficiency case (FRAP).

the measured circulation of the rotor hub passage vortex as a function of its radial height for all nine test cases. The values are presented relative to the best efficiency case, the rotor with the 2<sup>nd</sup> generation end wall profiling at the low injection rate. For all rotor geometries the circulation increases with increasing radial height in a relatively linear manner, however at a different sensitivity depending on the rotor geometry. For the rotor with cylindrical end walls the circulation increases by 4% per percent of radial height, the 1<sup>st</sup> and 2<sup>nd</sup> generation of end wall profiling reduce these sensitivities to 1.3% and 0.9% per percent radial height. The correlation between the circulation and the radial height is not unexpected. If the flow is more vortical it has stronger circulation and can be expected to rotate helically in the passage. The helical motion manifests itself as radial outward migration of the hub passage vortex.

The link between the circulation and the radial migration can also be seen in the radial gradient of the reduced static pressure on the rotor suction side. Figure 6.13 shows contour plots of normalised reduced static pressure  $C_{p_{red}}$

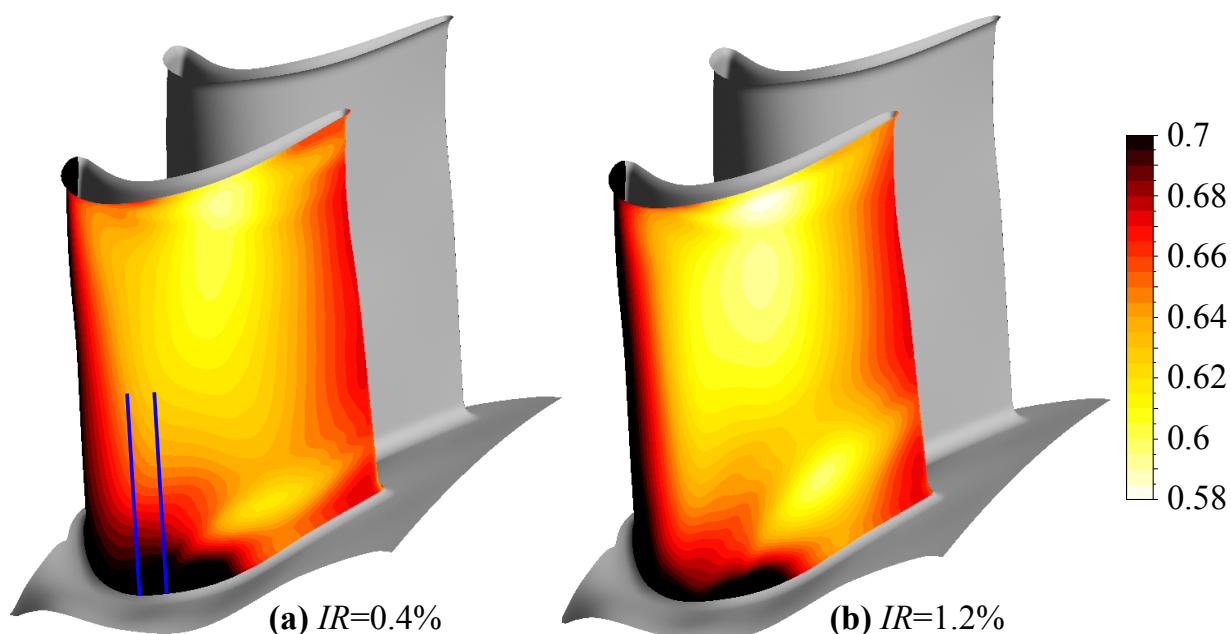


Figure 6.13.: Contour plot of normalised reduced static pressure  $Cp_{red}$  [-] on the rotor suction side (2<sup>nd</sup> end wall design) for the low and the high injection rates at the same phase in the cycle.

(Equation 5.1) on the rotor suction side (2<sup>nd</sup> end wall design) for the low and the high injection rates at the same phase in the cycle. The radial gradient of the reduced static pressure appears to be stronger at the early suction side close to the end wall for the high injection rate. Figure 6.14 shows two radial distributions of the radial gradient of the normalised reduced static pressure on the rotor blade suction side at two constant axial positions for the low and the high injection rates. For the high injection rate the radial gradient, which is pulling the low momentum fluid of the secondary flows towards the casing, is stronger at low radial coordinate. At higher injection rate the secondary flows on the early suction side are exposed to stronger radial gradients enhancing the radial migration of the suction side secondary flows. The simulated minimum reduced static pressure between 50% and 80% span reduces by approximately 2% per percent of injection rate.

Figure 6.13 shows the normalised reduced static pressure on the suction side of the rotor with the 2<sup>nd</sup> end wall design without pressure side separation. In the presence of separated pressure sides the distribution of the reduced static pressure on the rotor blade suction side is influenced by the exhausts of the pressure side bubbles. For the rotor with the 1<sup>st</sup> end wall design the pressure side bubble fluid is found to radially migrate towards the hub and then across the passage. The bubble fluid is accelerated by

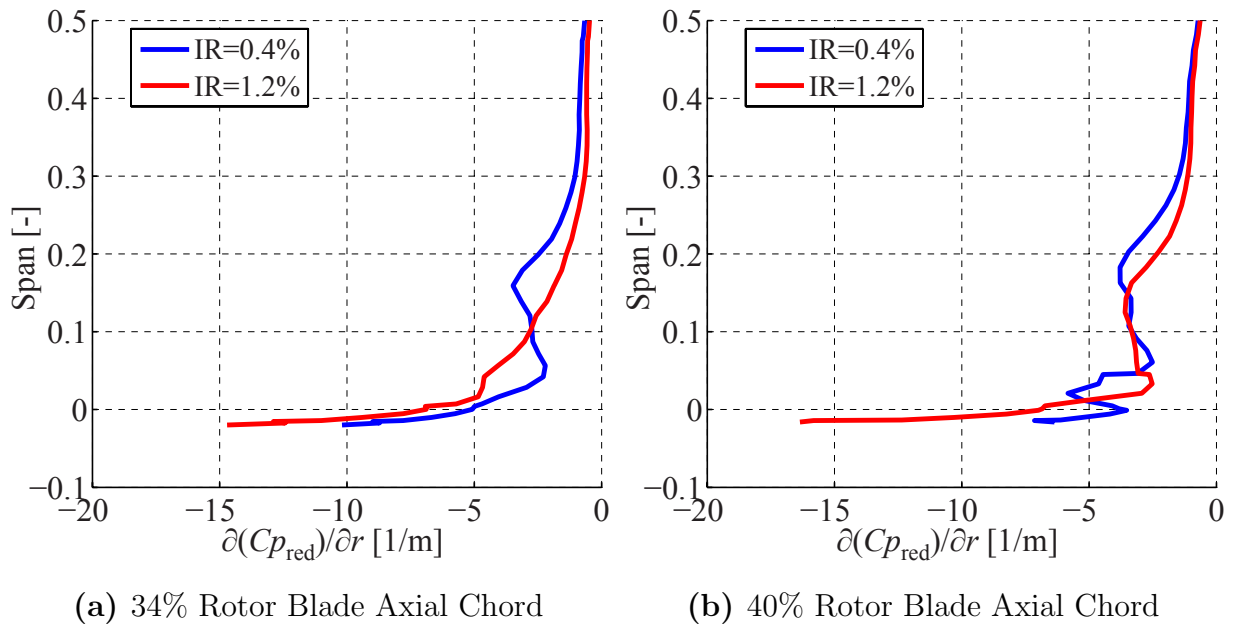


Figure 6.14.: Radial distribution of the radial gradient of normalised reduced static pressure  $\partial C_{p_{red}}/\partial r$  on the rotor suction side (2<sup>nd</sup> end wall design) at two axial locations for the low and the high injection rates. The blue lines in Figure 6.13 indicate the two axial locations of the radial distributions.

the cross passage pressure gradient and its kinetic energy increases. As a consequence the reduced static pressure in the suction side corner and the radial outwards gradient of the reduced static pressure on the rotor blade suction side increase. The analysis of the interaction between the purge flow and the pressure side separation (section 5.2) shows that the size of the bubble increases at higher injection rate. Therefore the reduced static pressure gradient on the rotor suction side not only increases due to the injection rate as shown in Figure 6.14, but also due to the increased amount of bubble fluid that is travelling across the passage and further increasing the reduced static pressure in the suction side corner. The combination of these two mechanisms further increases the radial migration of the secondary flows on the rotor suction side with the 1<sup>st</sup> end wall design, as shown by the measurements (Figure 6.9).

Figure 6.15 shows the maximum measured *rms* of the rotor hub passage vortex as a function of its radial coordinate for all nine test cases. The values are presented relative to the best efficiency case. The maximum experimental *rms* of the hub passage vortex confirms the trends with regard to its radial height observed for the circulation in Figure 6.12. For all rotor geometries the peak *rms* and the circulation increase with increasing radial height in a relatively linear manner, however at a different sensitivity. For

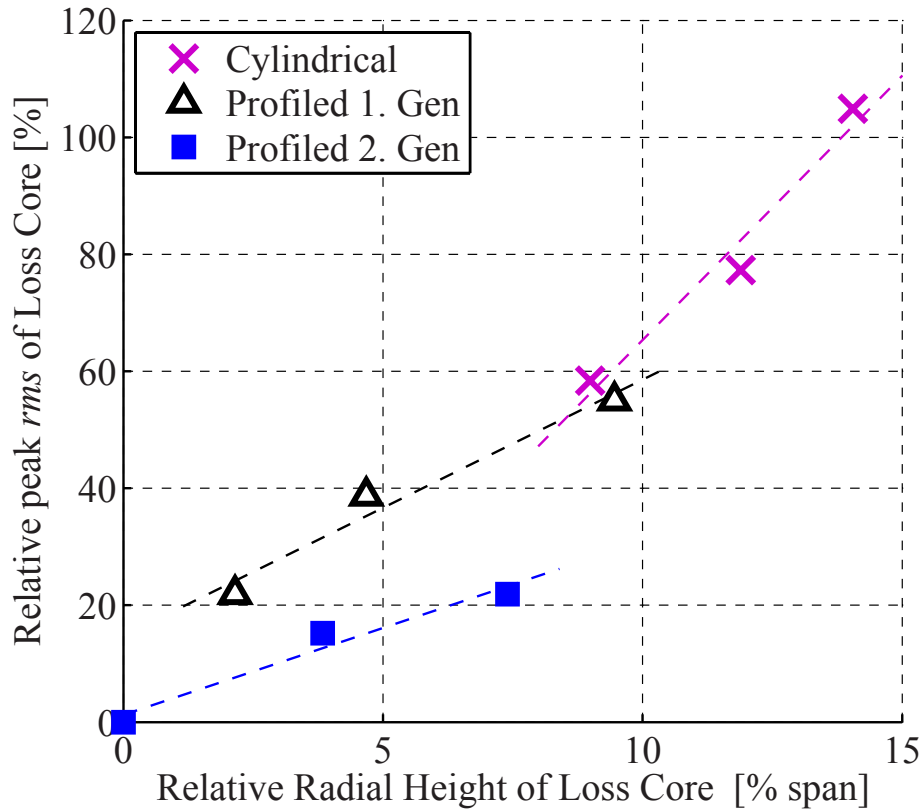


Figure 6.15.: Peak *rms* of the rotor hub passage vortex as a function of its radial height for all nine test cases. The values are presented relative to the best efficiency case (FRAP).

the rotor with cylindrical end walls the peak *rms* increases by about 9% per percent radial migration. The 1<sup>st</sup> and 2<sup>nd</sup> generation of end wall profiling reduce this sensitivity to 4% and 3% per percent of radial height. Not only the absolute level of *rms* increases with increasing radial height, but also the sensitivity of the *rms* to spanwise position. When considering all measurement cases irrespective of the rotor geometry, the maximum unsteadiness in the rotor hub passage vortex with regard to radial height increases at greater sensitivity at higher radius. In other words the radial migration of the hub loss core should be kept as small as possible when aiming to reduce the unsteadiness produced within the hub passage vortex. The reasons for the increase of this unsteadiness do not appear to be obvious. The following three mechanisms are proposed as a plan. Firstly, at increased radial migration of the hub passage vortex the end wall wall boundary layer, which is later rolled up by the vortex, gets more skewed and is therefore likely to have earlier transition. If so it would transport more turbulent bits of fluid which are then rolled up by the vortex. Secondly, the percentage of the span from which the rotor hub passage vortex

collects low-momentum fluid from upstream, increases with increased radial migration. These bits of low-momentum fluid, for example from the NGV1 passage vortex, can be expected to transport unsteadiness which then accumulates in the rotor hub passage vortex. Thirdly, at higher injection rate the vortex is likely to break down more easily in the process of interacting with the NGV2 potential field. If so, these vortex breakdown mechanisms would increase the unsteadiness of the rotor hub passage vortex.

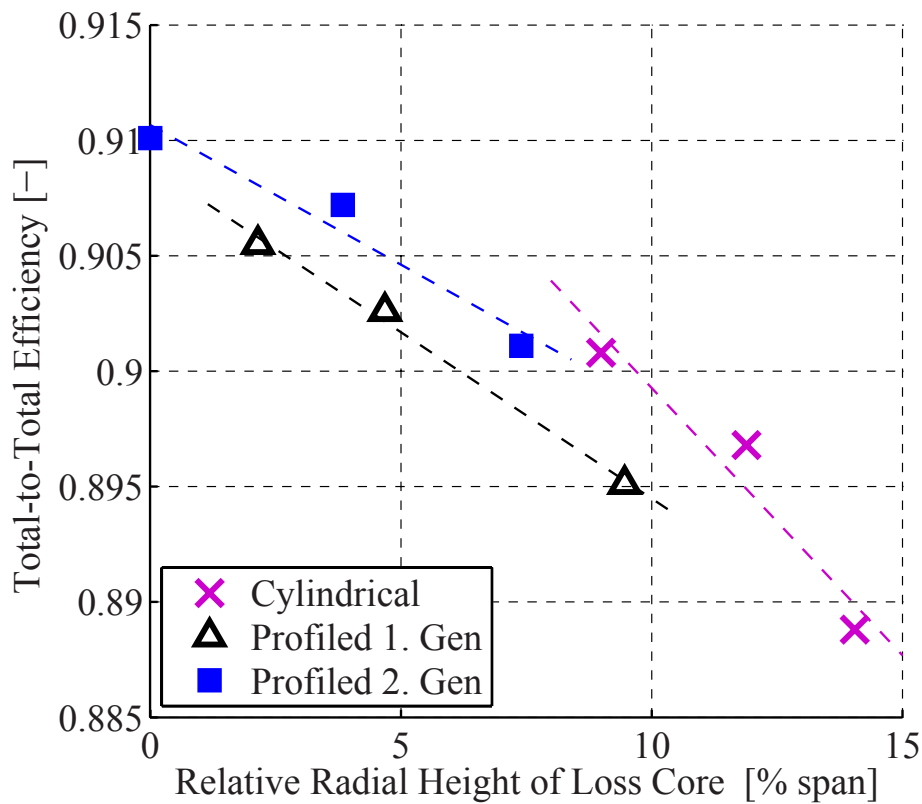


Figure 6.16.: Total-to-total stage efficiency  $\eta_{tt}$  as a function of the radial height of the rotor hub passage vortex for all nine test cases (5-hole probe).

Furthermore, the turbine stage efficiency appears to also scale with the radial coordinate of the hub loss core, as shown in Figure 6.16. The rotor with cylindrical end walls shows the highest sensitivity of the total-to-total stage efficiency compared to the radial height of the core of the rotor hub passage vortex. The rotor with cylindrical end walls also showed the highest efficiency of  $\eta_{tt}$  to rim seal purge flow.

## 6.3. Summary

In this chapter the combined effects of profiled end walls and purge flow are studied based on the consistent measurements of nine test cases. Three shrouded low-pressure rotor geometries with cylindrical, 1<sup>st</sup> and 2<sup>nd</sup> end wall designs are analysed at three levels of rim seal purge flow (0.4%, 0.8% and 1.2%). Two of the rotor geometries have separated rotor pressure sides at the chosen operating point.

At the rotor inlet the effects of the end wall profiling and the purge flow are much smaller compared to the rotor exit. For the investigated parameters, the injection rate and the rotor geometry with its associated bubble size appear to influence the average flow field at the rotor inlet in the same manner and can therefore be directly compared to each other. The static pressure increases by 0.75% per percent of injected purge flow. The Mach number directly correlates with the static pressure at an exchange rate of 1 to  $-3$ , a 1% increase of static pressure corresponds to a 3% drop of the Mach number.

The rotor with profiled end walls and without pressure side separation showed the highest efficiency for all purge flow levels (5-hole probe measurements at the rotor exit). The best efficiency was measured at the low injection rate,  $91.0\% \pm 0.37\%$ . Starting from the rotor with the 2<sup>nd</sup> end wall design, the total-to-total efficiency is reduced by  $0.33\% \pm 0.32\%$  on average due to the presence of a separated pressure side and by another  $0.75\% \pm 0.32\%$  on average when the rotor end wall profiling is removed. For all rotor geometries the efficiency decreases linearly with the addition of purge flow. The end wall profiling reduces the sensitivity of efficiency to purge flow twice as much (20% per percent of injected purge flow) as the suppression of the pressure side bubble. In terms of an exchange rate, the 1<sup>st</sup> rotor end wall design is able to compensate for the efficiency deficit due to 0.6% of additional purge flow. The 2<sup>nd</sup> end wall design removing the pressure side bubble can compensate for 0.8% of additional purge flow.

The effects on the rotor hub passage vortex caused by the rotor end wall design and the purge flow are intrinsically similar and can therefore be compared with each other. This has also been observed at the rotor inlet. For all geometries, the radial height of the hub loss core increased by about 10% span per percent of injected purge flow. The 1<sup>st</sup> end wall design and the suppression of the pressure side bubble (2<sup>nd</sup> end wall design) both reduced the overall span-wise position of the loss core by approximately 6% and 2% span respectively.

In the same manner, the additional purge flow increases the maximum root mean square values of the measured relative total pressure random part, the circulation and the reduction of relative total pressure in the hub loss core by 40%, 10% and 1% per percent injection rate respectively for the rotor with the 1<sup>st</sup> end wall design. However the sensitivities of these parameters to purge flow depend on the rotor geometry. Both non-axisymmetric end wall designs reduce the sensitivity to purge flow by approximately the same amount.

The parameters characterising the impact of the purge flow and the end wall profiling on the rotor hub passage vortex can also be analysed as a function of its radial coordinate. The peak *rms* and the circulation of the hub loss core appear to scale in a relatively linear manner with respect to the radial height. The sensitivity again depends on the rotor geometry. For example, the peak *rms* increases by 9% per percent radial migration towards the casing for the rotor with cylindrical end walls. This sensitivity is reduced to 3% in the presence of the 2<sup>nd</sup> end wall design and thicker airfoils. The total-to-total stage efficiency appears to also scale with the radial height of the hub loss core in a relatively manner, again at slightly different sensitivity depending on the rotor geometry.

# 7. Unsteady Rotor Hub Passage Vortex Behaviour

The study presented in chapter 3 has shown that the rim seal purge flow strongly interacts with the rotor hub passage vortex. The unsteady interaction between the rotor flow field and the purge flow influences the rotor hub passage vortex in various ways. For instance additional purge flow significantly increases the radial height, the unsteadiness and the circulation of the hub loss core. The rotor end wall profiling was successfully introduced to mitigate the negative effects of the purge flow on the rotor hub passage vortex.

Furthermore, the purge flow also influences the unsteady spatial movement of the hub loss core caused by the blade row interaction. In this chapter the influence of the purge flow injection rate on the unsteady spatial movement and behaviour of the hub loss core during one period is studied. The consequences for the downstream nozzle guide vane are also considered. Time-resolved measurements made with the FRAP at the low and the high rim seal purge flow injection rates are compared and studied. In this chapter only the rotor with the 1<sup>st</sup> end wall design is taken into account for the analysis.

## 7.1. Spatial Movement

Figure 3.20 shows the radial distribution of circumferentially mass and time-averaged measured streamwise vorticity  $\Omega_S$  at the rotor exit for the three tested injection rates. Assuming the centre of the rotor hub loss core to be at the spanwise position of maximum streamwise vorticity, the vortex radially migrates outwards by 10% absolute spanwise position per percent of injected purge flow (cf. section 3.3). For the following analysis the centre of the hub loss core is assumed to be at approximately 35% span at the high injection rate and at 23% span at the low injection rate.

Figure 7.1 shows two time space plots of the streamwise vorticity  $\Omega_S$  at the rotor exit for low and high injection rates. The radial position of the two

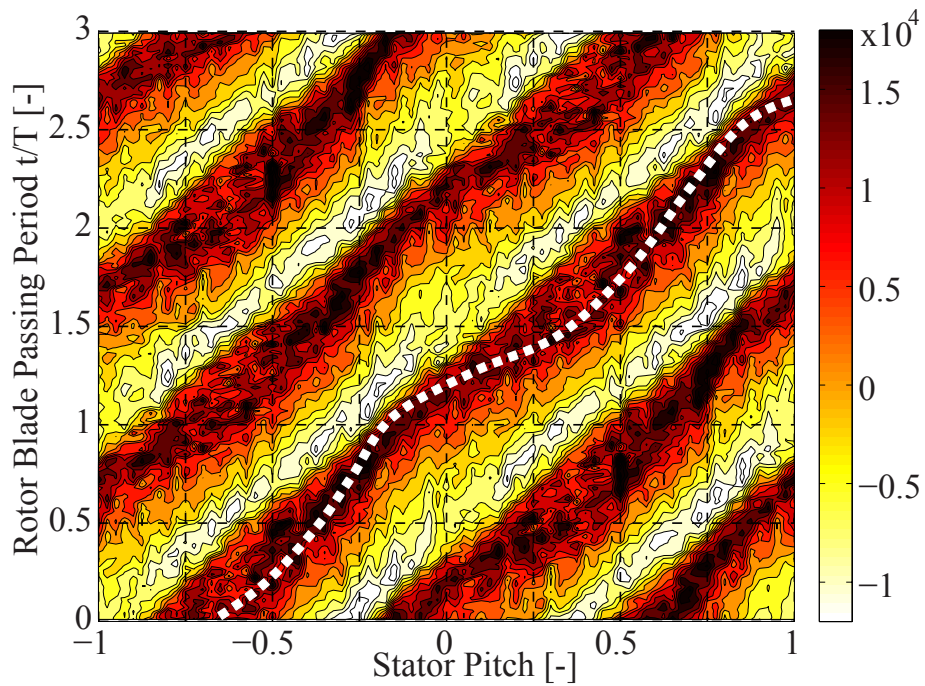
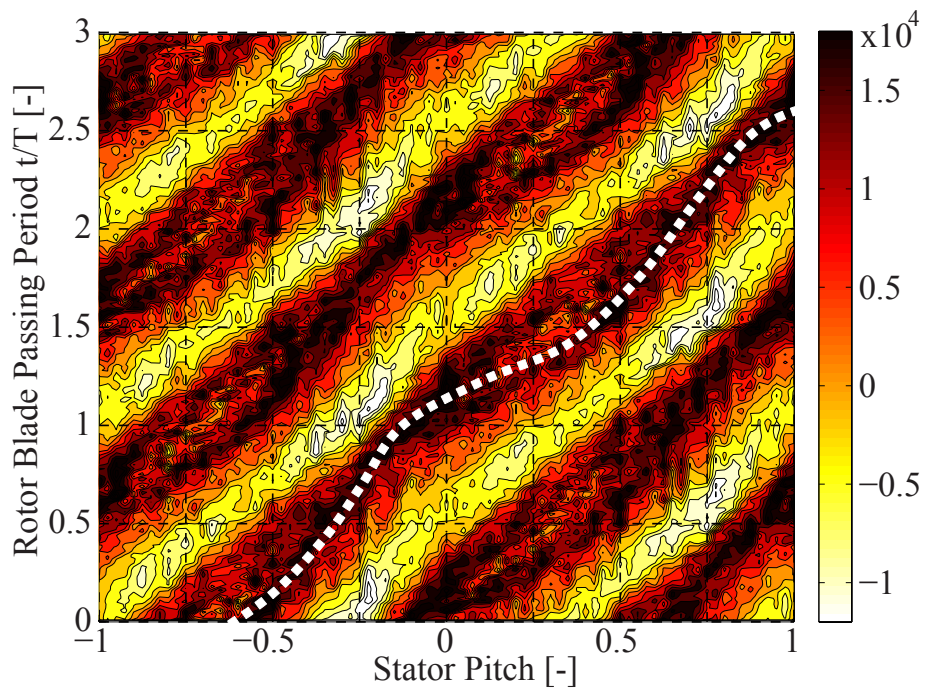
(a)  $IR = 0.4\%$  at 27% span.(b)  $IR = 1.2\%$  at 35% span.

Figure 7.1.: Time space plot in absolute frame of reference of the streamwise vorticity  $\Omega_s$  [1/s] for low and high injection rates at the rotor exit (FRAP).

plots was chosen not to be identical in order to take into account the radial migration of the hub passage vortex under the effect of purge flow. Both

plots are produced at the radial height of the nominal centre line of the hub loss core. The inclined high  $\Omega_s$  features are the signature of the rotor hub passage vortex, a moving flow element in the stationary frame of reference. The gradient of the inclined high  $\Omega_s$  feature in the time space plot corresponds to the circumferential velocity of the hub passage vortex. A steeper gradient corresponds to slower circumferential velocity (less distance per time). The dotted lines in Figure 7.1 represent the approximate centre of the hub loss core at a fixed radial position. For both injection rates the dotted lines have a kink per stator pitch and on either side of the kink the gradient is different. Therefore the circumferential velocity of the hub passage vortex is not constant. This effect must be due to the presence of the static pressure field of the downstream vane. The effect occurs for every rotor hub passage vortex at the same circumferential coordinate in Figure 7.1. The circumferential coordinate of the NGV2 leading edge can be defined with the corresponding time space plot of static pressure shown in Figure 7.2. The vertically stacked patches of high static pressure at around -0.95 and 0.05 stator pitch in Figure 7.2 are the signature of two neighbouring leading edges of the second nozzle guide vane. The fact that they are vertically stacked means that they are stationary in space with regard to time. The temporal variation of the static pressure potential field of the NGV2 leading edge is caused by the interaction with the passing rotor wakes; there is one trough per passing rotor wake and loss core.

The comparison of Figures 7.1 and 7.2 reveals that the circumferential velocity of the hub passage vortex peaks just in front of the second guide vane leading edge, just where the static pressure field also peaks. When the hub passage vortex is approaching the increased static pressure zone of the NGV2 leading edge, it first slows, but then quickly flips to the other side at high circumferential velocity and finally continues at blade speed.

When passing the static pressure potential field of the second nozzle guide vane the rotor hub loss core is being forced to stretch. As a consequence, it has to speed up and spin faster. The static pressure at the core drops and its kinetic energy increases, creating additional friction loss with the surrounding flow. The more the vortex is stretched, the faster it spins and the more loss is created at its core. Such a flow situation will also tend to locally bend and diffuse the vortex. These things are both classically understood to lead to vortex breakdown. In Figure 7.1 the diagonal track of the hub passage vortex can be seen to adopt a bifurcated form; this occurs for example at about (-0.9,0.6) and (0.1,2.25). Whilst it is not readily apparent why this is so, there is some similarity to the spiral vortex

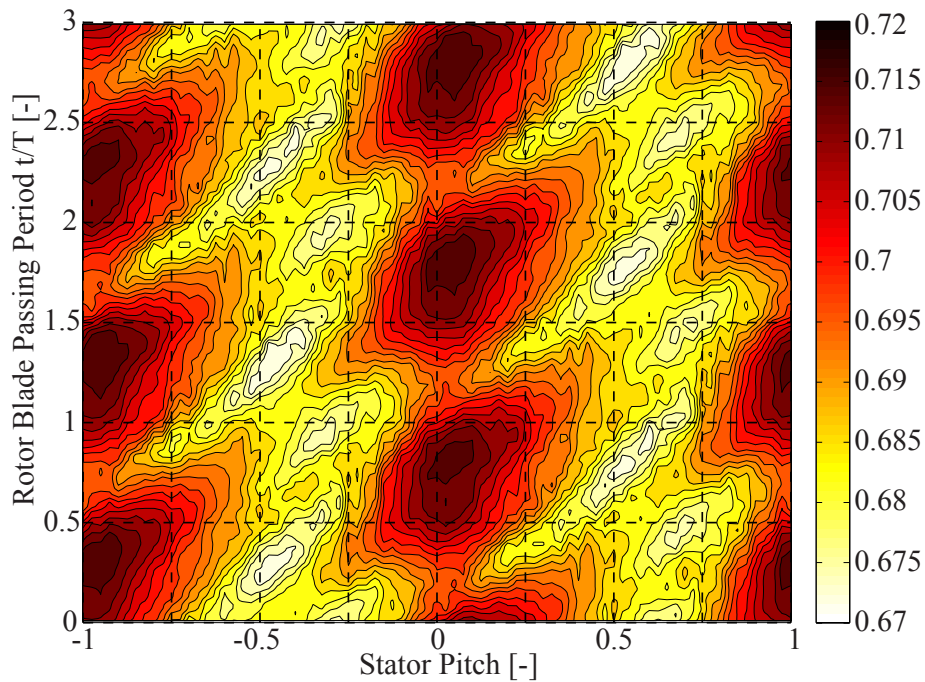
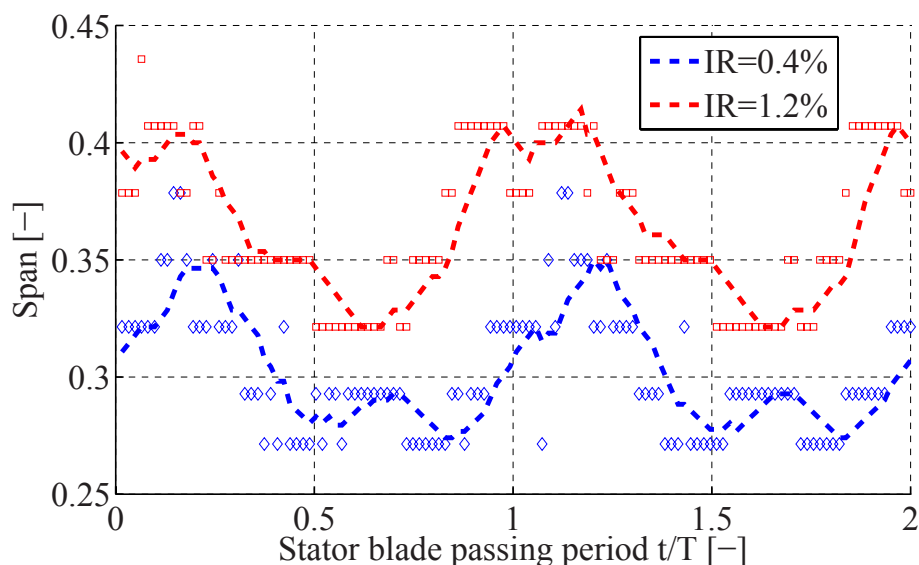


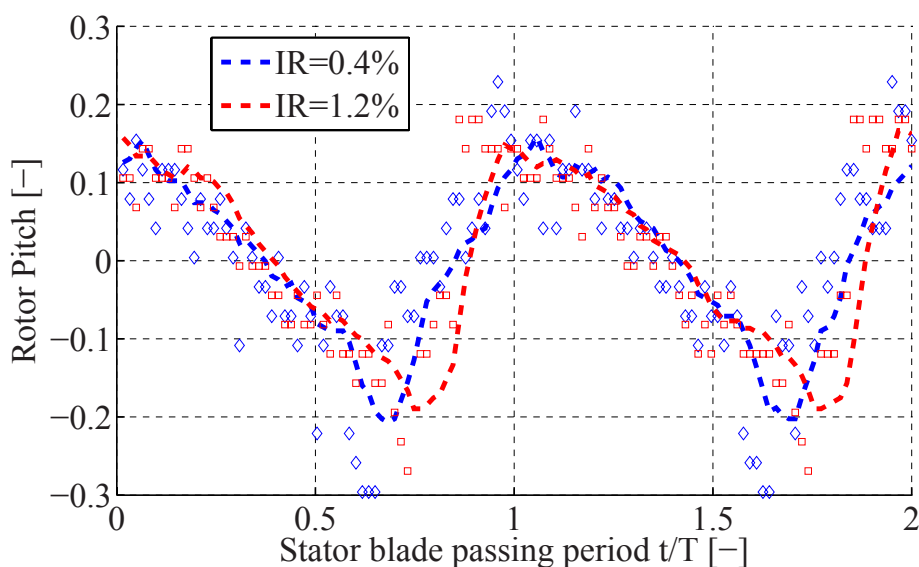
Figure 7.2.: Time space plot in absolute frame of reference of the normalised static pressure  $Cp_s$  [-] at the rotor exit ( $IR = 1.2\%$  at 35% span, FRAP).

breakdown mode reported by Kasper et al. [46]. However in this reference a NGV wake was studied at the rotor inlet, whereas here a rotor hub passage vortex entering the second nozzle guide vane is analysed. In the context of the vortex breakdown the swirl ratio ( $= V_{\theta, \max} / V_x$ ) of the rotor hub passage vortex has been evaluated in the reference system attached to the vortex and based on the unsteady FRAP measurements. The maximum evaluated swirl ratios stay at a relatively low level, below 0.23 at the low injection rate and below 0.25 at the high injection rate. This can be compared to a proposed critical swirl parameter for vortex breakdown of 1.2 from Greitzer et al. [33] for steady flows where stagnation conditions are preserved. Hence this critical swirl ratio has to be considered with caution as the rotor hub vortex under investigation is a vortex travelling through an unsteady flow field including a strong rotating pressure disturbance due to the NGV2.

Figures 7.3(a) and 7.3(b) show the spanwise height and the circumferential coordinate of the maximum experimental  $rms$  in the hub passage vortex in the rotor frame of reference at the rotor exit for low and high injection rates. The actual values of the maximum experimental  $rms$  during the cycle are given in Figure 7.5. The symbols in Figure 7.3 indicate the coordinates of the points of maximum  $rms$  which are part of the discrete measurement grid. The dashed lines show a moving average of the measurement results.



(a) Radial position of maximum *rms* of the relative total pressure signal in the hub passage vortex.



(b) Rotor relative circumferential position of maximum *rms* of the relative total pressure signal in the hub passage vortex.

Figure 7.3.: Unsteady spatial behaviour of hub loss core at the rotor exit for minimum and maximum injection rates (FRAP).

The time dimension on the x-axis covers two stator blade passing events. The two Figures show that the hub loss core is radially and circumferentially moving in the rotor frame of reference due to the blade row interaction. The radial migration of the hub loss core due to increased purge flow rate is confirmed in Figure 7.3(a), when the average of the two curves is compared. This also shows that the spanwise range covered by the loss core during one

period is not significantly influenced by the injection rate. The hub passage vortex travels approximately 10% in the radial dimension from peak to peak during one period for both injection rates. However, there appears to be a temporal phase shift between the two injection rates. At the high injection rate the hub passage vortex starts the radial migration 0.2 periods earlier compared to the low injection rate.

Figure 7.3(b) shows how the relative circumferential coordinate of the hub passage vortex within the rotor is changing during the period cycle due to the blade row interaction. The circumferential range is large, at approximately 40% rotor pitch, and is unaffected by the purge flow rate. The shape of the curves in Figure 7.3(b) is broadly a zigzag with a slow fall and a quick rise. The event associated with the quick rise is when the high pressure of the NGV leading edge goes by. The purge flow intensity changes the rate of rise of the curves in Figure 7.3(b), but does not influence the slow fall. Apparently the structure of the hub passage vortex, influenced by the strong purge flow, moves circumferentially more rapidly past the NGV2 leading edge potential field at the high injection rate.

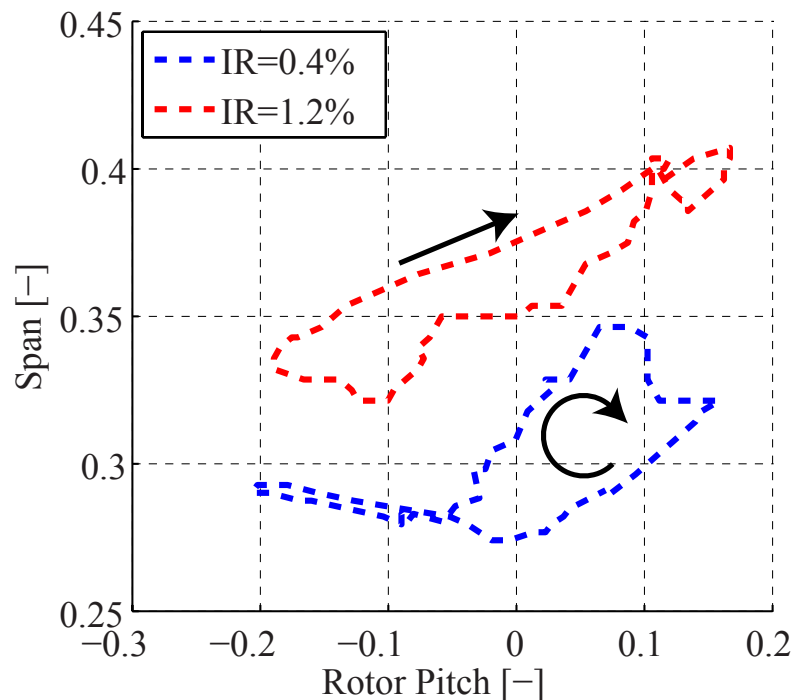


Figure 7.4.: Unsteady orbit in the rotor relative frame of the hub loss core centre during one stator blade passing period for minimum and maximum injection rates (FRAP). The orbit combines the results given in Figures 7.3(a) and 7.3(b).

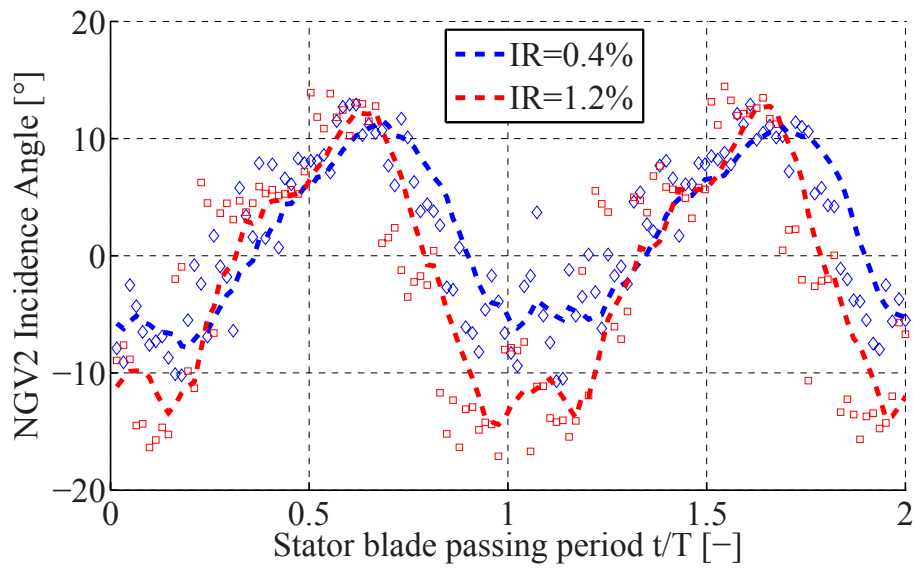
When combining Figures 7.3(a) and 7.3(b) an unsteady two-dimensional movement of the hub passage vortex due to the blade row interaction can

be derived. The orbit in the relative frame of the maximum experimental *rms* in the hub passage vortex in the rotor frame of reference is shown in Figure 7.4. When the hub passage vortex is forced by the rotor to pass in front of the NGV2 leading edge potential field its radial and relative circumferential coordinate increases (indicated by the arrows in Figure 7.4). When the loss core has circumferentially past the NGV2 potential field it reaches the maximum radial height and circumferential advance with regard to the rotor blade during one period. The opposite mechanism occurs when the hub passage vortex is between two NGV2 leading edge potential fields. The injection rate does not appear to significantly influence the structure of the orbit of the hub passage vortex in the rotor relative frame. However the injection rate increases the overall radial height of the orbit but has a smaller influence with regard to the rotor pitch position during one period.

## 7.2. Influence on NGV2

The spatial movement of the hub passage vortex described causes the incidence of the hub passage vortex flow on the NGV2 to fluctuate unsteadily. Figure 7.5(a) shows the measured unsteady incidence on the NGV2 at the positions of the hub passage vortex defined in Figures 7.3(a) and 7.3(b). The symbols indicate the measurement and the dashed lines the corresponding moving average. Comparing the measurements at low and high injection rates, the maximum negative incidence on the NGV2 is decreasing by  $10^\circ$  and the maximum positive incidence is increasing by  $2^\circ$ . The range of incidence between minimum and maximum increases by about  $15^\circ$  per percent of injected purge flow. This additional positive and negative incidence can be expected to increase the loss at the NGV2 for the higher injection rate. The incidence variation is slightly influenced by the radial migration of the hub loss core. The NGV2 has only a  $1^\circ$  variation in inlet angle over the 10% height range of the vortex motion (Figure 7.3(a)).

Figure 7.5(b) shows the maximum *rms* value measured at the positions of the hub passage vortex defined in Figures 7.3(a) and 7.3(b). The higher overall *rms* level at the high injection rate is as expected and has already been described in the context of Figure 3.23. The variation of the *rms* signature of the rotor hub passage vortex is broadly a symmetrical zigzag for both injection rates, Figure 7.5(b). The minimum of the *rms* values occurs just as the pressure starts to rise due to the downstream leading edge and is almost unaffected by the purge flow rate. The *rms* level rapidly



(a) NGV2 incidence at the centre of hub passage vortex.

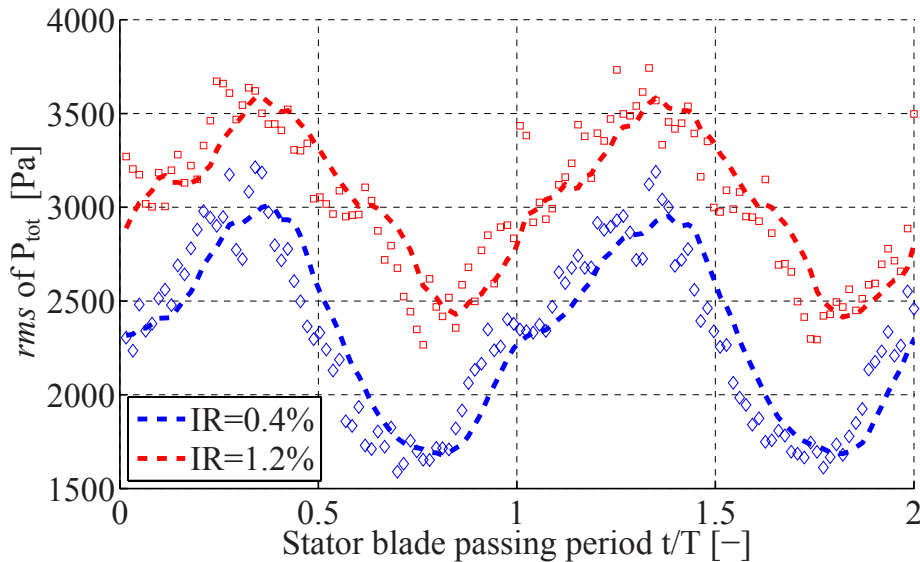
(b) Maximum  $rms$  of relative total pressure at the centre of hub passage vortex.

Figure 7.5.: Unsteady behaviour of the hub loss core at the rotor exit for minimum and maximum injection rates (FRAP).

increases as the hub passage vortex is wrapped around the NGV2 leading edge. This effect is stronger with less purge flow and weaker with more. Whilst the hub passage vortex  $rms$  is elevated at the higher injection rate, the variation between maximum and minimum  $rms$  over the vane passing cycle is diminished.

## 7.3. Summary

Time-resolved measurements at the rotor (1<sup>st</sup> end wall design) exit for the low and high injection rates are compared in order to analyse the influence of the purge flow injection rate on the unsteady spatial movement and behaviour of the hub loss core during one period. The measurements showed a highly unsteady movement of the hub loss core due to the blade row interaction. The core of the hub passage vortex was found to travel 10% span in the radial direction and 40% rotor pitch in the circumferential direction under the effect of the downstream stator blade passing event. These numbers are unaffected by the injection rate. However at a higher injection rate the hub loss core swings 30% more rapidly past the NGV2 leading edge potential field. At this injection rate, the hub loss core is transporting higher unsteadiness at lower static pressure. The unsteady movement of the hub passage vortex was found to locally increase the range of the incidence on the NGV2 between minimum and maximum by 15° per percent of injected purge flow, increasing the loss at the NGV2.



## 8. Summary and Conclusions

The thesis presents a combined experimental and numerical investigation with the objective of studying the interaction mechanisms between the rim seal purge flow and non-axisymmetric end walls in a low-pressure turbine environment. Three shrouded low-pressure rotor geometries were studied at three levels of rim seal purge flow. The measurements were performed in the one-and-half stage shrouded model axial turbine at the Laboratory for Energy Conversion using miniature size fast-response probe technology. The non-dimensional parameters of the turbine match real engine conditions. The experiments are complemented by corresponding time-accurate numerical predictions.

### 8.1. Concluding Remarks

The combined experimental and computational investigation covering nine test cases leads to the following concluding remarks:

- Non-axisymmetric rotor hub end wall profiling can be used to reduce the sensitivity of efficiency to purge flow when included in the design process. The presented rotor hub end wall design reduced the measured sensitivity of efficiency to purge by 30% to 1.12% per %*IR*.
- The measured turbine total-to-total stage efficiency (5-hole probe) increased by  $0.75\% \pm 0.32\%$  on average due to rotor hub end wall profiling.
- The presented non-axisymmetric end wall design is able to compensate for the efficiency deficit caused by 0.6% of additional rim seal purge flow.
- About 20% of the overall stage efficiency improvement due to the end wall profiling can be attributed to the beneficial effect of the profiled shroud end wall, 80% are from the hub end wall profiling.

- The purge flow was found to strongly interact with the rotor hub passage vortex for all tested rotor geometries. The sensitivities of the rotor hub passage vortex experimental maximum unsteadiness (60% per %*IR*), circulation (20% per %*IR*) and minimum relative total pressure ( $-2.5\%$  per %*IR*) could be approximately halved in the presence of the 2<sup>nd</sup> rotor hub end wall design.
- 1% of purge flow was found to increase the measured mass-weighted loss based on the isentropic efficiency by 4% in the hub passage vortex.
- The efficiency, the unsteadiness and the circulation of the hub passage vortex appear to scale by its radial coordinate. The radial migration of the rotor hub loss core should be minimised during the design phase.
- The presence of a separated rotor pressure side reduced the measured total-to-total stage efficiency by  $0.33\% \pm 0.32\%$ .
- The purge flow indirectly interacts with the pressure side separation bubble. The purge flow has a negative effect on the size and shape of pressure side separation by causing negative incidence at rotor inlet.
- Non-axisymmetric rotor hub end wall profiling can be used to reduce the volume and the maximum size of the pressure side separation and to reduce the loss generated by the fluid shed from the bubble.
- Rotor hub end wall profiling up to the platform leading edge improves the unsteady interaction between the purge flow and the free stream at the rim seal exit, maximum radial velocities are reduced by 50%.
- The unsteady blade row interaction causes the core of the rotor hub passage vortex to travel 10% span and 40% rotor pitch during one cycle. The purge flow does not significantly influence the radial and circumferential dimension of the orbit but its dynamics.
- Purge flow should be included in the end wall and blade design process of a low-pressure turbine, especially in the presence of a separated pressure side.

## 8.2. Summary

### Purge Effects

The injection of purge flow between the rotor and nozzle guide vane causes the static pressure to rise by 1% and the Mach number to drop by approximately 3% per percent of injection rate at the rotor inlet. The reduction of Mach number causes negative incidence on the rotor leading edges. Close to the hub the maximum measured change of incidence is  $-9^\circ$ .

The purge flow affects the rotor exit flow field only below 65% span and significantly interacts with the hub passage vortex. The unsteady rotor flow field causes the purge flow to collect on the rotor blade suction side at one circumferential location. The measured maximum non-deterministic unsteadiness in the hub loss core increased by 30% to 60%, the circulation by 10% to 20% per percent of injected purge flow. The streamwise vorticity in the hub passage vortex not only concentrates at a higher spanwise position, but also tends to be stretched in the circumferential direction under the effect of increased purge flow.

An attempt was made to quantify the additional loss created by the purge flow in the rotor hub loss core. A time and mass-averaged integral of the measured isentropic efficiency in the hub loss core decreases by 4% per percent of injected purge flow.

With the use of particle tracks two potential loss mechanisms were proposed for particles leaving the rim seal cavity. Firstly, the significant relative velocity mismatch near the rim seal between purge flow and free stream fluid is causing the loss to increase with increasing purge flow rate due to friction and viscous dissipation. Secondly, the rotor was found to do work on the rim seal purge flow in the early rotor passage by accelerating it in the circumferential direction.

Based on a statistical approach using the particle tracking tool the different flow structures involved in the rotor hub passage vortex were numerically weighted. It was found that approximately 10% to 20% of the hub passage vortex is coming from the rim seal cavity depending on the injection rate. The pressure side bubble fluid was found to represent only 1% to 3% of the flow in the hub passage vortex, again depending on the amount of purge flow. The rest can be attributed to rotor boundary layer and NGV1 secondary flows.

## Rotor Hub End Wall Effects

The reaction evaluated based on the pneumatic pressure measurements was found to decrease by 0.3% on average in the presence of end wall profiling (1<sup>st</sup> generation), due to modifications of the static pressure in the hub loss core region at the rotor exit. The rotor hub end wall profiling influences the unsteady behaviour of the rotor hub passage vortex. Only the 1<sup>st</sup> hub end wall design is considered when studying the unsteady effects on the hub loss core region. The end wall profiling reduces the average radial coordinate of the hub passage vortex by 5% span and the non-deterministic unsteadiness in the hub loss core by 25%. The peak streamwise vorticity nearly doubles and the dissipation function increases by a factor of 2 to 3 in the absence of non-axisymmetric rotor hub end walls.

The 2<sup>nd</sup> hub end wall was optimised and designed for a thicker blade in the hub region which also removes the pressure side separation present with the 1<sup>st</sup> end wall design. The improvements due to the removal of the bubble and due to the successful 2<sup>nd</sup> end wall design are difficult to distinguish.

## Shroud End Wall Profiling

Both shroud end wall designs can be analysed and compared to each other as the blade design was unaltered in the tip region. The beneficial effects in the flow field in the tip region caused by the 2<sup>nd</sup> shroud end wall design were found to be nearly twice as high compared to the 1<sup>st</sup> shroud design. The 2<sup>nd</sup> shroud end wall especially performs better above 95% span. The minimum time-averaged relative total pressure increases by 1%, the Euler work term by 6%, the entropy rise by 15% and the non-deterministic unsteadiness by 5% above 90% span in the presence of the 2<sup>nd</sup> shroud end wall design. The change in *rms* of the relative total pressure occurs within a limited circumferential region and in the unsteady interaction zone between the rotor tip passage vortex and the shroud leakage flow.

## Pressure Side Bubble

The presented analysis of the pressure side bubble relies entirely on unsteady CFD simulations and therefore needs to be considered with some care. The prediction of the behaviour of the pressure side separation and of the underlying shear stresses strongly depends on the transition and the turbulence models of the CFD code used in the context of this work.

Two of the three experimentally investigated rotors have separated pressure sides at the chosen operating point. Time-accurate CFD simulations showed a strong interaction between the size and shape of the pressure side bubble and the nozzle guide vane wake when it is convected through the rotor. Depending on the relative position of the blade rows the bubble can nearly disappear for a limited period of time. During one period the bubble was found to disappear twice and build up again after having disappeared. During one period the NGV wake hits the rotor twice, therefore there may be a link between the two elements. The 1<sup>st</sup> end wall design successfully reduces the volume and maximum size of the pressure side separation but does not appear to influence the described unsteady behaviour.

The 1<sup>st</sup> end wall design successfully reduces the volume and maximum size of the pressure side separation and influences the bubble shedding mechanism. In the presence of profiled hub end walls particle tracking calculations showed that the pressure side bubble fluid migrates radially towards the hub, then across the passage inside a vortical structure attached to the profiled hub end wall and then leaves the rotor inside the hub passage vortex. With cylindrical end walls the pressure side bubble fluid is directly shed into the free stream at approximately 10% span and then leaves the rotor blade row underneath the hub passage vortex at low radial height.

For both end wall geometries (cylindrical and 1<sup>st</sup> generation) the rim seal purge flow was found to have a strong negative effect on the size of the pressure side bubble as it increases the static pressure by 1% per percent of injected purge flow at the rotor inlet. As a consequence, the relative Mach number and flow yaw angle decrease causing negative incidence on the airfoil stimulating the separation process.

The rotor with the 2<sup>nd</sup> end wall design combined with the thicker rotor blades in the hub region does not show separated pressure sides, even at injection rates reaching 3%.

## Cavity Exit Flow Field

The axial position of the probe traverse plane at the rotor inlet makes it possible for the 4-hole probe, FRAP and FENT probe to measure in the rim seal cavity above the rim seal lip and to capture the rim seal purge flow effects in this region. The unsteady blade row interaction causes the purge flow to pulsate at the exit of the rim seal. There is one burst of flow per NGV1 passing event in rotor frame of reference which locally increases the unsteadiness and the radial velocities at increased injection rate.

CFD analysis revealed two axial zones at the rim seal exit where the purge flow is leaving the rim seal cavity, zone 1 between 5% and 60% where most of the purge flow leaves the cavity, especially at high injection rate, and zone 2 between 90% and 100% non-dimensional axial rim seal coordinate. Particles tracks revealed a toroidal vortical structure in the rim seal exit cavity.

The end wall profiling reaches up to the rotor hub platform leading edge and therefore successfully reduces the maximum radial velocity at the rim seal exit by up to 50% close to the rotor disk. The wavy shape of the rotor hub platform leading edge due to the end wall profiling enables more purge flow to leave the rim seal cavity in a more axial direction, at lower spanwise position and along the hub end wall.

## Stage Efficiency

The rotor with profiled end walls and without pressure side separation showed the highest efficiency for all purge flow levels (5-hole probe measurements at the rotor exit). The best efficiency was measured at the low injection rate,  $91.0\% \pm 0.37\%$ . The end wall design increased the total-to-total efficiency by  $0.75\% \pm 0.32\%$  on average, the removal of the pressure side bubble by  $0.33\% \pm 0.32\%$ . Given the facts that the end wall profiling does not change the capacity of the turbine and only slightly reduces the overall reaction at the chosen operating point, the measured efficiency improvement can be considered to be relevant.

Furthermore, the 2<sup>nd</sup> end wall design successfully reduced the linear sensitivity of the purge flow to the injection rate by 30% from  $-1.541\%$  per %*IR* with cylindrical end walls to  $-1.17\%$  per %*IR*. In terms of an exchange rate, the 1<sup>st</sup> rotor end wall design is able to compensate for the efficiency deficit due to 0.6% of additional purge flow. The 2<sup>nd</sup> end wall design also removing the pressure side bubble can compensate for 0.8% of additional purge flow. The beneficial contribution of the shroud end wall design to the overall stage efficiency improvement is approximately five times lower compared to the overall efficiency improvement.

The measured 1.5-stage efficiency improvement due to the 1<sup>st</sup> end wall design is  $0.8\% \pm 0.32\%$  and slightly higher compared to the 1-stage efficiency. Hence, the rotor end wall profiling also tends to increase the efficiency of the second nozzle guide vane.

## Combined Effects

The effects on the rotor hub passage vortex caused by the rotor end wall design and the purge flow are intrinsically similar and can therefore be compared with each other. The additional purge flow increases the maximum unsteadiness, the circulation and the relative total pressure in the hub loss core for all rotor geometries. With cylindrical end walls these sensitivities are 60%, 20% and  $-2.5\%$  per %*IR*. However the sensitivities of these parameters to purge flow depend on the rotor geometry and can be approximately halved in the presence of the 2<sup>nd</sup> end wall design. Depending on the rotor geometry the purge flow causes the hub passage vortex to radially migrate by 7% to 10% per percent of injected purge flow.

The parameters characterising the impact of the purge flow and the end wall profiling on the rotor hub passage vortex can also be analysed as a function of its radial coordinate. The peak *rms* and the circulation of the hub loss core as well as the stage efficiency appear to scale in a relatively linear manner with respect to its radial height. The sensitivity again depends on the rotor geometry.

## Rotor Hub Passage Vortex Behaviour

Time-resolved measurements showed a highly unsteady movement of the hub loss core due to the blade row interaction. The core of the hub passage vortex was found to travel 10% span in the radial direction and 40% rotor pitch in the circumferential direction under the effect of the downstream stator blade passing event. These numbers are unaffected by the injection rate. However at a higher injection rate the hub loss core swings 30% more rapidly past the NGV2 leading edge potential field. At this injection rate, the hub loss core transports higher unsteadiness at lower static pressure. The unsteady movement of the hub passage vortex was found to locally increase the range of the incidence on the NGV2 between minimum and maximum by  $15^\circ$  per percent of injected purge flow, also increasing the loss at the NGV2.

## 8.3. Suggestions for Future Work

Among all the different topic discussed in this work, the pressure side bubble offers the highest potential to be further investigated. The description of the pressure side bubble mainly relies on the unsteady CFD simulations.

In a real low-pressure turbine application the Reynolds numbers may be lower than the Reynolds number of the rotor investigated during this work. The influence of the Reynolds number on the unsteady behaviour, size, volume and fluid shedding mechanism and the corresponding sensitivities should be investigated.

Measurements at the rotor exit showed fluctuating radial vorticity and circumferential speed of the rotor wake when time space plots are considered. These measurements indicate varying lift on the rotor airfoil which may interact with the pressure side separation bubble. The change in lift might be the reason for the bubble to shed its fluid.

In the present work the behaviour of the pressure side bubble was investigated using time-accurate CFD predictions. Rotor mounted instrumentation would allow one to experimentally verify the numerical prediction of the behaviour and size of the pressure side separation.

The predictions, especially in the region of the pressure side separation, can be improved when using large eddy simulation (LES) or direct numerical simulation (DNS) as soon as they become affordable in terms of computing power and cost.

The nature of the unsteady flow field in the rim seal and in the upstream shroud cavity are intrinsically similar, with the difference of a net mass flow out of the cavity for the rim seal cavity and a net mass flow in the cavity for the upstream shroud cavity. The work of Barmपालias et al. [3] shows that an intelligent design of the cavity volume and aspect ratio leads to an increase in stage efficiency. The presented design guide lines can be applied to the rim seal cavity and the potential performance benefits should be assessed.

The solidity of the blade rows has an influence on the amount of required rim seal purge flow. With more blades the maximum static pressure variation caused by the blade potential fields is reduced at the rim seal exit. Hence, less purge flow is required to prevent the hot gases to ingest in the cavity. On the other hand a higher blade count increases the weight and cost of the turbine. The presented work provides information about the potential efficiency benefits due to the reduction of purge flow at higher solidity. This efficiency benefit can be compared to the economical penalties caused by the increased blade count and an optimum can be found.

The results of this work have shown that the radial migration of the rotor hub passage vortex increases the loss. Maybe a series of rotor design modifications could be made with the intent to keep the rotor passage vortex at the lowest radius possible. Within the mechanical stress constraints a

combination of twist, blade lean and end wall profiling might be used to minimise the radial migration of the hub loss core.

In the presented work the shroud end wall profiling has improved the relative loss and efficiency in the tip region. However it is not known whether the same improvements due to a non-axisymmetric shroud can be achieved when it is cut back. In this context the interaction of the shroud cavity exit flow and the main flow could be investigated in order to better understand the unsteady interaction mechanisms involved.

An attempt should be made in order to incorporate the latest achievements in the context of this work and related to the probe technology, such as matching grid, pitch angle sensitivity in sheared flows, influence of the probe access hole and the deflection of the probe due to the aerodynamic load. Taking into account all these corrections the measurement accuracy is expected to improve, especially for the pitch angle and radial velocity.

Finally it should be investigated whether the sensitivity reduction to purge flow achieved for the tested rotor geometries is generic and can be repeated for other rotor geometries.



# Bibliography

- [1] U.S. Energy Information Administration. World electricity data. <http://www.eia.gov/iea/elec>, 2011.
- [2] M. J. Atkins. Secondary Losses and End-Wall Profiling in a Turbine Cascade. *IMechE*, C255/87:29–42, 1987.
- [3] K. G. Barmpalias. *Steam Turbine Aerodynamics and Geometry Optimization for Effective Reduction of Leakage Flow Interactions*. PhD Thesis, Diss. ETH No. 19904, Zurich, Switzerland, 2011.
- [4] K. G. Barmpalias, A. I. Kalfas, R. S. Abhari, T. Hirano, N. Shibukawa, and T. Sasaki. Design Considerations for Axial Steam Turbine Rotor Inlet Cavity Volume and Length Scale. In *Proceedings of the ASME Turbo Expo, GT2011-45217*, Vancouver, 2011.
- [5] F. Bashforth and J. C. Adams. An Attempt to Test the Theories of Capillary Action by Comparing the Theoretical and Measured Forms of Drops of Fluid, with an Explanation of the Method of Integration Employed in Constructing the Tables which give the Theoretical Forms of Such Drops. *Cambridge University Press*, 1883.
- [6] T. Behr. *Control of Rotor Tip Leakage and Secondary Flow by Casing Air Injection in Unshrouded Axial Turbines*. PhD Thesis, Diss. ETH No. 17283, Zurich, Switzerland, 2007.
- [7] T. Behr, A. I. Kalfas, and R. S. Abhari. Unsteady Flow Physics and Performance of a One-and 1/2-Stage Unshrouded High Work Turbine. *Journal of Turbomachinery-Transactions of the ASME*, 129(2):348–359, 2007.
- [8] T. Behr, A. I. Kalfas, and R. S. Abhari. Control of Rotor Tip Leakage through Cooling Injection from the Casing in a High-Work Turbine. *Journal of Turbomachinery-Transactions of the ASME*, 130(3):031014, 12p., 2008.

- [9] T. Behr, L. Porreca, T. Mokulys, A. I. Kalfas, and R. S. Abhari. Multistage Aspects and Unsteady Flow Effects of Stator and Rotor Clocking in an Axial Turbine with Low Aspect Ratio Blading. *Journal of Turbomachinery-Transactions of the ASME*, 128(1):11–22, 2006.
- [10] Th. E. Biesinger. *Secondary Flow Reduction Techniques in Linear Turbine Cascades*. PhD Thesis, University of Durham, UK, 1993.
- [11] A. Binder, W. Forster, K. Mach, and H. Rogge. Unsteady Flow Interaction Caused by Stator Secondary Vortices in a Turbine Rotor. *Journal of Turbomachinery-Transactions of the ASME*, 109(2):251–257, 1987.
- [12] J. P. Bindon. The Measurement and Formation of Tip Clearance Loss. *Journal of Turbomachinery of the ASME*, 111(3):257–263, 1989.
- [13] J. Boudet, N. J. Hills, and J. W. Chew. Numerical Simulation of the Flow Interaction Between Turbine Main Annulus and Disc Cavities. In *Proceedings of the ASME Turbo Expo, GT-2006-90307*, Barcelona, 2006.
- [14] M. J. Brear, H. P. Hodson, Paloma Gonzalez, and N. W. Harvey. Pressure Surface Separations in Low-Pressure Turbines - Part 2: Interactions with the Secondary Flow. *Journal of Turbomachinery of the ASME*, 124(3):402–409, 2002.
- [15] M. J. Brear, H. P. Hodson, and N. W. Harvey. Pressure Surface Separations in Low-Pressure Turbines - Part 1: Midspan Behaviour. *Journal of Turbomachinery-Transactions of the ASME*, 124(3):393–401, 2002.
- [16] G. Brennan, N. W. Harvey, M. G. Rose, N. Fomison, and M. D. Taylor. Improving the Efficiency of the Trent 500 HP Turbine Using Non-Axisymmetric End Walls: Part I: Turbine Design. In *Proceedings of the ASME Turbo Expo, 2001-GT-0444*, 2001.
- [17] V. S. P. Chaluvadi, A. I. Kalfas, and H. P. Hodson. Blade Row Interaction in a High-Pressure Steam Turbine. *Journal of Turbomachinery-Transactions of the ASME*, 125(1):14–24, 2001.
- [18] V. S. P. Chaluvadi, A. I. Kalfas, and H. P. Hodson. Vortex Transport and Blade Interactions in High Pressure Turbines. *Journal of Turbomachinery-Transactions of the ASME*, 126(3):395–406, 2004.

- [19] J. W. Chew, S. Dadkhah, and A. B. Turner. Rim Sealing of Rotor-Stator Wheelspaces in the Absence of External Flow. *Journal of Turbomachinery-Transactions of the ASME*, 114(2):433–438, 1992.
- [20] N. A. Cumpsty. *Compressor Aerodynamics*. Longman, 1989.
- [21] E. M. Curtis, H. P. Hodson, M. R. Banieghbal, J. D. Denton, R. J. Howell, and N. W. Harvey. Development of Blade Profiles for Low-Pressure Turbine Applications. *Journal of Turbomachinery-Transactions of the ASME*, 119(3):531–538, 1997.
- [22] S. Dadkhah, A. B. Turner, and J. W. Chew. Performance of Radial Clearance Rim Seals in Upstream and Downstream Rotor-Stator wheelspaces. *Journal of Turbomachinery-Transactions of the ASME*, 114(2):439–445, 1992.
- [23] C. D. Dean. On the Necessity of Unsteady Flow in Fluid Machines. *Journal of Basic Engineering -Transactions of the ASME*, 81(1):24–28, 1959.
- [24] M. E. Dejc and A. E. Zarjankin. Methods of Increasing the Efficiency of Turbine Stages. *Teploenergetika*, 2:18–24, 1960.
- [25] J. D. Denton. Loss Mechanisms in Turbomachines. *Journal of Turbomachinery-Transactions of the ASME*, 115(4):621–656, 1993.
- [26] V. Dossena, A. Perdichizzi, and M. Savini. The Influence of Endwall Contouring on the Performance of a Turbine Nozzle Guide Vane. *Journal of Turbomachinery-Transactions of the ASME*, 121(2):200–208, 1999.
- [27] A. Duden, I. Raab, and L. Fottner. Controlling the Secondary Flow in a Turbine Cascade by 3D Airfoil Design and Endwall Contouring. In *Proceedings of the ASME Turbo Expo, 98-GT-072*, 1998.
- [28] K. Ettlin. *Interaction Mechanisms Between Probe and Turbine Boundary Layer*. ETH Zurich, Semester Thesis, 2011.
- [29] T. Germain, M. Nagel, and R.-D. Baier. Visualization and Quantification of Secondary Flows: Application to Turbine Bladings with 3D-Endwalls. In *Proceedings of the 8<sup>th</sup> ISAIF*, Lyon, 2007.

- [30] S. Girgis, E. Vlastic, J.-P. Lavoie, and S. H. Moustapha. The Effect of Secondary Air Injection on the Performance of a Transonic Turbine Stage. In *Proceedings of the ASME Turbo Expo, GT-2002-30340*, Amsterdam, 2002.
- [31] C. Gossweiler. *Sonden und Messsystem fuer schnelle aerodynamische Stroemungsmessung mit piezoresistiven Druckgebern*. PhD Thesis, Diss. ETH No. 10253, Zurich, Switzerland, 1993.
- [32] D. G. Gregory-Smith, C. P. Graves, and J. A. Walsh. Growth of Secondary Losses and Vorticity in an Axial Turbine Cascade. *Journal of Turbomachinery-Transactions of the ASME*, 110(1):1–8, 1988.
- [33] E. M. Greitzer, C. S. Tan, and M. B. Graf. *Internal Flow, Concepts and Applications*. Cambridge University Press, Camebridge, 1st edition, 2004.
- [34] S. Harrison. The Influence of Blade Lean on Turbine Losses. *Journal of Turbomachinery-Transactions of the ASME*, 114(1):184–190, 1992.
- [35] J. C. Hartland, D. G. Gregory-Smith, N. W. Harvey, and M. G. Rose. Nonaxisymmetric Turbine End Wall Design: Part II - Experimental Validation. *Journal of Turbomachinery-Transactions of the ASME*, 122(2):286–293, 2000.
- [36] N. W. Harvey, M. G. Rose, M. D. Taylor, S. Shahpar, J. C. Hartland, and D. G. Gregory-Smith. Nonaxisymmetric Turbine End Wall Design: Part I - Three-Dimensional Linear Design System. *Journal of Turbomachinery-Transactions of the ASME*, 122(2):278–285, 2000.
- [37] W. R. Hawthorne. Secondary Circulation in Fluid Flow. *Proceedings of the Royal Society of London. Series A, Mathematical and Physical Sciences*, 206(1086):374–387, 1951.
- [38] W. R. Hawthorne. Rotational Flow Through Cascades. *Journal of Mech. and Appl. Math*, 3, 1955.
- [39] H. P. Hodson and W. N. Dawes. On the Interpretation of Measured Profile Losses in Unsteady Wake-Turbine Blade Interaction Studies. *Journal of Turbomachinery-Transactions of the ASME*, 120(2):276–284, 1998.

- [40] H. P. Hodson and R. G. Dominy. The Off-Design Performance of a Low-Pressure Turbine Cascade. *Journal of Turbomachinery of the ASME*, 109(2):201–209, 1987.
- [41] J. C. R. Hunt, A. A. Wray, and P. Moin. Eddies, Streams, and Convergence Zones in Turbulent Flows. In *Proceedings of the Summer Program (SEE N89-24538 18-34)*, pages 193–208, Center for Turbulence Research, 1988.
- [42] G. L. Ingram, D. G. Gregory-Smith, M. G. Rose, N. W. Harvey, and G. Brennan. The Effect of End-Wall Profiling on Secondary Flow and Loss Development in a Turbine Cascade. In *Proceedings of the ASME Turbo Expo, GT-2002-30339*, 2002.
- [43] Airports Council International. <http://www.airports.org>, 2011.
- [44] ISO. *Guide to the Expression of Uncertainty in Measurement (GUM)*. International Organisation for Standardisation (Geneva, Switzerland), ISBN 92-67-1011889, 1st edition, 1993.
- [45] C. E. Kachel and J. D. Denton. Experimental and Numerical Investigation of the Unsteady Surface Pressure in a Three-Stage Model of an Axial High Pressure Turbine. *Journal of Turbomachinery of the ASME*, 128(2):261–272, 2004.
- [46] Ch. Kasper, M.G. Rose, S. Staudacher, and J. Gier. A Study of Unsteady Secondary Flow in a Water Flow Axial Turbine Model. In *Proceedings of the ASME Turbo Expo, GT2008-50239*, 2008.
- [47] N. Kobayashi, M. Matsumoto, and M. Shizuya. An Experimental Investigation of a Gas-Turbine Disk Cooling System. *Journal of Engineering for Gas Turbines and Power-Transactions of the ASME*, 106(1):136–141, 1984.
- [48] P. Kupferschmied. *Zur Methodik zeitaufgeloester Messungen mit Stroemungssonden in Verdichtern und Turbinen*. PhD Thesis, Diss. ETH No. 12474, Zurich, Switzerland, 1998.
- [49] L. S. Langston. Secondary Flows in Axial Turbines - A Review. *Heat Transfer in Gas Turbine Systems, Annals of the New York Academy of Sciences*, 934(1):11–26, 2001.

- [50] L. S. Langston, M. L. Nice, and R. M. Hooper. 3-Dimensional Flow within a Turbine Cascade Passage. *Journal of Engineering for Power-Transactions of the ASME*, 99(1):21–28, 1977.
- [51] Ch. Lenherr. *High Temperature Fast Responce Aeordynamic Probe*. PhD Thesis, Diss. ETH No. 19367, Zurich, Switzerland, 2011.
- [52] Ch. Lenherr, A. I. Kalfas, and R. S. Abhari. High Temperature Fast Response Aerodynamic Probe. *J. Eng. Gas Turbines Power-Transactions of the ASME*, 133(1):011603, 10p., 2011.
- [53] M. Mansour. *A 48kHz Bandwidth, 1.8mm Diameter Entropy Probe for Aerothermal Loss Measurements in Turbomachinery Flows*. PhD Thesis, Diss. ETH No. 18087, Zurich, Switzerland, 2009.
- [54] M. Mansour, N. Chokani, A. Kalfas, and R. S. Abhari. Time-resolved Entropy Measurements Using a Fast Response Entropy Probe. *Measurement Science and Technology*, 19(11), 2008.
- [55] M. Mansour, N. Chokani, A. Kalfas, and R. S. Abhari. Unsteady Entropy Measurements in a High Speed Radial Compressor. *Journal of Engineering for Gas Turbines and Power*, 130(2), 2008.
- [56] R. Marini and S. Girgis. The Effect of Blade Leading Edge Platform Shape on Upstream Disk Cavity to Mainstream Flow Interaction of a High-Pressure Turbine Stage. In *Proceedings of the ASME Turbo Expo, GT2007-27429*, Montreal, 2007.
- [57] T. Matsunuma. Unsteady Flow Field of an Axial-Flow Turbine Rotor at a Low Reynolds Number. *Journal of Turbomachinery-Transactions of the ASME*, 129(2):360–371, 2007.
- [58] C. McLean, C. Camci, and B. Glezer. Mainstream Aerodynamic Effects Due to Wheel-space Coolant Injection in a High-Pressure Turbine Stage: Part I - Aerodynamic Measurements in the Stationary Frame. *Journal of Turbomachinery-Transactions of the ASME*, 123(4):687–696, 2001.
- [59] C. McLean, C. Camci, and B. Glezer. Mainstream Aerodynamic Effects Due to Wheel-space Coolant Injection in a High-Pressure Turbine Stage: Part II - Aerodynamic Measurements in the Rotational Frame. *Journal of Turbomachinery-Transactions of the ASME*, 123(4):697–703, 2001.

- [60] R. N. Meyer. The Effect of Wakes on the Transient Pressure and Velocity Distribution in Turbomachines. *Journal of Basic Engineering -Transactions of the ASME*, 80(1):1544–1552, 1958.
- [61] A. V. Mirzamoghadam, G. Heitland, and K. M. Hosseini. The Effect of Annulus Performance Parameters on Rotor-Stator Cavity Sealing Flow. In *Proceedings of the ASME Turbo Expo, GT2009-59380*, Orlando, 2009.
- [62] A. V. Mirzamoghadam, G. Heitland, M. C. Morris, J. Smokte, M. Malak, and J. Howe. 3D CFD Ingestion Evaluation of a High Pressure Turbine Rim Seal Disk Cavity. In *Proceedings of the ASME Turbo Expo, GT2008-50531*, Berlin, 2008.
- [63] J. Moore. Wake and an eddy in a Rotating, Radial-Flow Passage, Part 1: Experimental Observations. *ASME Journal of engineering for Power*, 95(3):205–212, 1973.
- [64] J. Moore and R. Adhye. Secondary Flows and Losses Downstream of a Turbine Cascade. *Journal of Engineering for Gas Turbines and Power-Transactions of the ASME*, 107(4):961–968, 1985.
- [65] J. Moore, D. M. Shaffer, and J. G. Moore. Reynolds Stresses and Dissipation Mechanisms Downstream of a Turbine Cascade. *Journal of Turbomachinery of the ASME*, 109(2):258–267, 1987.
- [66] A. W. H. Morris and R. G. Hoare. Secondary Loss Measurements in a Cascade of Turbine Blades with Meridional Wall Profiling. *ASME Paper No. 75-WA/GT-13*, 98(2), 1975.
- [67] S. H. Moustapha, G. J. Paron, and J. H. T. Wade. Secondary Flows in Cascades of Highly Loaded Turbine Blades. *Journal of Engineering for Gas Turbines and Power-Transactions of the ASME*, 107(4):1031–1038, 1985.
- [68] Y. Okita, M. Nishiura, S. Yamawaki, and Y. Hironaka. A Novel Cooling Method for Turbine Rotor-Stator Rim Cavities Affected by Mainstream Ingress. *Journal of Engineering for Gas Turbines and Power-Transactions of the ASME*, 127(4):798–806, 2005.
- [69] J. H. P. Ong, R. J. Miller, and S. Uchida. The Effect of Coolant Injection on the Endwall Flow of a High Pressure Turbine. In *Proceedings of the ASME Turbo Expo, GT2006-91060*, Barcelona, 2006.

- [70] OPEC Organization of Petroleum Exporting Countries. <http://www.opec.org>, 2012.
- [71] G. Paniagua, R. Denos, and S. Almeida. Effect of the Hub Endwall Cavity Flow on the Flow-Field of a Transonic High-Pressure Turbine. *Journal of Turbomachinery-Transactions of the ASME*, 126(4):578–586, 2004.
- [72] R. Parker and J. F. Watson. Interaction Effects Between Blade Rows in Turbomachines. *Proc. of I.Mech.E*, 186(21), 1972.
- [73] A. Pfau. *Loss Mechanisms in Labyrinth Seals of Shrouded Axial Turbines*. PhD Thesis, Diss. ETH No. 15226, Zurich, Switzerland, 2003.
- [74] A. Pfau, J. Schlienger, A. I. Kalfas, and R. S. Abhari. Virtual Four Sensor Fast Response Aerodynamic Probe (FRAP). In *The 16th Symposium on Measuring Techniques in Cascades and Turbomachines*, Cambridge, UK, 2002.
- [75] A. Pfau, J. Schlienger, A. I. Kalfas, and R. S. Abhari. Unsteady, 3-Dimensional Flow Measurement Using a Miniature Virtual 4 Sensor Fast Response Aerodynamic Probe (FRAP). In *Proceedings of the ASME Turbo Expo, GT2003-38128*, Atlanta, 2003.
- [76] L. Porreca. *Aerothermal Optimization of Partially Shrouded Axial Turbines*. PhD Thesis, Diss. ETH No. 17138, Zurich, Switzerland, 2007.
- [77] L. Porreca, M. Hollenstein, A. I. Kalfas, and R. S. Abhari. Turbulence Measurements and Analysis in a Multistage Axial Turbine. *Journal of Propulsion and Power*, 23(1):227–234, 2007.
- [78] L. Porreca, A. I. Kalfas, and R. S. Abhari. Optimized Shroud Design for Axial Turbine Aerodynamic Performance. *Journal of Turbomachinery-Transactions of the ASME*, 130(3):031016, 12p., 2008.
- [79] T. J. Praisner, E. Allen-Bradley, E. A. Grover, D. C. Knezevici, and S. A. Sjolander. Application of Non-Axisymmetric Endwall Contouring to Conventional and High-Lift Turbine Airfoils. In *Proceedings of the ASME Turbo Expo, GT2007-27579*, volume 6, 2007.

- [80] P. Rebholz. *Unsteady CFD Simulation of Purge Flow in the Presence of Profiled NGV and Rotor End Walls*. ETH Zurich, Master Thesis, 2011.
- [81] K. Reid, J. Denton, G. Pullan, E. Curtis, and J. Longley. The Effect of Stator-Rotor Hub Sealing Flow on the Mainstream Aerodynamics of a Turbine. In *Proceedings of the ASME Turbo Expo, GT-2006-90838*, Barcelona, 2006.
- [82] G. Riollet. Curved Channels Through which a Gas or Vapor Flows. *United States Patent 3529631*, 1970.
- [83] M. G. Rose. Non-Axisymmetric Endwall Profiling in the HP NGVs of an Axial Flow Gas Turbine. In *Proceedings of the ASME Turbo Expo, 94-GT-249*, 1994.
- [84] M. G. Rose. *Unsteady Flows in Axial Turbines*. Verlag im Internet GmbH, dissertation.de, Institut fuer Luftfahrtantriebe (ILA), Stuttgart University, 2011.
- [85] M. G. Rose and N. W. Harvey. Turbomachinery Wakes: Differential Work and Mixing Losses. *Journal of Turbomachinery-Transactions of the ASME*, 122(1):68–77, 2000.
- [86] M. G. Rose, N. W. Harvey, P. Seaman, D. A. Newman, and D. McManus. Improving the Efficiency of the Trent 500 HP Turbine Using Non-Axisymmetric End Walls: Part II: Experimental Validation. In *Proceedings of the ASME Turbo Expo, 2001-GT-0505*, 2001.
- [87] R. P. Roy, G. Xu, J. Feng, and S. Kang. Pressure Field and Main-Stream Gas Ingestion in a Rotor-Stator Disk Cavity. In *Proceedings of the ASME Turbo Expo, 2001-GT-0564*, New Orleans, 2001.
- [88] H. Sauer, R. Muller, and K. Vogeler. Reduction of Secondary Flow Losses in Turbine Cascades by Leading Edge Modifications at the Endwall. *Journal of Turbomachinery-Transactions of the ASME*, 123(2):207–213, 2001.
- [89] H. Schlichting. *Grenzschicht-Theorie*. G. Braun, Karlsruhe, 1951.
- [90] J. Schlienger. *Evolution of Unsteady Secondary Flows in a Multistage Shrouded Axial Turbine*. PhD Thesis, Diss. ETH No. 15230, Zurich, Switzerland, 2003.

- [91] P. Schuepbach. *Influence of Rim Seal Purge Flow on the Performance of an End Wall Profiled Axial Turbine*. PhD Thesis, Diss. ETH No. 18458, Zurich, Switzerland, 2009.
- [92] P. Schuepbach, M. G. Rose, R. S. Abhari, T. Germain, I. Raab, and J. Gier. Improving Efficiency of a High-Work Turbine Using Non-Axisymmetric Endwalls. Part II: Time-Resolved Flow Physics. In *Proceedings of the ASME Turbo Expo, GT2008-50470*, Berlin, 2008.
- [93] P. Schuepbach, M. G. Rose, R. S. Abhari, T. Germain, I. Raab, and J. Gier. Effects of Suction and Injection Purge-Flow on the Secondary Flow Structures of a High-Work Turbine. *Journal of Turbomachinery-Transactions of the ASME*, 132(2), 2010.
- [94] P. Schuepbach, M. G. Rose, R. S. Abhari, and J. Gier. Influence of Rim Seal Flow on the Performance of an Endwall-Profiled Axial Turbine. *Journal of Turbomachinery-Transactions of the ASME*, 133(1), 2011.
- [95] M. Sell, J. Schlienger, A. Pfau, M. Treiber, and R. S. Abhari. The 2-Stage Axial Turbine Test Facility *LISA*. In *Proceedings of the ASME Turbo Expo, 2001-GT-0492*, New Orleans, 2001.
- [96] O. P. Sharma and T. L. Butler. Predictions of Endwall Losses and Secondary Flows in Axial Turbine Cascades. *Journal of Turbomachinery-Transactions of the ASME*, 109(2):229–236, 1987.
- [97] O. P. Sharma, T. L. Butler, H. D. Joslyn, and R. P. Dring. 3-Dimensional Unsteady-Flow in an Axial-Flow Turbine. *Journal of Propulsion and Power*, 1(1):29–38, 1985.
- [98] C. H. Sieverding. Recent Progress in the Understanding of Basic Aspects of Secondary Flows in Turbine Blade Passages. *Journal of Engineering for Gas Turbines and Power-Transactions of the ASME*, 107(2):248–257, 1985.
- [99] C. H. Sieverding and P. Van den Bosche. The Use of Coloured Smoke to Visualize Secondary Flows in a Turbine Blade cascade. *Journal of Fluid Mechanics*, 134:85–89, 1983.
- [100] H. B. Squire and K. G. Winter. The Secondary Flow in Cascade of Airfoils in a Nonuniform Stream. *Journal Aeronautical Sciences*, 18(4):271–277, 1951.

- [101] W. Sturm, H. Scheugenpflug, and L. Fottner. Performance Improvements of Compressor Cascades by Controlling the Profile and Side-wall Boundary-Layers. *Journal of Turbomachinery-Transactions of the ASME*, 114(3):477–486, 1992.
- [102] W. Traupel. *Thermische Turbomaschinen, Band I, Thermodynamisch-stroemungstechnische Berechnung*. Springer-Verlag, Berlin [etc.], 3rd edition, 1988.
- [103] J. A. Walsh and D. G. Gregory-Smith. The Effect of Inlet Skew on Secondary Flows and Losses in a Turbine Cascade. *IMechE*, C275/87, 1987.
- [104] A. Yamamoto. Production and Development of Secondary Flows and Losses in Two Types of Straight Turbine Cascades: Part I - A Stator Case. *Journal of Turbomachinery-Transactions of the ASME*, 109(2):186–193, 1987.
- [105] A. Yamamoto. Production and Development of Secondary Flows and Losses in Two Types of Straight Turbine Cascades: Part II - A Rotor Case. *Journal of Turbomachinery-Transactions of the ASME*, 109(2):194–200, 1987.
- [106] A. Yamamoto and H. Nouse. Effects of Incidence on Three-Dimensional Flows in a Linear Turbine Cascade. *Journal of Turbomachinery of the ASME*, 110(4):486–496, 1988.



# A. Nomenclature

## Symbols

$A$	area	[m <sup>2</sup> ]
$C_{ax}$	axial chord	[-]
$C_P$	specific heat	[J/kg/K]
$C_p$	normalised pressure	[-]
$Ct$	normalised temperature	[-]
$h$	specific enthalpy	[J/kg]
$I$	specific rothalpy	[J/kg]
$IR$	injection rate	[%]
$K$	calibration sensitivity coefficients	[-]
$k$	coefficients of calibration polynomial	[-]
$k$	uncertainty coverage factor	[-]
$M$	torque	[Nm]
$M$	Mach number	[-]
$\dot{m}$	mass flow	[kg/s]
$P$	pressure	[Pa]
$\bar{P}$	time-averaged pressure part	[Pa]
$P'$	random pressure part	[Pa]
$\tilde{P}$	periodic pressure part	[Pa]
$Q$	Q-factor	[1/s <sup>2</sup> ]
$R$	gas constant	[J/kg/K]
$Re$	Reynolds number	[-]
$r$	radial coordinate	[m]
$s$	entropy	[J/kg/K]
$T$	temperature	[K]
$T$	blade passing period	[s]
$t$	time	[s]
$U$	blade speed	[m/s]
$U$	voltage	[V]

$V$	velocity	[m/s]
$x$	axial coordinate	[m]
$Y$	total pressure loss coefficient	[-]
$y^+$	non-dimensional wall distance	[-]

## Greek

$\gamma$	pitch angle	[°]
$\eta$	efficiency	[-]
$\theta$	circumferential coordinate	[rad]
$\kappa$	ratio of specific heats	[-]
$\Pi$	turbine pressure ratio	[-]
$\rho$	density	[kg/m <sup>3</sup> ]
$\varphi$	yaw angle	[°]
$\omega$	rotational speed	[rps]
$\Omega$	vorticity	[1/s]
$\Phi$	viscous dissipation function	[1/s <sup>2</sup> ]
$\mu$	laminar viscosity	[Pa·s]
$\Psi$	circulation	[m <sup>2</sup> /s]
$\chi$	availability	[J/kg]

## Subscripts

atm	atmospheric
cavity	flow quantity in rim seal cavity
DC	direct current
ex	row exit
$i$	velocity component index
in	turbine inlet
is	isentropic
$j$	velocity component index
main	main flow quantity
$r$	radial coordinate
red	reduced flow quantity
ref	reference quantity
rel	relative frame
s	static flow quantity
S	streamwise

---

$t$	stagnation flow quantity
$tt$	total-to-total
$x$	axial coordinate
$\gamma$	pitch angle
$\theta$	circumferential coordinate
$\varphi$	yaw angle
1.5	total-to-static 1.5 stages

## Abbreviations

CFD	computational fluid dynamics
EXP	measured data
FENT	fast entropy probe
FEM	finite element method
FRAP	fast response aerodynamic probe
GUM	guide of uncertainty in measurements
LEC	Laboratory for Energy Conversation
LDA	laser doppler anemometry
NGV1	first nozzle guide vane
NGV2	second nozzle guide vane
PIV	particle image velocimetry
PT <sub>100</sub>	platinum resistance thermometer
R1	blade row
<i>rms</i>	root mean square
1. Gen.	first end wall design
2. Gen.	second end wall design
3D	three-dimensional
4HP	4-hole probe
5HP	5-hole probe



## B. List of Publications

Jenny, P., Lenherr, C., Kalfas, A. I. and Abhari, R. S. "Effect of Unsteady Blade Row Interaction on Hot Streak Migration in an Axial Turbine", ASME Turbo Expo, Glasgow, 2010, GT2010-23034, accepted for publication in ASME Journal of Turbomachinery, 134(5), September 2012

Jenny, P., Abhari, R. S., Rose, M. G., Brettschneider, M. and Gier, J., "A Low Pressure Turbine with Profiled End Walls and Purge Flow Operating with a Pressure Side Bubble", ASME Turbo Expo, Vancouver, 2011, GT2011-46309, accepted for publication in Journal of Turbomachinery

Jenny, P., Abhari, R.S., Rose, M.G., Brettschneider, M., Gier, J., Engel, K., "Low-Pressure Turbine End Wall Design Optimisation and Experimental Verification in the Presence of Purge Flow", 20th International Symposium on Air-Breathing Engines, Gothenburg, Sweden, ISABE Paper Presentation, 2011

Jenny, P., Abhari, R.S., Rose, M.G., Brettschneider, M., Gier, J., Engel, K., "Unsteady Rotor Hub Passage Vortex Behavior in the Presence of Purge Flow in an Axial Low Pressure Turbine", ASME Turbo Expo, Copenhagen, 2012, GT2012-69256, accepted for publication in Journal of Turbomachinery

Basol, A. M., Jenny, P., Lenherr, C., Kalfas, A. K., and Abhari, R. S., "Hot Streak Migration in a Turbine Stage: Effect of Mixing on Hot Streak Attenuation", Journal of Engineering for Gas Turbines and Power, 133(6), 2011

Lenherr, C., Jenny, P., Kalfas, A. I. and Abhari, R. S., "Time-Resolved Measurements of Hot Streaks in an Unshrouded Turbine Using a Novel High Temperature FRAP Probe." 19th International Symposium on Air-Breathing Engines, Montreal, Canada, ISABE Paper Presentation, 2009

Rose, M.G., Jenny, P., Abhari, R.S., Gier, J., "Experimentally Observed Unsteady Work at Inlet to and Exit from an Axial Flow Turbine Rotor", ASME Turbo Expo, Copenhagen, 2012, GT2012-69207, accepted for publication in Journal of Turbomachinery

Regina, K., Basol, A. M., Jenny, P., Kalfas, A. K., and Abhari, R. S., "Hot Streak Shaping and Migration in an Axial Turbine", International Gas Turbine Congress, Osaka, 2011, IGTC2011-ABS-0020

# C. Curriculum Vitae

## Personal Data

Philipp Jenny, born 5<sup>th</sup> August 1982 in Zurich, Switzerland

## Professional Experience

- 2008-2012    Research assistant and doctoral student, Laboratory for Energy Conversion, ETH Zurich
- 2007         End of study project, Performance Department, Rolls-Royce plc, Derby, United Kingdom
- 2006-2007    Industry project, in collaboration with the Performance Department, Airbus, Toulouse, France
- 2006         Research project, Department of flight mechanics, ONERA, Toulouse, France

## Education

- 2007         Dual master degree T.I.M.E.
- Master in mechanical engineering, Swiss Federal Institute of Technology, Lausanne
  - Master degree, Ecole nationale supérieure de l'aéronautique et de l'espace (SUPAERO), Toulouse, France
- 2005-2007    Studies at Ecole nationale supérieure de l'aéronautique et de l'espace (SUPAERO), Toulouse, France
- 2002-2005    Studies at Swiss Federal Institute of Technology, Lausanne